An Experimental Investigation into Smart Radio Environments

James Rains

Submitted in fulfilment of the requirements for the
Degree of Doctor of Philosophy

School of Engineering
College of Science and Engineering
University of Glasgow

December 2023

Abstract

The potential for dynamically manipulating the wireless channel introduces a revolutionary concept in wireless communication systems known as the smart radio environment (SRE). Recent works have suggested that SREs hold the promise of delivering unprecedented performance benefits to wireless networks. However, a notable gap exists as the overwhelming majority of published works on this subject lack a robust data-driven approach. This investigation into SREs sets out to bridge the chasm between theory and reality. Novel reconfigurable intelligent surface (RIS) prototypes have been developed, whose electromagnetic properties have been designed to efficiently reshape the wireless propagation environment to our advantage. Two extensive field measurement campaigns have been undertaken. A series of measurements obtained within RIS-aided wireless communication setups throughout an indoor environment reveal that substantial increases in channel gain are possible through strategic placement and configuration of these smart reflectors. Furthermore, frequency domain measurements obtained throughout an existing multi-antenna urban macrocell reveal the potential for contemporary networks to benefit from the SRE concept. The benefits RISs can bring to multiple-input multiple-output (MIMO) outdoor networks are revealed, alongside potentially detrimental impacts in the form of a reduced effective rank and increased interference. This works sheds a light on a number of practical issues, from design and implementation, to real-world deployment of RISs.

List of Publications

Published works relevant to this thesis are as follows:

Journals

J. Rains, J. ur Rehman Kazim, A. Tukmanov, T. J. Cui, L. Zhang, Q. H. Abbasi, and M. A. Imran, **"High-resolution programmable scattering for wireless coverage enhancement: An indoor field trial campaign,"** *IEEE Transactions on Antennas and Propagation*, vol. 71, pp. 518–530, Jan. 2023.

M. Usman, **J. Rains**, T. J. Cui, M. Z. Khan, J. ur Rehman Kazim, M. A. Imran, and Q. H. Abbasi, **"Intelligent wireless walls for contactless in-home monitoring,"** *Light: Science & Applications*, vol. 11, Jul 2022.

J. u. R. Kazim, A. Tahir, **J. Rains**, T. J. Cui, A. Jabbar, M. A. Jamshed, M. Ur-Rehman, A. Alomainy, M. A. Imran, and Q. H. Abbasi, **"In-home monitoring using wireless on the walls for future healthcare: Real-world demonstration,"** *Advanced Intelligent Systems*, vol. 5, July 2023

S. Hassouna, M. A. Jamshed, **J. Rains**, J. u. R. Kazim, M. U. Rehman, M. U. Rehman, M. Abualhayja, L. Mohjazi, T. J. Cui, M. A. Imran, and Q. H. Abbasi, **"A survey on reconfigurable intelligent surfaces: Wireless communication perspective,"** *IET Communications*, , vol. 17, pp. 497–537, Jan. 2023.

J. Rains, A. Tukmanov, Q. H. Abbasi, and M. A. Imran, **"Channel Measurements within a RIS-Aided Urban Macrocell,"** *Under review*, Dec. 2023.

Book chapters

J. Rains, J. ur Rehman Kazim, A. Tukmanov, L. Zhang, Q. H. Abbasi, and M. A. Imran, **"Practical Design Considerations for Reconfigurable Intelligent Surfaces,"** *Intelligent Reconfigurable Surfaces (IRS) for Prospective 6G Wireless Networks*, John Wiley & Sons, Dec. 2022

J. R. Kazim, **J. Rains**, M. A. Imran, and Q. H. Abbasi, **"Application and Future Direction of RIS,"** " *Intelligent Reconfigurable Surfaces (IRS) for Prospective 6G Wireless Networks*, John Wiley & Sons, Dec. 2022

Conferences

J. Rains, A. Tukmanov, Q. Abbasi, and M. Imran, **"RIS-Enhanced MIMO Channels in Urban Environments: Experimental Insights,"** in 2024 *18th European Conference on Antennas and Propagation (EuCAP)*, IEEE, Mar. 2024. Nominated for *Best Measurement Paper* award.

J. Rains, J. U. R. Kazim, A. Tukmanov, L. Zhang, Q. Abbasi, and M. Imran, **"Fully- addressable varactor-based reflecting metasurface with dual-linear polarisation for low power reconfigurable intelligent surfaces,"** in 2023 *17th European Conference on Anten- nas and Propagation (EuCAP)*, IEEE, Mar. 2023

J. Rains, J. U. R. Kazim, A. Tukmanov, L. Zhang, Q. Abbasi, and M. Imran, **"Varactor-Based Reconfigurable Intelligent Surface with Dual Linear Polarisation at K-Band"**, *2022 IEEE International Symposium on Antennas and Propagation and USNC-URSI Radio Science Meeting (APS/URSI)*, IEEE, July 2022

J. Rains, J. ur Rehman Kazim, A. Tukmanov, L. Zhang, Q. H. Abbasi, and M. Imran, **"Reflecting metasurface unit cell design with multi-bit azimuthal control,"** in *1st Interna- tional Conference on Microwave, Antennas and Circuits (ICMAC)*, 2021

J. Rains, J. ur Rehman Kazim, L. Zhang, Q. H. Abbasi, M. Imran, and A. Tukmanov, **"2.75-bit reflecting unit cell design for reconfigurable intelligent surfaces,"** in *2021 IEEE International Symposium on Antennas and Propagation and USNC-URSI Radio Science Meeting (APS/URSI)*, IEEE, Dec. 2021

S. Hassouna, **J. Rains**, J. U. R. Kazim, M. Ur Rehman, M. Imran, and Q. H. Abbasi, **"Investigating the data rate of intelligent reflecting surface under different deployments,"** in *2022 IEEE International Symposium on Antennas and Propagation and USNC-URSI Radio Science Meeting (AP-S/URSI)*, IEEE, July 2022.

S. Hassouna, **J. Rains**, J. Rehman Kazim, M. Ur Rehman, M. Imran, and Q. H. Abbasi, **"Discrete phase shifts for intelligent reflecting surfaces in ofdm communications,"** in *2022 International Workshop on Antenna Technology (iWAT)*, IEEE, May 2022.

List of Acronyms

5G	5th Generation
AMC	Artificial magnetic conductor
BPF	Bandpass filter
BS	Base station
BT	British Telecom
DAC	Digital to analog converter
DC	Direct current
EIRP	Effective isotropic radiated power
EES	Engineered electromagnetic surface
EPSRC	Engineering and Physical Sciences Research Council
ETSI	European Telecommunications Standards Institute
FDD	Frequency division duplexing
FPGA	Field programmable gate array
GRC	GNURadio companion
IRS	Intelligent reflecting surface
LC	Inductive-capacitive
LNA	Low noise amplifier
LoS	Line of sight
MIMO	Multiple-input multiple-output
MEMS	Micro-electromechanical systems

NLoS Non-line of sight

NR New radio

OFDM Orthogonal frequency division multiplexing

PA Power amplifier

PBC Periodic boundary condition

PDP Power delay profile

PEC Perfect electrical conductor

PIN Positive-intrinsic-negative

PSO Particle swarm optimisation

RCS Radar cross section

RET Remote electrical tilt

RIS Reconfigurable intelligent surface

RF Radio frequency

RoF Radio over fiber

RWG Rectangular waveguide

SDM Software-defined metasurface

SISO Single-input single-output

SOLT Short-open-load-through

TE Transverse-electric

TM Transverse-magnetic

TDD Time division duplexing

UC Unit cell

UE User equipment

USRP Universal software radio peripheral

VLoS Virtual-line of sight

VNA Vector network analyser

WI Wireless Insite

Contents

List of Tables

List of Figures

Acknowledgments

I would like to thank my academic supervisor, Prof. Muhammad Imran, who has been a constant source of support and inspiration throughout my PhD journey, offering many a word of wisdom. I would like to make known my great appreciation for the unwavering efforts of my academic supervisor, Prof. Qammer Abbasi, without whom this work would not have been possible. His mentorship and networking abilities are unparalleled, affording me opportunities to extend the scope of the work far beyond the shires of Scotland.

My sincere thanks go to my industrial supervisor, Dr. Anvar Tukmanov, for his consistent contributions to this research, offering an invaluable industry-focused outlook. Anvar went well out of his way to ensure success on the field trials work detailed in this thesis. I also would like to thank the Wireless Research Group at British Telecom for their insights and logistical support. As well as British Telecom themselves, and the Engineering and Physical Sciences Research Council (EPSRC) for funding this research.

A big shout-out to Dr. Jalil ur Rehman Kazim whose collaborative spirit rendered many aspects of this work successful. The list of fellow postgraduate researchers and staff that I called upon throughout this work would need a paper to itself - this is a product of the research culture that Profs. Imran and Abbasi have created within the CSI group. Nonetheless, I would like to thank collaborators Prof. Lei Zhang, Dr. Shuja Ansari, Dr. Muhammad Usman, Muhammad Zakir Khan, Saber Hassouna, Abdul Jabbar, Jaspreet Kaur, Dr. Muhammad Ali Jamshed, Dr. Zia Ullah Khan, and Dr. Kenechi Omeke.

I want to communicate my gratitude to Prof. Andreas Molisch and Dr. Naveed Abbasi at the University of Southern California for hosting me and facilitating a successful collaboration.

I want to convey my great appreciation for my family, many of whom I got to meet for the first time throughout the latter stages of this PhD. I would like to thank my mother Lorraine Denise Turney, my father Joseph Andrew Rains, and my brother Matthew Alexander Rains for their support and for their patience during my long absence. Lastly, I would like to express my deepest gratitude to my confidante, Cristhian Mace. She is a beacon of support, encouragement, and inspiration.

In acknowledgment,
James Samuel Rains

Declaration

I declare that, except where explicit reference is made to the contribution of others, that this thesis is the result of my own work and has not been submitted for any other degree at the University of Glasgow or any other institution.

James Rains

Chapter 1

Introduction

1.1 Background and motivation

As the world becomes more connected through the abundance of mobile devices such as smart phones, sensor networks, and autonomous vehicles, the burden on wireless communications infrastructure becomes ever-greater. According to the Ericsson mobility report released in November 2022 [9], mobile networks now carry more than 300 times more data traffic than in 2011. With the introduction of the fifth generation (5G) mobile network technology standard, predicted to account for over 5 billion mobile subscriptions by 2028, this figure is set to continue accelerating [10]. This increasing demand has been met by introducing multi-antenna technologies and state of the art modulation and coding schemes [11], but there is much scope for further development of enabling technologies and this thesis aims to explore a subset of these.

1.1.1 The radio environment

In a conventional cell-based wireless communications system, many users are located at the cell edge, where signal strength from the base station (BS) is significantly reduced and fading caused by obstructions and multipath propagation can be detrimental to service coverage [12]. For example, a common scenario is depicted in Fig. 1.1, where a base station wishes to serve a user terminal, denoted here as user equipment (UE), such as a smart phone, but it is located the other side of an occlusion such as an office building. The dominant component of the radiation from the base station appears to reflect from a nearby building. In this scenario, the wireless link is known as a non-line of sight (NLoS) communication channel. NLoS channels are characterised as relying on multipath propagation to reach the end nodes and wireless networks typically operate with mixed line of sight (LoS) and NLoS conditions. In this case, the user terminal will experience large fluctuations in received signal strength and this is highly location- and frequency-dependent.

Current solutions to extend wireless coverage include the deployment of additional base sta-

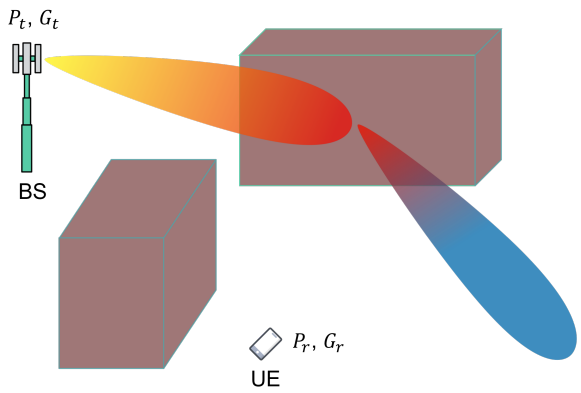

Figure 1.1: System model for conventional communication link with blockage from a nearby occlusion. The dominant path from the base station (BS) reflects in a specular-like fashion from a nearby structure. Received power levels at the user equipment (UE) are highly location- and frequency-dependent and quality of service may be reduced.

tions and the use of regenerative relays [13] [14]. The former approach comes with the high cost of site planning compounded with high power requirements and a fixed backhaul link. Regenerative relays overcome some of the challenges of installing new base stations, but still require non-negligible power levels and are not yet mature enough to provide reliable full-duplex operation [15] [16]. These approaches involve injecting more electromagnetic energy into the wireless environment through extra radio frequency (RF) chains, creating additional interference. Recently, a means of manipulating the wireless propagation environment to improve signal propagation characteristics, without the need to add additional radio sources to the system has attracted much attention from academia and industry [17].

1.1.2 The smart radio environment

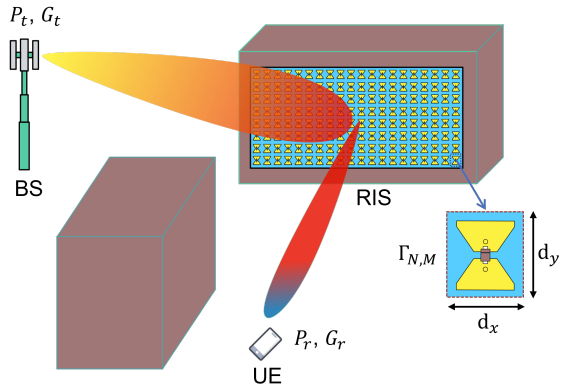

Figure 1.2: System model for RIS-aided communication link. An occlusion results in significant path loss between the transmitter base station and receiver user equipment. A RIS mounted on a building structure with line of sight to the transmitter and receiver redirects and reshapes the incident electromagnetic wave such to maximise the channel gain.

Mitigation of the effects of the wireless channel on a communication link is typically only performed at the end nodes (i.e., the BS and UE). Equalisation is performed and precoding schemes are utilised successfully in contemporary multiple-input multiple-output (MIMO) wireless systems [18]. However, the wireless channel remains uncontrollable. If we were able to make small modifications to the electromagnetic environment, it could be possible to jointly optimise not only the end nodes, but also certain characteristics of the wireless channel itself. Novel composite materials with controllable electromagnetic behaviour could enable us to program the propagation environment.

Recent advances in composite materials have given rise to what are known as metasurfaces. Metasurfaces, the two-dimensional equivalent of metamaterials [19], typically consist of a repeating pattern of electrically conducting elements, known as unit cells, printed on a dielectric substrate. These surfaces can provide wave transformations that are tailored for a (typically narrow) frequency band. Wave transformations of particular interest for wireless communications applications are beamforming and beam focusing. When embedding the constituent elements with a means of tunability, it is possible to create programmable metasurfaces whose wave transformation capabilities can be varied considerably. More advanced functionality has recently been revealed such as space-time modulation schemes and magnetless non-reciprocal scattering [20]. Inclusion of a processing unit and a means of remotely programming the metasurface results in what has been coined a reconfigurable intelligent surface (RIS), also known as an intelligent reflecting surface (IRS).

1.2 Problem statement

The smart radio environment paradigm, which leverages RISs, has been extensively explored in theory with mathematically-tractable models. These theoretical models have provided valuable insights into the potential benefits of RISs for enhancing wireless communication systems. However, at present, there is limited experimental verification of this concept in realistic scenarios. This gap in empirical evidence poses several significant challenges and opportunities for the field:

Real-world applicability: While theoretical models suggest that RISs can improve signal propagation and coverage, real-world wireless environments often introduce complexities that theoretical models do not fully account for. Experimental verification is essential to assess the feasibility and practicalities of implementing RIS in diverse, dynamic, and interference-prone wireless communication scenarios. Compared with prior works that often employ simplified measurement setups that are typically unrealistic and/or closely controlled to favor RIS propagation, this thesis details an extensive measurement campaign within an unmodified real-world multi-antenna urban macrocell.

Performance validation: Theoretical models often make simplifying assumptions about the

behavior of RIS and their interactions with wireless signals. Experimental verification is necessary to validate the actual performance gains that can be achieved through RIS deployment. This includes assessing metrics such as signal quality, coverage, energy efficiency, and interference management in real-world settings. This thesis goes beyond the scalar measurements of past works and provides details on the RIS-aided channel across wide bandwidths. Most RIS trials to date have employed single-directional antennas at terminal points, partly to simulate the directivity of antenna arrays. Yet, this approach risks skewing outcomes in favor of RIS-aided channels by inadvertently excluding valuable multipath components. Furthermore, the spatial characteristics of channels play a vital role in MIMO systems, an aspect that warrants deeper empirical exploration. Limited attention has been given to the effects of deploying RISs across a broad fractional bandwidth and their influence on channel delay characteristics. Previous investigations have primarily concentrated on narrow bandwidths, disregarding the broader spectrum utilized in contemporary cellular systems, like 5G sub-6 GHz channels boasting bandwidths of up to 100 MHz. Investigating delay spread variation induced by RISs is crucial as it directly impacts signal distortion brought about by propagation environments. The measurements undertaken in this thesis shed a light on these aspects of the RIS-aided channel that have until now been given limited attention.

Optimal design and configuration: Realistic experimental verification can inform the design and configuration of RIS systems. To maximise their impact, researchers and industry practitioners need insights into the most effective deployment strategies, optimal RIS placement, RIS resolution, and adaptive control mechanisms that can endure changing wireless conditions. Increased RIS phase resolution of a RIS prototype is explored to determine measurable performance enhancement and a trade-off analysis factoring in the increased complexity is performed. Although RISs have been coined as being nearly-passive devices, this has not necessarily been reflected in RIS prototypes detailed in the literature, with a typical power consumption above 1W. This thesis details the implementation of a RIS prototype that is truly near-passive, consuming only milliwatts of power in its configured state whilst maintaining full control over all RIS elements at both linear polarisations.

Industry adoption and standardisation: The transition from theory to practical implementation requires industry adoption and standardisation. By providing empirical evidence of RIS benefits and limitations, experimental verification can accelerate the integration of RIS and other smart technologies into commercial wireless networks.

1.3 Aims of the thesis

In light of the above considerations, this thesis aims to bridge the existing gap by conducting comprehensive experimental studies that evaluate the performance of RIS technology within diverse real-world wireless communication scenarios. Through these experiments, we seek to

provide valuable insights, practical recommendations, and empirical evidence that can guide the future development and deployment of RIS technology and contribute to the advancement of the smart radio environment paradigm. The core purpose of this thesis is to shed light on the potential impacts on system performance resulting from the inclusion of RISs within sub-6 GHz mobile communication networks. Key milestones are:

- The development of novel RIS prototypes. Specifically, designing and prototyping a multi-bit RIS capable of providing digital reflection local coefficient control beyond the state of the art. Additionally, the development and performance verification of a power-efficient RIS capable of 3-dimensional beamforming in independent polarisations.
- Deployment of RISs within real-world wireless communication systems. This work aims to ascertain measurements of RIS-aided communication systems in a wide range of scenarios indoors and outdoors. Specifically, RIS-aided point-to-point indoor communication systems will be investigated and an iterative algorithm will be verified for a varying angle and distance relative to the RIS. Additionally, an outdoor multi-antenna system will be sounded with and without the introduction of a RIS.
- Performance analysis following high-quality channel measurements. Following extensive measurement campaigns, metrics of interest are to be extracted from complex channel coefficients in the form of channel gain, channel rank, and other temporal and spatial channel characteristics. Thereby informing any performance benefits of RISs on channel capacity and wireless coverage.

1.4 Thesis outline and contributions

The structure of the thesis is as follows.

Chapter 2 provides a thorough introduction to the operating principles, system descriptions, testbeds, measurement approaches, and existing field trial works of RISs. Various modeling approaches are explored and an antenna array-like description is formulated. Modeling is taken from a macroscopic level down to a local level to give a simplified overview of RIS operation. A system-level description extends the single-antenna RIS model to a multi-antenna, composite channel model with a statistical description. RIS measurement techniques at the local and macro-level are summarised. Drawing out the theory into practice, state of the art RIS testbeds are detailed, followed by a review of recent RIS-aided communication field trials.

Chapter 3 explores design strategies for digital RISs. High-performance reconfigurable metasurface design techniques are investigated, leading to the development and validation of two novel prototypes with unique characteristics. A nature-inspired approach is taken to optimise

RISs at the unit-cell level. Namely, a 3-bit RIS capable of high-resolution phase control capable of beamsteering in azimuth, and a 1-bit dual-linear polarised low power RIS with 3-dimensional beam control. The reflection coefficient responses are verified for both designs through specular measurements, where close resemblance to simulation is observed. The far-field to far-field beamsteering behaviour of the 1-bit RIS is verified through outdoor radiation pattern measurements, further confirming the reliability of a physics-compliant RIS model detailed in Chapter 2.

Chapter 4 contains results from a field trial campaign within an indoor environment, where several NLoS communication scenarios are enhanced through the introduction of a 3-bit RIS. An iterative algorithm is introduced for RIS configuration optimisation to maximise the channel gain between two directional antennas. The scenarios considered are a lobby area, a corridor junction, and a multi-floor link. Significant channel improvements are observed, with the RIS capable of flattening the frequency response of the wireless channel within a wide operating band.

Chapter 5 details a comprehensive measurement campaign throughout an outdoor urban macrocell with a 1-bit RIS capable of 3-dimensional beamforming. A noise-resistant RIS beam search algorithm is introduced to overcome the difficulties of the low signal-to-noise ratio (SNR) presented by a long-distance wireless link. The operating distance of a frequency-domain channel sounder is increased through a custom radio over fiber-based range extender. Complex channel coefficients are ascertained for a 4×4 MIMO system for several RIS and receiver locations. Enhancements in channel gain and variations in spatial and temporal channel characteristics are revealed.

Chapter 6 concludes the thesis with a summary and a look into potential future directions of this research. Based on the findings of this data-driven research, recommendations are made for the real-world application of RISs from an academic and industrial perspective.

Chapter 2

Literature review

This chapter provides an overview of the theoretical underpinnings relevant to the contents of this thesis as well as the current state of the literature. The literature review is structured as follows. Firstly, the operating principles of RISs are explored, starting with a more general approach to analysis of metasurface structures, followed by a simplified antenna array-like description valid for the structures introduced in this thesis. A system description of RIS-aided communications follows, coupling the statistical description of multipath channels with the deterministic behaviour of wave interaction with RISs. In-keeping with the experimental nature of this work, a review of measurement techniques for local and global RIS electromagnetic behaviour is given, followed by a look at the state of the art in RIS implementations. The literature review concludes with a summary of previous RIS-aided communication field trials and a critical review of gaps in the RIS field trials literature.

2.1 Operating Principles

2.1.1 Modeling approaches

Generalised sheet transition conditions

There are several means of analysis available to us to analyse the behaviour of reflecting-type metasurfaces. A common analysis method involves enforcing boundary conditions valid for electrically-thin planar structure known as generalised sheet transition conditions (GSTCs). GSTCs consider the metasurface as an electromagnetic discontinuity that can be described by surface-averaged susceptibility tensors [21]. Referring to Fig. 2.1, the GSTCs for linear and time-invariant metasurfaces are represented in terms of Maxwell's equations via :

$$\hat{\mathbf{z}} \times \Delta\mathbf{H} = j\omega\mathbf{P}_{\parallel} - \hat{\mathbf{z}} \times \nabla_{\parallel} M_z \tag{2.1}$$

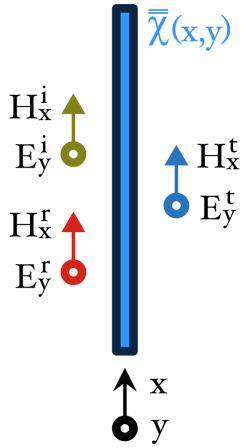

Figure 2.1: Diagram of the fields in close proximity to a metasurface described by its surface-averaged susceptibility tensor, $\bar{\bar{\chi}}$.

$$\Delta\mathbf{E}\times\hat{\mathbf{z}} = j\omega\mu_0\mathbf{M}_{\parallel} - \frac{1}{\varepsilon_0}\nabla_{\parallel}P_z\times\hat{\mathbf{z}} \tag{2.2}$$

where $\mathbf{P}$ and $\mathbf{M}$ are the surface-averaged electric and magnetic polarisation densities. These account for the induced electric and magnetic dipole moments of the constituent metasurface elements, subject to the incident electric and magnetic fields. The Δ operator corresponds to the differences between the field components at each side of the metasurface:

$$\Delta\Psi_u = \hat{\mathbf{u}}\cdot\Delta\Psi\Big|_{z=0^-}^{z=0^+} = \Psi_u^t - (\Psi_u^i + \Psi_u^r) \tag{2.3}$$

with $\Psi = \{\mathbf{E},\mathbf{H}\}$, $u = \{x,y,z\}$, and i, t, and r corresponding to the incident, transmitted, and reflected field components. By averaging the electric and magnetic field components over an electrically-small surface area of the metasurface, the polarisation densities can be described in terms of surface-averaged susceptibility tensors:

$$\mathbf{P} = \varepsilon_0\bar{\bar{\chi}}_{ee}\cdot\mathbf{E}_{av} + \frac{1}{c_0}\bar{\bar{\chi}}_{em}\cdot\mathbf{H}_{av} \tag{2.4}$$

$$\mathbf{M} = \bar{\bar{\chi}}_{mm}\cdot\mathbf{H}_{av} + \frac{1}{\eta_0}\bar{\bar{\chi}}_{me}\cdot\mathbf{E}_{av} \tag{2.5}$$

With $\mathbf{E}_{av} = \frac{1}{2}(\mathbf{E}^t + (\mathbf{E}^r + \mathbf{E}^i))$ and similarly for the average magnetic field components. The surface-averaged susceptibility tensor, $\bar{\bar{\chi}}_{ee} = \begin{bmatrix}\chi_{ee}^{xx} & \chi_{ee}^{yx}\\ \chi_{ee}^{xy} & \chi_{ee}^{yy}\end{bmatrix}$ and so on. Where ee refers to electric to electric field interaction, mm magnetic to magnetic field interaction, and em magnetic to electric field interaction etc.

Substituting (2.4) and (2.5) into (2.6) and (2.7), and assuming only tangential polarisation

currents (i.e., $P_z = M_z = 0$), we obtain [22]:

$$\hat{\mathbf{z}} \times \Delta\mathbf{H} = j\omega\varepsilon_0 \bar{\bar{\chi}}_{ee} \cdot \mathbf{E}_{av} + jk_0 \bar{\bar{\chi}}_{em} \cdot \mathbf{H}_{av} \tag{2.6}$$

$$\Delta\mathbf{E} \times \hat{\mathbf{z}} = j\omega\mu_0 \bar{\bar{\chi}}_{mm} \cdot \mathbf{H}_{av} + jk_0 \bar{\bar{\chi}}_{me} \cdot \mathbf{E}_{av} \tag{2.7}$$

For non-gyrotropic (i.e., no transformations between polarisations) and reciprocal metasurfaces, four surface-averaged susceptibilities are relevant and these are determined in terms of the field differences and surface-averaged fields [22]:

$$\chi_{ee}^{xx} = \frac{-\Delta H_y}{j\omega\varepsilon_0 E_{x,av}}, \qquad \chi_{ee}^{yy} = \frac{\Delta H_x}{j\omega\varepsilon_0 E_{y,av}}, \qquad \chi_{mm}^{xx} = \frac{\Delta E_y}{j\omega\mu_0 H_{x,av}}, \qquad \chi_{mm}^{yy} = \frac{-\Delta E_x}{j\omega\mu_0 H_{y,av}} \tag{2.8}$$

We can craft the surface-averaged susceptibilities for a desired wave transformation using (2.8). As an example, for an incident transverse-electric (TE) plane wave with average power P_0 at angle θ_i relative to broadside, the electric and magnetic field components at the surface are defined in a similar fashion to [17] :

$$E_y^i(x,y) = \sqrt{2P_0}\exp(-jk_0\sin(\theta_i)x) \tag{2.9}$$

$$H_x^i(x,y) = \frac{\sqrt{2P_0}}{\eta}\cos(\theta_i)\exp(-jk_0\sin(\theta_i)x) \tag{2.10}$$

where k_0 is the wavenumber of free space. For maximum reradiation at angle θ_r, we can define the field components:

$$E_y^r(x,y) = \sqrt{2P_0}A_r\exp(-jk_0\sin(\theta_r)x) \tag{2.11}$$

$$H_x^r(x,y) = -\frac{\sqrt{2P_0}}{\eta}A_r\cos(\theta_r)\exp(-jk_0\sin(\theta_r)x) \tag{2.12}$$

where A_r is a scaling term accounting for reflection losses. Substituting these values into (2.8), with zero transmitted field components and $E_x^u = 0$, $H_y^u = 0$, we obtain [17]:

$$\chi_{ee}^{yy}(x) = \frac{j2}{k_0}\frac{\cos\theta_i - A_r\cos\theta_r\exp(-jk[\sin\theta_r - \sin\theta_i]x)}{1 + A_r\exp(-jk[\sin\theta_r - \sin\theta_i]x)} \tag{2.13}$$

$$\chi_{mm}^{xx}(x) = \frac{j2}{k_0}\frac{1 + A_r\exp(-jk[\sin\theta_r - \sin\theta_i]x)}{\cos\theta_i - A_r\cos\theta_r\exp(-jk[\sin\theta_r - \sin\theta_i]x)} \tag{2.14}$$

With the remaining susceptibility components set to zero. Importantly, (2.13) is periodic in x with period $2\pi/(k_0(\sin\theta_r - \sin\theta_i))$. For a fixed θ_i, the period of this function determines the

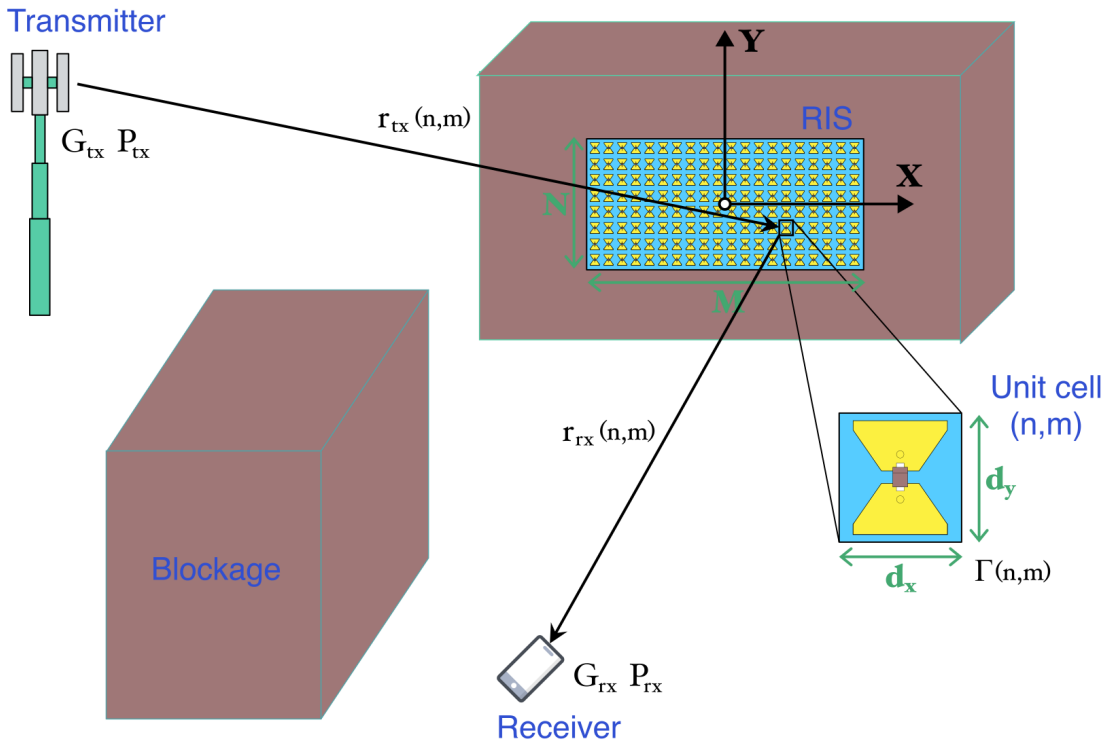

Figure 2.2: System model for a RIS-aided communication link between a transmitter base station and receiver user handset.

angle of maximum re-radiation. Modulation of the surface-averaged susceptibility of a reflecting metasurface in a periodic fashion thus enables beamsteering functionality. Means of extracting surface-averaged susceptibility from a given metasurface element geometry through full-wave simulation are explored in [22], details of which shall not be repeated here. Instead, a synthesis approach involving local reflection coefficients will be detailed next, offering a simpler means of analysis relevant to the geometries of the metasurfaces investigated in later chapters.

Antenna array-like formulation

An analysis approach that is valid for the radiative near-field and far-field was recently introduced by Degli-Esposti et al. [23]. Referring to Fig. 2.2, if we can separate the electric field contributions from subsections of the surface (e.g., each unit cell), we can model the RIS with an antenna array-like formulation. The electric field observed at an observation point, p, can be defined via the summation of the electric field contributions re-radiated from the N row by M column arrangement of unit cell elements [23]:

$$E(p) = \sum_{m=1-\frac{M}{2}}^{M/2} \sum_{n=1-\frac{N}{2}}^{N/2} \Delta E(p|n,m) \tag{2.15}$$

With ΔE being the contribution to the total electric field from unit cell (n,m) seen at point p

[23].

$$\Delta E(p|n,m) = \Delta E_0^r(p|n,m)\sqrt{f(\theta_{rx}(p|n,m))}\Gamma_{n,m}\exp\left(-j\frac{2\pi}{\lambda}(r_{tx}(n,m)+r_{rx}(p|n,m))\right) \quad (2.16)$$

Where $f(\theta_{rx})$ is the unit cell radiation pattern magnitude in the direction of the observation point θ_r, and r_{tx}, r_{rx} the respective distances to the source and the observation point from the origin located at the center of the RIS. $\Gamma_{n,m}$ is the local reflection coefficient of unit cell (n,m) [24]. The local reflection coefficients provide one with a mechanism to control wave transformations and is defined in the next section. The scaling term ΔE_0^r is derived such that it satisfies energy conservation. According to antenna theory [25], the power intercepted by an antenna, P_i, at angle θ_i is directly proportional to the effective aperture, A_e, of the antenna:

$$P_i = \frac{|E_i|^2}{2\eta}A_e(\theta_i) = \frac{|E_i|^2}{2\eta}\frac{\lambda^2}{4\pi}f(\theta_i) \quad (2.17)$$

$$|E_i|^2 = \frac{\eta}{2\pi}\frac{P_{tx}G_{tx}}{r_{tx}^2} \quad (2.18)$$

Where E_i is the incidence electric field, η is the characteristic impedance of free space, λ is the wavelength of the incident electromagnetic wave, and r_i is the distance to the source. P_{tx} and G_{tx} are the transmit power and transmit antenna gain, respectively.

The re-radiated power from a unit cell can be found via [25]:

$$P_r = \int_0^{2\pi}\int_0^{\pi}\frac{|\Delta E^r(p)|^2}{2\eta}r^2\sin\theta\, d\theta\, d\phi \quad (2.19)$$

$$= 2\pi\frac{|\Delta E_0^r(p)|^2}{2\eta}\int_0^{\pi/2} f(\theta)r_{rx}^2(n,m)\sin(\theta)d\theta \quad (2.20)$$

Where $\Delta E^r(p)$ is similarly defined as (2.16). For the lossless case, we can determine ΔE_0^r by setting the incident and re-radiated power at the unit cell equal, being equations (2.17) and (2.19), respectively.

$$\frac{|E_i|^2}{2\eta}\frac{\lambda^2}{4\pi}f(\theta_{tx}) = 2\pi\frac{|\Delta E_0^r(p)|^2}{2\eta}\int_0^{\pi/2} f(\theta)r_{rx}^2(n,m)\sin(\theta)\,d\theta \quad (2.21)$$

Since $|E_i|^2 = \frac{\eta}{2\pi}\frac{P_{tx}G_{tx}}{r_{tx}^2(n,m)}$, solving for ΔE_0^r:

$$\Delta E_0^r = \sqrt{\eta \frac{\lambda^2}{16\pi^3} \frac{f(\theta_{tx})}{\int_0^{\pi/2} f(\theta)\sin(\theta)d\theta} \frac{P_{tx}G_{tx}}{r_{tx}^2 r_{rx}^2}} \tag{2.22}$$

Substituting (2.22) into (2.16):

$$\Delta E(p|n,m) = \sqrt{\frac{\eta P_{tx}G_{tx}\lambda^2}{16\pi^3 r_{tx}^2 r_{rx}^2}} \sqrt{\frac{f(\theta_{tx})f(\theta_{rx})}{\int_0^{\pi/2} f(\theta)\sin(\theta)d\theta}} \Gamma_{n,m} e^{-j\frac{2\pi}{\lambda}(r_{tx}(n,m)+r_{rx}(n,m))} \tag{2.23}$$

The power seen at the receiver is then determined via:

$$P_{rx} = \frac{G_{rx}}{2\eta}|E(p)|^2 = \frac{G_{rx}}{2\eta}\left|\sum_{m=1-\frac{M}{2}}^{M/2}\sum_{n=1-\frac{N}{2}}^{N/2}\Delta E(p|n,m)\right|^2 \tag{2.24}$$

Substituting (2.23) into (2.24) [26]:

$$P_{rx} = P_{tx}G_{tx}G_{rx}\frac{d_x d_y \lambda^2}{64\pi^3}\left|\sum_{m=1-\frac{M}{2}}^{M/2}\sum_{n=1-\frac{N}{2}}^{N/2}\Gamma_{n,m}\sqrt{F_{n,m}^{combine}}\,\frac{e^{-j\frac{2\pi}{\lambda}(r_{tx}(n,m)+r_{rx}(n,m))}}{r_{tx}(n,m)r_{rx}(n,m)}\right|^2 \tag{2.25}$$

With $F_{n,m}^{combine} = \frac{f(\theta_{tx})f(\theta_{rx})}{\int_0^{\pi/2} f(\theta)\sin(\theta)d\theta}$.

As can be expected, the received power is directly proportional to the product of the transmit power, transmitter antenna gain, and receiver antenna gain. The received power is inversely proportional to the product of the squared distances to the respective unit cells, scaled as a function of the incidence and re-radiation angles according to the unit cell radiation patterns, $f(\theta)$. Selection of f depends on the effective apertures of the unit cells and this function must satisfy energy conservation. In aperture-type antennas, the effective aperture upper bound is constrained by the physical dimensions of the antenna. In this case, the effective aperture, A_e, must satisfy [23]:

$$A_e \leq d_x d_y \tag{2.26}$$

To avoid the early onset of grating lobes, the unit cell lateral dimensions should be less than $\lambda/2$ [27]. By definition, the directivity, $D = \frac{4\pi}{\lambda^2}A_e$, of a unit cell is constrained by:

$$1 \leq D \leq \frac{4\pi}{\lambda^2}\left(\frac{\lambda}{2}\right)\left(\frac{\lambda}{2}\right) = \pi \tag{2.27}$$

One function that satisfies these constraints is the cosine raised to the power:

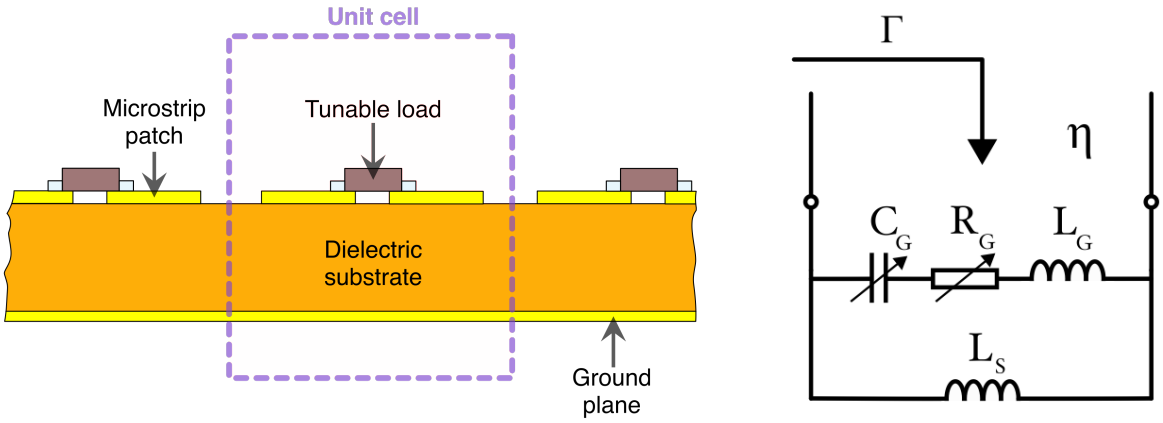

(a) (b)

Figure 2.3: Cut view of a generic reconfigurable metasurface (a). Equivalent circuit model of a unit cell (b).

$$f(\theta) = \cos^{\gamma}(\theta) \tag{2.28}$$
$$0 \leq \gamma \leq 0.57$$

This function with $\gamma = 0.5$ is utilised for the RIS-aided beemsteering employed in chapters 3, 4, and 5 as part of the RIS forward model.

2.1.2 The local reflection coefficient

The local reflection coefficient, $\Gamma_{n,m}$, encompasses the spatial modulation across the surface of the RIS and facilitates its wave transformation properties [28]. At a point on the surface, r', the reflection coefficient in this context is defined as the ratio of the reflected and incident electric field components:

$$\Gamma(r') = \frac{E_r(r')}{E_i(r')} \tag{2.29}$$

Assuming negligible variation in the field components over the area of element (n,m), we can define a local reflection coefficient from the surface-averaged electric field components [29]. This approximation is valid when the periodicity of the unit cell is much less than one wavelength. The local reflection coefficient is a complex quantity describing the shift in magnitude, $\rho_{n,m}$, and phase, $\phi_{n,m}$:

$$\Gamma_{n,m} = \rho_{n,m} e^{j\varphi_{n,m}} \tag{2.30}$$

Assuming normal incidence of a uniform plane wave, we can model the local reflection

coefficient in terms of the impedance seen at the surface [19]:

$$\Gamma_{n,m} = \frac{Z_{n,m} - \eta}{Z_{n,m} + \eta} \tag{2.31}$$

where $Z_{n,m}$ is the surface-averaged impedance seen at element (n,m). Metallic patches printed on an electrically-thin grounded dielectric substrate can be modeled as a capacitive grid in parallel with an inductive surface [30]. That is, effectively a parallel inductive-capacitive (LC) tank circuit. An equivalent circuit model of this is shown in Fig. 2.3(b). The impedance of the capacitive grid is governed by the inter-element capacitance, the series inductance of the microstrip patches, as well as the series resistance, capacitance, and finite inductance of the tunable load. This is encompassed in the equation [30]:

$$Z_G = R_G + j\left(\omega L_G - \frac{1}{\omega C_G}\right) \tag{2.32}$$

where R_G, C_G, and L_G are the equivalent grid resistance, capacitance, and inductance, respectively. The grounded dielectric substrate is modeled as a shunt inductor whose inductance is directly proportional to the substrate thickness. This can be derived by considering the impedance looking into a short-circuited transmission line with characteristic impedance Z_0, propagation constant β, and length h [31]:

$$Z_S = jZ_0 \tan\beta h = j\sqrt{\frac{\mu_r\mu_0}{\varepsilon_r\varepsilon_0}} tan(\omega\sqrt{\mu_r\mu_0\varepsilon_r\varepsilon_0}h) \approx j\omega\mu_0 h \tag{2.33}$$

assuming $\mu_r = 1$ (i.e., the substrate is non-magnetic) and the product $\beta h \ll 1$. Equation (2.33) provides an approximate inductance for the grounded thin substrate as $L_S = \mu_0 h$. The impedance seen looking into unit cell (n,m) can then be approximated by:

$$Z_{n,m} = Z_G(n,m) \parallel Z_S = \frac{j\omega L_S\left(j(\omega L_G - \frac{1}{\omega C_G(n,m)}) + R_G(n,m)\right)}{j\left(\omega L_S + \omega L_G - \frac{1}{\omega C_G(n,m)}\right) + R_G(n,m)} \tag{2.34}$$

Example

As an example, the reflection coefficients associated with a RIS with a grid inductance of $L_G =$ 0.4 nH, substrate thickness of 2 mm corresponding with a shunt inductance $L_S = 2.5$ nH, and grid capacitance values of 0.6, 0.7, 0.8, and 0.9 pF are plotted in Fig. 2.4. The respective grid resistance values, R_G, are selected as 0.5, 0.6, 0.7, and 0.8 corresponding to the set of capacitance values. This varying resistance is typical for varactor-based RISs whose forward resistance is proportional to the junction capacitance [32]. It can be seen that the unit cells present a dispersive phase response and a magnitude drop that corresponds with $\approx 0^\circ$ (in-phase) phase response for each value of capacitance. Fig. 2.5 shows the reflection coefficient versus capacitance for several frequency points. It can be seen that the available phase range varies

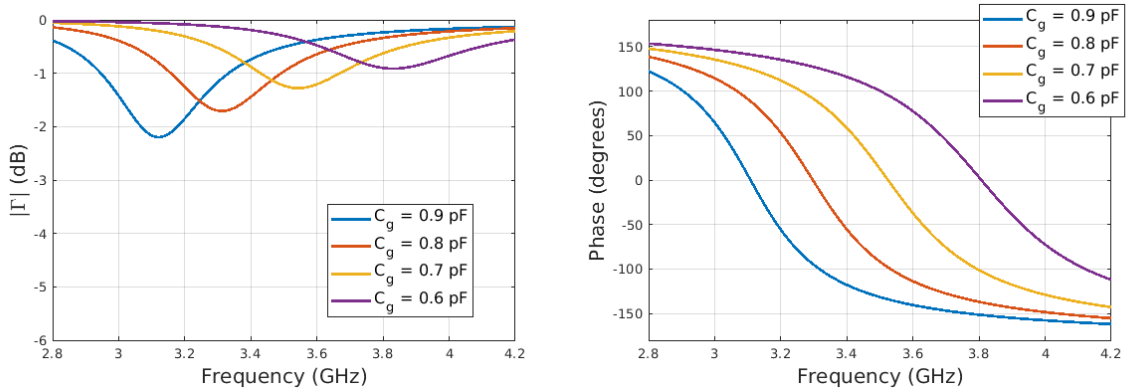

(a) (b)

Figure 2.4: Magnitude (a) and phase (b) versus frequency for an analytically modeled RIS element with varying capacitance.

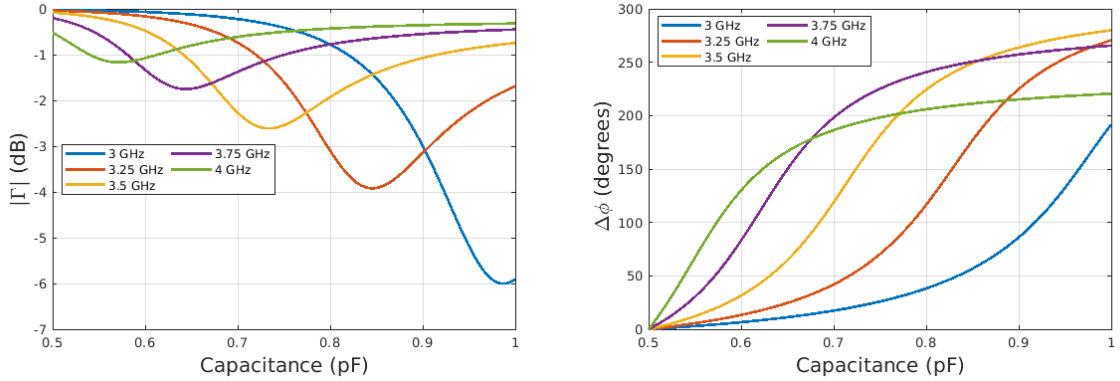

(a) (b)

Figure 2.5: Magnitude (a) and phase (b) versus capacitance for an analytically modeled RIS element with varying frequency.

significantly with frequency, as do the maximum reflection losses. For instance, 3.5 GHz offers up to 280° of phase agility with a maximum loss of 2.6 dB, while these values at 3 GHz are 191° and 6 dB, respectively.

Practical RIS implementations are constrained in the achievable values of reflection coefficients [33]. This is due largely to limited control circuit complexity, as well as the finite tuning range of available technologies. For the example given here, the >270° phase range at 3.5 GHz would cater for a 4-level reflection coefficient, providing phase shift values of 0°, 90°, 180°, and 270°. These coincide with grid capacitance values 0.5, 0.67, 0.75, and 0.93 pF, respectively. Constraining the reflection coefficients to these values of capacitance and employing equation (5.6) for received power via the RIS, the approximate beamsteering performance of a practical RIS can be analytically evaluated. Consider the system setup in Fig. 2.6. The RIS is located at the coordinate origin, while a transmitter located in the same horizontal plane, equipped with an antenna with a gain of 20 dBi, is located at a distance $r = 100$ m from the RIS. The transmit

antenna is oriented such that its maximum gain is directed towards the center of the RIS. A receiver antenna with similar characteristics is located at the same distance and is subjected to motion about a 180° span covering the half-space in front of the RIS. As was determined in the previous subsection on GSTCs, a phase gradient conforming to the following formula enables anomalous reflection in the azimuthal plane from the RIS, coupling an incident plane wave at angle θ_i into a main lobe that favors a direction θ_r [34]:

$$\frac{d\varphi(x)}{dx} = k_x^r - k_x^i = \frac{2\pi}{\lambda}(\cos\theta_r - \cos\theta_i) \tag{2.35}$$

Where φ is the phase of the reflection coefficient along x, and k_x^r and k_x^i are the wavenumbers about the x axis for the re-radiated and incident electromagnetic waves, respectively. Solving for φ:

$$\varphi(x) = \frac{2\pi}{\lambda}x(\cos\theta_r - \cos\theta_i) + \varphi_0 \tag{2.36}$$

where φ_0 is a constant phase offset. Discretising for the finite sized unit cells with periodicity d:

$$\varphi(n,m) = \frac{2\pi d}{\lambda}m(\cos\theta_r - \cos\theta_i) + \varphi_0 \tag{2.37}$$

For maximum re-radiation 45° from a wave incident broadside (90°) to the RIS with a unit cell periodicity of $d = \lambda/3$, we can set the phase profile to $\varphi(n,m) = \sqrt{2}\pi m/3$. The resulting received power for varying θ_{rx} with a 32 × 32 element RIS is plotted in Fig. 2.7 for three cases. In the first case, continuous reflection coefficient phase values are available in the range 0° to 360°, shown by the blue curve. In the second case, 4 phase values being 0°, 90°, 180°, and 270° are available, corresponding to the 2-bit case. Lastly, the reflection coefficient phases are limited to 2 states for a 1-bit RIS with phase values 0° and 180°. The corresponding reflection coefficient phases have been plotted in Fig. 2.8.

Observing Fig 2.7(a), a main lobe exists about 45° with power levels of -56.5, -57.5, and -60.3 dBm for the respective continuous, 2-bit, and 1-bit phase profiles. This is consistent with the analysis performed by Wu et al. [35] in which it was determined that an average gain reductions over the continuous case of 0.9 and 3.9 dB are observed for the 2-bit and 1-bit cases, respectively. A significant performance difference for the 1-bit case is the onset of an additional lobe that is equal in magnitude to the desired lobe. This is due to the symmetry of the phase profile required to generate the beam at 45° for the 1-bit case, whereas the 2-bit case is able to break this symmetry through interpolation of the additional phase states. Nonetheless, the side-lobe performance of the discretised cases deteriorates with reducing phase resolution due to phase errors [36]. A half-power beamwidth of 6.7° exists for the continuous phase gradient case and this remains similar for the discretised cases, being largely dependent on the aperture size.

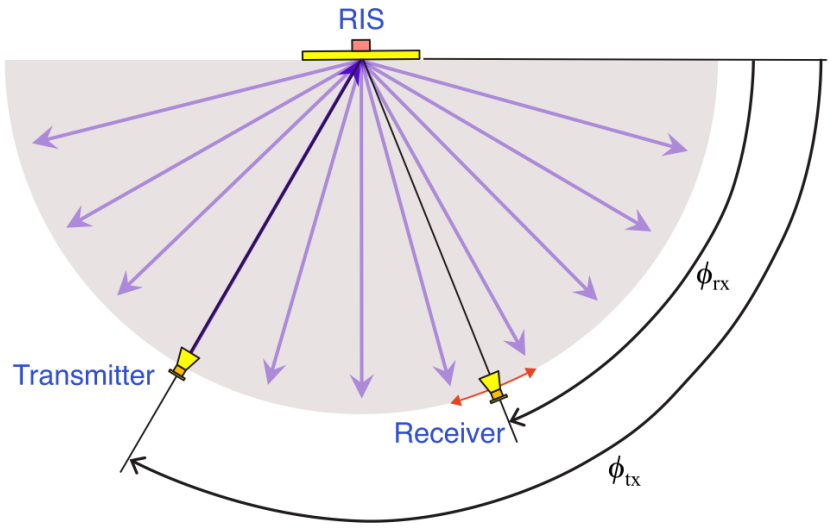

Figure 2.6: System diagram for the beamsteering analytical derivation.

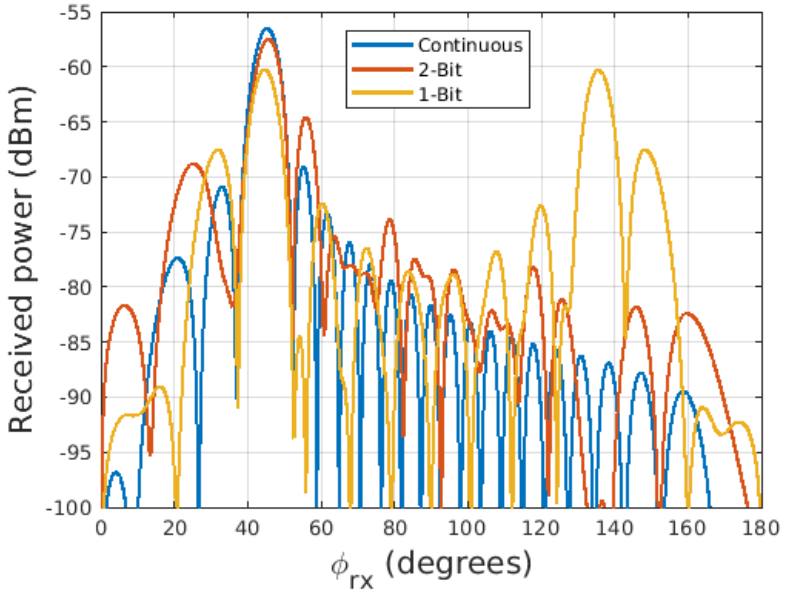

Figure 2.7: Received power versus azimuth angle for the phase gradient RIS example.

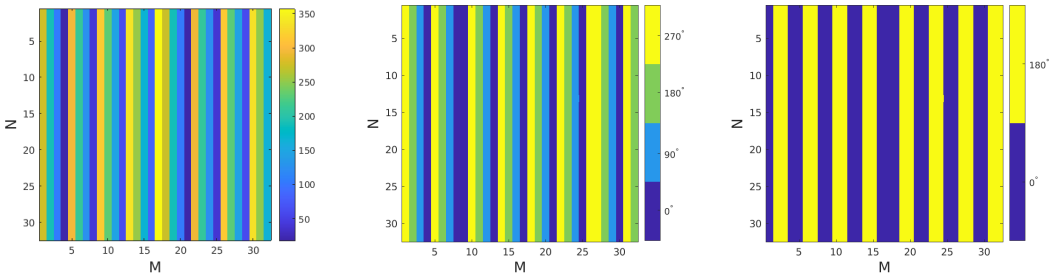

(a) Continuous (b) 2-Bit (c) 1-Bit

Figure 2.8: Phase of reflection coefficient versus unit cell position for the analytical model example.

2.1.3 Limitations of the model

The model described by equation (3.14) utilised throughout this thesis does not factor in the mutual coupling that is inherently present between unit cell elements. While geometrical features remain similar between configurations, the tunable loads between neighboring elements may exhibit differing impedances. The equivalent circuit model in Fig. 2.3(b) assumes that the unit cell is surrounded by unit cells with a similar tuned state. That is, the *local periodicity* assumption [37]. This approximation has been employed successfully in reflectarray design for several years [38], where it is assumed that the surface impedance profile is smoothly varying and therefore differing elements may impose a minimal perturbation on the local reflection coefficients of their neighbors.

The oblique incidence performance of the RIS on a macroscopic scale is factored into the model through the angle-dependent unit cell field patterns. However, this does not account for the apparent shift in operating point with oblique incidence that is common to the widely deployed topologies of metasurface that RIS rely on. Chen et al. introduced a model for an incident angle-dependent reflection coefficient where the grid impedance and shunt substrate inductance are functions of the elevation angle [39]. This model should be used with caution, however, as the authors suggest this apparent angle-dependent behaviour leads to a form of magnetless non-reciprocity. Fortunately, this was corrected by Wang et al. who verified channel reciprocity in a time division duplexing (TDD) RIS-aided communication setup at oblique incidence with two different RIS prototypes [40]. For completion, under certain circumstances, non-reciprocity can be introduced into RISs - but this is beyond the scope of this work [20].

Even with these limiting factors in the model, it will be shown in section 3.3.5 that (3.14) provides a reliable approximation for far-field to far-field beamsteering performance in a binary reflecting metasurface. Furthermore, this forward model is employed in chapter 5 to select RIS configurations in a long distance RIS-aided MIMO communication setup.

2.1.4 Performance considerations of resolution and geometry

RIS topologies are dependent on the degree of controllability required balanced with the implementation complexity, cost, and power consumption. For the reflecting-type RIS, we would ideally have access to the tuning component of each RIS element and be able to manipulate vertical and horizontal linear polarisations. Full-dimensional control enables independent adjustment of each individual element's properties within the RIS. This fine-grained control allows for precise manipulation of wavefronts, beamforming, and interference mitigation. This degree of control comes with significant implementation complexity that must be traded off with, for example, a reduction in phase resolution. On the other hand, a higher phase resolution can be practically realised by compromising on the addressability of the RIS elements [41].

Quantisation: In a study by Taghvaee et al. [33], various performance metrics of pro-

grammable metasurfaces with quantised phase shifts were investigated. The research compared beamsteering metasurfaces of 1, 2, and 3 bits phase resolution under normally incident waves, followed by reflection at $\theta_r = \phi_r = 45^\circ$. The authors evaluated metrics such as directivity, target deviation, sidelobe level (SLL), and half-power beamwidth (HPBW), while maintaining a fixed surface size and varying unit cell periodicity. Results indicated a 3dB increase in directivity when transitioning from 1 to 2 bits phase resolution, accompanied by noticeable enhancements in target deviation and sidelobe level. However, for unit cell periodicities below half a wavelength, the impact of increasing phase resolution from 2 to 3 bits was less pronounced, primarily resulting in slight improvements in sidelobe levels affected by quantisation errors in phase and unit cell size. The authors suggested that increasing the number of available unit cell states could compensate for the shift in operating point with increasing incidence angle, thus enhancing programmability at the expense of increased losses and circuit complexity.

Element grouping: A relevant recent work on RIS control reduction is that of Enqvist et al. in [41]. The authors investigated the effect of grouping RIS elements into sub-arrays and controlling groups with similar RIS reflection coefficients. Alongside RIS complexity reduction, the authors showed that this approach has the potential for 10 to 40% energy efficiency improvement and pilot overhead reduction. The authors compared the adverse effects of phase quantisation on the SNR for the number of sub-arrays for a fixed number of RIS elements. On average, a 3.9 dB SNR performance gap was calculated to exist between 1-bit and the case of no phase quantisation (i.e., continuous tuning). It was also verified that a 3-bit resolution offers performance close to that of a continuously tunable case. For a 1024-element RIS, this trend appeared to be constant when dividing the RIS into more than 32 subarrays. For example, 32 connected columns of 32 unit cells each. The authors determined that the SNR increases monotonically with the number of subarrays, hitting an upper limit for SNR at 1024 divisions (i.e., individual element control) with no noticeable tapering.

Phase resolution: High-resolution RISs have the potential to be band-limited due to the wide tuning range required [30]. Continuously and independently tunable unit cell reflection magnitude and phase would enable RISs precise control over EM transformations [42]. However, phase-dependent magnitude is inevitable due to the resonant nature of the elements. Variations in field intensity within the unit cells depend on the tuned state, with the highest field strength typically at the AMC frequency, where in-phase (i.e., 0°) reflection occurs. The intensity of the magnitude reduction brought about by this behaviour depends on the loss mechanisms present in the materials, such as dielectric loss, and tuning component resistance [30]. Zhang et al. investigated the effects of limited phase resolution on an uplink IRS-assisted communication system [43]. The authors employ a Rician model and assume the NLoS link via the IRS is dominant. The degradation of the achievable data rate versus surface size and unit cell phase resolution were respectively derived through optimisation to find the continuous phase shifts and subsequently selecting the closest quantised phases. It was found that the performance gap

between an ideal continuous phase resolution and coarse tuning closes as the surface becomes large. For a surface consisting of 300 elements, it was found that any improvement in data rate degradation is negligible beyond 3 bits phase resolution and the model exhibits below 5% degradation at 2 bits.

Power consumption: Power consumption is an important consideration for the selection of RIS tuning technology due to the electrical size of the devices. Biasing a large number of components requires associated digital circuitry with variable voltage and/or constant current requirements. Wang et al. recently studied the power consumption of several RIS prototypes of varying topologies [44]. The authors derived a power consumption model, breaking up RISs into their constituent control boards, drive circuits, and unit cells in order to contrast the power consumption trade-offs of 5 different RIS prototypes. The authors considered PIN diode, varactor, and RF switch type tuning mechanisms. The power consumption of varactor and RF switch type RISs was found to be negligible at the unit-cell level. However, the high voltage levels required for the varactor-based designs resulted in a higher power consumption at the control level. The authors determined that power consumption of the varactor-based design could be reduced by opting for a column-based element grouping mechanism at the expense of spatial resolution. Of relevance to this discussion is the PIN diode-based design, where the authors proposed configuration selection favoring the reverse-biased states of the diodes in order to reduce the overall power consumption.

Geometry of RISs is an important consideration and performance in the network can vary profusely depending on overall surface area, shape, and position of RISs at the macro-scale, as well as RIS element geometry and periodicity at the micro-scale. In general, the larger the RIS, the greater impact it will have on a wireless network [45]. This can be understood from two mechanisms. Firstly, RISs can intercept power proportional to the surface area they occupy. Following this, RISs re-radiate said power with a directivity proportional to the surface area for the far-field case, or with a focusing gain for the case of the radiative near-field. Bjornson and Sanguinetti set out the power scaling laws of RISs and determined the SNR for a RIS-aided communication system where the path via the RIS is dominant [46]. The authors set out a simple formula describing an N-element RIS impact on the SNR as:

$$\mathrm{SNR}_{RIS} = \frac{\mu^2 N^2 \beta_g \beta_h P_{tx}}{\sigma^2} \tag{2.38}$$

where μ is a fixed amplitude reflection coefficient, β_g and β_h are the transmitter-RIS and RIS-receiver channel gains, respectively. With transmit power, P_{tx} and noise standard deviation σ. At first glance, it would appear that RISs can impart a significant SNR improvement since the above formula suggests an N^2 improvement. This is tempered in part by the product of two path losses. There are caveats to this scaling, however, and these depend on the operating regime (i.e., near-field versus far-field) and is briefly covered next.

A RIS path-loss analytical framework was introduced by Danufane et al. [47] based on

the vector generalisation of Green's theorem. The physical optics-based model consisting of a closed-form integral caters for inclusion of the polarisation, RIS surface size, and EM transformations, alongside transmission and reception distances, enabling realistic exploration of RIS-aided communication network characteristics. The model utilises homogenised surfaces which are described through surface-averaged susceptibilities [19] with associated local reflection coefficients. The work shows path-loss is highly dependent on the RIS surface area, particularly in the electrically large operating region, where the received electric field strength is bounded even as the surface size tends to infinity. This phenomena is responsible for diminishing returns with increasing RIS size. For the case of the electrically small regime, it is derived that RISs acting as anomalous reflectors and planar focusing structures result in nearly equivalent electric field intensity at the receiver. This contrasts with the near-field regime where a reflection phase profile mimicking a concave mirror offers superior performance over a phase-gradient profile. Numerical results were derived, confirming the weighted-sum path-loss and product path-loss anomalous reflection scaling laws for short and long distances, respectively, while focusing lenses in both the short and large distance regimes are shown to be subject to the product path-loss model. The discrete nature of the unit cells are considered by discretising the model's integral equation, where absolute errors in the desired reflection angles are compared to unit cell periodicity. Danufane et al. demonstrate that the model also accurately describes spurious reflection effects brought about by a large unit cell periodicity.

2.2 System description of RIS-aided communications

The path loss model of equation (3.14) assumes a line of sight between the transmitter and the RIS, and the receiver and the RIS, and a negligible contribution via in the context of RIS deployment in real-world environments, where noise and multipath must be taken into account.

2.2.1 System model

At microwave frequencies, real-world environments give rise to rich multipath propagation. The *isotropic scattering environment* assumption implies that radio signals propagate uniformly in all directions, with no preferred scattering or reflection angles. This assumption simplifies the complex interactions between radio waves and the multitude of obstacles and surfaces present in urban settings. In reality, urban environments are teeming with buildings, streets, vehicles, and other structures that can scatter and reflect signals in various directions. By assuming isotropic scattering, more tractable models can be developed. For the case of a single transmitter and single receiver, we can model the received signal at the receiver from a transmitted signal x as [18]:

$$y = h_d x + w \tag{2.39}$$

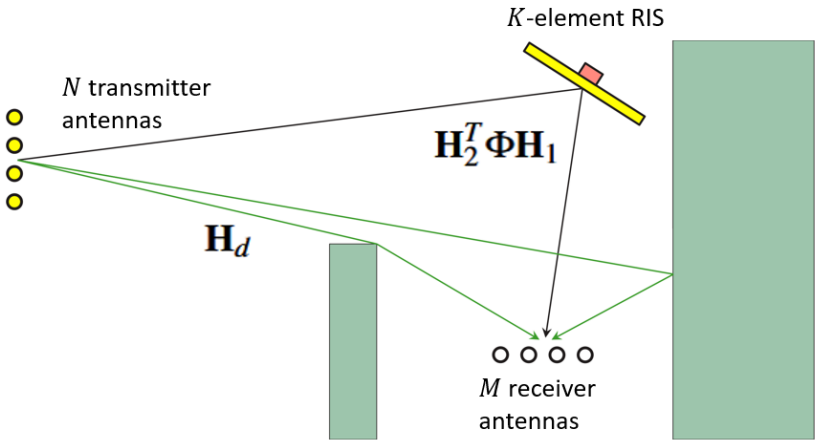

Figure 2.9: MIMO system setup for RIS-aided communications subject to occlusions.

where h_d is a complex-valued Rayleigh-distributed direct path channel coefficient $h_d \sim \mathcal{N}_{\mathbb{C}}(0, \sigma_d^2)$ with variance σ_d^2. The noise is encompassed by $w \sim \mathcal{N}_{\mathbb{C}}(0, \sigma_n^2)$ with variance σ_n^2. The signal x is defined as:

$$x = \sqrt{E_s} P s \tag{2.40}$$

where E_s is the average energy per symbol, P accounts for power control, and s is a unit-variance symbol [18]. The model in (**??**) can be adjusted to account for the contribution from a RIS by considering the channel response between the transmitter and the RIS, followed by the response between the RIS and the receiver. While these respective channels can be given a statistical description, the RIS is a deterministic structure [48], and its contribution to the composite channel is described by its set of complex local reflection coefficients for its $K = NM$ elements, $\Phi = \text{diag}(\rho_1 e^{-j\phi_1}, \ldots, \rho_K e^{-j\phi_K})$.

The Tx-RIS and RIS-Rx channels are defined via $\mathbf{h}_1 = [h_{1,1}, ..., h_{1,N}]^T$ and $\mathbf{h}_2 = [h_{2,1}, ..., h_{2,N}]^T$, respectively, with a resulting received signal with the composite channel [18]:

$$y = \left(\mathbf{h}_2^T \Phi \mathbf{h}_1 + h_d\right) x + w \tag{2.41}$$

According to [49], in an isotropic scattering environment, the channel coefficient vectors $\mathbf{h_1}$ and $\mathbf{h_2}$ are independent, and they are distributed as $\mathbf{h_i} \sim \mathcal{N}_{\mathbb{C}}(0, d_x d_y \mu_i \mathbf{R})$. Where μ_i is the average intensity attenuation and $\mathbf{R}$ is the $K \times K$ normalised spatial correlation matrix.

Extension of this model to multiple antennas can be performed by transforming the channel responses into matrices. For L transmit antennas, $\mathbf{H}_1$ of size $K \times L_1$ contains the complex channel coefficients between the respective antennas and the RIS elements. Similarly for the RIS to receiver channels with $\mathbf{H}_2 \in \mathbb{C}^{K \times L_2}$ for L_2 receiver antennas. The channel responses not via the RIS are represented by an $L_1 \times L_2$ matrix, $\mathbf{H}_d$. The resulting system is given by [45]:

$$\mathbf{y} = \left(\mathbf{H}_2^T \Phi \mathbf{H}_1 + \mathbf{H}_d\right) \mathbf{x} + \mathbf{w} \tag{2.42}$$

where this time the received signal is a vector $\mathbf{y}$ of the contributions from the respective receiver antennas. Similarly for the noise vector, $\mathbf{w}$. The nature of the transmitted signal is generally of the form $\mathbf{x} = \mathbf{Fs}$ where $\mathbf{F}$ is the precoder responsible for spatial formatting of the transmission [18]. Referring to Fig. 2.9, the composite RIS-aided MIMO channel, which is subsequently utilised in chapter 5, is given by:

$$\mathbf{H} = \mathbf{H}_2^T \Phi \mathbf{H}_1 + \mathbf{H}_d \tag{2.43}$$

2.2.2 Metrics

Channel capacity

The capacity of a communication channel is the highest spectral efficiency at which reliable data transmission is possible. With an optimal precoder and power allocated through waterfilling [18], the capacity in bits per second per Hertz (bps/Hz) for the MIMO channel $\mathbf{H}$ can be determined from [50]:

$$C = \sum_{i=1}^{L_{\min}} \log_2 \left(1 + \frac{P_i^* \lambda_i^2(\mathbf{H})}{N_0}\right) \tag{2.44}$$

where $L_{\min} = \min(L_1, L_2)$, N_0 is the noise spectral density, and λ_i is the i^{th} eigenmode of $\mathbf{H}$, and P_i^* are the power allocations. A data stream can be supported for each non-zero λ_i and it is through this phenomena that MIMO systems can realise significant spectral efficiency gains over their SISO counterparts. The *condition number* of a channel matrix reflects how well the system can separate and transmit independent data streams through its spatial channels [51]. It is defined as:

$$\kappa(H) = \frac{\lambda_{\max}(\mathbf{H})}{\lambda_{\min}(\mathbf{H})} \tag{2.45}$$

For a fixed total power gain, a MIMO channel with a condition number of 1 exhibits the highest spectral efficiency, where it can be considered a system which operates $L_{\min}$ independent spatial streams.

2.3 RIS measurement approaches

2.3.1 Scattering parameters

Most measurement techniques applied to RISs rely on scattering parameters (S-parameters) and these are briefly covered here. S-parameters are a type of network parameter and describe systems in terms of incident, reflected, and transmitted waves in the form of a scattering matrix [31]. For a two-port network, the scattering parameters can be represented in a 2×2 matrix of the form:

$$\mathbf{S} = \begin{bmatrix} S_{11} & S_{12} \\ S_{21} & S_{22} \end{bmatrix} \tag{2.46}$$

The reflection coefficient at port 1, S_{11}, is defined as the ratio of the reflected to incident voltage when port 2 is terminated in a matched load [31]:

$$S_{11} = \left.\frac{V_1^-}{V_1^+}\right|_{V_2^+=0} = \Gamma_1\big|_{V_2^+=0} \tag{2.47}$$

Similarly for S_{22}. The transmission coefficient from port 1 to port 2, S_{21}, is determined by the ratio of the outgoing voltage at port 2 to the incident voltage at port 1:

$$S_{21} = \left.\frac{V_2^-}{V_1^+}\right|_{V_2^+=0} \tag{2.48}$$

The S-parameter description can easily be extended to an N-port network, with the respective reflection coefficients on the diagonal and transmission parameters on the off-diagonal elements. The scattering description lends itself well to measurements, with S-parameters ascertained directly through a vector network analyser (VNA).

The contribution of the local reflection coefficient, Γ, to dynamic waveform control of RISs was explored in section 2.1. The following section explores how the reflection coefficient can be determined in simulation and measurement.

2.3.2 Reflection coefficient simulation techniques

The simulation of RIS elements largely relies on Floquet's theorem and the application of periodic boundary conditions (PBCs) [27]. When dealing with electrically-large periodic structures like RISs, simulating electromagnetic properties across an entire structure is computationally expensive. This is where PBCs come into play. PBCs exploit the periodicity of the metasurface to reduce the simulation domain's size. By applying these boundary conditions, it is possible to simulate only a single unit cell of the periodic structure and then replicate the results across the entire structure using Floquet's theorem. This approach significantly reduces the computational resources and time required for simulations. It is particularly advantageous when studying the

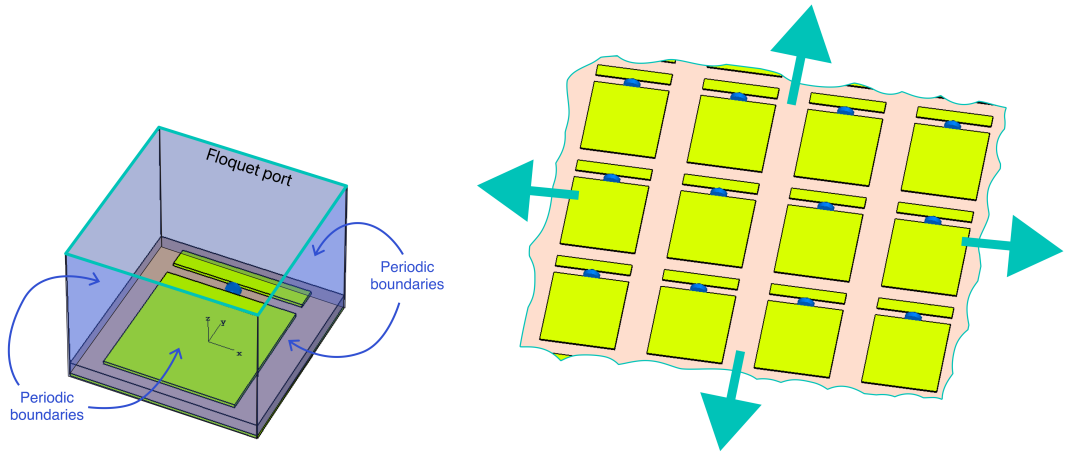

(a) (b)

Figure 2.10: Diagram showing periodic boundary conditions applied to a single element (a) and the equivalent structure in the calculation of the single unit cell subject to periodic boundaries (b).

periodic structure's response to varying frequencies, incident angles, or polarization states, as it enables efficient parametric sweeps without recalculating the entire structure for each parameter variation [52]. Fig. 2.10(a) shows a model of a unit cell composed in the CST Microwave Studio software package. The boundaries are highlighted on the lateral borders. The excitation port, being a Floquet port, is parallel to the structure at approximately 10 times the substrate thickness. The equivalent structure is shown in Fig. 2.10(b), where copies of the elements extend to infinity in the lateral directions.

The reflection coefficient for the single linearly-polarised RIS element in Fig. 2.10 can be determined from the scattering parameters (S-parameters) seen at the Floquet port. In this case, the ratio of the transmitted to the received power from the driven port. The reflction coefficient can be derived after de-embedding the S-parameters to cancel the delay between the port and the unit cell. This de-embedding procedure involves replacing the element with a perfect electrical conductor (PEC) and subtracting the resulting simulated phase from the calculated unit cell S-parameters [53].

2.3.3 Reflection coefficient measurement techniques

The two most common measurement techniques for verifying the reflection coefficient behaviour of RISs are the *specular reflection* [54] and the *waveguide simulator* or *rectangular waveguide* (RWG) methods [55]. The specular reflection approach is the most straight-forward and will be discussed here first.

Specular reflection measurement technique

In this reflection coefficient measurement approach, a full-size RIS is required. This method involves programming the RIS as a specular reflector and measuring the transmission between two directional antennas placed at equal and opposite angles with respect to the RIS [54]. The local reflection coefficient for a given tuned element state is approximated by setting the entire surface to that state, followed by measuring the transmission parameters between the antennas via the RIS. The RIS prototype must be large enough such that the unit cells composing the RIS present a similar impedance to an impinging plane wave. That is, wave contributions subject to variation in the reflection response of the unit cells close to the surface edges can be safely ignored. This is an important consideration as the local reflection response factors in the close coupling between elements, largely through a capacitive grid-type arrangement. A typical indoor measurement setup is depicted in Fig. 2.11. Two identical directional antennas (horn antennas in most instances) are aligned with the center of the RIS prototype at a distance $>2D^2/\lambda$ where D is the largest lateral dimension of the sample under test and λ is the shortest wavelength of interest. An anechoic chamber hosts this setup to minimise contamination from environmental reflections. The antennas are separated at equal angles φ with respect to broadside of the surface. A VNA is connected to the antennas through coaxial cables and calibrated such that the calibration planes are at the input ports to the antennas, removing residual errors and calibrating out the cable delay. A reference transmission versus frequency measurement, $S_{21}^{\mathrm{ref}(f)}$, is then ascertained with a highly conducting metallic plate such as copper or aluminium of the same dimensions as the RIS sample. Following this, specular reflection via the RIS is measured, $S_{21}^{k}(f)$, for a total of K configurations. The de-embedded reflection coefficients at incident angle φ can then be approximated by:

$$\Gamma^{k}(f,\varphi) = \frac{S_{21}^{k}(f,\varphi)}{S_{21}^{\mathrm{ref}}(f,\varphi)} = \rho_k e^{j\phi_k} \tag{2.49}$$

Where ρ_k and ϕ_k are the magnitude and phase of the local reflection coefficient when the unit cell is tuned to its kth surface impedance value at the incident angle of interest. For instance, in a 3-bit metasurface, $K = 8$ and therefore one would extract 8 sets of reflection coefficient measurements per incidence angle. This simple analysis has not considered variations in polarisation and incident angle in elevation, but has been explored further in works such as [1] and [54]. A tangible example is the measurement setup for ascertaining relection coefficients investigated by Alvarez et al. [1] shown in Fig. 2.12.

Rectangular waveguide measurement technique

A different approach spawned from the simulation of large planar phased array antennas is the RWG approach introduced by Hannan and Balfour [56], otherwise known as the *waveguide simulator* approach. This is depicted in Fig. 2.13 and involves measuring propagation through a

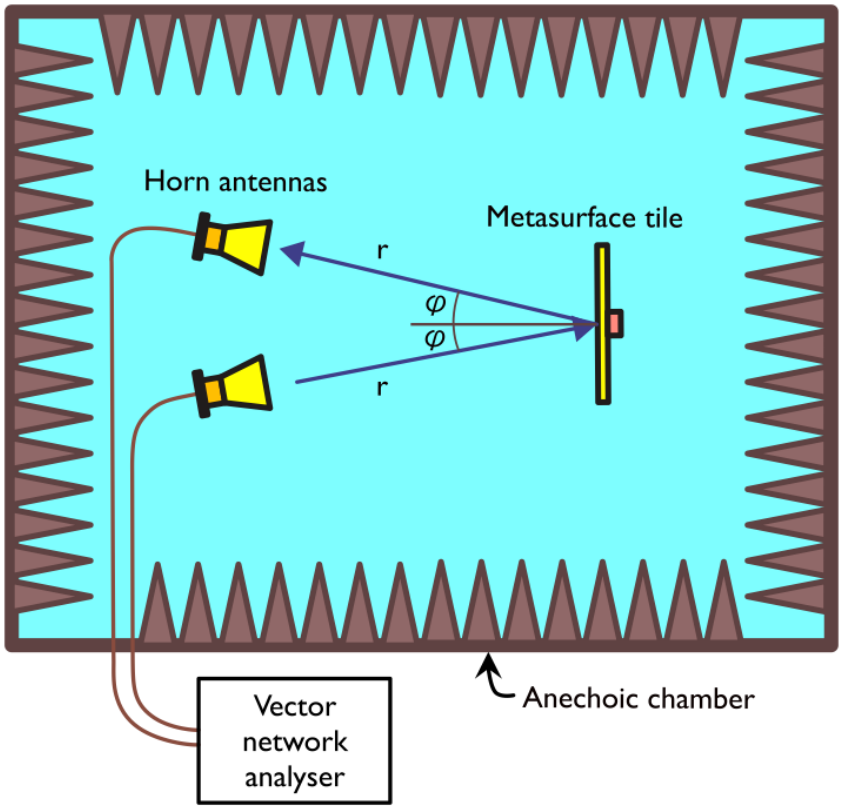

Figure 2.11: Reflection coefficient measurement setup for the specular reflection technique.

rectangular waveguide loaded with a metasurface sample. Subject to probe excitation at the end of the waveguide, the system can be modeled as the propagation of two plane waves alternately reflecting from perfectly conducting walls of spacing d, satisfying the relationship:

$$|\sin\theta| = \frac{\pi}{kd} = \frac{\lambda_0}{2d} \tag{2.50}$$

By image theory, m half-elements can be placed at the end of the RWG to replicate a perioidic structure (so long as there is appropriate lateral symmetry in the unit cell design). The RWG width is then related to the unit cell periodicity by $d = m(p/2)$. Therefore:

$$|\sin\theta| = \frac{\lambda_0}{mp} \tag{2.51}$$

and the number of half-elements, m, is used to determine the range of measured θ. With the periodicity constrained $<\lambda_0/2$ to avoid the early onset of grating lobes [27]:

$$p = \frac{\lambda_0}{m|\sin\theta|} < \frac{\lambda_0}{2} \tag{2.52}$$

This results in the constraint $m > 2$. That is, the RWG technique is valid in this context for the simulation of 1.5 unit cells. A practical value is $m = 2$ to avoid having to integrate unit cells into the waveguide walls. The cutoff frequencies for the first two TE modes, TE_{10} and TE_{20},

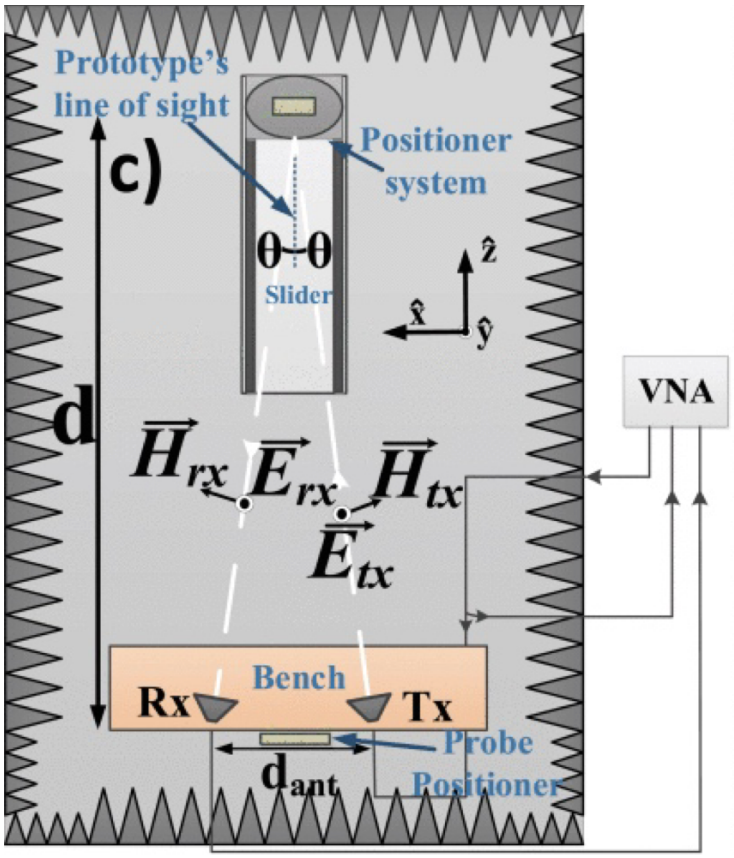

(a)

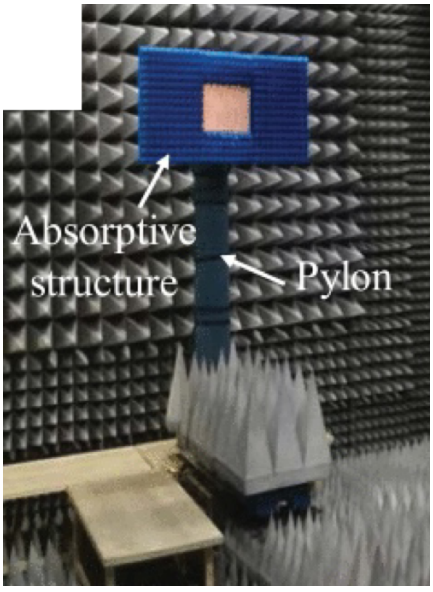

(b)

(c)

Figure 2.12: Measurement setup for a specular measurement of the reflection coefficient of a metasurface adapted from [1] (a). The sample is positioned within an absorptive structure mounted on an adjustable pylon (b). Horn antennas are positioned on tripods and adjusted according to the required incidence angles and polarisations (c). ©2020 IEEE.

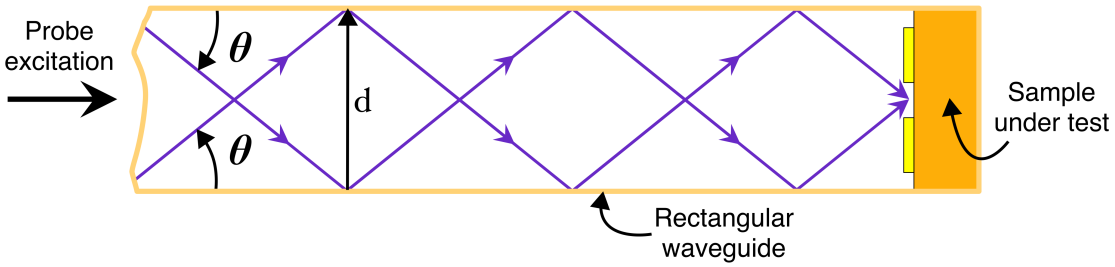

Figure 2.13: Diagram of the rectangular waveguide reflection coefficient measurement technique

are found via $f_{10} = f_{20}/2 = c/2d$, where c is the speed of light in a vacuum. From this information, (2.50) can be used to determine the effective incidence angles at the lower and upper cutoff frequencies as 30° and 90°, respectively. This means that when the frequency of excitation is increased, the incidence angle of the pair of equivalent plane waves is increased. Therefore, frequency sweep measurements cannot be decoupled from oblique incidence measurements. A single port of the VNA is utilised for these measurements in the form of a return loss measurement. The calibration plane is placed before the probe input. These measurements, however, are not directly compared to simulated data under periodic boundary conditions. Rather, this measurement is of such a low complexity that it can easily be modeled in a full-wave simulation of the probe-fed waveguide with loading from the sample [57]. Fig. 2.14 has been extracted from the work by Wang et al. [2] and shows the measurement system setup for waveguide simulation of a broadband 1-bit RIS operating centered at 8.6 GHz. The measured reflection phases, denoted as *WGS*, bear close resemblance to the simulated phase with an oblique incidence angle of 30° denoted by *PBC*.

Comparison

In the RWG approach, only a small sample is required, thereby offering a signficant cost reduction compared to the specular approach. However, this approach is limited in its applicability to unit cells that are symmetric about the lateral axes. That said, this method has been used to successfully characterise asymmetrical designs such as those found in [57] and [58]. The RWG method provides less information than the specular reflection method, as in the latter it is possible to facilitate a broad frequency sweep for fixed incidence angles. The complexity difference is notable, however, in that the fabrication of a large RIS structure is not necessary in the RWG method, enabling cost-effective parametric studies of RIS elements.

2.3.4 Beam pattern measurement techniques

Methods for determining the electromagnetic behaviour of RISs bear resemblance to the well-established antenna measurement techniques. The most relevant of which are those applied to reflectarrays [59]. These are effectively 2D reflector dishes consisting of an electrically-

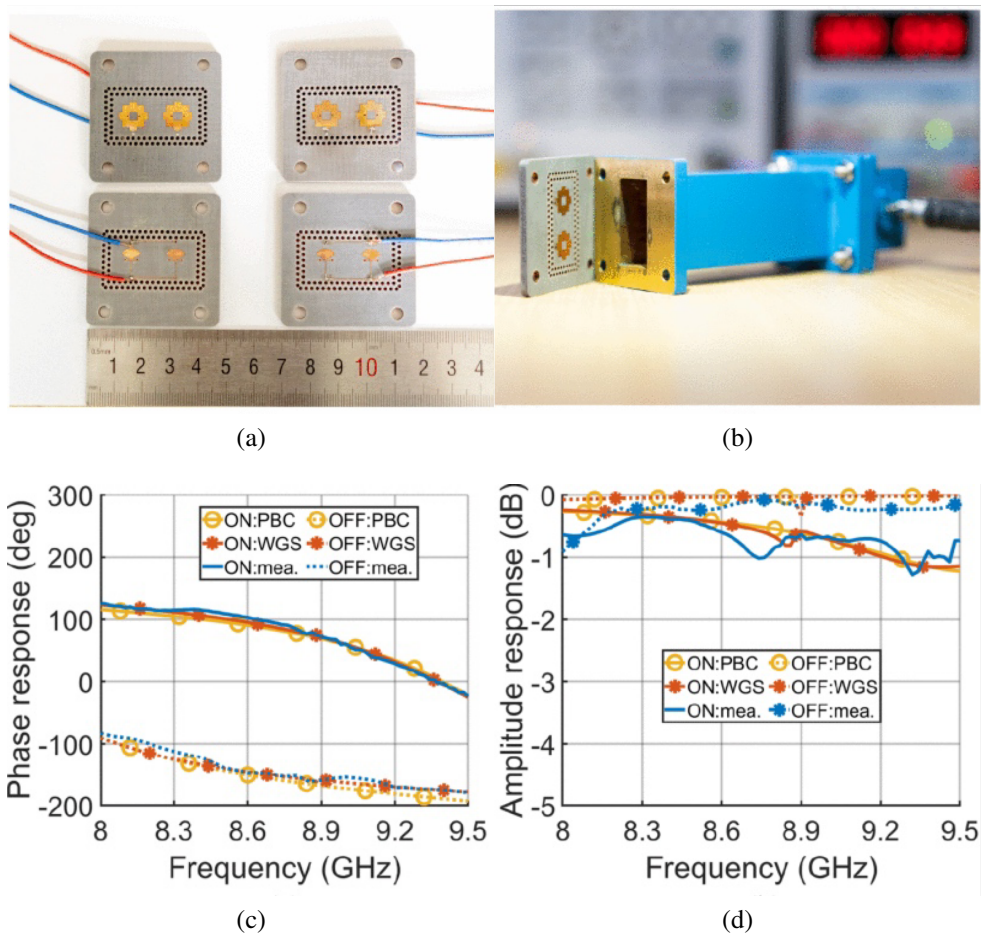

Figure 2.14: Rectangular waveguide reflection coefficient measurement setup from [2]. Fabricated unit cell samples as a load (a) and the rectangular waveguide (b). Measured phase from (denoted WGS) compared to simulated phase (c) denoted as PBC. Respective magnitudes (d). ©2020 IEEE.

large array of shaped reflecting elements illuminated by a feeding antenna placed within the radiating near-field region of the reflector. RISs differ in that the feeding antenna is typically placed further away, and its position may not necessarily be fixed. While measurements of the beam shaping performance of RISs is not as widely documented, there are two common approaches to performance verification in the literature. Namely, reflectarray-type measurement approaches [6] [58] and far-field to far-field approaches [60]. Practically speaking, the former case is useful for determining the performance of a RIS-aided wireless link when one of the end nodes is in close proximity to the RIS (i.e., at a distance proportional to the width of the RIS) or the RIS is very large, thereby warranting determination of its near-field behaviour. In outdoor scenarios such as the one that will be covered in chapter 5, a more realistic deployment relies more on far-field to far-field beamsteering via the RIS. The choice of the former is convenient for its compactness, which is particularly important at sub-6 GHz frequencies where the far-field distance can be large, and this will be covered first.

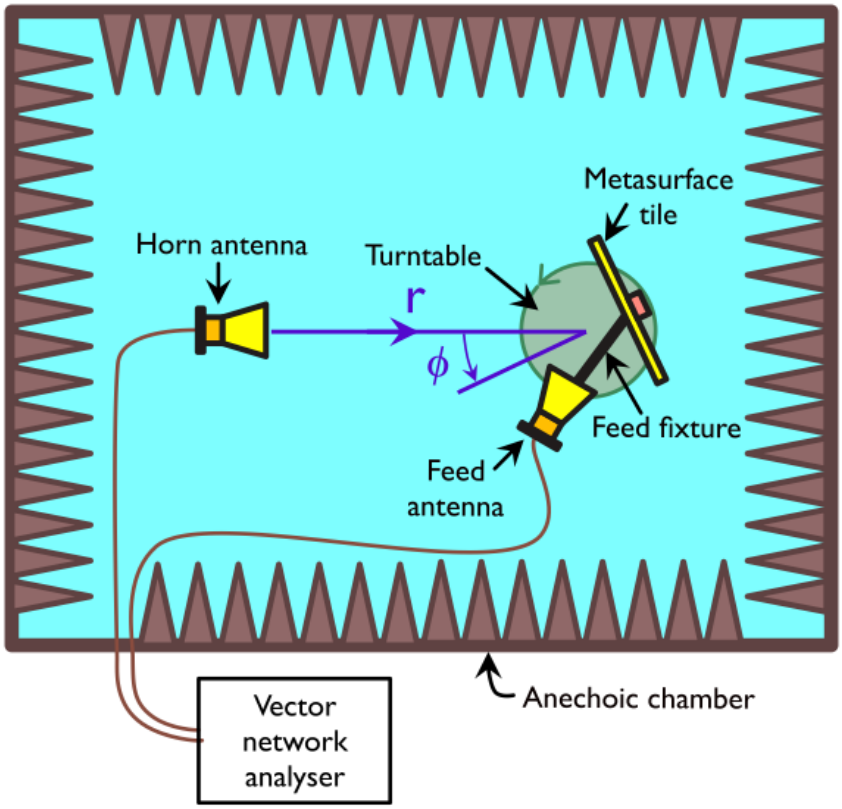

Figure 2.15: Beamforming measurement setup in a reflectarray configuration.

Reflectarray-type measurements

Fig. 2.15 depicts a reflectarray-type measurement setup for radiative near-field to far-field beamforming. A horn antenna is excited and the power is sampled by a feed antenna fixed to a rotating platform (e.g., a turntable). The turntable hosts the RIS sample, with the feed antenna attached via a fixture and directed towards the center of the RIS. As the turntable is rotated, the transmission parameters between the antennas are ascertained and, after post-processing, the beam pattern can be determined. The metrics usually sought in this type of setup are the combined gain of the feed antenna and RIS. An example from a work by Popov et al. [3] has been reproduced in Fig. 2.16. The volume required for the reflectarray-type measurement can be further reduced by employing a near-field probe as the sampling antenna and exciting the feed antenna, such as in the works by Yang et al. [6] and Han et al. [61].

Far-field to far-field measurements

A typical far-field to far-field measurement setup is depicted in Fig. 2.17. This is similar to the topology used in the example in section 2.1. In this case, both of the antennas are situated in the far-field region of the RIS. The re-radiated power is sampled along the radius r through movement of the receiver antenna with a pivot point situated at the center of the RIS. In these measurements, the RIS and antennas are not considered as part of the same antenna system,

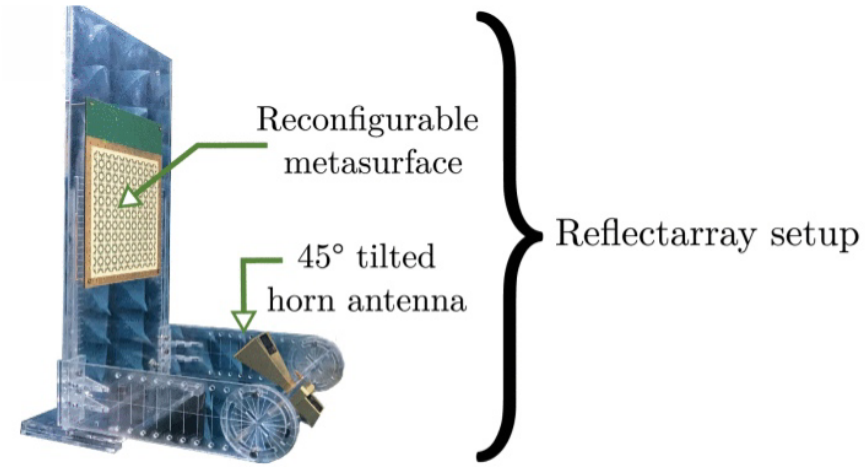

(a)

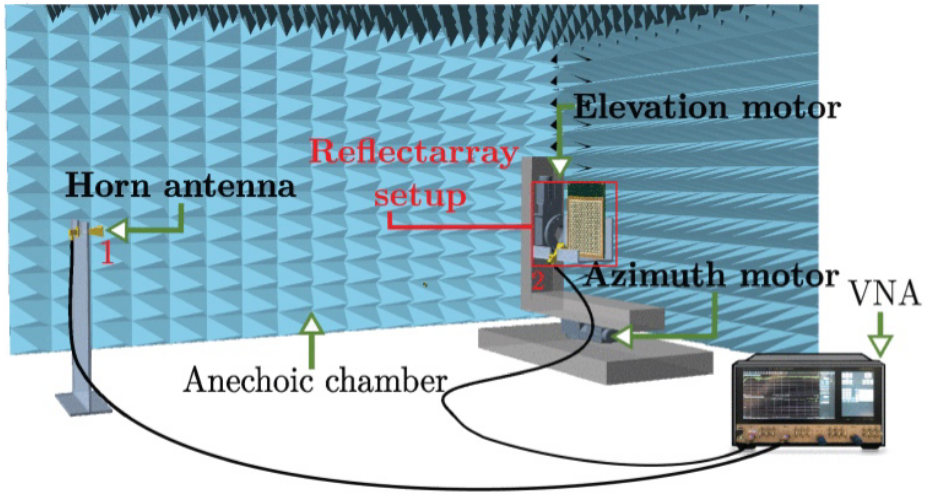

(b)

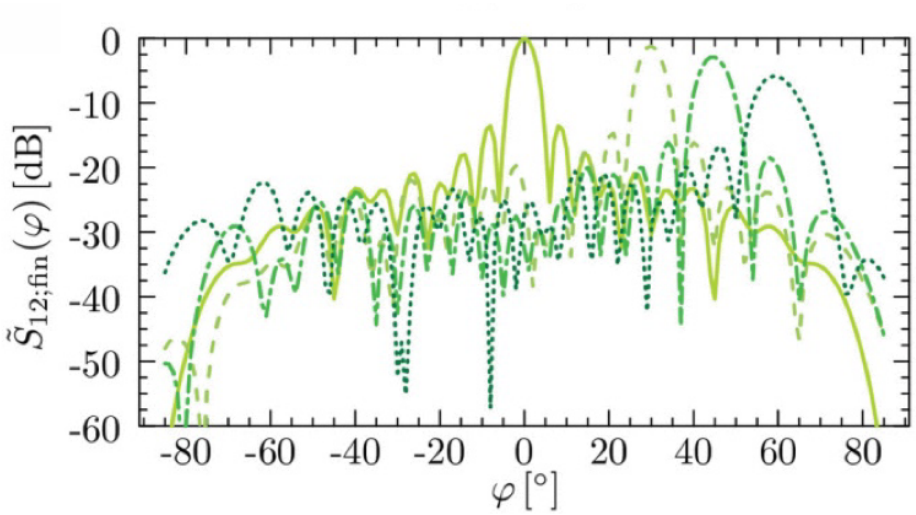

(c)

Figure 2.16: Reflectarray-type measurement setup for a binary metasurface (a). Complete anechoic chamber measurement setup (b). Resulting normalised azimuthal beam patterns for 4 RIS configurations (c). Adapted from [3]. ©2021 Frontiers.

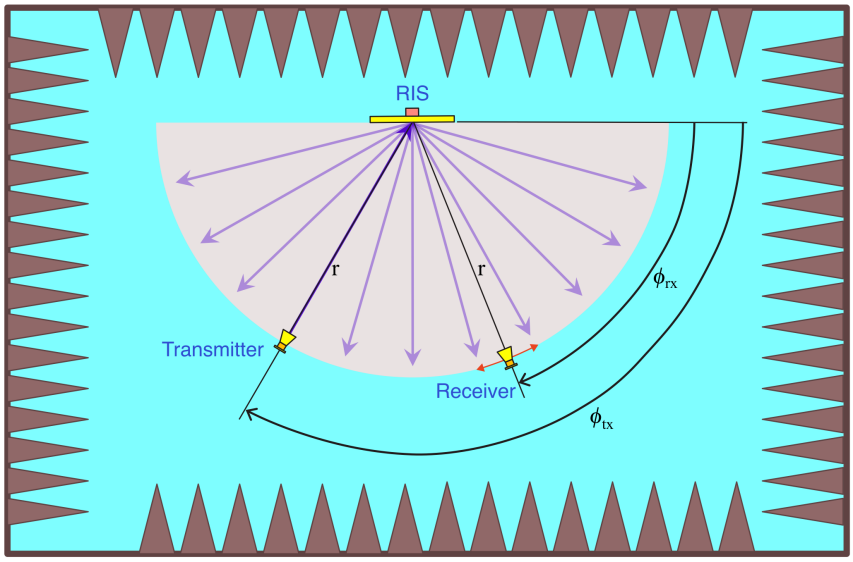

Figure 2.17: Beamforming measurement setup in a far-field to far-field configuration.

but rather the RIS can be considered as a controllable interacting object as part of the wireless channel. Therefore, the notion of antenna gain that might apply as part of characterising an end node does not necessarily apply in this case. Therefore, the beam patterns in the far-field to far-field case are usually normalised for a maximum gain of 0 dB. An example of this type of setup has been adapted from the work by Wolff et al. [4], seen in Fig. 2.18(a). The authors employed a fixture allowing motion of the receiver antenna about a hemisphere surrounding the metasurface sample, keeping the transmit antenna fixed in place. The resulting beam patterns are plotted in Fig. 2.18(b), demonstrating beamsteering capabilities between broadside and 65° off-broadside.

Comparison

The far-field to far-field approach is more demanding in terms of required measurement area. While an anechoic chamber accommodating a distance of r plus room for the turntable and samples is required for the reflectarray-based approach. On the other hand, the far-field to far-field measurement approach requires a semicircular area with a diameter $2r$. This requires an anechoic chamber of length and width $2r$ and r, respectively. For example, a RIS of dimensions $0.5m \times 0.5m$ measured at 4 GHz requires a chamber of length and width more than 13.3 m and 6.7 m, respectively (using $r = 2D^2/\lambda$ where D is the largest dimension of the RIS). This volume may be beyond the capabilities of commonly available anechoic chambers in research institutions. For instance, the anechoic chamber employed to measure the beam patterns of the dual-polarised prototype in chapter 3 has dimensions of 8 $m \times 4$ $m \times 4$ m. In such cases, it is possible to resort to outdoor measurements but with reduced accuracy due to the unavoidable ground bounce and other sources of multipath propagation [62].

This concludes the coverage of RIS measurements in this chapter. Combinations of these

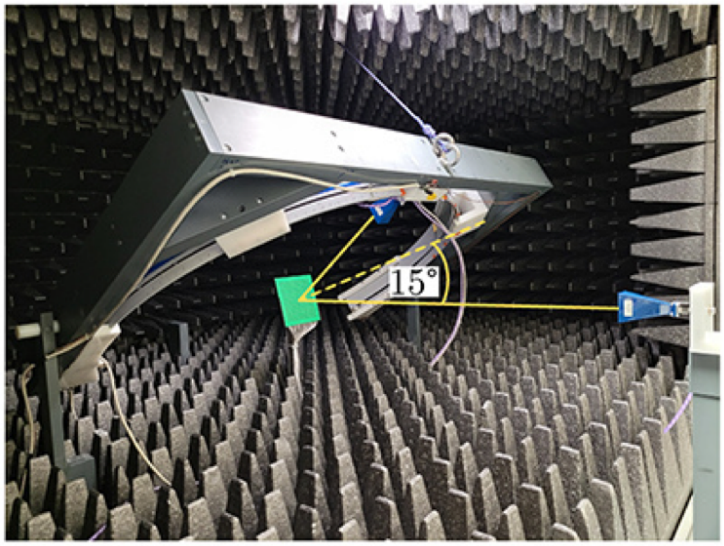

(a)

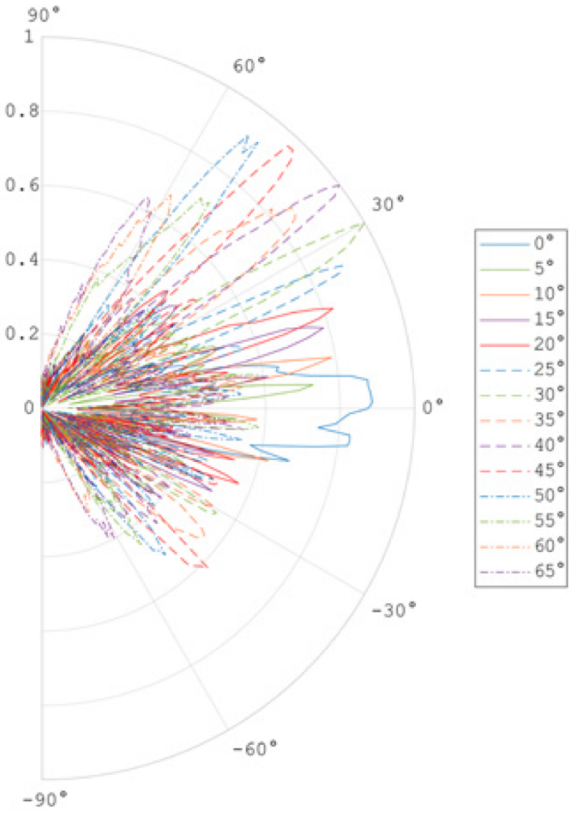

(b)

Figure 2.18: Far-field to far-field measurement setup for a continuously tunable metasurface (a). Resulting beam patterns for beamsteering between broadside and 65° off-broadside. From [4]. ©2023 AIP Publishing.

approaches have been utilised for the work covered in the chapter that follows which explores design strategies for reconfigurable metasurfaces.

2.4 RIS testbeds

Now that the operating principles of RISs have been reviewed, this section provides a summary of RIS designs in the literature.

2.4.1 Programmable unit cells

As introduced in section 2.1.2, in the microwave region, the local reflection coefficient of a RIS element can be varied by placing a tunable load between sets of microstrip patches, such as a varactor diode or a positive-intrinsic-negative (PIN) diode switch [63] [64]. PIN diodes are desirable for their low voltage requirements, enabling interfacing with off-the-shelf shift registers. At sub-6 GHz, PIN diodes are utilised as switches, with forward-biased states acting as a series resistance of a few ohms and a reverse-biased state with a series capacitance typically below 1 pF. A single PIN diode can be employed to realise a single pair of local reflection coefficients, which can be represented by 1-bit, (i.e., two state) complex values. A varactor diode interfaced with voltage level shifter circuitry can be utilised to the same effect [64]. A greater number of unit cell reflection states can be realised by employing more PIN diodes per unit cell or interfacing varactor diodes with digital to analog converters (DACs) [65]. The former can be realised with more shift registers and results in higher current consumption per unit cell, whereas the later requires biasing circuitry with a higher complexity. The application-dependent trade offs of unit cell resolution versus control circuitry complexity and power consumption are explored in [66].

Literature on reconfigurable reflectarrays, being similar in architecture to transmission-based RIS systems, and reconfigurable metasurfaces provides an abundant source of techniques for dynamic control of unit cell reflection characteristics [67] [68]. Two common methods of reflection response control in reconfigurable reflectarrays are that of tunable delay lines and tunable resonant elements. The former technique involves coupling a radiating element to a transmission line section, the electrical length of which is varied to provide differing phase shift characteristics, prior to coupling and re-radiation of the incident wave. The latter technique involves altering the resonant frequency of the radiating element itself through reactive loading or switching geometry [57].

Tsilipakos et al. showed that loading a pair of conducting patches with a variable resistive-capacitive (RC) element was shown to offer a 300° continuous phase range in [69]. The unit cell design offers mimimal loss and, when the capacitance values across a supercell were optimised, it was shown to offer anomalous reflection with a radiation efficiency of 98%. Alongside a resistance variation of the unit cell, the design may offer a tunable magnitude response for applications such as tunable perfect absorption and higher-order modulation schemes.

A tunable unit cell element employing a shorted substrate integrated waveguide (SIW) section, loaded with shunt varactors and slot-coupled to a resonant patch was demonstrated by J.

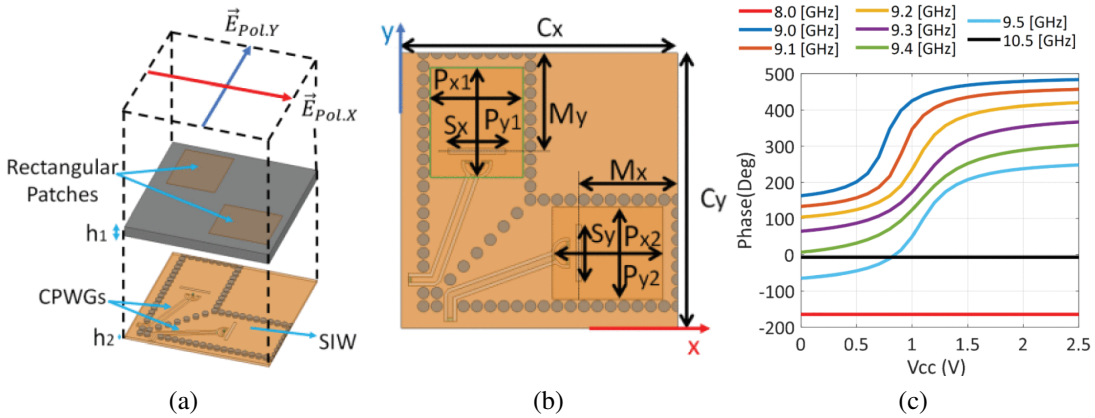

Figure 2.19: Substrate integrated waveguide-based RIS unit cell. Two ports are loaded with varactor diodes. Reproduced from [5]. ©2019 IEEE.

Zang et al. [70]. The varactors provide continuous tuning of the effective length of the SIW section whilst the biasing network is well shielded from the radiating and tuning components. The work in [5] extends the SIW slot-coupled patch into a dual-polarisation device, depicted in Fig. 2.21, with individually controllable phases for the orthogonal wave components.

A reconfigurable metasurface with independent magnitude and phase response was proposed by Ashoor et al. [71], where a PIN diode-loaded dipole-ring resonator and varactor-loaded split ring resonator are operated as coupled resonators. The conductance of the PIN diode if controlled by a forward-bias voltage to enable magnitude control, whilst the varactor reverse-bias voltage enables phase control. Beamforming capabilities are demonstrated with a significant improvement of side-lobe level over uniform magnitude control at the expense of dissipative loss. Symmetric and asymmetric beam splitting with a Chebyshev magnitude distribution was demonstrated through full-wave simulation of a 48 unit cell structure.

The authors of [6] created a multi-functional FPGA-controlled reconfigurable metasurface capable of varying reflection phase of 1600 individually controllable, 1-bit, single-polarisation unit cells. The anisoptropic property of this surface is utilised for linear to linear polarisation conversion. Beam steering, beam shaping, and agile scattering are demonstrated, the performance of which was optimised via a genetic algorithm and a 2D-IFFT technique to substantially improve optimisation efficiency.

The aforementioned 1-bit unit cell works involved a similar unit cell design of resonant elements connected to or isolated from ground, the resulting phase difference over the frequency band being of a convex shape with its peak at the artificial magnetic conductor (AMC) frequency of the unit cell, as is the case in similar designs [72] [2]. However, it is possible to achieve a broadband linear curve for reflection phase through the current-reversal mechanism [73]. Montori et al. [74] presented a microstrip patch coupled to a polarisation-shifting slotline network which is switched between edges of the patch in the orthogonal polarisation to provide a precise

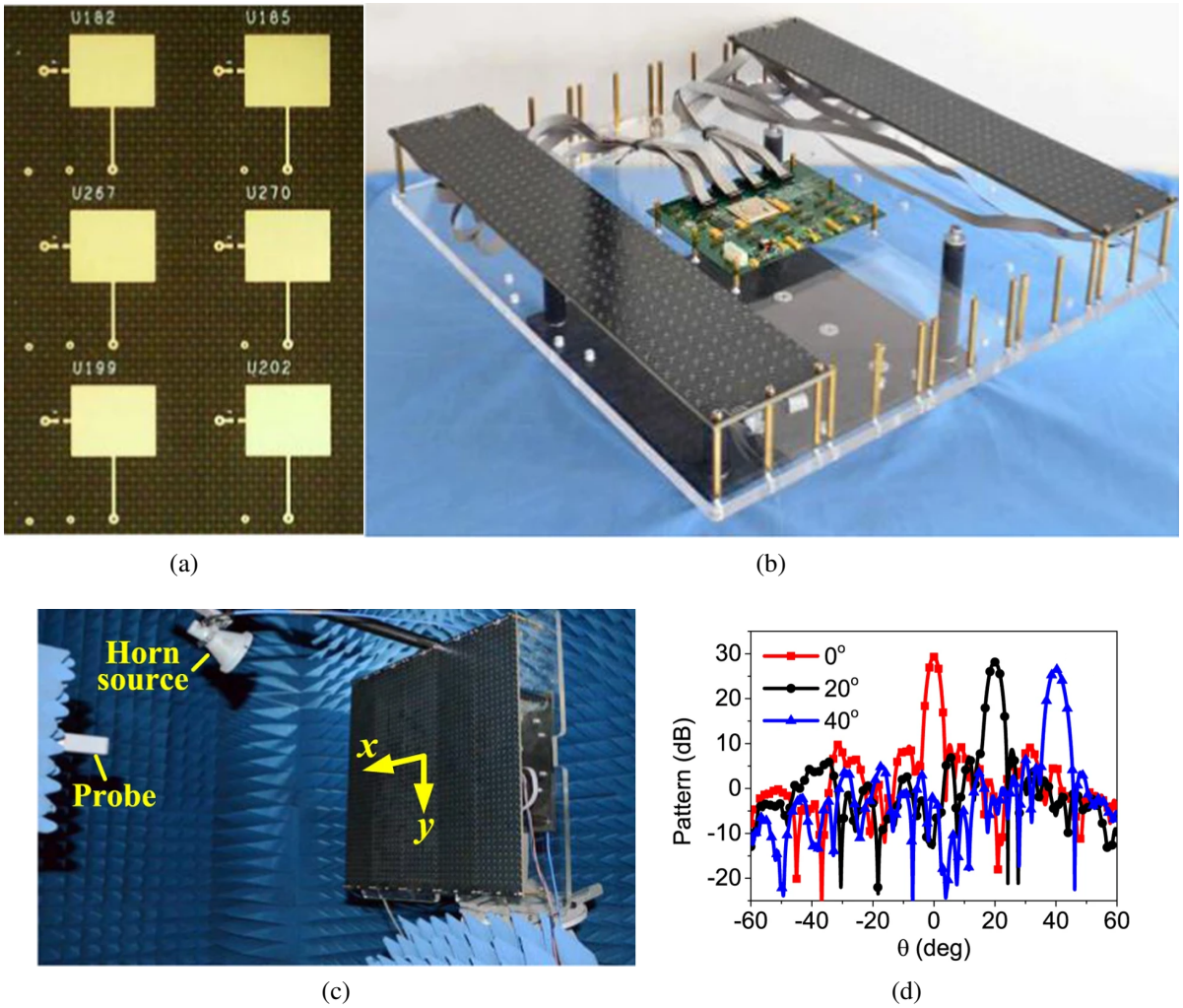

Figure 2.20: 1-bit PIN diode-based RIS prototype. Fabricated 1-bit unit cells (a), fabricated prototype with two tiles and a control board (b), pattern measurement setup (c), and resulting gain patterns (d). Reproduced from [6]. ©2016 Nature.

180 degree phase difference. This was utilised for a 1-bit reflectarray for imaging applications at W-band. An improved bandwidth of 1-bit metasurface behaviour can be achieved through compensation of the nonlinearity of the phase-frequency curve. Huang et al. [75] presented a unit cell design for 1-bit operation extended over a broad bandwidth through a combination of coarse tuning with a PIN diode and fine tuning with a varactor to compensate for the dispersion of the scatterers. These unit cells were utilised to provide multiple elementary functions, realising beam splitting, beam steering, polarisation conversion, and radar cross section (RCS) reduction, demonstrating significant improvement in RCS reduction bandwidth over previous works.

Although the nonidealities of such coarse phase partitions are revealed in the form of directivity reduction and increased sidelobe levels when compared to continuous phase tuning, the merits of the 1-bit architecture include the simplicity of its control network and reduced computational complexity. It has been shown that a multitude of wave transformation functions are possible with only 2 reflection phase states per unit cell [76]. In order to mitigate the effects of poor quantisation-lobe level performance in 1-bit reflecting element designs, Kashyap et al. [77] proposed a phase-delay randomisation scheme where each unit cell is subject to a uniformly-distributed random phase offset such that the periodicity of the phase-rounding quantisation error is broken. It was shown that a significant sidelobe level improvement was possible by introducing random line lengths in delay-line loaded reflecting patches. Through 2-bit RIS unit cells, reflection phase states of $\phi_r \in [0, \pi/2, \pi, 3\pi/2]$ are available. Several examples of 2-bit coding metasurface unit cells based on segmented resonant elements are available in the literature [63,78–80]. The authors in [63] developed a two-bit digital unit cell element composed of an irregular hexagonal patch with PIN diodes connected to biasing lines at its top and bottom edges. In [78], the unit cells are composed of two nested capacitively-loaded square loops, each embedded with PIN diodes, to provide a narrowband phase partition of 90 degrees.

Similar to the polarisation-switching 1-bit element detailed in [74], the authors in [81] developed an extension of this element to provide 2-bit operation. A slotline coupling network facilitating the current reversal mechanism is given switchable paths that provide an additional 90 degree phase shift to each of the original 0 and 180 degree states. This unit cell was then utilised to create an RIS-based communication system with beam steering capability [7].

A 2-bit metasurface element based on an antenna-filter-antenna type structure has been documented in [82] which exhibits a bandpass filter type response. A crossed slot is coupled to stripline resonators to form switchable 3- and 4-pole magnitude and phases responses. The filter responses at the centre frequency exhibit switchable 180° and 90° respective phase shifts and, when combined with the current reversal mechanism, produce the desired 360° and 270° phase shifts as well. Like the above-mentioned current reversal mechanism-based unit cells, the reflected wave for this design is polarised in the orthogonal mode to the incident wave. While the increased complexity may be undesirable, the nature of this design produces a flat magnitude

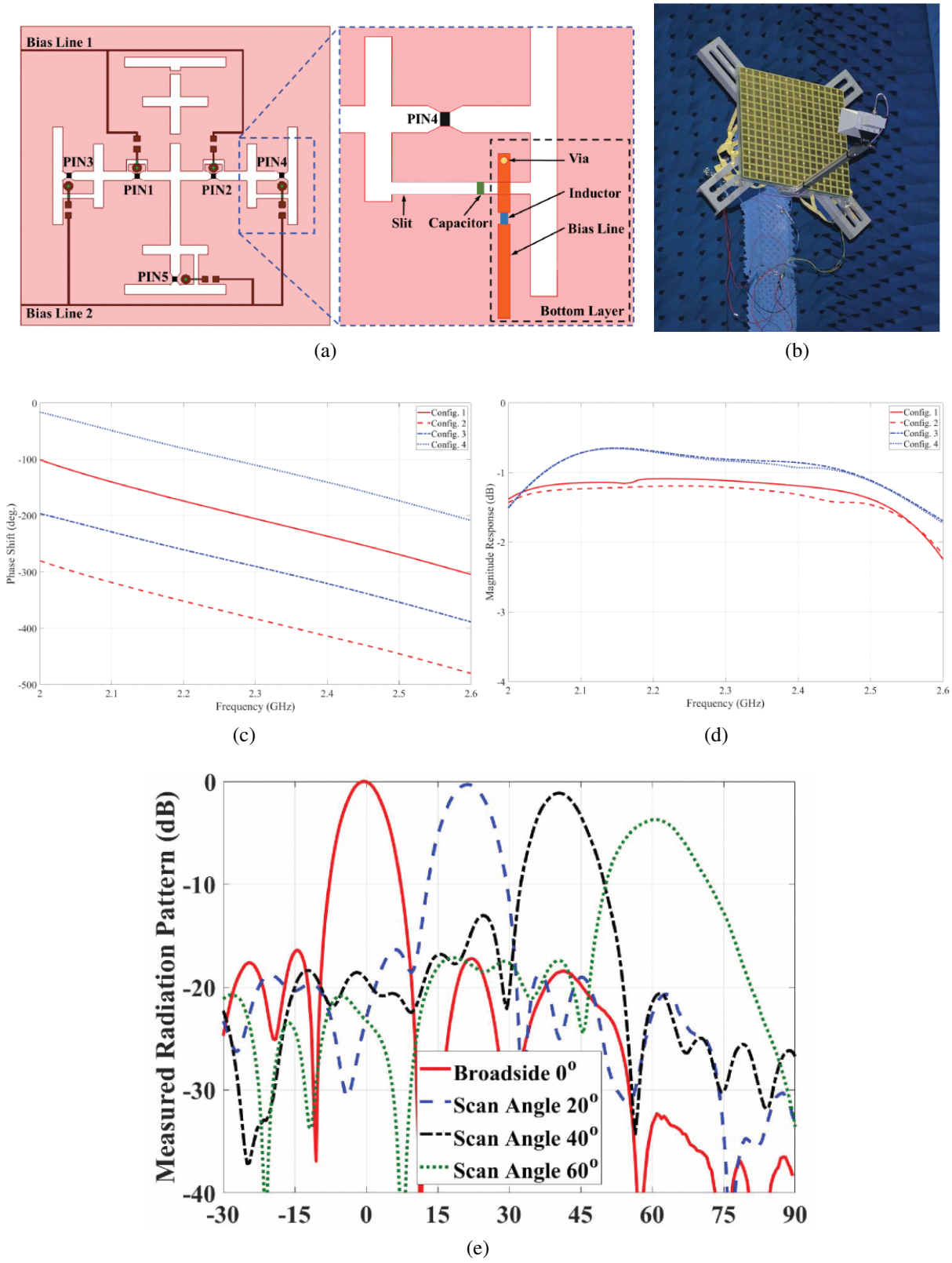

Figure 2.21: Broadband 2-bit polarisation-rotating RIS. Unit cell design with biasing topology (a), fabricated device in reflectarray-type measurement setup (b), local phase response (c), local magnitude response (d), and beam patterns for 4 configurations (e). Reproduced from [7]. ©2020 IEEE.

response over the passband and an improved phase-frequency error performance over a broader bandwidth compared to segmented resonant elements.

To enable greater flexibility with required phase shifts and oblique incidence behaviour, higher resolution RIS unit cells can be utilised. However, with increased phase agility comes greater complexity, volume, power, and fabrication cost. For instance, the increased number of lossy components results in a marked absorption of incident energy. Where the directivity improvement for a shift from 2 bits to 3 bits of resolution might result in a directivity improvement at oblique angles of 1-1.5 dB [83], the additional losses through component resistances and bias network parasitics may in fact result in a net gain reduction. Higher resolution discrete-phase unit cells are less common in the literature. While 3-bit segmented resonator-type unit cells can be implemented through connecting 4 optimised patches with 3 PIN diodes or MEMS switches, it is difficult to realise sufficient phase alignment over a useful bandwidth. While 2-bit unit cell designs only require a phase range of 270°, 3-bit unit cell designs require 315°. This additional phase range is typically achieved through implementing a higher unit cell reflective Q-factor, leading to a steeper phase-frequency gradient [84]. The higher Q of the resonators results in a larger current flow through the discrete elements and therefore greater losses, as well as increased phase-frequency error due to the increased dispersion associated with narrower resonance. Saifullah et al. [85] recently proposed a 3-bit unit cell design employing 4 PIN diodes driven by 3 control lines to facilitate 8 phase states. The design is addressable column-wise for azimuthal reflection control and maintains losses of less than 1.3 dB at X-band.

Multi-bit reflection phase behaviour is also possible through the method of vector synthesis, where the unit cell reflection phases are subject to temporal variation. This has been demonstrated by Zhang et al. [86], where a 2-bit metasurface is driven with 16 sets of time-coding sequences to realise 4-bit operation with 360° phase coverage at a harmonic frequency. An FPGA-controlled prototype was constructed and anomalous reflection measurements revealed a significant sidelobe level improvement over the 2-bit design.

This concludes a summary of the recent progress in reflecting-type metasurfaces for application in RISs. Following on from this is a summary of works providing a means of addressing RIS unit cells in a practical fashion.

2.4.2 Configuration mechanisms

The biasing network of an RIS provides a means of control over the individual unit cell reflection characteristics. The structure of this network is dependent on the tuning mechanism and the desired degrees of freedom of EM control. For example, for a 1-bit RIS structure utilising an array of PIN diode-loaded unit cells with control in the azimuthal-plane, a biasing network might consist of columns driven by voltages such that the respective PIN diodes in a single column are reverse or forward-biased for 0 and 180°, respectively. These types of networks are commonly designed to be driven by FPGAs. For control in both ϕ and θ (i.e., 2-dimensional beamsteering),

RISs require a more complex biasing network that supports individually addressable unit cells.

The complexity of biasing circuitry for RISs is dependent on factors such as the tuning scheme, the number of unit cells, and the periodicity of the unit cells. Continuous tuning is typically dependent on digital-to-analog converters (DACs) where, for individual control of unit cell elements with analog signals, an ADC channel is required for each unit cell. The DACs subsequently require digital control signals which may be in the form of well-known serial communication protocols such as SPI and I2C, with the associated circuitry and clock signals.

Electrical tuning of varactor diodes, requiring a variable DC voltage typically between 0 and 30V, is achieved through employing DACs. DACs are a mature technology with the capability for a single DAC IC to provide multiple channels, thereby serving multiple unit cells each. The required volume of DACs for a large surface of individually controllable unit cells may be costly and the output voltage range can be a limiting factor, thereby requiring additional amplification circuitry. Biasing of PIN diodes is readily achieved through providing a forward bias voltage usually between 0.7 and 1.5 volts with a typical operating current around 1-10 mA. These requirements can be readily achieved by digital circuitry, such as through microcontroller IO ports, thereby reducing bias network volume and cost at the expense of coarser tuning.

An effective method of mitigating the parasitic effects of biasing circuitry is to utilise light sources in a similar fashion to optoisolators, allowing the bias routing circuitry to be electrically isolated from the radiating components. An optically-controlled reconfigurable metasurface was developed by Zhang et al. [87], where a set of PIN photodiodes provide biasing voltage for unit cell subarrays loaded with varactor diodes. The work introduces the concept of an *optically integrated digital platform* metasurface, where photodiodes, connected to a set of varactor-controlled unit cells, are illuminated with varying intensity light, allowing remote tuning of the metasurface and therefore eliminating the bulky biasing circuitry associated with conventional reconfigurable metasurfaces.

A reduction in biasing network complexity in reconfigurable reflectarrays through row-column control was recently proposed by Artiga [88]. In this scheme, element phase shifts are controlled row-wise and column-wise such that, where rows and columns overlap, an additive phase shift results. For an $N \times M$ metasurface, this scheme only requires $N + M$ analog control lines as opposed to $N \times M$. The work also proposes a 1-bit row-column control scheme in which an XOR function is applied to digital unit cells. The work demonstrates that gains close to those of per-element control of 1- and 2-bit unit cells with a row-column control scheme utilising an iterative random search algorithm, at the expense of increased sidelobe levels.

A potential enabling technology of programmable propagation environments is the concept of hypersurfaces, where unit cells are separated into tiles and each tile is connected to a control node offering switching control alongside intra-tile networking capability. Kossifos et al. [89] proposed a hypersurface consisting of an array of unit cells connected to application-specific integrated circuits (ASICs), each providing a tunable impedance and grid communication node.

These embedded controllers are arranged in a grid and form a network where each controller can communicate with its neighbors, enabling information such as switching instructions to be routed to the respective unit cells. The appeal of ICs is not only in their simplicity from an all-in-one tuning and control solution, but also in the ability to produce ICs of very small size, thereby rendering the prospect of implementing the required unit cell periodicity of approximately $1\ mm \times 1\ mm$ at 60 GHz a viable endeavour [90].

Communication between unit cell controller ICs introduces the problem of synchronisation for reliable information transfer. A global clock signal would usually be employed in this regard. However, routing such a signal to each unit cell over a large surface area results in spurious radiation of the clock harmonics to the detriment of the wireless spectrum. Timing constraints of synchronous digital circuitry are important considerations, where harmful clock skew can result in setup and hold violations. In high-speed digital design, clock skew is mitigated through ensuring that all traces carrying a given signal are of the same length as the longest signal path. However, over densely populated PCBs with large board surface areas, maintaining synchronisation becomes difficult to achieve. RISs embedded with tuning and control ASICs could instead employ asynchronous circuits to exchange control data, as discussed in the context of adaptive metasurfaces by Petrou et al. [90], where information exchange between components is facilitated by delay-insensitive data-driven protocols and the absence of a clock network results in a marked reduction in power consumption.

While there are techniques to reduce the volume of routing circuitry between tuning mechanisms at the expense of some functionality, such as employing a distributed configuration network, it is possible to eliminate the need for physical connections between unit cells through wireless inter-cell connectivity, enabling high-speed individual unit cell control [91] [92]. The scheme proposed in [91] involves a hypersurface structure with ASICs operating as wireless transceiver-capable unit cell controllers. Two communication channels are considered, with the first scenario employing a blind via as a radiating element within the metasurface substrate above the ground plane. The second scenario considers a dedicated layer in which a monopole is embedded in a dielectric between two conducting planes in the form of a parallel-plate waveguide. For the first scenario, full-wave simulations are carried out and the structure optimised to maximise unit cell to unit cell communication links whilst minimising perturbations to the unit cell behaviour and path loss through leakage from the substrate. The second scenario is considered qualitatively, given the reduced complexity of propagation within the parallel-plate structure, demonstrating an improved transmission efficiency over first scenario at the expense of greater fabrication complexity.

Software-defined metasurfaces have been proposed [93] and consist of a distributed network of controller ICs with unit cell-level nanonetworks controlling sections of the conductors of which the unit cells are composed. The unit cells are broken up into smaller individually controllable cells in order to realise granular, fully reconfigurable element geometry. The proposed

unit cell technology in this work utilises a layer of graphene, where sub-unit cell regions of the surface are exposed to electrostatic biasing to create conducting sections which, when combined, form unit cell elements of the desired geometry. Reconfigurable conducting sections of software-defined metasurfaces would provide much broader functionality and tuneability than is achieved through employing rigid unit cells with finitely tunable materials and discrete components.

The aforementioned techniques rely on constantly available bias signals to maintain the tuning mechanisms in their required states, resulting in control circuitry requirements that scale up vastly with desired degrees of control. To overcome the need for an isolated connection to each unit cell in element-wise control, it would be ideal to have a means of maintaining the unit cell state when the bias signal is removed, thereby exhibiting a form of memory. unit cell tuning elements with memory could enable a grid arrangement of biasing lines, where each unit cell can be individually addressed by a row-column pair. Chua Mem-components [94] may offer this functionality in the form of memresistors, meminductors, and memcapacitors. That is, components whose respective resistance, inductance, and capacitance exhibit hysteresis.

Driscoll et al. demonstrated electrically controlled persistent frequency tuning of a metasurface in a work entitled *Memory Metamaterials* [95]. The authors utilise the highly hysteretic insulator-to-metal (IMT) phase transition of vanadium dioxide (VO2) to generate a form of mem-capacitance. A metasurface consisting of gold split-ring resonators on a VO2 film was shown to respond an increase in temperature with a decrease in resonant frequency. The effect is due to the increase in the material permittivity of the VO2 specimen when exposed to the current-induced local heating. The shift in resonant frequency remains present after the VO2 has thermalised back to its original temperature due to the strong hysteresis in the IMT, enabling the electrical characteristics of the metasurface to be controlled by electrical pulses.

Georgiou et al. [96] proposed a type of reactive mem-component based on a poly disperse red 1 acrylate (PDR1A) substrate. When the PDR1A specimen is exposed to circularly polarised (CP) light, a photomechanical response ensues which results in an expansion of the substrate of up to 25%. On removal of the CP light, the substrate gradually contracts to its original state, retaining a type of memory. The thermal relaxation time can be reduced by a factor of 8 through exposing the substrate to linearly polarised (LP) light. The work proposes employing the PDR1A substrate as the dielectric in a capacitor, with one of the capacitor plates consisting of a transparent conductor, indium tin oxide (ITO), such that illumination of the PDR1A may occur, resulting in a tunable capacitance range of 20%. unit cells with mem-capacitors as tuning mechanisms may each include LP and CP LED pairs arranged in an anti-parallel fashion, driven individually through respective forward and reverse currents. A means of creating a mem-inductor is also proposed and can be achieved through modification of the aspect ratio of the capacitor and connecting lines, tuned in a similar fashion. This technique was subsequently utilised for an optically-programmable metasurface absorber [97] in which unit cells consist-

ing of square patches are connected at the corners through memcapacitors, enabling a tunable impedance to maintain a 95% absorbance over a 2.7% bandwidth.

Pulse width modulation (PWM) is commonly employed in applications requiring a variable voltage source and is often used in driving LED matrices, often over large surface areas, due to the relaxed requirements on flickering. For use in electrical biasing in reconfigurable metasurface applications, a low-pass filter would be required at each PWM output so as to not modulate the reflected signal, detracting from the benefit of the low cost and simplicity of PWM. Pollock et al. [98] have shown, however, that the tuned element itself may act as a low pass filter and PWM is viable when two conditions are met - the driving force of the element should have a response time much faster than the PWM frequency and the driving frequency must be much faster than the natural frequency of the device. For the control of RF-MEMS based metasurface unit cells, the electrostatic fields applied to the elements typically require a supply voltage in the region of 50-250V, usually supplied through a combination of a DAC and high voltage amplifier controlled via a microprocessor. Pollock et al. discussed a means of replacing these expensive components with a high voltage on-off switch that can easily be controlled with a microprocessor, requiring only a fixed DC power supply. The work investigated how PWM could be used to control MEMS parallel plate actuators, comb-drive actuators, and deformable mirrors, demonstrating precise analog control by driving the actuators with a PWM frequency well above the device natural frequencies. Improved linearity of the positional response with voltage times duty cycle is demonstrated, compared to the nonlinear response of DC control, adding to the appealing characteristics of this simple biasing mechanism.

2.4.3 Advanced functionality

Recent literature has introduced more advanced reconfigurable metasurface designs offering functionalities such as full polarisation wave transformations [99], simultaneous transmission and reflection control [100], and magnetless non-reciprocity [101]. For instance, Hu et al. recently demonstrated arbitrary polarisation conversion at sub-6 GHz through temporal variation of the anisotropy of a dual-polarised reflective reconfigurable metasurface [99]. Incident waves may be transformed to exhibit polarisation characteristics anywhere on the Poincaré sphere. The authors experimentally verified conversion of a linearly polarised incident wave to circular polarisation at the fundamental frequency, as well as linear to elliptical polarisation at harmonics. This arbitrary polarisation conversion could find applications in polarisation diversity and encoding schemes in intelligent communication networks.

Simultaneous reflection and transmission-based metasurfaces extend wave control to both half-spaces. Bao et al. introduced a programmable metasurface capable of beam steering reflecting and transmitting modes with full polarisation control [100]. The authors demonstrated that through careful selection of the 1-bit metasurface coding patterns, combinations of beam-steering, beam-focussing, and diffusion could be achieved for full-space passive wave manipu-

lation. An optically-transparent version of this metasurface may be seamlessly integrated into windows and thin walls in urban settings for increased degrees of freedom in programmable radio environments. This may greatly enhance outdoor-to-indoor reception in current cellular networks [102].

Metasurface-enabled magnetless non-reciprocity is another phenomena that may be exploited in future wireless communication systems [103]. Zhang et al. recently reported experimental data of programmable non-reciprocal reflection at sub-6 GHz [101]. Employing a 2-bit programmable metasurface subject to time-varying control signals, the authors demonstrated anomalous reflection that was no longer beholden to time-reversal symmetry. This type of spatio-temporal metasurface scheme could find applications in nonreciprocal wireless systems where the transmitting and receiving channels are separated, as well as shifting isolation and mixing to free-space for reduced transceiver complexity.

This concludes the review of relevant RIS hardware implementations. The next section explores one of the significant applications of this technology in the form of RIS-aided wireless communications.

2.5 Field trials in RIS-aided communication systems

RIS-aided wireless communications have seen an enormous amount of interest in the last 5 years. The emergence of RIS is emblematic of the ongoing search for solutions that can mitigate the limitations of conventional wireless communication systems. Traditional wireless networks often struggle with issues such as signal attenuation, interference, and limited spectral efficiency, especially in dense urban environments or indoor settings. With the ability to adaptively manipulate the electromagnetic environment, RISs open up a plethora of possibilities, from boosting signal strength in shadowed areas to reducing interference in crowded spectrum, thereby improving the overall quality and efficiency of wireless connectivity. RISs have emerged as a promising solution to these concerns, but work is still underway to fully understand the true impact of this technology. At present, there is still significant progress to be made on data-driven research in this area, with the vast majority of published works not supported by experimental evidence. Some of the most relevant recent works shall be discussed here. Table 2.1 provides a list of notable data-driven RIS-aided communication works.

As a starting point, several recent reviews of the RIS-related experimental verification literature [110] [111] [112] have included the *RFocus* project by Arun and Balakrishnan [104]. Although not strictly a reflecting-type metasurface, the authors introduced an array of programmable scatterers in the form of switch-connected microstrip dipoles. The authors note the rationale for the project was to move the burden of increasing antenna size for improved channel gain from the end nodes to the environment. This is particularly important for electrically-small devices such as *Internet of Things* sensors, which suffer from poor radiation efficiency

Table 2.1: Notable data-driven works in RIS-aided communications

Year / Ref.	**RIS type**	**Frequency / Bandwidth**	**Setup**	**Antennas**	**Scenarios**	**Strengths**	**Weaknesses**
2020 [104]	CMOS switch based	2.4 GHz / 38 MHz	SISO	Omni-directional	Office mixed LoS/NLoS	Scalable approach, large number of sample points	Limited to signal strength measurements, low RIS resolution
2021 [64]	Varactor-based	5.6 GHz / 10 MHz	SISO	Directional	Indoor NLoS & outdoor rooftops	First outdoor long-range RIS measurement, significant channel gain enhancement	Limited to directional antennas in the RIS near-field, limited bandwidth, low RIS resolution
2021 [105]	PIN diode-based	5.8 GHz / 20 MHz	SISO	Directional	Ground-level via building obstruction	Far-field patterns measured, wide coverage area verified	Limited bandwidth, limited realistic scenarios, low RIS resolution
2021 [3]	PIN diode-based	29.5 GHz / 3 GHz	SISO	Directional	Room to room via corridor	Fully-addressable, dual-linear RIS	Power hungry, limited measurement scenarios
2022 [106]	Varactor-based	3.5 GHz / -	SISO	Directional	Room to room via corridor junction	Continuously tunable RIS, horizontal beam sweep verified	Limited scenarios and bandwidth, limited to scalar measurements
2023 [107]	Varactor-based	2.6 & 5.8 GHz / 20 MHz	MIMO / SISO	Directional	Outdoor commercial network, corridor junction	Real-world 5G network, multiple realistic scenarios, real user handsets	Sub-optimal RIS optimisation, limited bandwidth
2023 [108]	PIN diode-based	2.6 GHz / 190 MHz	SISO	Directional	Office, corridor junction, outdoor junctions	Multiple scenarios, wide bandwidth	Limited to directional antennas, low RIS resolution
2023 [109]	Static	5.8 GHz / 150 MHz	MIMO	Omni-directional	Commercial indoor WiFi network	Demonstrates truly passive metasurface-aided network, novel pattern optimisation framework	Unrealistic base station setup, no programmability

as a trade-off for their small footprint [113]. The authors introduced a scalable configuration algorithm which is suitable for the limited dynamic range of commodity receivers. The experiment setup involved a RIS-like prototype consisting of 3200 elements split into groups of 40 across 80 printed circuit boards. Microstrip elements of length $\lambda/4$ were connected end-to-end via RF switches and tuned to operate around 2.4 GHz. The experiment took place within a complex office environment consisting of several interior walls, dividers, and other commonly found interacting objects. The prototype was placed along a central wall with a receiver placed in close proximity. The position of a transmitter was varied throughout the office environment, with mixed LoS and NLoS conditions, where it was discovered that the RFocus system offered a median power improvement of 9.5 dB and a median 100% channel capacity improvement.

Pei et al. [64] performed indoor and long-range outdoor field trials with a varactor diode-based 1-bit RIS consisting of 1100 unit cell elements in a 20 row by 55 column arrangement. Operating at 5.8 GHz, the lateral dimensions of the RIS were 79 cm (15.2λ) in width and 31 cm (6λ) in height. To reduce feed network complexity and power consumption, unit cells were grouped in columns consisting of 5 unit cells each. A greedy fast beamforming algorithm was introduced, iteratively increasing the received power at a single receiver (Rx) antenna from a single-antenna transmitter (Tx), facilitated by an Rx-RIS feedback loop. In an indoor NLoS scenario, a receive horn antenna and the RIS formed a reflectarray-type arrangement and the received power was iteratively increased from a transmitter placed behind a thick concrete wall. Compared to a copper plate of similar dimensions to the RIS, the received power improvement was as much as 26 dB. Experiments were performed on a rooftop, with a receiver placed within a few meters from the RIS and a transmitter located at 50 m and 500 m. With the Tx-RIS-Rx forming a virtual line of sight (VLoS) link, the authors demonstrated received power improvements of 27 dB and 14 dB, respectively with a power consumption of only 1W. Although the rooftop trials in this work did not involve realistic blockages, a directional antenna on the receiver ensured a limited direct path between the transmitter and receiver.

Trichopoulos et al. [105] introduced a monoplanar reconfigurable metasurface operating at 5.8 GHz with 160 individually-addressable 1-bit PIN diode-based unit cells in a 10 row by 16 column arrangement. The lateral dimensions of the prototype were 41.4 cm (8λ) in width and 25.9 cm (5λ) in height. The VIAless approach of this design, as well as a wide unit cell periodicity of $\lambda/2$ ensures scalability to operation at mmWave, at the expense of additional parasitic spatial modes. The authors utilised a codebook-based beamforming algorithm. A realistic outdoor measurement campaign was performed in a line-of-sight scenario and a scenario with significant blockage between the transmitter and receiver antennas. The authors mapped coverage improvement for reception from an omnidirectional antenna placed in the blockage region 35 meters from the RIS. Compared to the case of no RIS, average received power improvement of 6 dB and a maximum improvement of 8 dB was demonstrated.

The aforementioned works only considered 1-bit RISs due largely to their low complexity.

However, as explored in section 2.1.2, increasing the phase resolution of RISs has a notable effect on the achievable gain and beam pattern purity, even when moving from 1-bit to a 2-bit tunability. Araghi et al. [106] performed field trials at 3.5 GHz with a continuously tunable varactor-based RIS of dimensions $1.2m \times 1.2m$. The authors investigated a SISO communication system between two rooms via horn antennas, with a transmitter antenna placed in an adjacent 30 m broadside to the RIS, dynamically steering the incident electromagnetic energy towards a nearby receiver. The authors released an associated video, where they demonstrated dynamic reconfiguration of the RIS to maintain a video link while the receiver was in motion. The continuous nature of the unit cell tuning mechanism in this work doubtlessly comes at the cost of a significant complexity increase compared to the digital tuning mechanisms of similar works.

RIS deployment within a commercial 5G network was recently documented by Sang et al. [114]. The authors conducted field trials in various urban scenarios, including under-tower shadow zones, indoor shadow zones, and outdoor shadow zones with the end nodes being a user handset and two different commercial base stations operating at 2.6 GHz as the receiver and transmitters, respectively. A 1-bit RIS is configured by employing a forward model based on the approximate transmitter and receiver positions relative to the RIS. An average 19% user throughput improvement was witnessed within a region directly beneath a building-mounted 5G base station. Regions within two floors of an office building served by the building-mounted base station benefited from a doubling of throughput. Outdoor regions served by a pole-mounted base station, suffering from occlusions of nearby buildings were also investigated. The authors demonstrated a notable improvement in the cell-edge (i.e., those located <5% of the CDF curve) performance when deploying the RIS, with increases in RSRP, SINR, and throughput of 3.3, 1.45, and 79 Mbps, respectively. The work provides a first look at the potential of effectively retro-fitting RISs within contemporary networks for performance enhancement.

Pei et al. [107] recently documented another RIS-aided SISO communications field trial campaign with two different RIS prototypes operating at 2.6 and 5.8 GHz, respectively. These frequencies were selected to cover two different wireless network implementations. Namely, a 5G network operating about 2.6 GHz and a 5.8 GHz WiFi band. A low complexity two-step spatial oversampling codebook algorithm was developed for RIS configuration selection. This effectively amounts to codebook-based scanning in the azimuthal plane, followed by the elevation plane, with repetitions of this until convergence. The codebook relies on a forward model similar to (3.14). Three scenarios are considered for the 5.8 GHz RIS, with experiments carried out in a corridor junction, an office environment, and on a rooftop. The authors investigated the effects of RIS positions on the performance of the RIS indoors, where it was found that a RIS placed in the center of the longest wall in the office area provided near-uniform coverage. The RIS effectively ironed out any regions of poor coverage in the office, with up to 20.5 dB of channel gain improvement over the reference case. For the 2.6 GHz RIS, the authors conducted experiments within an outdoor 5G commercial network. Employing a commercial handset as the

receiver employing an omnidirectional antenna served from a base station at a distance of 100 m, the authors observed an average 5.5 dB reference power increase compared to the specular reflector case. The authors noted that they observed higher power gains compared to the reference case when transceivers at the end nodes were equipped with highly directional antennas. While this finding is important, it also highlights an apparent flaw in the experiment.

A common justification for the use of directional antennas in these experiments is that antenna arrays would probably be deployed at the end nodes, and these would likely form a directional beam towards the RIS to maximise the channel gain. This ignores, however, any alternative paths with comparable channel gain and ultimately biases the results in favor of RIS deployment. A sober look at RIS field trials should consider realistic end nodes that do not filter out beneficial multipath components.

Broadband channel characteristics and the effects of RIS on temporal channel characteristics were explored in a recent work by Sang et al. [108]. Based on comprehensive measurements, the authors derived modified empirical models for the RIS-assisted SISO channels at 2.6 GHz. The scenarios of interest were RIS-aided propagation around the corner of a building, a corridor junction, and an outdoor to indoor wireless link. As opposed to the previous works employing software defined radios and/or commercial transceivers, this field trials work performed VNA-based measurements to extract richer information from the channel. Similar to [107], the authors measured the effects of RIS orientation on system performance.

Operating at mmWave bands presents challenges of high susceptibility to blockages, limiting reliable communication to LoS scenarios. RISs may provide significant coverage enhancement at mmWave for their ease of scalability means that they can provide large effective aperture gains via VLoS paths which can follow the user equipment in the region of interest. Greenerwave have been commercially developing PIN diode-based dual-polarised 1-bit reconfigurable metasurfaces for use as passive access point extenders at mmWave frequencies, as is detailed in the work by Gros et al. [58]. The authors introduced a 400-element RIS in a 20 by 20 arrangement with lateral dimensions of 10 $cm \times 10$ cm ($\approx 10\lambda \times 10\lambda$) with a centre operating frequency of 28.5 GHz. In their experiment, a blockage is created with a right-angled barrier which could equally be the corner of a building. Introducing a VLoS link via the outside corner of the barrier resulted in a 25 dB improvement compared to a copper plate of similar dimensions, with a 3dB bandwidth of over 250 MHz. A 1600 element (40×40) version of this RIS design was also utilised by Popov et al. in [3] as a passive range extender to serve a user in a room from a transmitter antenna in a corridor. The RIS was placed in the corridor on a wall opposite the room doorway, forming a VLoS link and realising a 30 dB received power improvement at 29.5 GHz over a 3 GHz bandwidth, with a power consumption below 6 W.

An honorable mention in this review is the concept of *electromagnetic skins* recently introduced by Oliveri et al. [115] [109]. These are effectively a passive version of the RIS concept. Textured surfaces with fixed scattering properties are embedded into the propagation environ-

ment with a similar function to RISs in terms of improving network performance metrics, but without the complexity and overhead of their reconfigurable cousins. Although the theoretical underpinnings of this technology have been available in the literature for some time (e.g., [116]), modern computing power has likely contributed to a renewed interest in their application in reshaping the radio environment. For instance, Wireless Insite, a ray-tracing tool utilised by network planners, has recently introduced a static metasurface simulation feature based on the uniform ray description of metasurfaces introduced by de Jong [117].

This section has provided an overview of the incremental progress of previous works in bringing smart radio environments to the real world.

2.6 Comparison with current technologies

RISs are not the first technology to be introduced that claim to act as intermediary between the transmitter and receiver. Repeater technologies have been supported since the inception of the 3rd Generation (3G) wireless standard [118]. Relays offer a means of wireless range extension without the need to deploy costly base stations and their associated backhaul [119]. Similar to RISs, they play a role in shaping the propagation environment, albeit requiring active components such as power amplifiers [120]. Relays mainly fall into two categories: repeaters and Layer 3 (L3) relays (also known as *decode and forward* relays). A repeater simply amplifies the received RF signal, including noise, and forwards it to the destination. On the other hand, an L3 relay, equipped with physical and MAC layer processors, decodes the received RF signal before forwarding a regenerated signal, often in a different format, to the end receiver based on its own scheduler's decision. Essentially, an L3 relay functions as a small-scale base station with a wireless backhaul. However, L3 relays face limited utility due to their complex physical layer protocols and expensive equipment. Repeater technology, being typically more affordable and standards-transparent compared to L3 relays, is more commonly used. Repeaters are currently deployed selectively in areas affected by coverage holes. Despite being predecessors to RISs, relays haven't gained much traction from industry [121].

Utilisation of relays may lead to increased network power consumption and necessitate a higher capital expenditure for deployment when compared to RISs [121]. Moreover, the network spectral efficiency provided by relay-aided systems is contingent upon the duplexing protocol utilized for transmission. Hardware costs can be reduced by employing half-duplex repeaters, where the input and output links are time-multiplexed. If a half-duplex relaying protocol is employed, simultaneous transmission by transmitters and relays on the same physical resource is not possible. This challenge can be addressed by employing a full-duplex relaying protocol. However, this comes at the expense of introducing significant loop-back self-interference at the relay due to concurrent transmission and reception of signals. Co-channel interference can be generated at the destination since relays and transmitters emit different information on the same

physical resource. Full-duplex further increases the signal processing complexity and power consumption of the relays. On the other hand, RISs are inherently full-duplex since they are passive, reciprocal devices.

A relevant comparison arises between RISs and repeaters or amplify and forward (AF) relays since both forward signals without digital processing. The trade-off between RISs and AF relays depends on factors such as the cost of active components versus the lower gain of near-passive RIS elements, as well as the reduced digital control in repeaters versus the control overhead in RISs required for achieving necessary beamforming gain [122]. With the aid of numerical simulations, Renzo et al. compared the performance of RISs and relays [16]. The authors derived the scaling laws of the respective devices. The authors determined that RISs offer a less favorable SNR scaling with respect to distance, but this is countered by quadratic scaling of SNR with respect to the RIS size. The authors suggest a sufficiently large RIS operating as an anomalous reflector has the potential to outperform relay-aided transmission whilst conforming to far-field (i.e., electrically small) conditions.

Sun et al. recently investigated the performance of RISs compared to network-controlled repeaters (NCR) in a system-level simulation [123]. The authors evaluated several performance metrics in Frequency Range 1 (FR1) and Frequency Range 2 (FR2) bands. The findings from their study indicate that in FR1, RIS can surpass NCR in average received power under specific system parameter settings, with the signal to inference plus noise ratio (SINR) performance for RIS potentially being better than that of NCR. The authors found, however, that in FR2, NCR can outperform RIS in both average received power and SINR under certain system parameter settings. They observed that RIS offers more flexibility in deployment and applications compared to NCR . This is at the expense of increased overhead and complexity in the design of the protocol architecture and control methods.

Furthermore, Huang et al. [124] proposed a framework for optimising a RIS-aided multi-input single-output (MISO) communication system for maximum spectral efficiency. The authors compared their approach utilising successive fractional programming to relay-assisted systems. The approach appears to achieve near-optimal spectral efficiency. The resulting analysis suggests a 300% increase in energy efficiency in comparison to a relay-aided communications scenario. Ye et al. elucidated these findings with further with performance comparisons with spatially-distributed RISs [125].

Distinctions between RISs and relays

In summary, a number of important distinction between RISs and relays are as follows:

- RISs have more degrees of freedom for manipulating the channel such as through scattering and absorption, alongside passive beamforming [17].
- RISs contain no RF chains nor amplification, relying instead on focusing gain and/or enhancing spatial channel characteristics [126].

- Amplify and forward relays not only amplify the desired signal, but also noise and therefore raise the noise floor of the system [16]. RISs, on the other hand, are theoretically noise-free.
- RISs can be realised with low cost, size, weight, and power. Relays are power-hungry and come with a significant price tag. Early results suggest an increase in energy efficiency compared to relays [125].
- RISs do not suffer from self-interference and are inherently full-duplex [118] [127].
- Relays can offer wireless coverage extension without the need for a control link for reconfiguration, reducing overhead [128].

2.7 Network versus user control of RISs

Network versus user control is an important consideration for RIS deployment [121]. Ordinarily, the wireless network infrastructure is controlled at the base station side. For instance, the weights applied to apply electrical or mechanical beam tilt in base station antennas typically found in 5G macrocells. By extension, it could be assumed that RISs would find themselves controlled in a centralised fashion as a part of the air interface. Compared to the alternative i.e., a user-controlled RIS, scheduling may be relatively straight-forward. This does, however, place the burden of optimising the RIS on the base station with the associated overhead [129]. On the other hand, users in proximity to a RIS could share control through an auxiliary protocol such as Bluetooth. Optimisation could be performed with users, each allocated time slots, adjusting the RIS configuration and relying on a reference signal from the base station as feedback.

Advantages of a network-controlled approach include centralised optimisation allowing efficient resource allocation and coordination amongst RISs [121]. The selected RIS configurations will depend on channel conditions and network traffic, and base stations are typically better equipped to have oversight of this. Similarly, base station typically have the computational power capable of handling the complexity of algorithms and optimisation techniques associated with RIS control. That said, the centralised control could lead to significant communication overhead if efficient RIS optimisation algorithms are not developed, and this problem scales with RIS size [128].

A user-controlled approach allows users to customize RIS configurations according to their preferences, optimising signal strength, mitigating interference, or enhancing privacy. RISs in close proximity to users could be programmed via short-range control links [130]. This approach offloads the computational burden from the base station onto the user. However, this may lead to suboptimal network-wide performance if RIS configurations are not coordinated among users or with the network infrastructure [129]. This lack of coordination among may lead to interference

or conflicts in the wireless communication environment and would lead to a reliance on user cooperation.

In practice, a hybrid approach that combines elements of both network-controlled and user-controlled RIS may offer the most promising solution. For instance, the network infrastructure could provide overarching coordination and optimization while allowing users to fine-tune RIS configurations within predefined parameters. Release 18 of the 3rd Generation Partnership Project (3GPP) standard introduced a framework for network-controlled repeaters (NCRs) employing beamforming [131]. This could serve as an indicator as to how network-controlled RISs might be approached by industry. One control mechanism is that of *side control information*. This side control information would be shared between the base station and the NCR and contains, for example, timing, beam, and power control information.

2.8 Selection of antenna architecture

The choice of antennas can have a significant impact on the channel observed by the end nodes. In mobile networks, user handsets are typically equipped with multiple low-gain antennas to cater for a wide range of frequency bands and to maximise the opportunity to intercept useful power [132]. On the other hand, base stations are typically equipped with sector beam antenna arrays with a high-gain fan-shaped beam and beamsteering capabilities [133]. For RIS deployment, the choice of antennas is critical for a successful implementation. RISs have the most significant impact on a communications channel when the end nodes are in the line of sight of the RIS capture area [134]. That is, the half-space broadside to the RIS elements. With this in mind, several works have experimentally verified RIS operation using directional antennas such as horns [135] [105]. Directional antennas at the end nodes of a RIS-aided channel are less susceptible to multipath fading than their lower-gain counterparts due to the transformation from an NLoS channel to a VLoS channel [136].

Omnidirectional antennas deployed at a user handset can detect a desired signal from a wide range of directions [137]. This can be advantageous if the direction of the transmission or the dominant path is unknown. However, this can also increase the chances of detecting an interfering signal and multipath components that can lead to large-scale fading [138]. The impact of antenna choice, omnidirectional versus directional, on RIS-aided communications is quantitatively demonstrated in Chapter 4. It is shown that directional antennas may skew the observations in favor of RIS deployment since paths of favorable propagation may be filtered out by the narrow field of view of a directional antenna, thereby making the reference case without RIS deployment appear to be less favorable.

MIMO antenna systems with associated precoding and equalisation enable mitigation of interference and multipath effects whilst enabling favorable paths to be tapped into, for example, for spatial multiplexing [18]. Several works have considered RISs in the context of multi-

antenna communication systems, with a large body of literature dedicated to signal processing aspects of RIS-aided MIMO communications [112]. There is currently, however, limited experimental evidence to corroborate this research [139].

Antenna polarisation considerations are paramount to optimise signal propagation and system performance. Selecting antennas and RIS topologies with compatible polarisation characteristics ensures efficient energy transfer between the transmitter, RIS, and receiver [44]. Matching the polarisation of incident waves with the RIS element polarisation ensures wave transformations are performed in a predictable and efficient fashion [140]. Moreover, the choice of antennas with adjustable polarisation capabilities enables the RIS to adapt to varying polarisation conditions in the environment, thereby mitigating polarisation-induced losses and enhancing communication reliability [141]. Furthermore, polarisation diversity techniques, such as deploying antennas and RISs with orthogonal polarisations, can be leveraged to combat fading effects and improve link robustness [142].

2.9 Summary

This chapter has provided a thorough introduction to the many technical concepts considered in this thesis. Modeling approaches were explored and simplified analytical models of RIS behaviour were derived, with both deterministic and stochastic considerations accounted for. A review of measurement techniques at the local and macroscopic levels was compiled, followed by a review recent of RIS testbeds. Finally, a review of data-driven works in RIS-aided communication systems was given.

The following gaps in the RIS-aided communications literature have been identified as warranting further investigation:

- **Higher phase resolution**: One significant gap in the literature that can be identified from the summarised work is the lack of field trials with RISs exhibiting a phase resolution beyond 1-bit. As discussed in section 2.1.2, theoretically, a higher phase resolution results in increased beam pattern purity and enhanced channel gain. Whether this increased phase resolution translates to measurable performance enhancement in practice should be explored further, including a trade-off analysis factoring in the increased complexity.

- **Spectral and temporal effects**: Few works have considered the impact of introducing RISs over a large fractional bandwidth and on the delay characteristics of the channel. Existing studies have mainly focused on a limited bandwidth, while modern cellular systems utilise much wider channels, such as 5G sub-6 GHz with a channel bandwidth of 100 MHz. Delay spread is an important factor in determining signal distortion introduced by the propagation environment. At the time of writing, only a single work [108] could

be found that observed the changes in temporal channel characteristics through the introduction of RISs.

- **Multi-antenna systems**: The majority of current experimental RIS-aided communications works only consider a SISO communication setup. Contemporary cellular communication systems employ multiple antennas at the end nodes and these are exploited to compensate for the effects of multipath and to mitigate path loss. Most RIS field trials thus far have only considered single directional antennas at the end nodes, in part to emulate the directivity of an antenna array. Doing so, however, may bias results in favor of RIS-aided communication channel due to useful multipath components being effectively filtered out. Additionally, the spatial structure of the channel is an important consideration in MIMO systems and this has yet to be thoroughly investigated through experiment.

- **Real-world communications infrastructure**: The field trials reviewed in section 2.5 were selected in part due to their realism. The scenarios considered were within or in proximity to building structures offering challenging propagation conditions. However, the end nodes were largely controlled (e.g., antennas selected/positioned/aligned to offer a good LoS with the RIS), offering less of an indication as to how RISs might benefit existing communications infrastructure.

This thesis aims to address these identified shortcomings through the development of novel RIS prototypes, followed by extensive measurement campaigns in realistic wireless communication scenarios. This concludes the introductory content of the thesis, and the first technical chapter covering design strategies of the aforementioned RIS prototypes follows.

Chapter 3

Reconfigurable metasurface design strategies

3.1 Introduction

To explore the impact of incorporating RISs into wireless propagation scenarios, the initial step involved the creation of reflecting-type reconfigurable metasurface testbeds. This chapter covers two RIS designs. Namely, a 3-bit column-controlled RIS and a 1-bit dual-polarised low power RIS, which have been employed in the field trials of subsequent chapters 4 and 5, respectively. Following on from the RIS modeling considerations covered in section 2.1, this chapter applies the local reflection coefficient description to RIS unit cell optimisation.

3.2 Multi-bit reconfigurable intelligent surface

Most published RIS experimental testbeds have only considered a 1-bit individually-addressable unit cell design due to the low complexity and small configuration overhead compared to higher resolution designs [143]. A greater number of unit cell reflection states can be realised by employing more PIN diodes per unit cell or interfacing varactor diodes with digital to analog converters [65]. The former can be realised with additional shift registers and results in higher current consumption per unit cell, whereas the later requires more expensive biasing circuitry. The application-dependent trade offs of unit cell resolution versus control circuitry complexity and power consumption is an open research area. Recently, several promising PIN-diode based designs have been utilised for this purpose due to their simplicity, low loss, and simple configuration networks which can interface directly with digital circuitry. However, currently reported PIN-diode based testbeds are limited to 2-bits (4 phase state) operation due in part to the complexities of extending this resolution, where performance appears to diminish due to losses introduced with more discrete components and parasitics introduced by the associated biasing circuitry. Recently, a near 3-bit PIN diode-based UC design was introduced with favourable

magnitude performance [150]. However, due to the biasing arrangement, this design is confined to use in a column-driven design and 4 PIN diodes are employed as opposed to a favourable 3 PIN diode design. This chapter discusses a means of improving on the phase resolution compared to 2-bit designs whilst keeping the minimal 3 PIN diodes.

A major challenge in achieving high phase resolution is that of phase alignment, particularly when attempting to minimise the number of required components. A small change in dimension can affect multiple phase states at once, rendering manual tuning approaches futile for any design above 2 bits. Perruisseau-Carrier et al. [55] developed a particle swarm optimisation (PSO) algorithm in order to solve the problem of phase alignment in a reflecting UC employing 5 pairs of MEMS switches in a pseudo-ring arrangement. The authors achieved excellent linear phase alignment of 32 phase states over a 200° phase range. The method employed techniques to minimise the full-wave computation time by harnessing UC symmetry, perfect electric conductor-perfect magnetic conductor (PECPMC) boundaries, and employing discrete ports in place of MEMS switches for offline computation of all phase states at each iteration. PECPMC boundaries were found to achieve sufficiently similar results to the more accurate periodic boundary condition (PBC) boundaries used conventionally to approximate the behaviour of periodic structures – this meant that transient solver calculations could be performed at each iteration as opposed to more computationally expensive frequency domain solver calculations. This chapter introduces a UC design capable of exhibiting discrete phase control beyond existing 2-bit designs with only a single additional active switching element while omitting vias, reducing fabrication complexity, and speeding up simulation time for optimisation. Additionally, a new way of visualising the change in operating point with oblique incidence angle for reflecting UCs with several quantised phases is proposed.

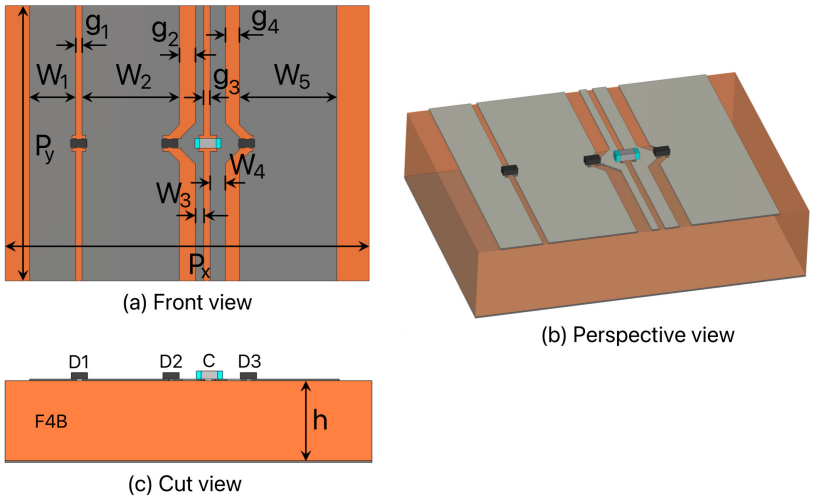

Figure 3.1: Multi-bit unit cell design used in this work. The unit cell consists of 5 rectangular patches on an F4B substrate, connected by 3 PIN diodes and a capacitor.

Table 3.1: Dimensions for Multi-Bit Unit Cell Design

Parameter	Dimensions (mm)
Periodicity, P_x P_y	22.5 15.0
Patch width, W_1 to W_5	6.0 0.9 0.5 6.0 2.9
Patch spacing, g_1 to g_4	0.9 0.4 1.0 0.4
Substrate thickness, h	5.0

3.2.1 Unit cell design

The proposed unit cell (UC) design can be seen in Fig. 3.1 with associated dimensions in table 3.1. The UC consists of 5 microstrip patches directly connected to adjacent UCs above and below, and connected to neighboring patches via 3 PIN diodes, d_1 to d_3, and a DC blocking capacitor, C. The component arrangement enables common DC biasing signals to be applied to several unit cells in a column-wise fashion while maintaining an RF path through C, whose self-resonant frequency can be chosen such that it acts as a near-short circuit at the band of interest. The components employed here are Skyworks SMP1321-040LF PIN diodes and an AVX U-Series 3.6 pF 0402 capacitor. The patches are mounted on a grounded F4BM-2 substrate with $\varepsilon_r = 2.65$ and $tan\delta = 0.001$.

The UC was simulated with the commercial software CST Studio Suite employing the frequency domain solver with periodic boundary conditions. The PIN diodes were factored into the simulation by employing discrete ports at the component locations such that the system resembled a 4-port network (i.e., the incident wave and 3 PIN diode ports). This was followed by post-processing in which the reflection responses for the 8 PIN diode configurations were obtained by substituting the manufacturer-provided S-parameters in a similar fashion to Perruisseau-Carrier et al. [55] in their MEMS-based UC design. The S-parameters of the DC blocking capacitor were included in the simulation as lumped elements. A 5 mA biasing current was assumed for the *on* condition of the PIN diodes, while a 0 V voltage was simulated for the *off* condition. The UC was optimised for 3.75 GHz operation and the resulting simulated phase and magnitude responses for the 8 biasing configurations can be seen as the dashed curves in Fig. 3.2. The resulting average reflection loss at 3.75 GHz is 1.5 dB, with the largest loss at the 180° state of 3.5 dB. The losses are attributed mostly to the finite resistance of the PIN diodes. The optimisation procedure to achieve the high resolution phase response of this design is discussed in the sections that follow.

3.2.2 S-Parameter description

For the reflection coefficient extraction, we can consider the system with a linearly polarised (in line with the PIN diode orientation) plane wave as port 1, and the 3 respective PIN diodes as

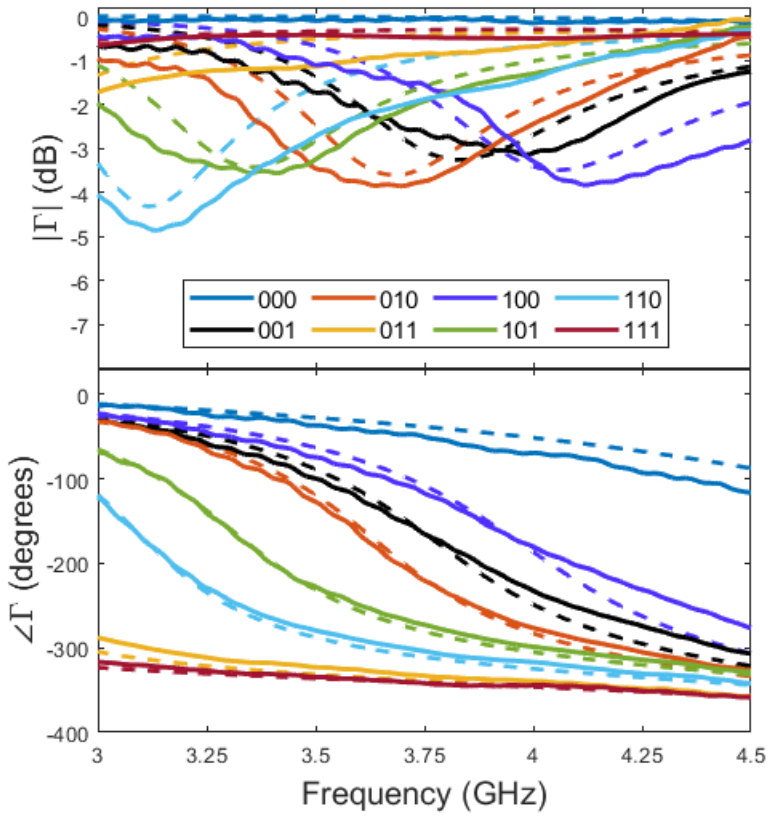

Figure 3.2: Simulated (dashed curves) and measured (solid curves) reflection response for 8 digital states of 3-bit reflecting metasurface.

ports 2 to 4, as depicted in Fig. 3.3. Power reflected from each port can be described by a vector **b** and is defined by the multiplication of the extracted scattering matrix, $\bar{\mathbf{S}}$, with the input power at each port, **a**:

$$\mathbf{b} = \bar{\mathbf{S}}\mathbf{a} \tag{3.1}$$

$$\bar{\mathbf{S}} = \begin{bmatrix} S_{11} & \cdots & S_{1N} \\ \vdots & \ddots & \vdots \\ S_{N1} & \cdots & S_{NN} \end{bmatrix} \tag{3.2}$$

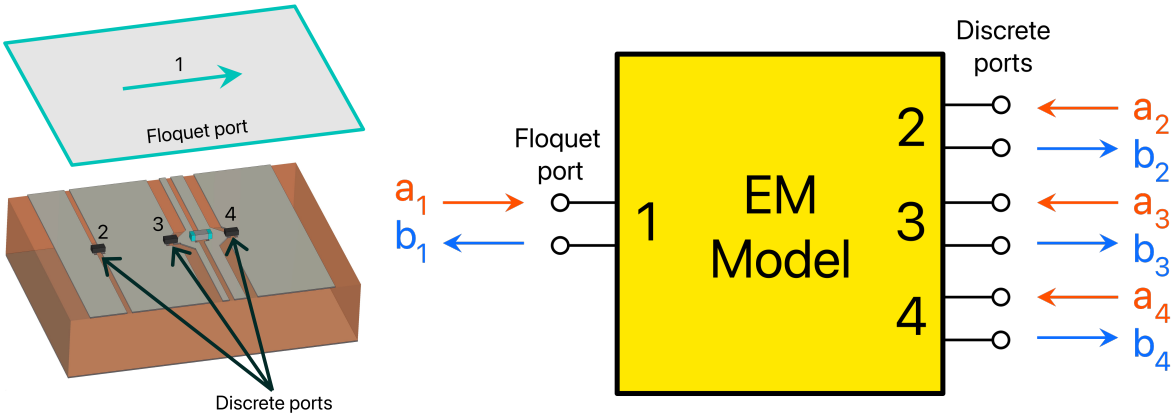

(a) (b)

Figure 3.3: Port layout for the 3-bit metasurface unit cell. Diagram showing port locations (a) and S-parameter abstraction (b).

$$S_{ij} = \left.\frac{b_i}{a_j}\right|_{a_k=0,\ \text{for } k\neq j} \tag{3.3}$$

For instance, the output power seen at port 1 when the remaining ports are terminated in a reference load:

$$b_1 = S_{11}a_1 + S_{12}a_2 + S_{13}a_3 + S_{14}a_4 \tag{3.4}$$

Input powers a_2 through a_4 can be derived by considering the power reflected from each PIN diode load due to b_2 through b_4 entering the respective loads:

$$\mathbf{a_{2-4}} = \begin{bmatrix} a_2 \\ a_3 \\ a_4 \end{bmatrix} = \begin{bmatrix} \Gamma_2 b_2 \\ \Gamma_3 b_3 \\ \Gamma_4 b_4 \end{bmatrix} \tag{3.5}$$

where Γ_i is the reflection coefficient of the PIN diode load:

$$\Gamma_i = \frac{Z_i^{\text{PIN}} - Z^{\text{ref}}}{Z_i^{\text{PIN}} + Z^{\text{ref}}} \tag{3.6}$$

where Z_i^{PIN} is the equivalent impedance of PIN diode i biased to a given state and Z^{ref} is the characteristic impedance used to derive the S-parameters of the PIN diode measurements (taken as 50Ω for this work).

Substituting the values for a_{2-4} into 3.1:

$$\begin{bmatrix} b_1 \\ b_2 \\ b_3 \\ b_4 \end{bmatrix} = \begin{bmatrix} S_{11} & \cdots & S_{14} \\ \vdots & \ddots & \vdots \\ S_{41} & \cdots & S_{44} \end{bmatrix} \begin{bmatrix} a_1 \\ a_2 \\ a_3 \\ a_4 \end{bmatrix} = \begin{bmatrix} S_{11} & \cdots & S_{14} \\ \vdots & \ddots & \vdots \\ S_{41} & \cdots & S_{44} \end{bmatrix} \begin{bmatrix} a_1 \\ \Gamma_2 b_2 \\ \Gamma_3 b_3 \\ \Gamma_4 b_4 \end{bmatrix} \tag{3.7}$$

We are interested in the information *port 1* has to offer based on the loads presented to the 3 other ports. Therefore, solving for S_L in $b_1 = S_L a_1$:

$$S_L = S_{11} + \begin{bmatrix} S_{12} & S_{13} & S_{14} \end{bmatrix} \left(\mathbf{I} - \begin{bmatrix} S_{22} & \cdots & S_{24} \\ \vdots & \ddots & \vdots \\ S_{42} & \cdots & S_{44} \end{bmatrix} \begin{bmatrix} \Gamma_2 & 0 & 0 \\ 0 & \Gamma_3 & 0 \\ 0 & 0 & \Gamma_4 \end{bmatrix} \right)^{-1} \begin{bmatrix} S_{21} \\ S_{31} \\ S_{41} \end{bmatrix} \tag{3.8}$$

$\begin{bmatrix} S_{11} & \cdots & S_{14} \\ \vdots & \ddots & \vdots \\ S_{41} & \cdots & S_{44} \end{bmatrix}$ is obtained from a single full-wave simulation run.

$\begin{bmatrix} \Gamma_2 & 0 & 0 \\ 0 & \Gamma_3 & 0 \\ 0 & 0 & \Gamma_4 \end{bmatrix}$ is obtained from measurement data of the PIN diodes.

The reflection coefficients are then obtained by solving S_L using (3.8) 8 times for the 8 PIN diode states.

3.2.3 Achieving distinct configurations

Compared to lower resolution UC designs, achieving sufficiently distinct reflection characteristics between diode configurations whilst minimising the UC complexity is challenging. Ideally, for each additional bit of resolution, it should be possible to utilise a single additional active element such that additional losses and configuration network complexity are minimised. However, without additional degrees of freedom it is necessary to find an exact set of parameters in an increasingly complex UC to satisfy the desired set of reflection responses. Manual tuning of these parameters is prohibitively time consuming when attempting to align 8 phase curves, since

a change in a single parameter can affect all states at once.

We have utilised a particle swarm optimisation (PSO) algorithm to determine the parameter values due to its simplicity and the real-valued nature of the parameters [8]. PSO is a population-based optimisation algorithm whose population members, known as *particles*, each consisting of a set of parameters subject to optimisation. These particles collectively work to minimise a cost function through knowledge of the current global and their own local best set of parameter values. This is a technique that has been described as mimicking the way insect colonies cooperate to find food [144], with each member of the colony changing its search pattern according to the knowledge accumulated by themselves and the colony as a whole.

We have based our PSO implementation on the work by [55]. In this design, the substrate thickness, h, was fixed at 5 *mm* while the 11 remaining parameters were subject to optimisation. The aim of the algorithm was to maximise the uniformity of the set of phase shifts about the operating frequency whilst minimising the reflection loss. One measure of phase shift uniformity utilised for discretely tunable reflecting UC designs is that of the equivalent bit number, N_{bit}, defined as:

$$N_{bit} = \log_2\left(\frac{360}{\sqrt{12}\sigma_p}\right) \tag{3.9}$$

$$\sigma_p = \sqrt{\frac{\sum_{m=1}^{M}(\Delta\phi_m)^3}{12 \times 360}} \tag{3.10}$$

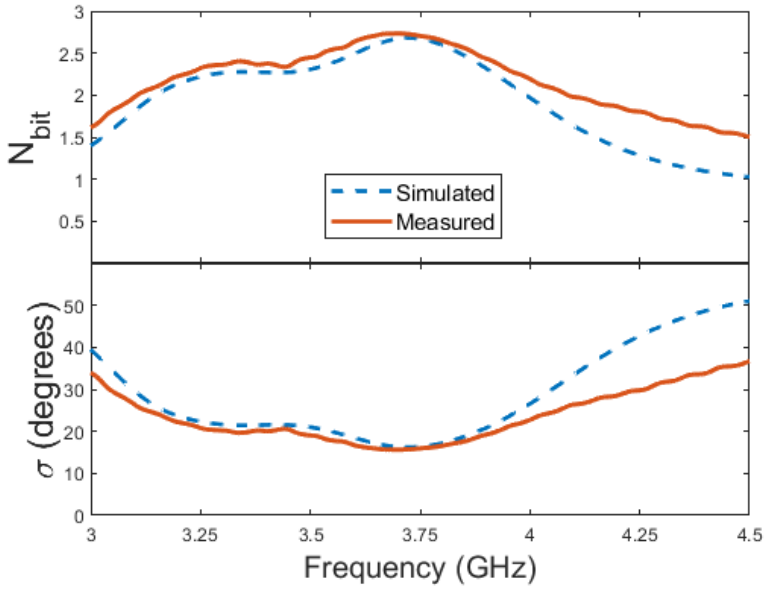

Figure 3.4: Equivalent bit number (top) and phase standard deviation (bottom) for the 3-bit reflecting metasurface.

where σ_p is the phase standard deviation for M configurations and $\Delta\phi_m$ are the phase dif-

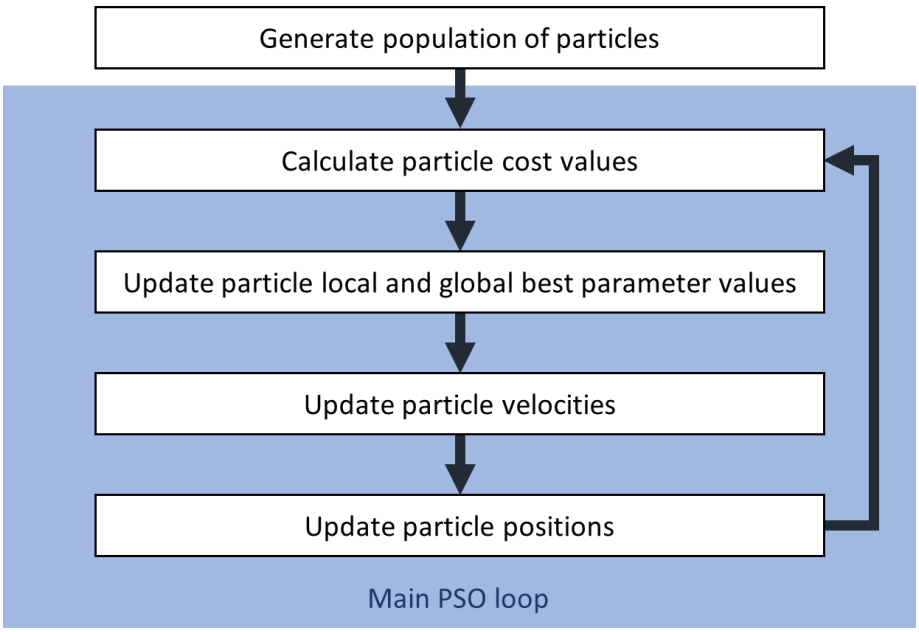

Figure 3.5: Chart showing particle swarm optimisation algorithm employed for optimisation of the set unit cell reflection responses. Adapted from [8].

ferences between respective adjacent phase values. N_{bit} is a figure of merit and is useful for visualising the operating point of the digital UC. For example, a 4-state reflecting UC with 90° phase separation has an N_{bit} of 2 about its centre frequency, with N_{bit} typically reducing when moving away from this frequency. For instance, Luyen et al. [145] defined a working bandwidth of a 2-bit reflecting UC as the region where N_{bit} is 1.7 or higher while maintaining losses below 1 dB. For the reflection response in Fig. 3.2, the equivalent bit number at 3.75 GHz is 2.75 due to only achieving 7 instead of 8 distinct phase shifts. This response provides an acceptable improvement over 2-bit designs, with 3 additional available phases interpolating the 90° steps.

The PSO algorithm is summarised in Fig. 3.5. To begin, a population of particles is generated, each of which consists of a set of randomly generated parameter values for patch widths w_1 to w_5, patch spacing g_1 to g_4, and UC periodicities p_x and p_y within practical constraints. The main loop ensues, consisting of calculating the cost functions for each set of parameter values, followed by updating the local and global best sets of parameters for each particle, adjusting each particle's velocity based on these best values, followed by updating the particle positions (i.e., the associated parameter values) based on the respective velocities. The main loop repeats until convergence.

The cost function of the PSO algorithm was chosen as (3.11), where $\overline{\Gamma}(i)$ is the mean reflection magnitude for the 8 PIN diode configurations of particle i. Coefficients α_1 and α_2 were chosen as 1.5 and 0.5, respectively, to emphasise the phase separation over the magnitude performance.

$$f_{cost}(i) = \alpha_1(3 - N_{bit}(i)) + \alpha_2(1 - \overline{\Gamma}(i)) \tag{3.11}$$

In order to reduce computation time on processing the set of parameters for each particle, a single frequency point was simulated for the 4-port network. For the UC geometry explored here, the PSO algorithm produced the 7 phase state result of Fig. 3.2 to maximise N_{bit}, though was also capable of producing 8 distinct states whose spacing was less desirable on approaching $\pm 180°$. The optimised periodicity along the principal UC polarisation was 22.5 *mm*, resulting in under $\lambda_0/3$ UC spacing in the operating region.

The substrate thickness, h, contributes largely to the bandwidth, with a thicker substrate leading to a larger bandwidth and a drop in resonant frequency alongside an associated reduction in achievable reflection phase range. It was found that a substrate thickness of $h = 5mm$ provided a sufficient bandwidth while achieving nearly 300° phase range.

3.2.4 Oblique incidence performance

Due to its electrically-thin nature, the proposed UC predominantly interacts with the tangential electric and magnetic components of incident waves and their ratio, the characteristic impedance seen at the surface, changes with incidence angle [146]. The change in operating point (i.e., the N_{bit} maximum) with elevation incidence angle, θ_i, and polarisation has been plotted in Fig. 3.6(a), where Fig. 3.6(b) denotes the relevant coordinate system. The reflection response of the proposed UC varies according to the polarisation and there is a notable shift of the desired reflection response upwards in frequency when subject to a obliquely arriving TE wave. This shift is manifested in the phase values of the set of UC states appearing to group closer together at the operating frequency. The TE wave operating point can be seen to shift from 3.75 GHz at $\theta_i = 0°$ to 4.15 GHz at $\theta_i = 45°$. For TM waves at $\phi_i = 0°$, this apparent shift in operating region is less pronounced.

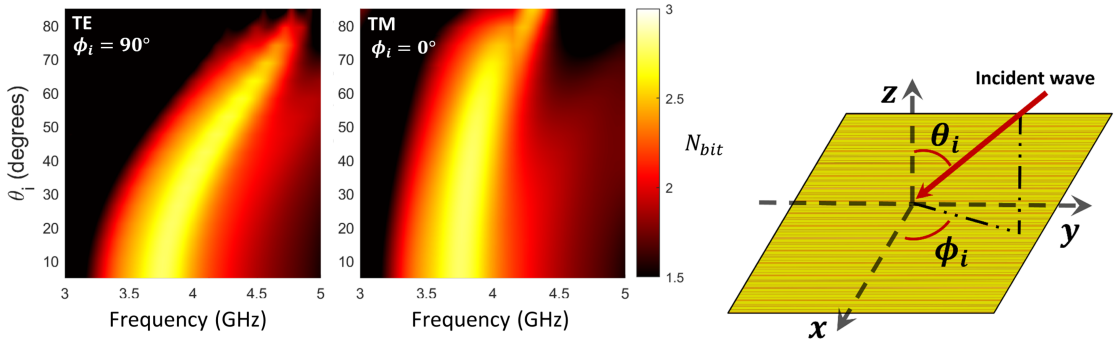

(a) (b)

Figure 3.6: Oblique incidence effects on the achievable phase resolution, N_{bit}. (a) oblique incidence effects on the operating point of the unit cell design for TE and TM polarisations. (b) diagram showing oblique incidence measurement coordinate system superimposed on a tile of proposed units cells, aligned such that the PIN diodes are oriented along the x axis.

3.2.5 Fabrication

The fabricated RIS can be seen in Fig. 3.7. Due to fabrication constraints on the lateral dimensions, the RIS was split into 6 tiles, each containing an arrangement of 16 $\times$ 24 unit cells. The lateral dimensions of this design are 1.08 m (13.5λ) in width and 0.72 m (9λ) in height. The total number of addressable columns on each tile is 32 (i.e., two rows of 16 columns), each controlled by 3 digital values for a total of 96 bits per tile. Accordingly, each tile contains 12 shift registers, which are interfaced with an external controller consisting of an FPGA and Raspberry Pi single-board computer. The control link is maintained over a 2.4 GHz WiFi connection between a PC and the Raspberry Pi.

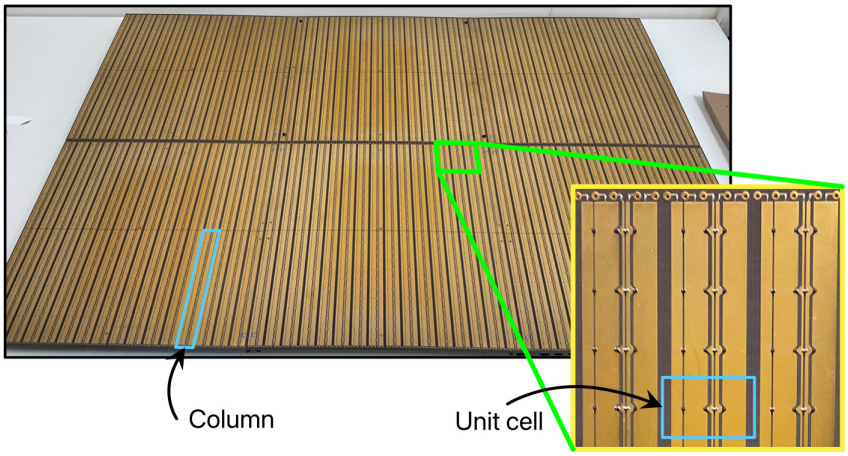

Figure 3.7: Fabricated reconfigurable intelligent surface. Inset shows column structure with choke inductors at the top. Column highlighted consists of a group of 12 unit cells whose patches are connected top and bottom.

The PIN diodes require a bias voltage of 0.83 V at the design current of 3 mA. On a per-unit cell basis, this voltage is easily accommodated by off-the-shelf shift registers. However, source drivers were necessary in order to supply enough current to drive 12 PIN diodes per digital output. These are connected in series with the shift register outputs. At full load (i.e., all outputs at digital high), each source driver consisting of 8 output pins is required to source 288 mA. Assuming on average half of the PIN diodes are on at any one moment, the PIN diodes alone consume 8.6 W. By no means does this meet the definition of ultra-low power required to justify the deployment of RISs, but this does not pose limitations on the investigation of the benefits of a higher phase resolution presented here. Varactor diodes should be employed if low power consumption is required, such as the testbed recently demonstrated by Pei et al. [64].

3.2.6 Performance analysis

The purpose of specular reflection measurements from the 3-bit RIS is to verify the programability of the reflection coefficients. The control observation in this regard is the specular reflection

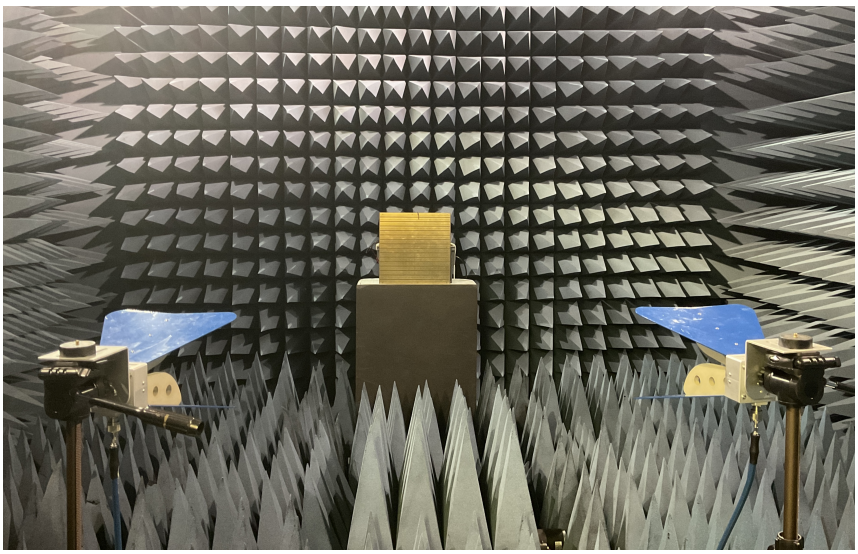

Figure 3.8: Measurement setup in an anechoic chamber for ascertaining global reflection characteristics. Two identical standard gain horn antennas in a horizontal polarisation configuration are placed in the horizontal plane from the center of a single RIS tile. The antennas are placed at 4 meters, 10 degrees from normal to the RIS and aligned to the RIS center with a laser pointer and spirit level. A Rohde and Schwarz ZVH8 VNA is connected to the horn antennas for the S21 measurements, with calibration performed by replacing the RIS with an aluminium plate of similar dimensions.

response of a homogeneous metal sheet of similar dimensions to a single RIS tile. Due to practical limitations in antenna placement, we are constrained to observation angles that are greater than 0° to prevent antenna overlap. Additionally, the antennas are separated $> 5\lambda$ to reduce mutual coupling introducing ripples into the magnitude measurements [147]. The key performance indicator for this experiment is the conformity with simulated reflection behaviour within the band of interest across the programmed states of the metasurface, corresponding to a change in the diode bias voltages. A single RIS tile was placed in an anechoic chamber to ascertain its global reflection characteristics, as shown in Fig. 3.8. The tile was oriented such that the columns of patches were horizontally arranged. Two identical standard gain horn antennas in a vertical polarisation configuration were placed in the horizontal plane from the center of the RIS tile. The antennas were placed at a distance of 4 meters, 10 degrees from normal to the RIS and aligned to the RIS center with a laser pointer and spirit level. A Rohde and Schwarz ZVH8 VNA was connected to the horn antennas for S21 measurements, with calibration performed by replacing the RIS tile with an aluminium plate of similar dimensions. The measured specular reflection magnitudes and phases for the 8 PIN diode configurations are plotted as the solid curves in Fig. 3.2. It can be seen that the phase response follows the trend of the simulation relatively closely, with some divergence towards the higher end of the band, while the magnitude response is within 1 dB for most states.

The average reflection loss at 3.75 GHz is 1.63 dB for the case of 3 mA PIN diode forward bias current. This loss can be reduced by increasing the bias current at the expense of a higher

power consumption. The resulting simulated average reflection loss for 1, 5, 10, and 20 mA bias current for each SMP1321 PIN diode is 1.90, 1.42, 0.89, and 0.77 dB, respectively. These current levels correspond to diode series resistances of approximately 3.1, 1.5, 1.1, and 0.9 Ω, respectively. The reflection loss improvement versus bias current diminishes with increasing current due to the asymptotic relationship between bias current and series resistance.

In their work, Pereira et al. introduced a 2-bit programmable reflectarray, and the useful bandwidth was considered where the phase resolution remains above 1.7 bits. This corresponds to a phase standard deviation lower than 32.5 degrees. There does not currently appear to be any convention for deciding the useful bandwidth beyond a 2-bit resolution. If we consider a phase standard deviation of 16.25 degrees (i.e., half that of a 2-bit design due to having double the number of states), this corresponds to an equivalent bit number of approximately 2.5 bits. Referring to Fig. 3.4, the design presented here can be seen to exhibit a phase standard deviation below 16.25 degrees in the frequency range of 3.62 to 3.78 GHz.

This prototype was successfully deployed in an indoor field trial campaign which is detailed in chapter 4. Next, the design of a low-power RIS prototype with full polarisation control is explored.

3.3 Low power, fully-addressable, dual polarisation RIS

In this section, a RIS prototype which overcomes some of the shortcomings of the multi-bit prototype is introduced. Namely, the significant power consumption, lack of beamsteering control in elevation, and polarisation limitations. Metasurface and control circuit co-design enabled the development of a 1-bit dual-polarised reflecting metasurface protoype with full azimuth and elevation control, and with individually-addressable unit cells. The fabricated device, consisting of 2048 individually addressable varactor diodes, consumes less than 10 mW of power in its configured state. The design methodology and tile performance are explored here. The far-field to far-field beamsteering performance of this device is discussed in section 3.3.5. Deployment of this design in a measurement campaign within an urban 5G macrocell is covered in chapter 5.

3.3.1 Design evolution

To meet the requirements of deployment in the 3.2 - 3.8 GHz 5G NR band, the desired performance characteristics are as follows:

- 3.2 - 3.8 GHz operating band
- > 100 MHz instantaneous bandwidth
- Band-tunable
- 1-bit phase shift, independent of polarisation
- Azimuth and elevation beamsteering capable
- Scalable design
- Minimal number of tuning components
- < 100 mW power consumption per tile

These requirements are typical for RISs designed for operation at sub-6 GHz, particularly the 100 MHz instantaneous bandwidth required by 5G networks. Band tunability, on the other hand, is not something usually offered by existing designs and will be briefly covered here. Band tunability is important due to the limited 1-bit bandwidth of conventional 1-bit reconfigurable metasurface designs [148]. Typically, the 1-bit behaviour is centred about a fixed frequency and, due to the dispersive nature of the reflection response, phase errors arise when moving out of this region. In this design, a combination of the tuning mechanism and the topology of the control circuitry enables tuning for a 1-bit response at all frequencies within the operating band.

Table 3.2: Unit Cell Dimensions

Parameter	Length (mm)	Parameter	Length (mm)
w	30	h	2
g	1.5	a, b	20.5, 20.5
q, r	9.2, 4.8	u, v	1.9, 2.8

The unit cell for this metasurface is shown in Fig. 3.9. The design consists of a square patch coupled to 2 parasitic patches through varactor diodes. The 2 tunable components being the minimum number required to serve the two orthogonal linear polarisations. The patches are etched onto a F4BM220 substrate with dielectric constant, $\varepsilon_r = 2.2$, and loss tangent, $\tan\delta = 0.001$, backed by a copper ground plane.

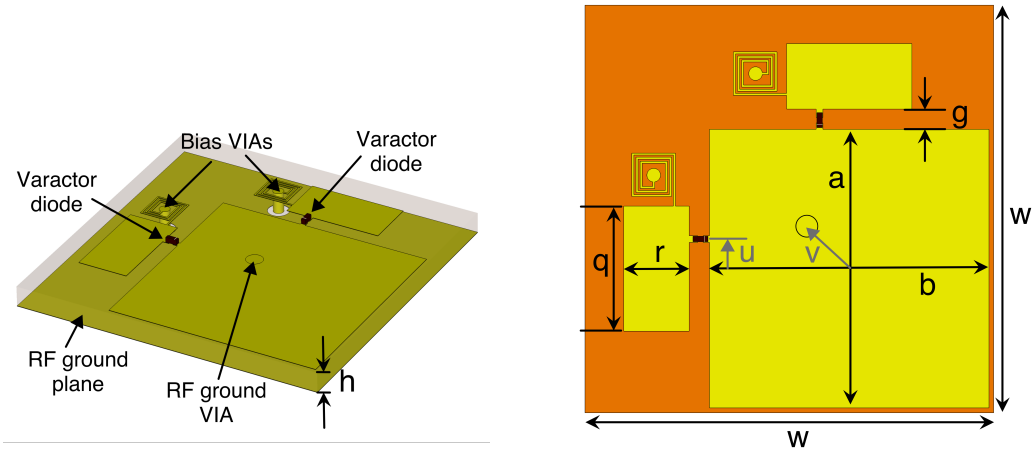

(a) (b)

Figure 3.9: Perspective view (a) and top view (b) of the unit cell design. Dimensions are given in Table I. A square microstrip patch printed on an F4BM220 dielectric substrate is connected to two parasitic patches through varactor diodes. The square patch is set to the upper varactor voltage whilst the respective parasitic patches are driven by a switchable voltage through the bias VIAs, providing a 1-bit response at both linear polarisations.

Cross-polarisation isolation is important to ensure the re-radiated co-polar field components are not significantly attenuated. The process used to ensure sufficient cross-polar isolation is detailed here. Fig. 3.10(a) depicts a single-polarisation version of the unit cell which is subject to a vertically-polarised plane wave. A 1 pF capacitive load results in a artificial magnetic conductor (AMC) response about 3.45 GHz. It can be seen that the cross-polarisation isolation, $|\Gamma_{21}|$, is below 40 dB and cross-polar coupling does not have a detrimental impact on the co-polar magnitude and phase response. The losses are attributed mostly to ohmic losses in the varactor diode.

When adding an additional parasitic patch for the horizontal polarisation, as depicted in Fig. 3.11(a), it can be seen that the magnitude response is significantly degraded, and resembles that

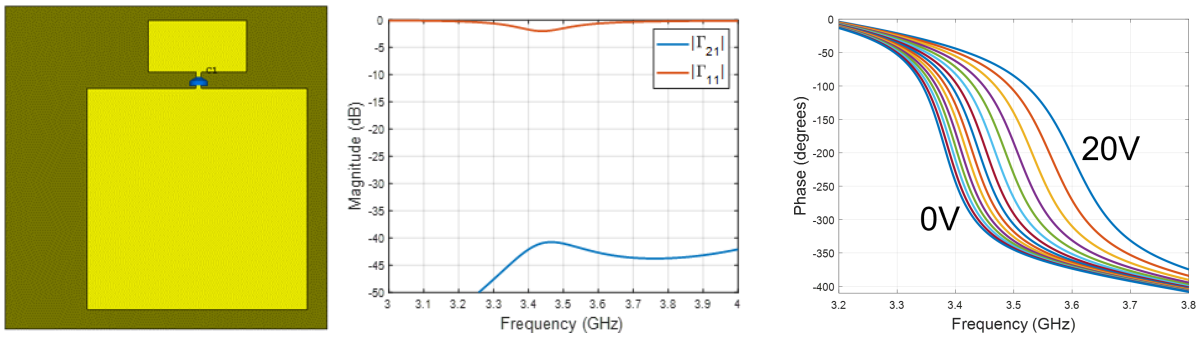

(a) (b) (c)

Figure 3.10: Top view (a) of single-polarisation coupled-patch unit cell for comparison. A square microstrip patch printed on an F4BM220 dielectric substrate is connected to a parasitic patch through a varactor diode. Plot (b) shows the magnitude response for a capacitance of 1 pF. Plot (c) shows the phase response for varactor voltages 0 V to 20 V.

of a polarisation converter. This undesirable behaviour is mitigated through simple changes in the geometry, as detailed next.

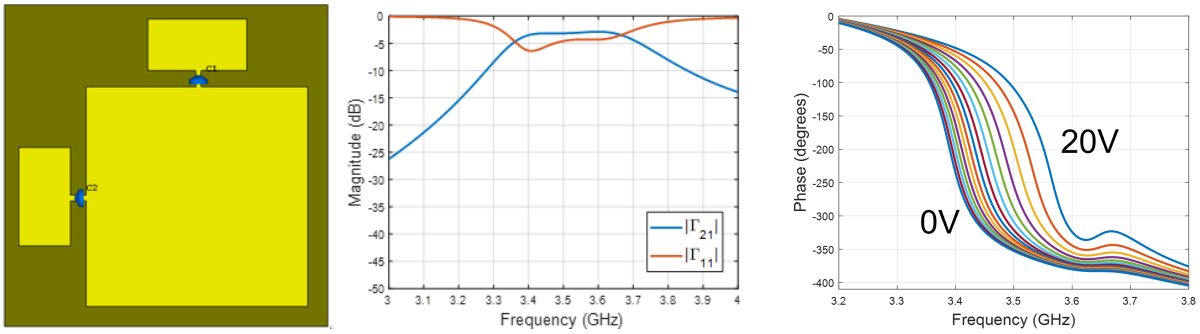

(a) (b) (c)

Figure 3.11: Top view (a) of sub-optimal dual-polarisation coupled-patch unit cell for comparison. A square microstrip patch printed on an F4BM220 dielectric substrate is connected to two parasitic patches through center-aligned varactor diodes. Plot (b) shows the magnitude response for a capacitance of 1 pF. Plot (c) shows the phase response for varactor voltages 0 V to 20 V.

3.3.2 Optimisation procedure

The geometrical parameters of the constituent unit cell periodicity, patches, varactor offset, and VIA offset have been subject to an optimisation procedure in order to meet the performance goals outlined in the introduction. The unit cell geometry was optimised utilising a PSO algorithm similar to that employed in section 3.2.3. The parameters subject to the algorithm detailed here are noted in Fig. 3.9(b). The substrate thickness, h, was kept at 2 mm to reduce fabrication costs. The unit cell was simulated in CST Studio Suite with the frequency domain solver and periodic boundary conditions. Two orthogonal Floquet ports were employed broadside to

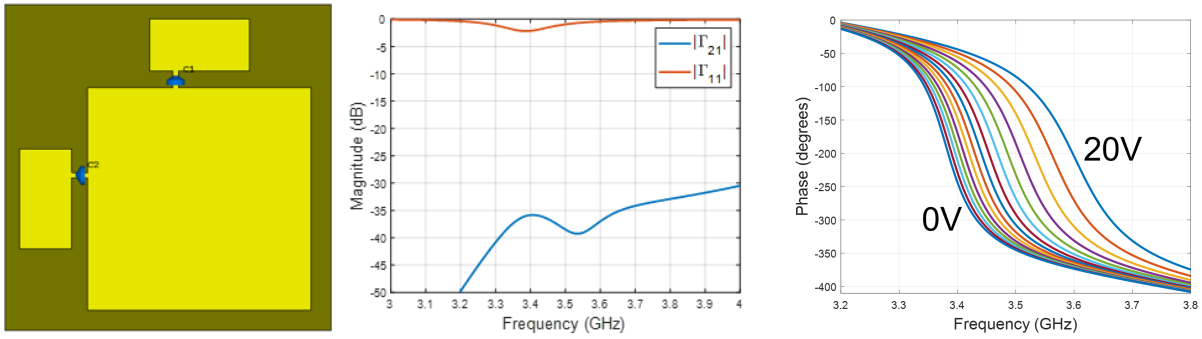

(a) (b) (c)

Figure 3.12: Top view (a) of an optimised dual-polarisation coupled-patch unit cell for comparison. A square microstrip patch printed on an F4BM220 dielectric substrate is connected to two parasitic patches through offset varactor diodes. Plot (b) shows the magnitude response for a capacitance of 1 pF. Plot (c) shows the phase response for varactor voltages 0 V to 20 V.

the surface to capture the co- and cross-polar reflection performance. The varactor diodes were simulated as discrete ports and the bias VIAs and inductors were omitted to reduce complexity during optimisation. Referring to Fig. 3.3.2, a slight modification to equation (3.8) is required to factor in the change of ports:

$$\begin{bmatrix} S_{11}^{L} \\ S_{21}^{L} \end{bmatrix} = \begin{bmatrix} S_{11} \\ S_{22} \end{bmatrix} + \begin{bmatrix} S_{13} & S_{14} \\ S_{23} & S_{24} \end{bmatrix} \left(\mathbf{I} - \begin{bmatrix} S_{33} & S_{34} \\ S_{43} & S_{44} \end{bmatrix} \begin{bmatrix} \Gamma_3 & 0 \\ 0 & \Gamma_4 \end{bmatrix} \right)^{-1} \begin{bmatrix} S_{31} & S_{32} \\ S_{41} & S_{42} \end{bmatrix} \tag{3.12}$$

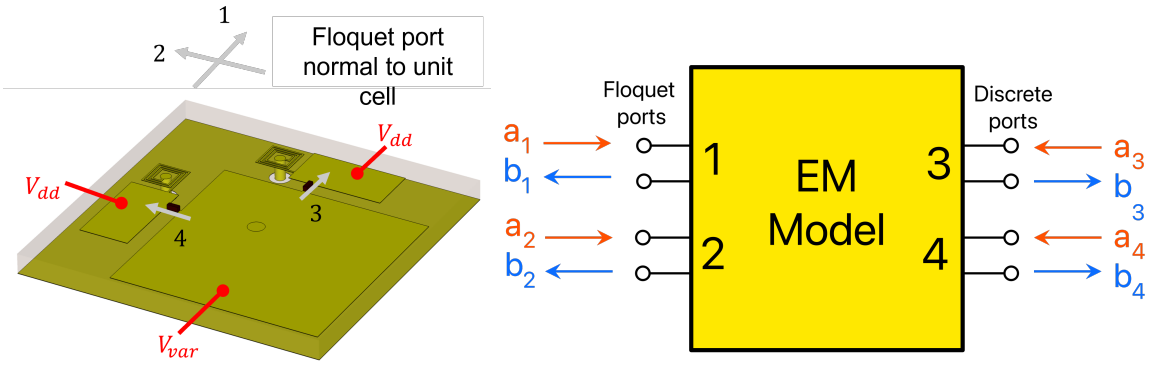

(a) (b)

Figure 3.13: Port layout for the 1-bit metasurface unit cell. Diagram showing port locations (a) and S-parameter abstraction (b).

Where S_{21}^{L} encompasses the coupling of power from the vertically-polarised incident wave and a horizontally-polarised re-radiated wave. Γ_i is the reflection coefficient of a varactor at a given voltage level at discrete port i. During each iteration, 80 particles were simulated, with the initial population normally distributed throughout the search space of parameters detailed in

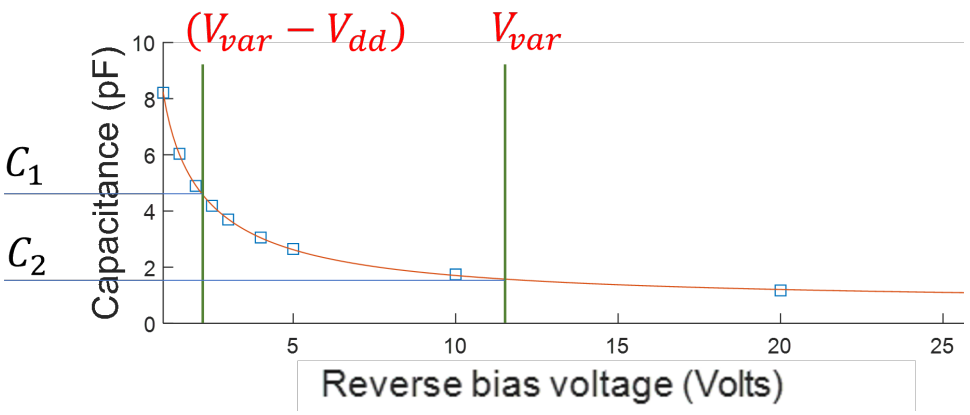

Figure 3.14: Capacitance versus voltage for the SMV1408 varactor diodes. Square points show the capacitance values extracted from the S2P files provided by the manufacturer. Solid curve shows the interpolated capacitance versus voltage. Voltage levels highlighted are subject to a voltage difference of V_{dd} typically around 10 V for the control circuitry employed in the prototype.

Fig. (b). Each particle was scored based on its best possible 1-bit performance given the set of available capacitances from the varactor diodes. The cost function was defined as:

$$f_{cost} = \alpha_1(1 - |S_{11}^L(C_1, C_2)|) + \alpha_2|S_{21}^L(C_1, C_2)| + \alpha_3\varepsilon(C_1, C_2) \tag{3.13}$$

Where α_1 to α_3 are the respective weighting coefficients, S_{11} is the co-polar reflection coefficient, S_{21} is the cross-polar transmission coefficient, and ε is the phase error in radians. C_1 and C_2 are the two capacitance values selected as follows. After a given particle (i.e., set of parameters) is simulated, post-processing is performed in which the discrete port is replaced by an equivalent load of that of the SMV1408 varactor. The load is simulated at voltage levels 0 - 20 V at 0.5 V intervals, with the corresponding capacitance values shown in Fig. 3.14. The pair of voltage levels resulting in minimising (3.13) determine the capacitances C_1 and C_2 used for scoring for that particle. This flexibility in the selection of bias voltage levels is due to the control circuit topology employed here, as detailed in the next section. The weighting coefficients, α_1, α_2, and α_3 were set to 0.2, 0.1, and 5, respectively.

The reflection response at four distinct voltage levels is plotted as the dashed curves in Fig. 3.15. These were generated by utilising the S2P data available for the SMV1408 varactors at the respective voltages. The reverse-bias voltage for the horizontally-arranged varactor is held fixed at 0 V, whilst the voltage levels for the vertically arranged varactor are set to 1, 3, 5, and 10 V. At 3.5 GHz there is a 248° phase variation between 1 and 10 V, which is more than sufficient for 1-bit operation. The simulated magnitude remains above approximately 1.4 dB at the center frequency, with the losses attributed mostly to the forward resistance of the varactor diodes. The optimised reflection performance at 3.5 GHz over the range of capacitance values for each varactor diode is plotted in Fig. 3.16.

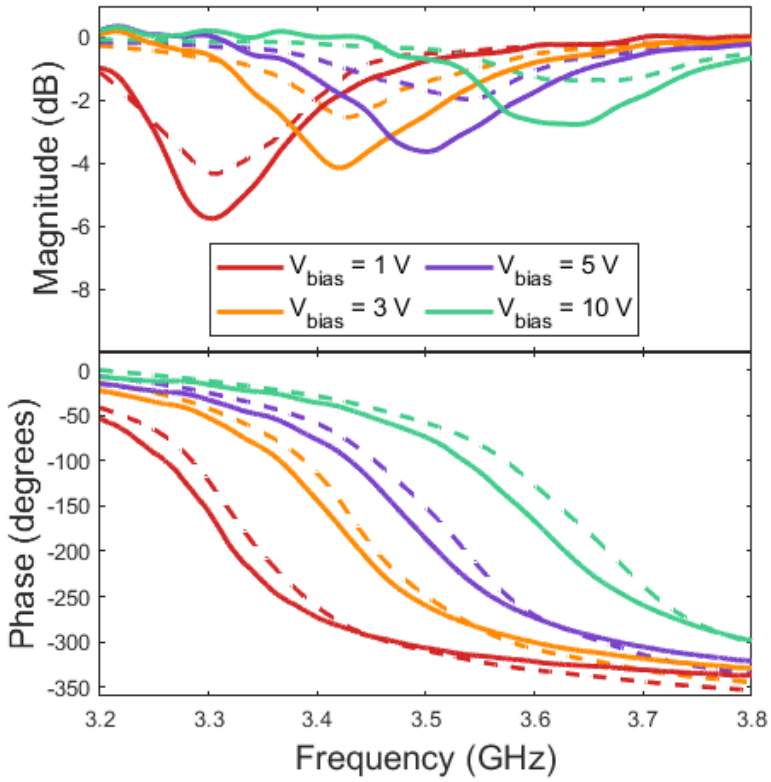

Figure 3.15: Global reflection response for co-polar varactor voltages of $V_1 = 1, 3, 5$, and $10\ V$, with the cross-polar varactors held at $V_2 = 0\ V$. Full-wave simulation results are given by the dashed curves and measured results given by the solid curves.

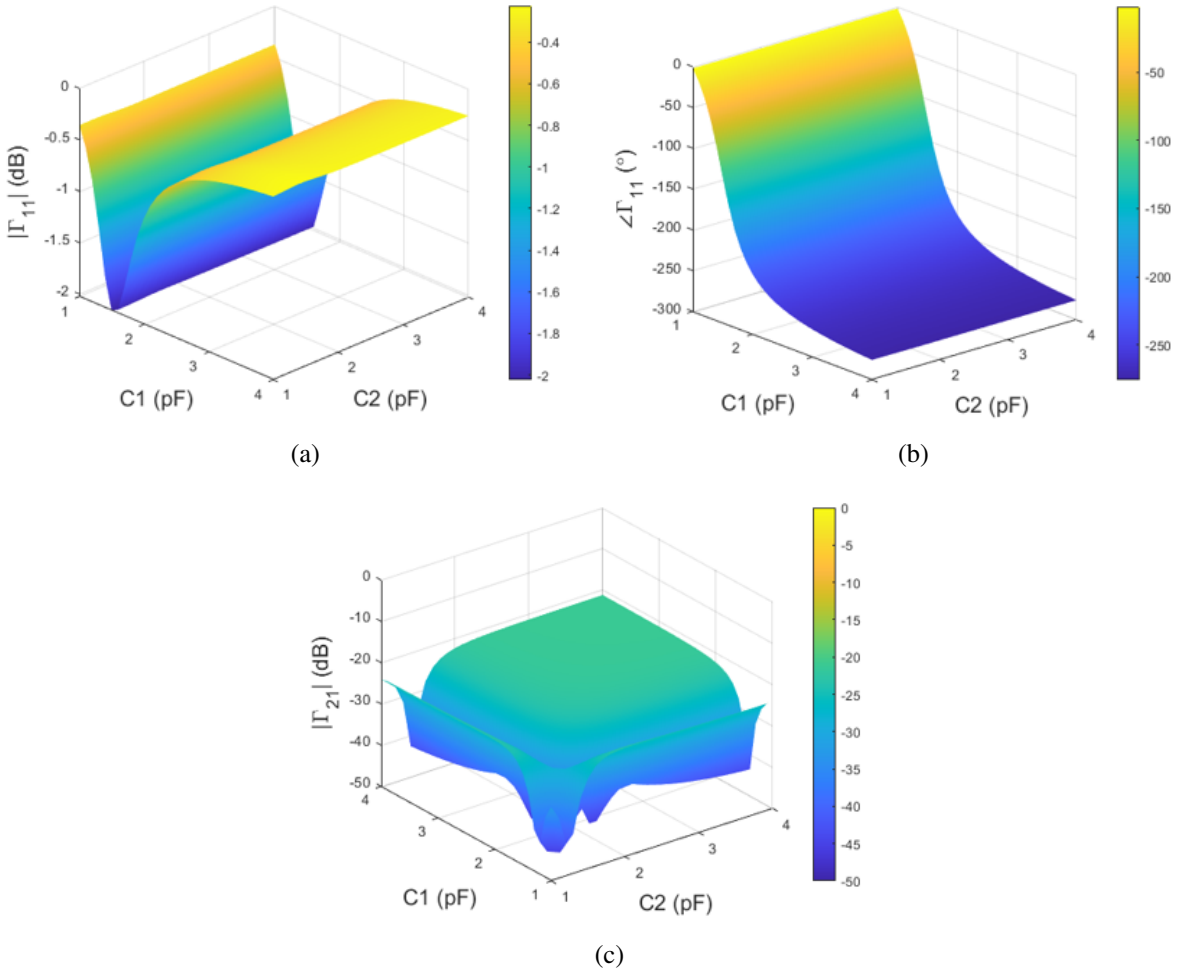

(a) (b)

(c)

Figure 3.16: Optimised reflection responses versus co-polar (C1) and cross-polar (C2) varactor capacitance for the unit cell design. Magnitude response (a), phase response (b), and cross-polar magnitude (c).

3.3.3 Control circuitry

While previous varactor-based RIS designs tend to limit the biasing control to groupings of unit cells [149] [150], this design offers two-level voltage control to each individual varactor diode. The control circuit topology is centred around high voltage shift registers with 32 push-pull outputs each. A representative circuit diagram of the setup of each shift register output port, interfacing with a varactor diode, is shown in Fig. 5.2. Each shift register can provide 1-bit control of the varactor diodes of 16 unit cells, providing a switchable voltage level determined by the logic voltage V_{DD}. With a DC voltage $V_S \geq V_{DD}$ applied to the square patches, the reverse bias voltages for the 0 and 1 logic states become V_S and $V_S - V_{DD}$, respectively.

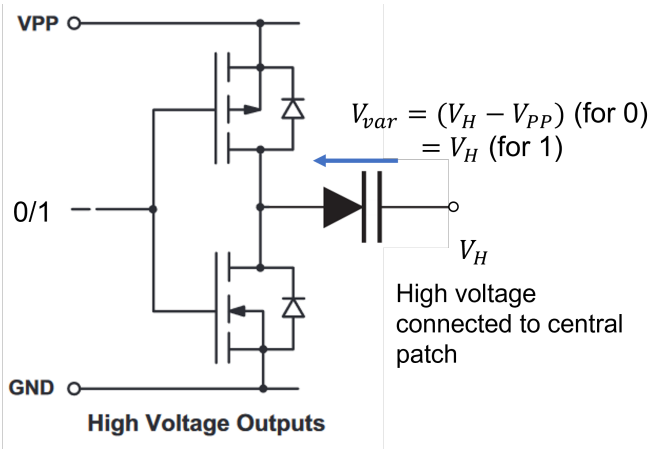

(a)

Figure 3.17: Circuit diagram of a HV5308 output port in push-pull configuration, interfacing with a varactor diode.

Tiles of dimensions 480 mm $\times$ 480 mm were fabricated, each consisting of an arrangement of 16 $\times$ 16 unit cells, one of which is shown in Fig. 3.19. The schematics for the prototype are detailed in Appendix A. Each metasurface tile contains 16 high voltage shift registers, each with 32 output pins, providing bias signals to 512 varactors. The PCB design of the control circuitry for a single tile is shown in Fig. 3.18. For a set configuration, the control circuitry consumes a quiescent power of approximately 3 mW due largely to the minimum quiescent current of the shift registers, with the varactor diodes drawing negligible current. By comparison, driving a similar number of PIN diodes with a typical 1 mA bias current with off-the-shelf logic circuitry would result in an average power consumption in the region of 1 W. The RIS is connected to a Raspberry Pi single-board computer, providing digital signals to program the shift registers and a WiFi interface for remote control.

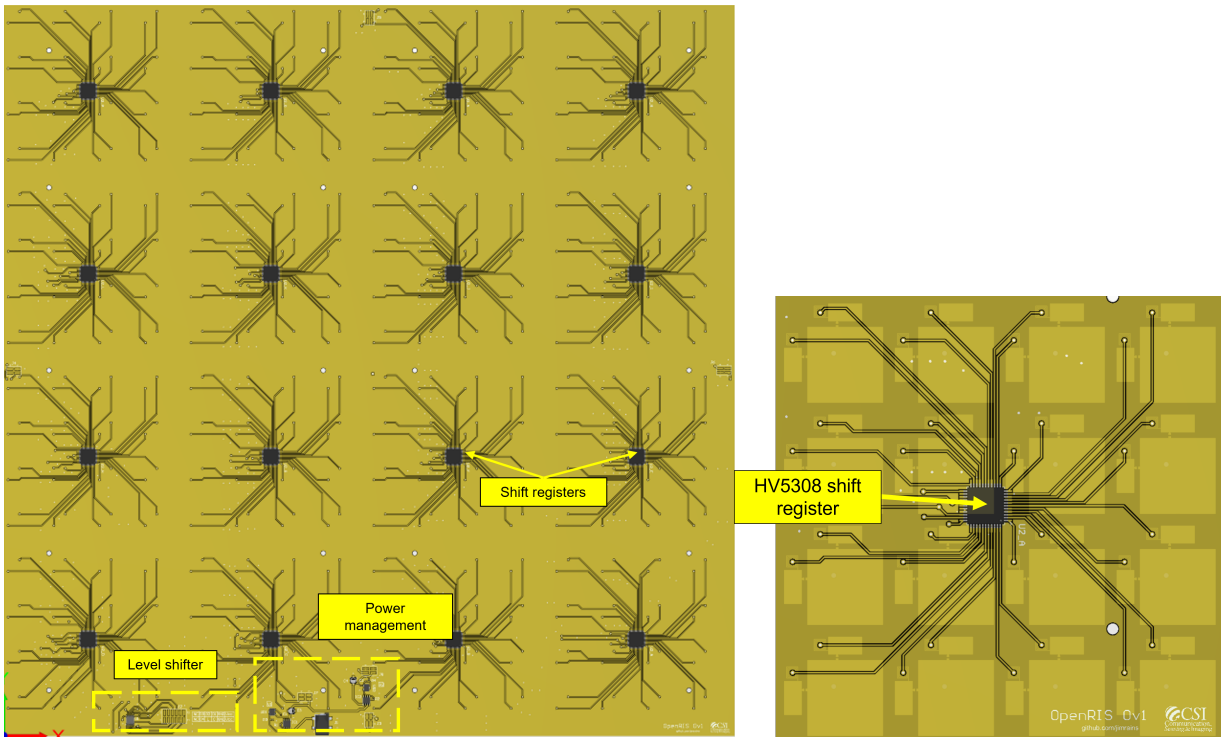

(a) (b)

Figure 3.18: Overview of control circuitry of designed PCB (a). One of the high voltage shift registers serving 16 unit cells (b).

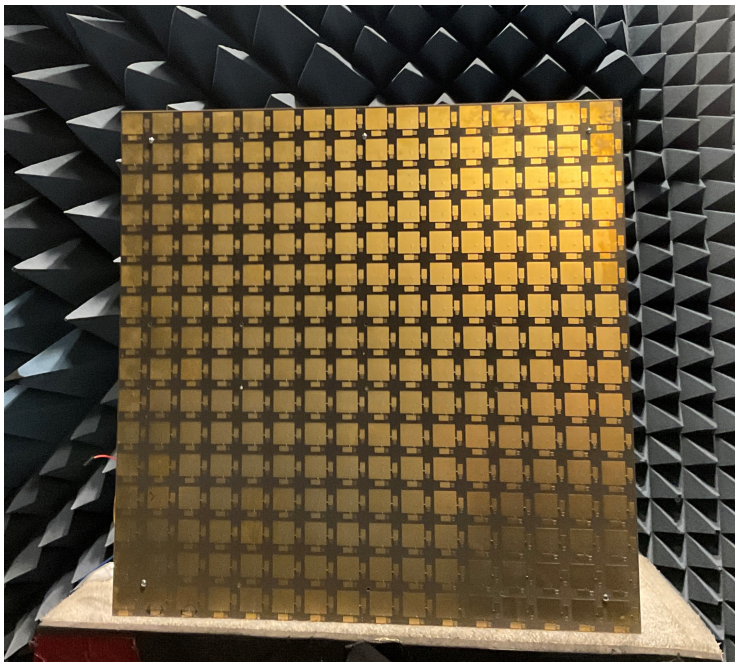

Figure 3.19: Front view of one of the fabricated metasurface tiles with an arrangement of 16×16 unit cells. Control circuitry is arranged on the back side of the metasurface.

3.3.4 Measurements

The purpose of specular reflection measurements for the 1-bit, dual-linear polarised RIS is to verify the programability of the reflection coefficients compared to those simulated with PBCs. Similarly to the 3-bit prototype, the control observation in this regard is the specular reflection response of a homogeneous metal sheet of similar dimensions to a single RIS tile. Additionally, due to practical limitations in antenna placement, we are constrained to observation angles that are greater than 0° to prevent antenna overlap. Similar constraints to the 3-bit device characterisation are placed on the antenna placement. The metric of interest for this experiment is the likeness of the specular measurements with the simulated reflection behaviour within the band of interest. The device is measured with the bias voltages of the RIS varactors as parameters.

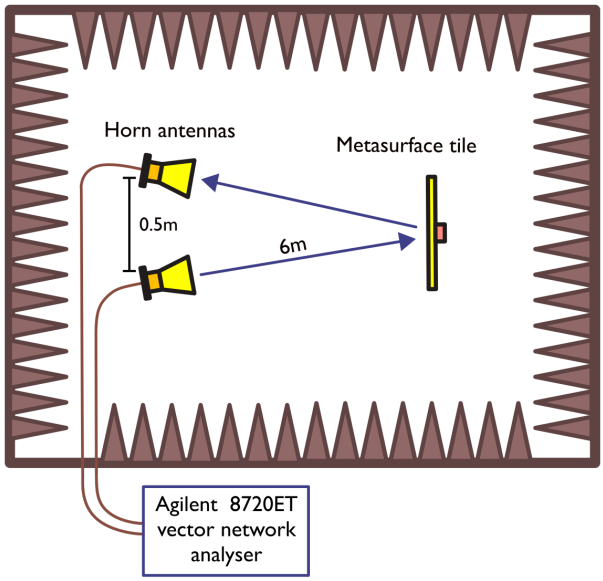

Figure 3.20: Measurement setup for ascertaining global reflection coefficients.

The measurement setup is depicted in Fig. 3.20. In a similar fashion to section 3.2.6, two standard gain horn antennas and a RIS tile were placed in an $8\ m \times 4\ m \times 4\ m$ anechoic chamber at a distance of 1.5 m from the chamber floor. The horn antennas were positioned 6 m from the center of the tile, with an inter-antenna spacing of 0.5 m. The antennas were connected by 5 m coaxial cables to an Agilent 8720ET VNA. Initially, both antennas were arranged in a vertical polarisation and the tile was replaced by a copper plate of similar dimensions. The system was calibrated in the S21 setting by normalising transmission via the copper plate. This was followed by measuring the S21 to ascertain the co-polar metasurface reflection for the voltage range 0-18 V. The cross-polar performance was then ascertained by a similar procedure, with one of the horn antennas oriented in a horizontal polarisation. The co-polar reflection behaviour versus bias voltage for several frequency points is plotted in Fig. 3.21. It can be seen that a 1-bit response can be achieved at all noted frequency points from 3.3 to 3.7 GHz, although the associated magnitude can vary as much as 6.5 dB. To broaden the bandwidth over which the

phase differences between two fixed voltage levels remains within $180 \pm 20°$, bias voltage levels which result in a peak phase difference of 200° at the center frequency of 3.5 GHz have been found as 2.5 V and 10 V. This is highlighted by the vertical dashed lines. The associated co-polar magnitudes, phases (solid curves), phase difference (dashed curves), and cross-polar magnitudes (dotted curves) have been plotted in Fig. 3.22. With these settings, the metasurface can be seen to exhibit a 1-bit bandwidth of approximately 160 MHz, a cross-polar isolation of 20 dB, and a maximum reflection loss of 4.2 dB at the lower band edge.

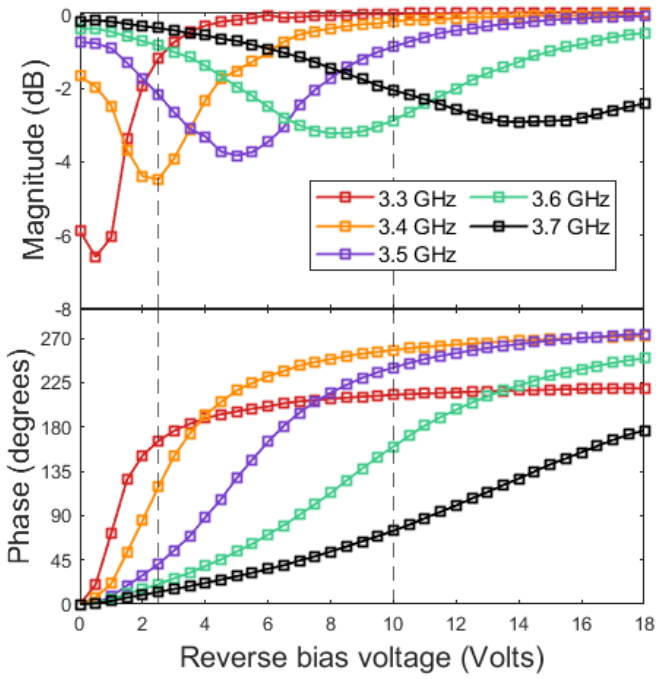

Figure 3.21: Measured reflection phase and magnitude versus voltage for 3.3, 3.4, 3.5, 3.6, and 3.7 GHz. Vertical dashed lines highlight the operating points, 2.5 V and 10 V, utilised for 1-bit operation centered at 3.5 GHz, as detailed in Fig. 3.22.

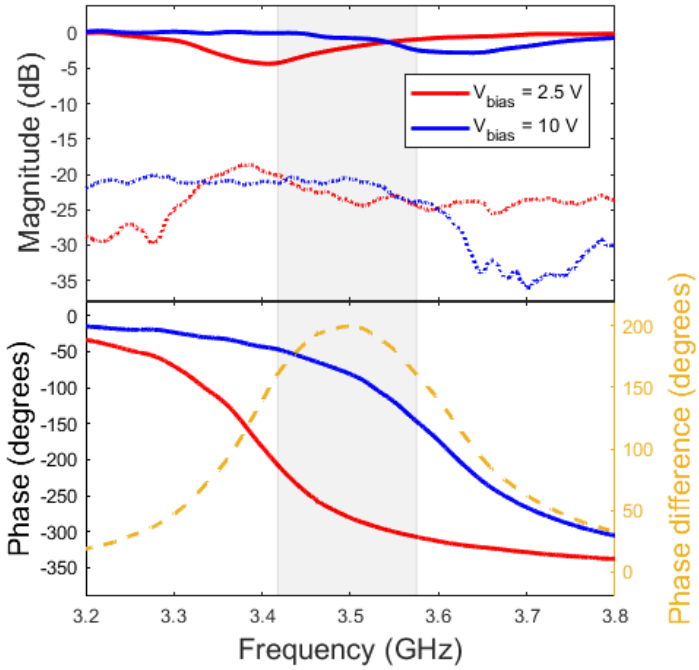

Figure 3.22: Measured reflection response for metasurface biased for 1-bit operation for 3.42 to 3.58 GHz. These values correspond to $V_{DD} = 7.5V$ and $V_S = 10V$. The co- and cross-polar reflection magnitude is given by the solid and dotted curves in the top plot, respectively. The phase difference between the two bias states is highlighted as the dashed curve in the bottom plot.

3.3.5 Beamsteering performance

Beam pattern measurements were ascertained to determine the dynamic beamsteering capability of the RIS prototype. Of interest was the far-field to far-field beamsteering response relevant for outdoor communication system scenarios. Due to limitations on the size of the available anechoic chamber, the experiment was constrained to an outdoor setting with antennas placed in the far-field to the RIS tile. The control case in these measurements is the co-polar specular reflection beam pattern for each transmitter angle. This corresponds with the RIS programmed to a homogenous state with no bias voltages applied to the varactor diodes. Performance indicators for these experiments are the conformance of the measured beam patterns to those predicted through simulation. The parameters under study were the azimuth angles of two identical horn antennas directed at the RIS, subject to a set of pre-determined RIS configurations. When a VLoS link between the Tx and Rx via the RIS is established, the dominant path can be considered a combination of two LoS paths. That is, the LoS path between the transmitter and the RIS, and the LoS path between the RIS and the receiver. We adopt here the physics-compliant path loss model recently verified by Tang et al. [26] to approximate the received power at the Rx for a given RIS configuration and Tx position. The model assumes any LoS link between the Tx and Rx is negligible. The received power, P_r, at the position of Rx via the $N \times M$ set of RIS elements, with unit cell dimensions $d_x \times d_y$, can be approximated by:

$$P_r = P_t \frac{G_t G_r d_x d_y \lambda^2}{64\pi^3} \left| \sum_{m=1-\frac{M}{2}}^{M/2} \sum_{n=1-\frac{N}{2}}^{N/2} \frac{\sqrt{F_{n,m}^{combine}}\, \Gamma_{n,m}}{r_{n,m}^t r_{n,m}^r} e^{\left(-j\frac{2\pi}{\lambda}(r_{n,m}^t + r_{n,m}^r)\right)} \right|^2 \tag{3.14}$$

with P_t the transmit power, G_t and G_r the respective Tx and Rx antenna gains, $r_{n,m}^t$ and $r_{n,m}^r$ the distance between unit cell (n,m) and the transmitter and receiver, respectively [26]. The term $F_{n,m}^{combine}$ takes into account the angle-dependent nature of the radiation patterns of the transmitter, unit cell reception, unit cell reradiation, and receiver, respectively. To maximise received power at the user equipment, the task is to find, within constraints of the operating environment (e.g., a wall-mounted RIS so as not to present an obstruction), the RIS dimensions, position, and set of unit cell bias states to maximise (3.14). Assuming constant local reflection magnitudes, on observing (3.14), it can be seen that if the local reflection coefficients, $\Gamma_{n,m}$, present phase shifts that compensate for the phase shifts attributed to the paths $r_{n,m}^t$ and $r_{n,m}^r$, the summation may be maximised since the electric field components associated with each path add coherently.

In the measurements presented here, we are interested in ascertaining the beam patterns for a set of 11 RIS configurations optimised to cover the half-space in azimuth in front of the RIS. Referring to the axes defined in the measurement setup in Fig. 3.23, these 11 configurations correspond to maximising (3.14) in 15° steps from 15° to 165°. The analytical azimuthal beam pattern cuts corresponding to 6 of the RIS configurations are shown in Fig. 3.24.

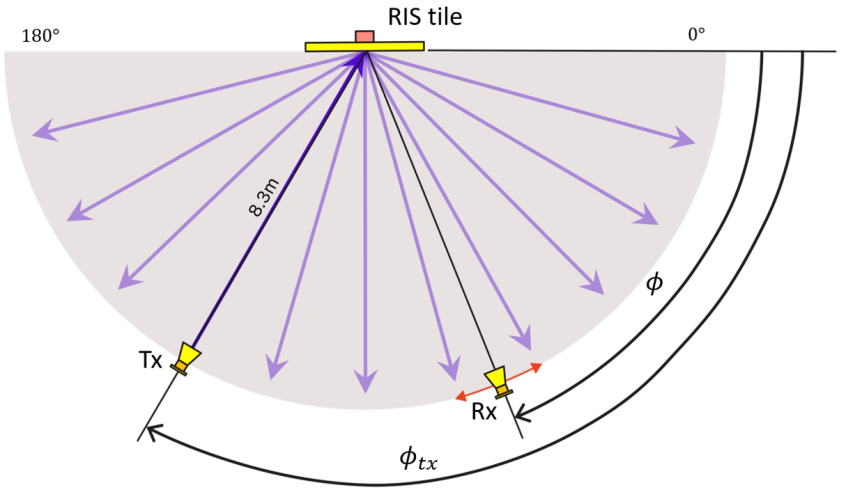

Figure 3.23: Far-field to far-field measurement setup for a single 16×16 element RIS tile.

Experiment setup

Measurements of the far-field to far-field beamsteering performance were conducted outdoors in a courtyard area. This was due to the limited size of the available anechoic chamber. The far-field distance from a single RIS tile is calculated to be 6.1 m and therefore the distances at which the transmitter and receiver antennas are placed should exceed this value. It was practically feasible to place the antennas at a distance of 8.3 m given area available for the experiment. The two antennas employed for this work were standard gain ridged horn antennas. These were connected to a Keysight PNA vector network analyser with calibration planes at the antenna ports. Since the measurements were taken outdoors in a built-up university campus, time gating was employed to reduce multipath effects. The power delay profile (PDP) for the measurement setup is plotted in Fig. 3.26. Time gating of width 5 ns was applied in the region of 60 ns in order to filter out wave components not interacting with the RIS.

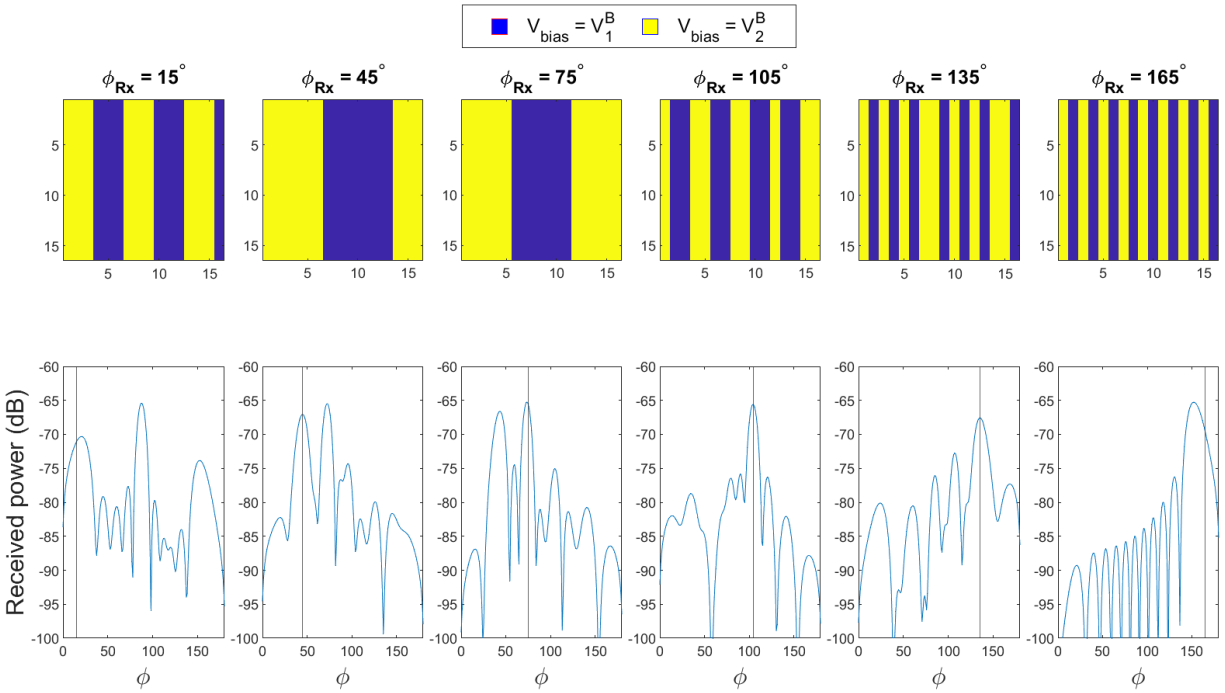

Figure 3.24: Analytical solutions for H-plane cuts of far-field pattern for an incident angle of $\phi_{tx} = 120°$. Corresponding RIS tile configurations (top) and H-plane cuts (bottom).

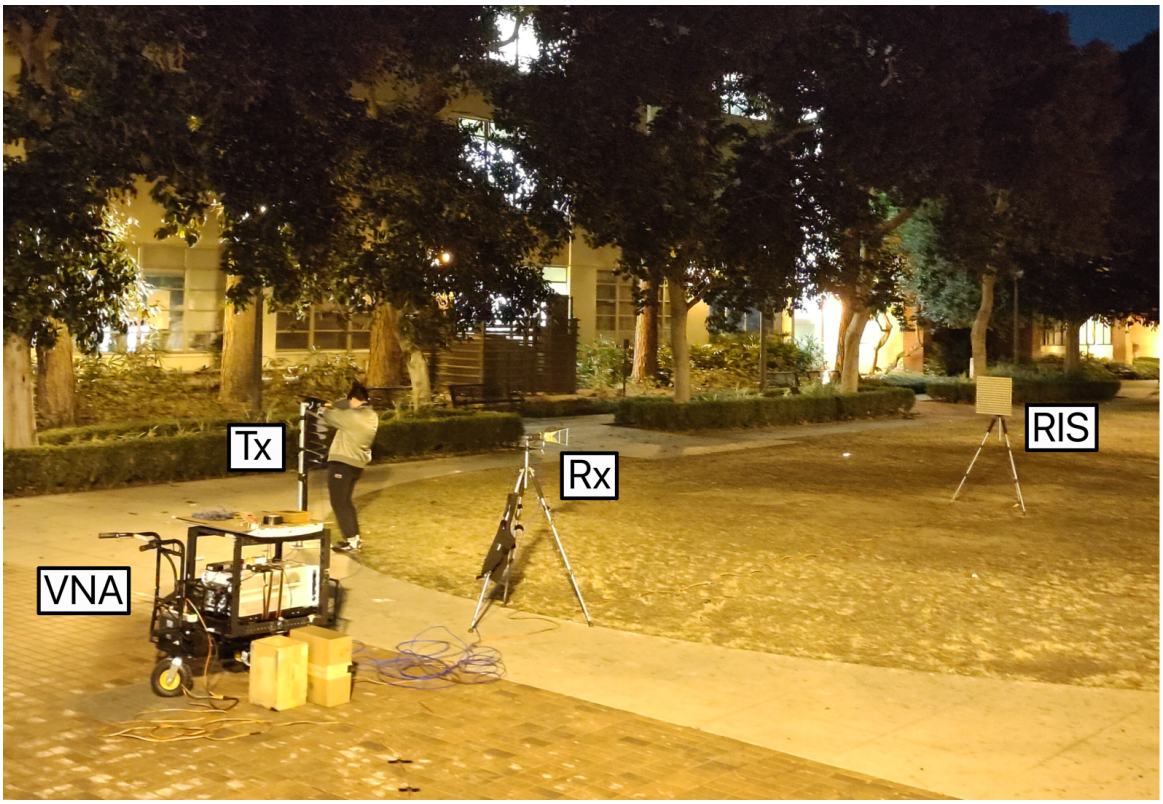

Figure 3.25: Photograph of the far-field to far-field measurement setup.

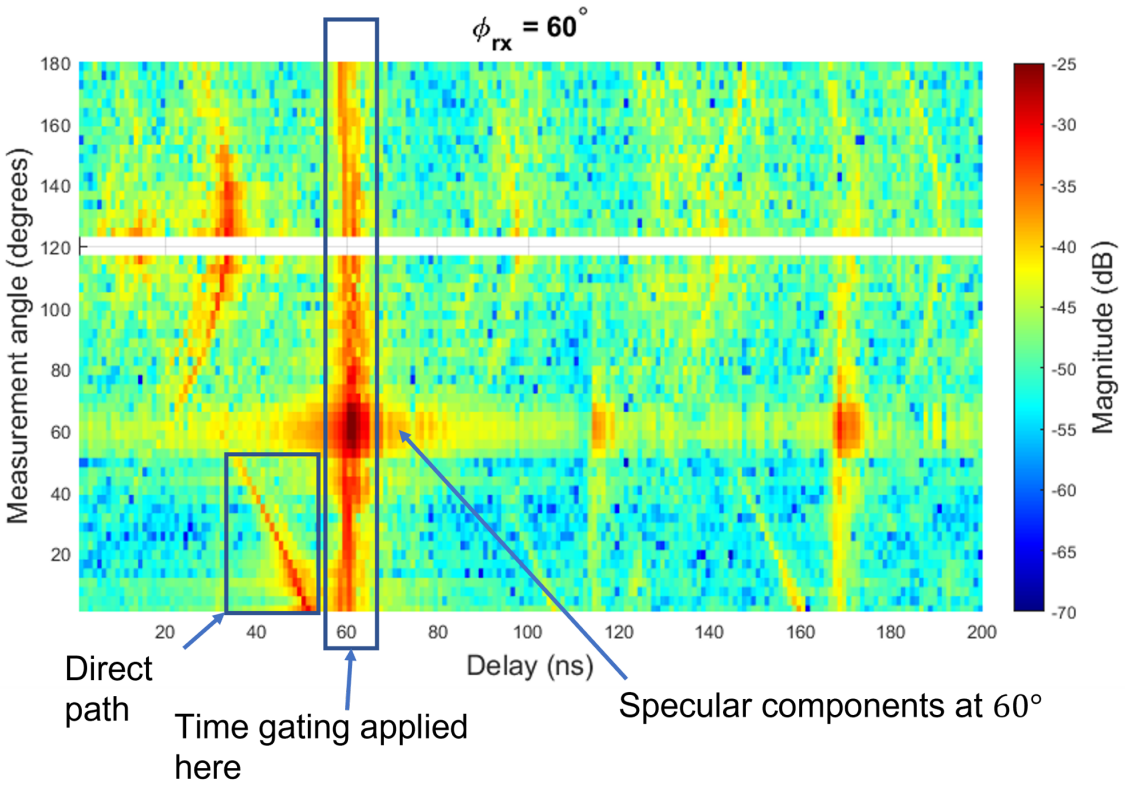

Figure 3.26: Power delay profile versus receiver position for the far-field to far-field measurement system.

During each measurement step, the transmitter antenna was fixed at the incidence angle of interest, ϕ_{tx}, aligned by a laser pointer and spirit level. The receiver antenna was positioned at a fixed receive angle and similarly aligned. The S21 measurements were then ascertained for the set of 11 configurations corresponding to the transmitter and receiver angles, ϕ_{tx} and ϕ_{rx}. Measurements were then obtained for the remaining receiver positions in 3° steps, corresponding to 61 receiver positions between 0° and 180°. Four transmitter angles were considered for this work, namely 90°, 105°, and 120°, and 135°.

Results

The vertically-polarised azimuthal beamsteering S21 measurements for incidence angles 90°, 105°, 120°, and 135° are shown in Fig. 3.27. The position and magnitude of the main lobes can be seen to be in good agreement with the analytical model. It can be seen that the specular beam magnitudes are typically 3 dB higher than the anomalously reflected beams. This is due to the quantised nature of the surface impedance profile corresponding to the anomalously reflecting configurations, compared to the homogenous metal plate-like configurations corresponding to specular reflection, which is naturally free from phase error.

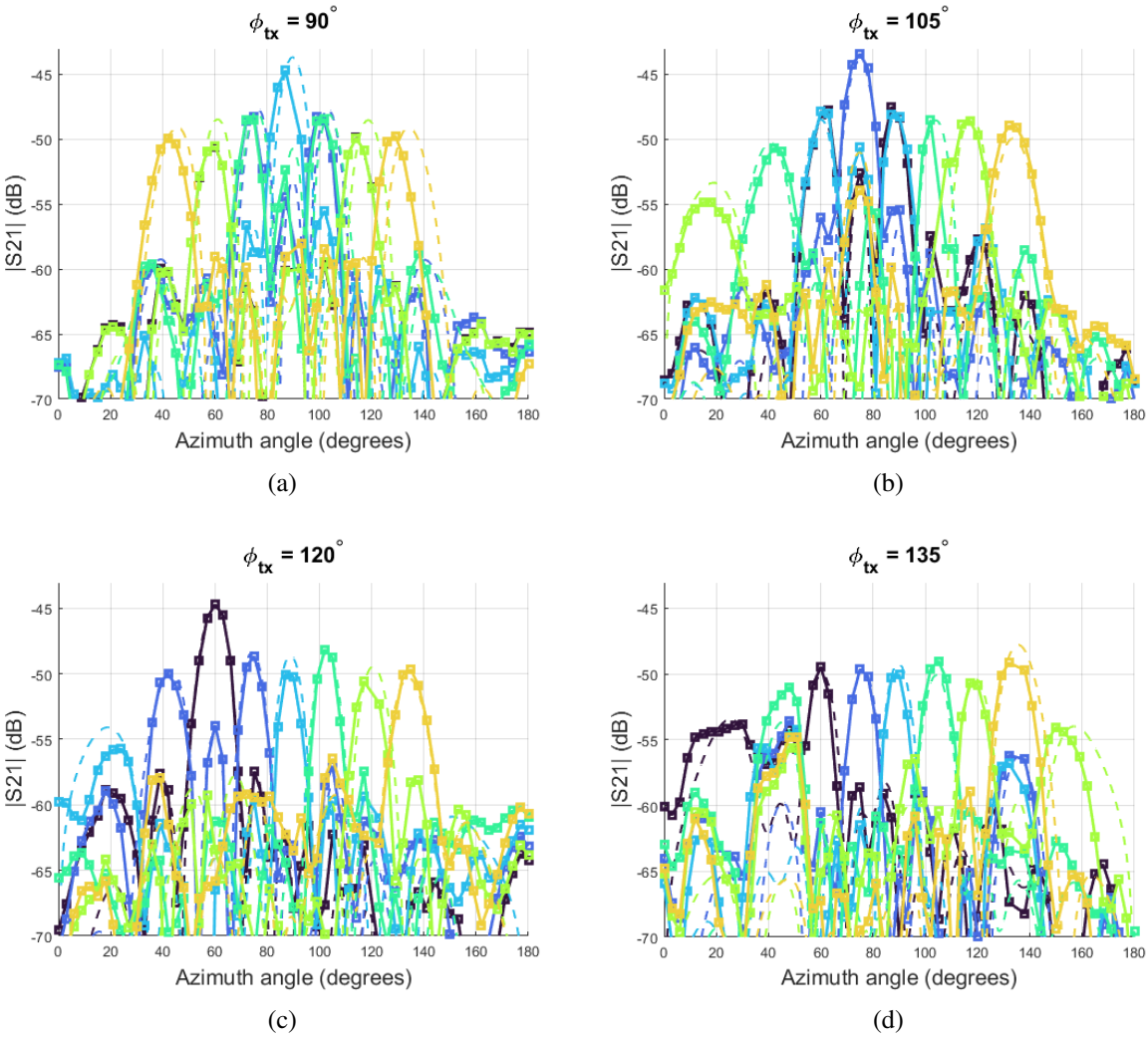

Figure 3.27: Measured S21 magnitude for the far-field to far-field setup of Fig. 3.23 (squared curves) for coupling incident waves at ϕ_{tx} to 60°, 75°, 90°, 105°, 120°, and 135°. Plots (a) to (d) correspond to incident angles 90°, 105°, 120°, and 135°, respectively. Dashed curves correspond to the respective analytical solutions.

Cross-polar measurements for the $\phi_{tx} = 120°$ case were ascertained in the same fashion, with the receiver antenna in the horizontal polarisation arrangement and the transmitter antenna held in a vertical polarisation as before. These have been plotted in Fig. 3.28(c), with the co-polar measurements for this incidence angle shown in 3.28(a) and (b) for the vertical-vertical and horizontal-horizontal polarisation cases. It can be seen that the cross-polar magnitude of the main lobes are typically 14-15 dB lower than the co-polar magnitudes.

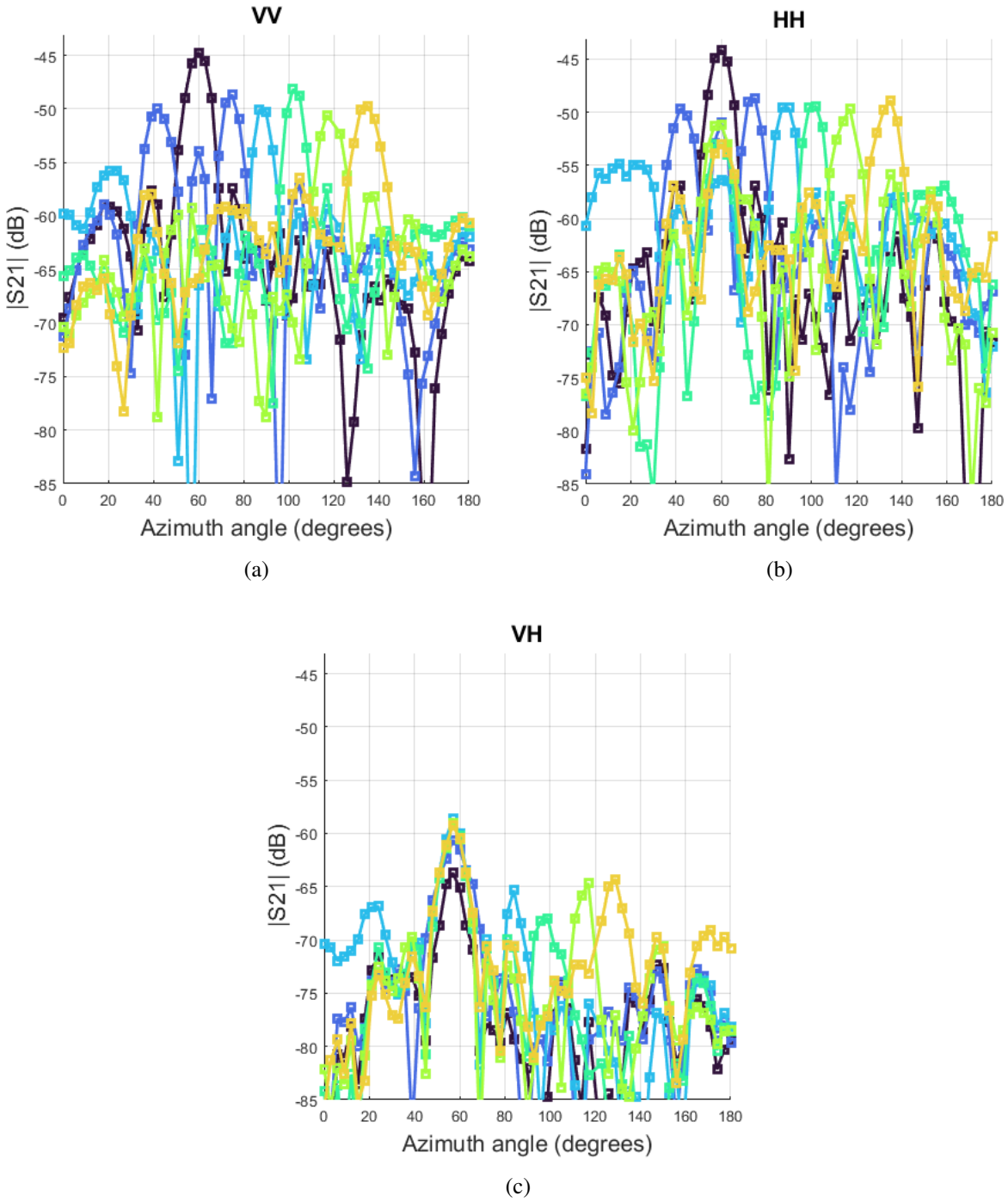

(a) (b)

(c)

Figure 3.28: Comparison of vertical-vertical (a), horizontal-horizontal (b), and cross-polar (c) S_{21} magnitudes for $\phi_{tx} = 120^{\circ}$ at 3.5 GHz.

Instantaneous bandwidth

The instantaneous bandwidth is defined here as the 3 dB bandwidth versus frequency for a given re-radiated beam direction. The anomalous reflection performance for the $\phi_{tx} = 120^\circ$ case is plotted in Fig. 3.29 for anomalous reflection directions 75°, 90°, 105°, and 135°, as well as the specular configuration corresponding to 60°. It can be observed that, outside of the operating band for which the 1-bit response is tuned (refer to Fig. 3.22), specular reflection is dominant. On approaching 3.4 GHz, power is coupled into the spatial modes associated with each desired direction, as well as some undesirable coupling into side-lobes. This trend continues until mid-band, where specular components are present likely due to phase error around 3.5 GHz. The instantaneous bandwidth varies from 335 MHz for the 90° configuration to 210 MHz for the 165° configuration (not shown). This is more than sufficient instantaneous bandwidth to cover channels at sub-6 GHz 5G. It can be seen that a split beam occurs in the 75° configuration, as predicted by the analytical formula for the 120° incidence condition. It will be seen later in chapter 5 that this behaviour is prominent in the far-field to far-field beam sweep experiments and is due to the overlap of the 1-bit configurations corresponding with the maximum power transfer for the respective directions.

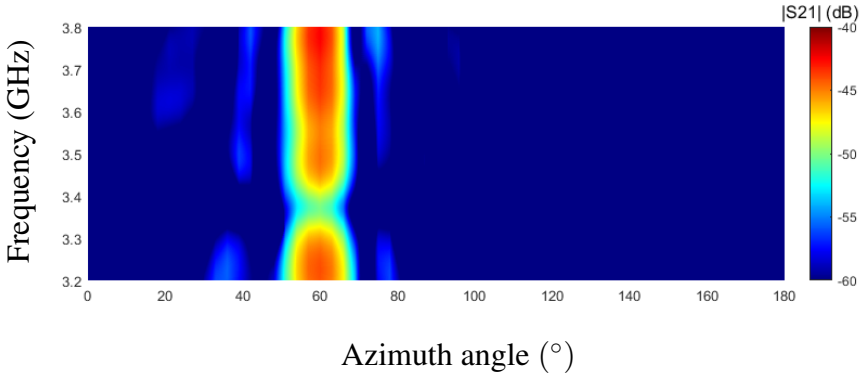

(a) 60°

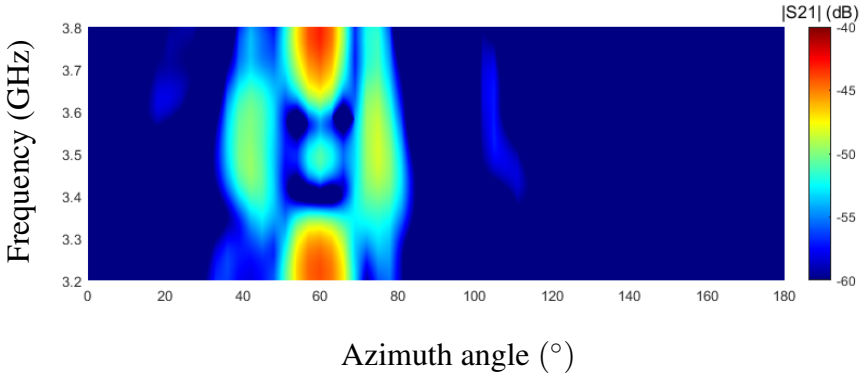

(b) 75°

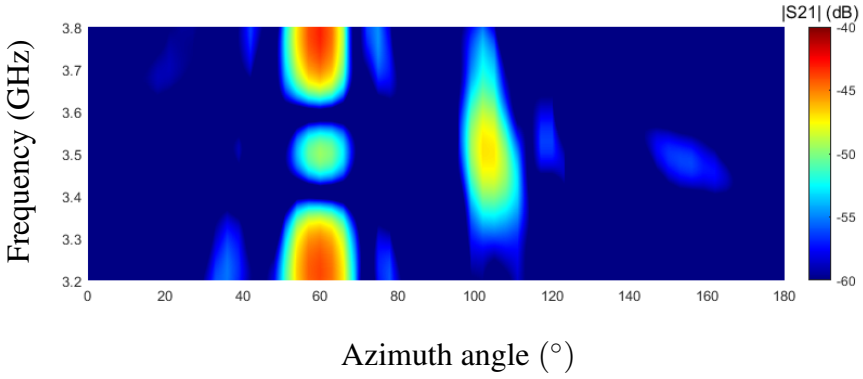

(c) 105°

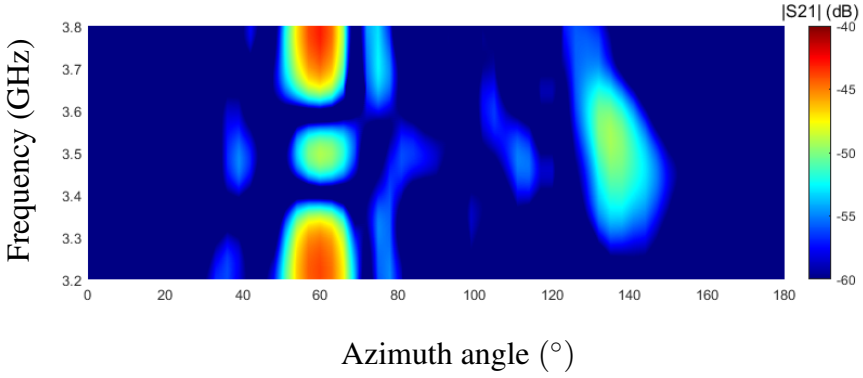

(d) 135°

Figure 3.29: $|S_{21}|$ versus angle across the 3.2 - 3.8 GHz band for 4 RIS configurations.

3.4 Summary

In this chapter, two RIS prototypes have been investigated and their performance verified. Namely, a 3-bit column-controlled RIS and a low-power dual-polarised 1-bit fully-addressable RIS. PSO has been shown to be a powerful optimisation technique for high performance digital reconfigurable metasurfaces employing PIN and varactor diodes. The varactor-based RIS has been evaluated as a far-field to far-field anomalous reflector. The analytical model of equation 3.14 has been utilised to generate configurations corresponding to successful beamsteering of the metasurface prototype over a wide range in the half-space normal to the surface. Additionally, the instantaneous bandwidth of the device as acting as an anomalous reflector has been investigated, showing promising performance across the 3.2 - 3.8 GHz 5G band. The 3-bit RIS prototype was utilised in an extensive indoor measurement campaign as detailed in chapter 4 that follows. Deployment of a larger version of the varactor-based metasurface design in a real-world network is the focus of chapter 5.

Chapter 4

Multi-bit RIS-enabled indoor point-to-point link enhancement

4.1 Introduction

In the last few years, details on several RIS experimental testbeds have been published, with experiments performed in a diverse set of scenarios at microwave and millimetre-wave (mmWave) bands [58] [64] [105] [3]. As noted in section 2.5, most published RIS experimental testbeds have only considered a 1-bit design due to its low complexity and small configuration overhead compared to higher resolution designs. Oftentimes in indoor communication scenarios, user equipment is co-located in the same horizontal plane. In these cases, beamsteering capability in elevation is underutilised. Similarly, when network equipment is situated at distances outside of the radiative near-field of the RIS, as well as in the same horizontal plane, the optimal RIS configuration often resembles columns of unit cells with similar reflection states. For the 1-bit RIS case, this usually results in the generation of spurious beams [76], therefore wasting transmitted power and the potential to cause interference with nearby user equipment. Beam pattern purity is greatly enhanced for 2-bit and 3-bit designs [83]. By utilising the column-connected approach to the RIS design detailed in section 3.2, elevation beam steering capability has been exchanged for a high reflection state resolution, thereby enabling performance enhancement in indoor communication scenarios without significant additional control circuit complexity. In this chapter, the performance benefits of a high phase-resolution RIS in indoor environments are explored. Three different SISO communication scenarios are considered.

4.2 Optimisation algorithm

The simple RIS optimisation algorithm presented here has been designed to find a RIS configuration which maximises the receiver power at a fixed location. When a VLoS link between the Tx and Rx via the RIS is established, the dominant path can be considered a combination of two

LoS paths. That is, the LoS path between the transmitter and the RIS, and the LoS path between the RIS and the receiver. The physics-compliant path loss model recently verified by Tang et al. [26] is adopted here to approximate the received power at the Rx for a given RIS configuration and Tx position. The model assumes any LoS link between the Tx and Rx is negligible. The received power, P_r, at the position of Rx via the $N \times M$ set of RIS elements, with unit cell dimensions $d_x \times d_y$, can be approximated by:

$$P_r = P_t \frac{G_t G_r d_x d_y \lambda^2}{64\pi^3} \times \left| \sum_{m=1-\frac{M}{2}}^{M/2} \sum_{n=1-\frac{N}{2}}^{N/2} \frac{\sqrt{F_{n,m}^{combine}}\,\Gamma_{n,m}}{r_{n,m}^t r_{n,m}^r} e^{(-j\frac{2\pi}{\lambda}(r_{n,m}^t + r_{n,m}^r))} \right|^2 \tag{4.1}$$

with P_t the transmit power, G_t and G_r the respective Tx and Rx antenna gains, $r_{n,m}^t$ and $r_{n,m}^r$ the distance between unit cell (n,m) and the transmitter and receiver, respectively [26]. The term $F_{n,m}^{combine}$ takes into account the angle-dependent nature of the radiation patterns of the transmitter, unit cell reception, unit cell reradiation, and receiver, respectively. To maximise received power at the user equipment, the task is to find, within constraints of the operating environment (e.g., a wall-mounted RIS so as not to present an obstruction), the RIS dimensions, position, and set of unit cell bias states to maximise (4.1). Assuming constant local reflection magnitudes, on observing (4.1), it can be seen that if the local reflection coefficients, $\Gamma_{n,m}$, present phase shifts that compensate for the phase shifts attributed to the paths $r_{n,m}^t$ and $r_{n,m}^r$. The summation may be maximised since the electric field components associated with each path add coherently.

Algorithm 1 Maximise Rx signal power

Input: Average received signal power, P_r, in
Output: RIS configuration, Γ, out

```
for n = 1 to N do
  for m = 1 to M do
    for k = 1 to K do
      Γ_{n,m} ← ρ_k e^{jφ_k};
      s_k = P_r;
    end for
    q ← index of maximum of s;
    Γ_{n,m} ← ρ_q e^{jφ_q};
  end for
end for
return configuration matrix Γ
```

For the prototype consisting of 192 columns of addressable unit cells, there are 8^{192} possible combinations of column configurations. It would clearly be an insurmountable task to test each configuration and find the optimal set of unit cell states for a given communication setup. The algorithm adopted for these field trials considerably narrows down the search space and is based on the adaptive optics-inspired approach employed by Gros et al. [58]. For the case of

the multi-bit RIS presented here, each grouping of column-connected unit cells is set to one of the 8 biasing configurations, $\rho_k e^{j\phi_k}$ where k is an integer $k \in [1,8]$, ρ_k and ϕ_k are the respective reflection magnitude and phase shift of configuration k. For each controllable column of 12 unit cells, the set of 8 unit cell biasing configurations is iterated through and received power measurements are taken for each. The configuration which results in the highest received power is then selected for that column and the process continues for the remaining columns. This process can then be repeated until received power improvement is negligible. The scheme assumes that the changes in the received signal power levels between individual column states can be reliably detected. This may not be the case for cases of low SNR and non-negligible interference. In the trials documented here the receiver was always placed in a line of sight with the RIS, and the transmit power and receive gain were selected such that the received power did not drop below the noise floor of the transceivers.

As noted in a similar approach taken by Pei et al. [64], convergence of this type of iterative algorithm is guaranteed so long as the channel is quasi-static, with received signal strength increasing monotonically. The effects of noise on a similar iterative algorithm applied to a 1-bit RIS prototype is discussed in chapter 5. One major advantage of this iterative approach is that it does not rely on any training sequence and holds no assumptions about the channel. It also does not rely on the accuracy of any forward model of the RIS. Algorithm 1 is inherently sub-optimal due largely to the phase-dependent magnitude of the RIS. The resulting received power improvement will depend on the order in which the columns are set. For the case of a negligible alternative path between the transmitter and the receiver, when setting the first few columns of the RIS, there is a good chance that the configurations with the lowest reflection magnitude will be selected. As the algorithm iterates through the subsequent columns, a balance must be struck between promoting phase-coherent electric field components and minimising reflection loss. This may result, on average, in a lower overall magnitude compared to what may have been achieved with more careful selection of the prior column states. Regardless, as can be observed in the remaining sections of this work, this approach results in a significant channel gain improvement in all scenarios considered.

4.3 RIS control link

There are a number issues that require consideration for the control link implementation between the RIS and end nodes. It is assumed here that the RIS is wirelessly controlled, as a wired link from a base station, for example, may nullify the significant deployment cost advantage of RISs. Selecting an appropriate wireless communication protocol is essential to ensure reliable data exchange between end nodes and the RIS, taking into account factors such as data rate [151], latency, and reliability [152]. The reliability of control signaling is important, necessitating the implementation of error detection and correction mechanisms, redundancy, and error recovery

protocols. Security is another critical consideration, requiring the implementation of encryption, authentication, and access control measures to safeguard control data from unauthorised access or tampering [153]. Additionally, scalability is important to accommodate large-scale RIS deployments, with communication protocols and network architectures designed to efficiently control not only individual but potentially many RISs [154]. Ensuring compatibility with existing communication infrastructure and standards simplifies deployment and interoperability with other devices and networks, facilitating seamless integration of RISs into various applications.

Using an out-of-band control channel for the RIS feedback loop frees up spectrum in the band of interest, where the higher data rate communication link the RIS is aiming to facilitate could be impacted by interference and synchronisation issues, for example. Short range, low energy communications standards such as Bluetooth could be utilised as this out-of-band channel [155]. For ease of implementation, we opted for 2.4 GHz WiFi for it was supported by both the Raspberry Pi microcontroller and the laptop computers used in the experiments.

4.4 Indoor field trials

The purpose of the experiments detailed here is to determine any performance benefits that may arise from the deployment of higher-resolution RISs within indoor environments. While received signal strength does not translate directly into a change in the SNR, for instance, it provides a means of comparison that can be ascertained with a low-complexity measurement setup. In this instance, with commercial off-the-shelf software-defined radios (SDRs). The positioning of the RIS was constrained such that it did not cause an obstruction and could be reasonably approximated to be wall-mounted or otherwise integrated into the environment. The parameters under study were the relative positions of the user terminals and the RIS reflection coefficient configurations. The reference signal power is used as a performance indicator, comparing the control case of an electrically-conducting plate to a programmable metasurface in its place. For an existing network equipment deployment, such as a 5G small cell, it may be desirable to extend coverage to adjacent rooms, corridors, or floors without significant investment in additional infrastructure, such as a backhaul link and multiple RF chains [15]. The strategic placement of a RIS on interior walls could be a cost-effective solution to circumventing indoor blockages, in theory, but there are currently relatively few measurement campaigns in the literature to confirm this. Three indoor coverage enhancement scenarios have been considered in this work and are representative of situations where an additional small cell might usually be installed [156]. Namely, an open lobby area adjacent to a common room, a junction between two long corridors, and a multi-floor scenario.

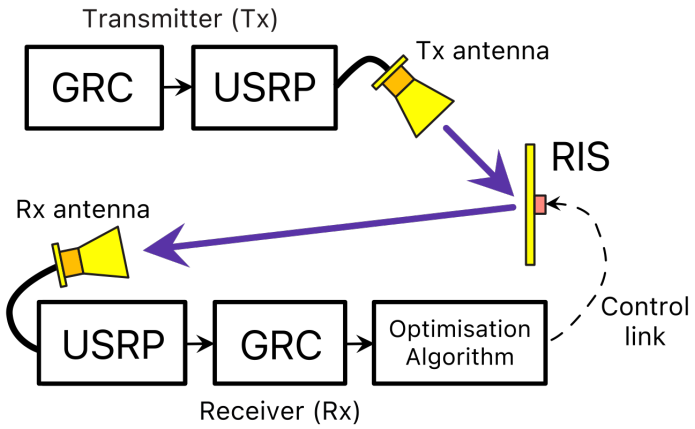

Figure 4.1: Diagram representing USRP-based communication link with the RIS feedback loop. The RIS and receiver form a feedback loop via a WiFi control link to iteratively increase the received signal strength.

4.4.1 Experiment setup

The 5G NR standard employs OFDM on uplink and downlink for its high spectral efficiency and resilience to fading. In each experiment performed here, similar to previous field trial works [64] [105], an OFDM signal with 20 MHz bandwidth and 312.5 kHz subcarrier spacing was selected as the transmit signal. The transmitted data was a randomly generated bit stream, with the signal processing performed by GNURadio Companion (GRC) software on laptop PCs. A block diagram of the RIS-aided communication link can be seen in Fig. 4.1.

National Instruments Universal Software Radio Peripheral (USRP) X300 devices were used at the transmitter and receiver side. The USRP transmit power was fixed at 0 dBm and the receive gain set to 15 dB for all scenarios. The antennas employed were a monopole antenna with a gain of 2 dBi, as well as a pair of Aaronia PowerLOG 70180 standard gain horn antennas with a gain of approximately 10 dBi in the operating region of interest. These were arranged in a horizontal polarisation configuration in order to facilitate interaction with the horizontally polarised RIS. In each scenario, the RIS position and orientation were selected so as to be parallel to an adjacent wall, emulating wall-mounted indoor deployment.

The measurements were performed as follows. All PIN diodes of the RIS were initially set to the all-unbiased (000) state. The receiver was placed with its antenna directed towards the RIS with the aid of a laser pointer. The transmitter continuously transmits the aforementioned OFDM-modulated signal towards the RIS, and the receiver continuously samples the average squared magnitude of the received signal via GRC. These power measurements are polled by the RIS optimisation algorithm and the connected columns were iteratively optimised until 5 iterations of the algorithm had passed. In our system setup, it was found that configurations could be reliably tested as a rate of 400 configurations per second. This rate allowed a sufficient interval for setting the RIS configuration, averaging the received power, and accounting

Table 4.1: Received power improvement for scenario I (versus aluminium plate)

Location		Rx Power Improvement (dB)	
Identifier	Coordinates (meters)	Monopole	Horn
A	(5, 11)	4.27	17.31
B	(1, 8.5)	8.93	17.11
C	(3, 6.4)	9.95	17.43
D	(1, 4.6)	7.01	15.47
E	(3, 2.5)	9.53	17.48
F	(3, 0)	16.10	9.12
G	(6, -2)	13.39	14.51
H	(11, -2)	3.97	7.47
I	(17, -2)	0.21	1.51
J	(23, -2)	2.54	5.04

for any sampling delay. For the adaptive optics-inspired approach employed here, the time to individually cycle through the 8 states of each of the 192 addressable columns is approximately 3.84 seconds. This resulted in an optimisation time of 19.2 seconds per measurement for the 1536 tested configurations iterated through 5 times. This time was acceptable due to the quasi-static nature of the channel during measurements and can easily be reduced through improved synchronisation of GRC, the control software, and digital hardware. Following optimisation, the received power was then measured, with averaging performed over 1 second intervals for 2 minutes. In order to ascertain a reference case, the measurements were repeated with the RIS replaced by an aluminium plate of similar dimensions.

4.4.2 Scenario I - Lobby

Scenario I is depicted in Fig. 4.2. The transmitter USRP connected to a horn antenna is placed in the *common room* at a height of 1 m and is directed towards the RIS placed in the *lobby*, forming a LoS link. The RIS is positioned at a height of 1 m to its centre and, utilising algorithm 1, was optimised to maximise the received power at 10 different locations within the lobby, denoted A to J, the coordinates of which can be found in table 4.1. The origin (0, 0) is considered at the centre of the RIS and the Tx is positioned at (20, 0) (i.e., 20 meters broadside to the RIS). This setup is a typical indoor coverage extension scenario, with some locations benefiting from a strong LoS link from the transmitter (i.e., positions G and F). On the other hand, the path towards positions A, B, and C results in attenuation and scattering via propagation through the adjacent rooms, as well as potentially not being served by the main lobe of the transmit horn antenna.

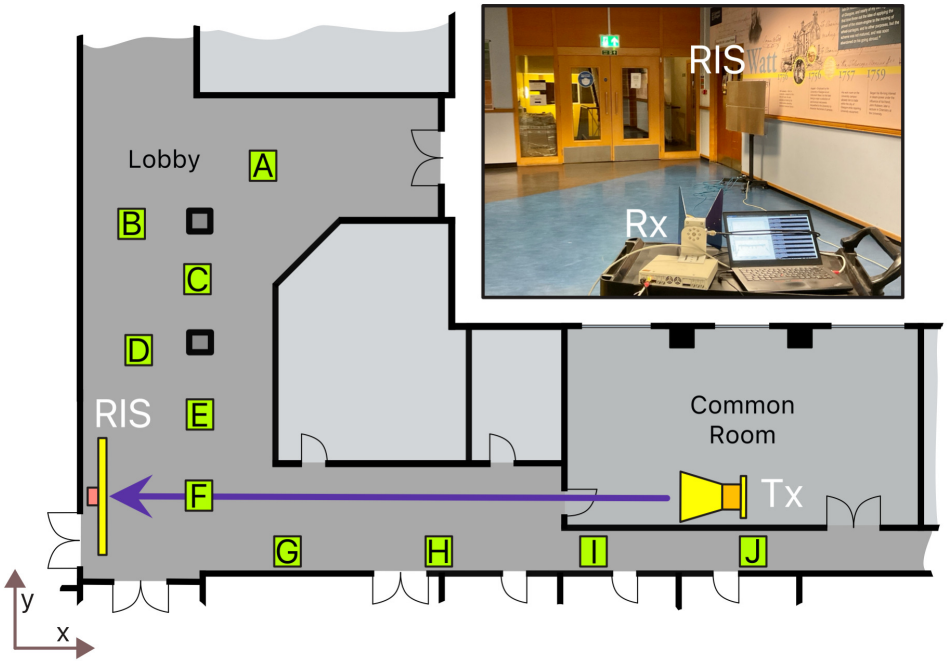

Figure 4.2: Experiment setup for scenario I. RIS in a lobby, with the transmitter (Tx) placed in an adjacent room, pointing via a doorway towards the RIS at a distance of 20 m. Locations A to J indicate receiver positions. Regarding the coordinates listed in table 4.1, the RIS is considered point (0, 0) and the transmitter at point (20, 0). The inset photo shows the receiver setup at position D.

Two different antennas were deployed at the receiver in order to compare the received power improvement performance, namely, a monopole antenna and a standard gain horn antenna. The monopole was found to exhibit acceptable (i.e., -10dB) return loss around 3.9 GHz which is within the operating region of the fabricated RIS, and therefore the experiment was performed at this frequency. The receiver PC, USRP, and antennas were placed on a 1m high trolley, as depicted in the photo in Fig. 4.2. The receiver was placed in one of the 10 locations throughout the lobby, with the receive antenna directed towards the RIS with the aid of a laser pointer.

The resulting power improvement over the metal plate for the monopole and horn antenna cases is shown in table 4.1. The horn antenna placed at positions A to E appears to benefit most from the introduction of the RIS due to the blockage caused by the adjacent rooms. The notable difference in improvement between the monopole and horn cases is due to the differing directivity of these antennas. Prior to optimisation of the RIS, the monopole receives power via NLoS paths from a more diverse set of directions compared to the horn antenna, resulting in a larger apparent improvement. Position I does not significantly benefit from the RIS in the monopole case and only marginal improvement of 1.51 dB for the horn case. This is likely due to the proximity of the transmitter to the adjacent wall, resulting in a much stronger NLoS signal path over the short distance.

Table 4.2: Received power improvement for scenario II (versus aluminium plate)

Location		Rx Power Improvement (dB)	
Identifier	Coordinates (meters)	Monopole	Horn
1	(2, 3)	20.41	22.23
2	(2, 8)	15.70	27.68
3	(2, 13)	15.9	16.84
4	(2, 18)	11.8	30.60

4.4.3 Scenario II - Corridor junction

In this experiment, a similar system setup to scenario 1 was adopted via a corridor junction, as depicted in Fig. 4.3. The RIS was placed at the junction between a wide and narrow corridor, with the surface normal to the narrow corridor, and can be considered point (0, 0). The transmitter, directed towards the RIS, was placed in the narrow corridor at a distance of 20 m (20, 0) from the RIS. Four receiver locations were selected, denoted positions 1 to 4, placed at 5 m intervals along the y axis, starting from (2, 2). The coordinates of the receiver positions alongside the resulting received power improvement at 3.9 GHz can be found in table 4.2. It can be seen that there is notable received power improvement in both the monopole and horn antenna cases, with up to 30.6 dB improvement at position 4.

For positions 1 and 3, the received power improvement appears to exhibit similar behaviour for both monopole and horn cases, whereas there is a significantly larger improvement for the horn antenna case at positions 2 and 4. Receivers served via NLoS propagation typically experience a wide power angle spectrum compared to LoS scenarios [157]. It can be expected that the monopole antenna more consistently captures power in a rich scattering environment since its peak antenna gain direction is less affected by its orientation. This is reflected in the results shown in Table 4.2, where the horn antennas achieve a significantly higher relative improvement compared to the monopole case. In their indoor channel sounding work, Wallace et al., [158] observed a more favorable channel gain performance in indoor NLoS scenarios whilst utilising a monopole array as opposed to a more directional patch antenna array. They posited it is likely due to the reduced multipath richness in the patch array case. Similarly, the smaller relative improvement in the monopole case for locations 2 and 4 is likely due to the fact that the monopole was receiving significantly more power in the reference case at those locations compared to the more directional horn antennas. Additionally, during reference measurements the horn antennas were directed at the aluminium reference plate whose scattering pattern exerts a greater influence on the received power than the monopole case due to the narrow field of view of the horn. The combination of the rich scattering environment and the variation in the nulls and sidelobes from the reference plate with respect to the receiver position results in the apparent improvement of the horn antenna exhibiting notably more variation than the monopole case.

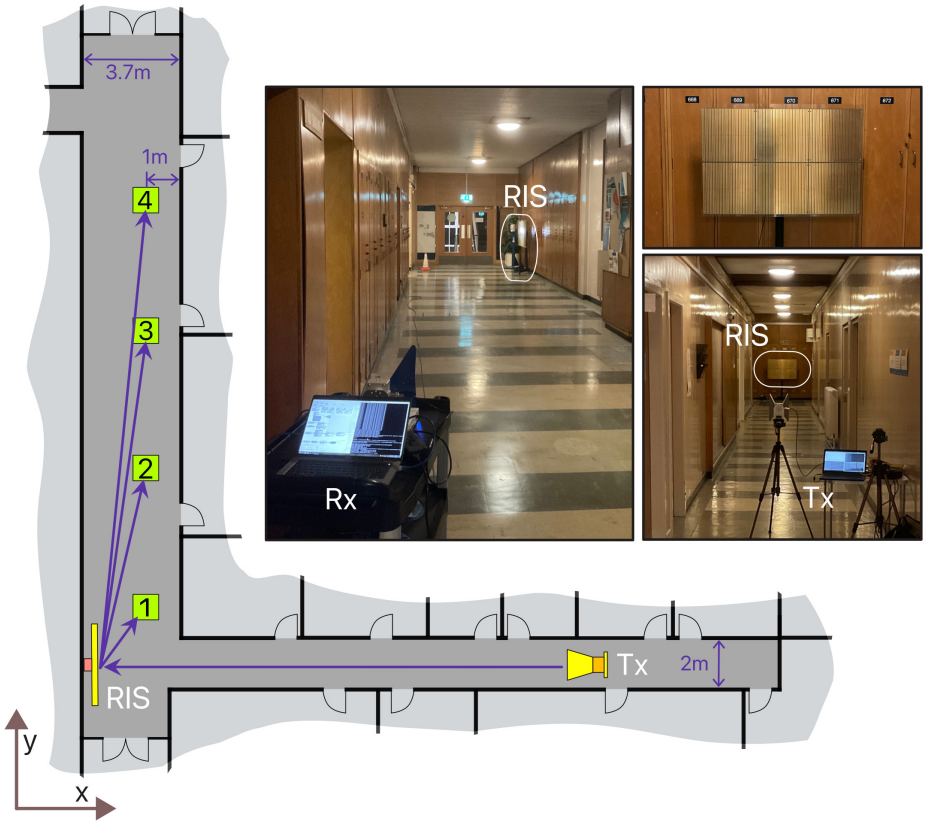

Figure 4.3: Experiment setup for scenario II. Transmitter is placed in a connecting corridor, pointing directly towards the RIS at a distance of 20 m. Locations 1 to 4 indicate receiver positions. Regarding the coordinates listed in table 4.2, the RIS is considered point (0, 0), with x broadside to the surface.

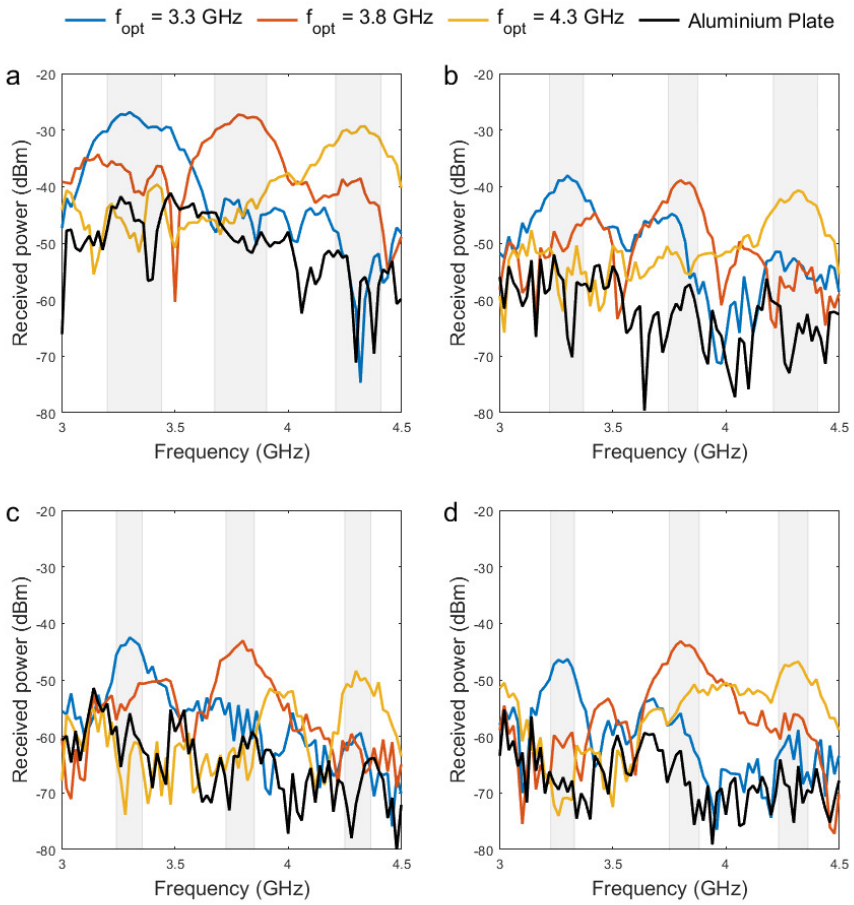

Figure 4.4: Received power versus frequency for scenario II. (a) to (d) show received power at positions 1 to 4, respectively. Optimisation of the RIS was performed at 3.3 GHz, 3.8 GHz, and 4.3 GHz, with a clear improvement over the metal plate of the same dimension. In plot (a) it can be seen that a received power improvement as much as 40 dB is achieved in the 4.3 GHz optimised configuration.

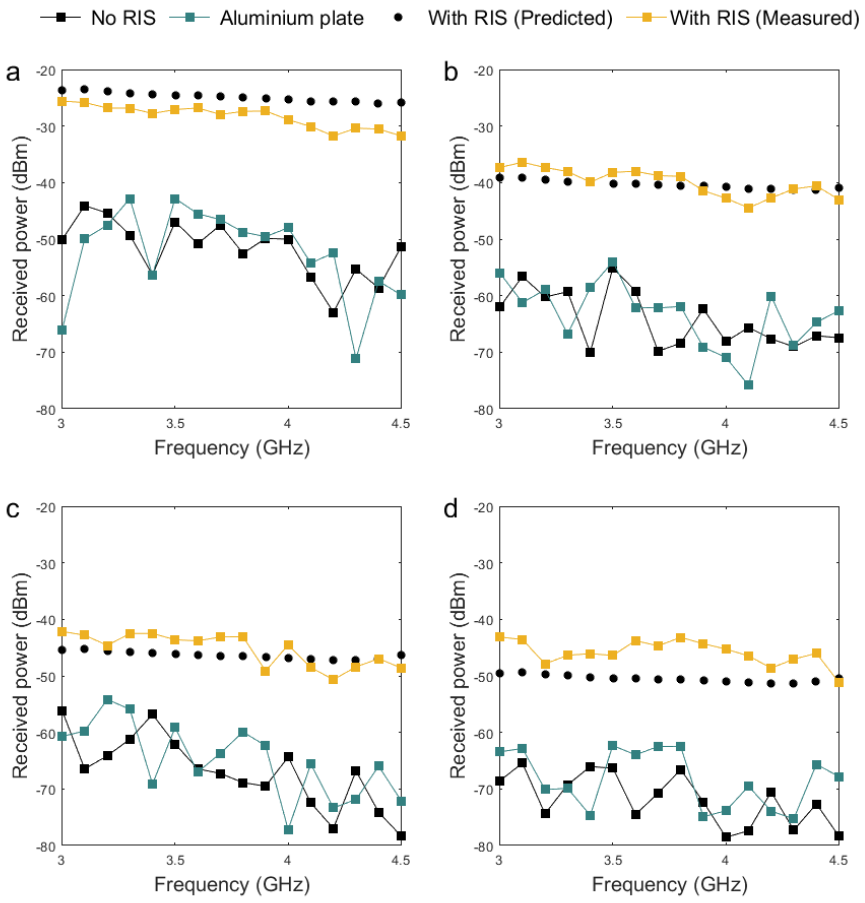

Figure 4.5: Envelope of the full set of curves from Fig. 4.4. Maximum received power in scenario II at positions 1 to 4 for steps of 100 MHz for the cases of no RIS, the aluminium reference plate, the path loss model of (4.1) for an optimised RIS, and measured optimised RIS. Received power improvement can clearly be achieved at intervals across the 1.5 GHz range.

In order to investigate the useful bandwidth of the RIS in this scenario, the experiment was repeated with the horn antenna at the receiver between 3 and 4.5 GHz at 100 MHz intervals. At each location, the RIS was optimised for a single frequency point, f_{opt}, followed by performing a sweep from 3 to 4.5 GHz at 20 MHz intervals and measuring the average received power for each interval. This was then repeated to obtain 16 frequency sweeps per location. The resulting received power versus frequency for $f_{opt} = 3.3$, 3.8, and 4.3 GHz, as well as for the aluminium plate, can be seen in Fig. 4.4. The 3 dB bandwidths for each case are highlighted by grey bars. Referring to Fig. 4.4, the aluminium plate case can be seen to be highly frequency-selective, as can be expected for a NLoS scenario. This selectivity can be eliminated over finite regions of the band when the RIS is optimised at the carrier frequency of interest.

The resulting maximum power improvement for each f_{opt} have been plotted in Fig. 4.5, where the aluminium plate case and the case of no RIS have been plotted for comparison, as well as the predicted Rx power from (4.1). It can be seen that the introduction of the RIS offers selective improvement across the entire 40% bandwidth of the investigation, with each configuration offering between 105 and 240 MHz instantaneous 3dB-bandwidth. Equation (4.1), subject to algorithm 1, can be seen to offer an excellent prediction of the maximum achievable power in this scenario for the cases of positions 1 to 3.

4.4.4 Scenario III - Floor to floor

Table 4.3: RIS Reflection Behaviour and Received Power Improvement for Scenario III

State			Resolution		
Config	$\lvert\Gamma\rvert$	$\angle\Gamma$	1-Bit	2-Bit	3-Bit
011	-0.77 dB	$-180°$			
111	-0.50 dB	$-174.1°$			
110	-1.60 dB	$-133.8°$			
101	-1.43 dB	$-92.9°$			
010	-2.91 dB	$-59.2°$			
001	-3.05 dB	$1.4°$			
100	-0.11 dB	$43.9°$			
000	-0.72 dB	$122.2°$			
Rx Power Improvement (dB)			18.48	20.45	21.13

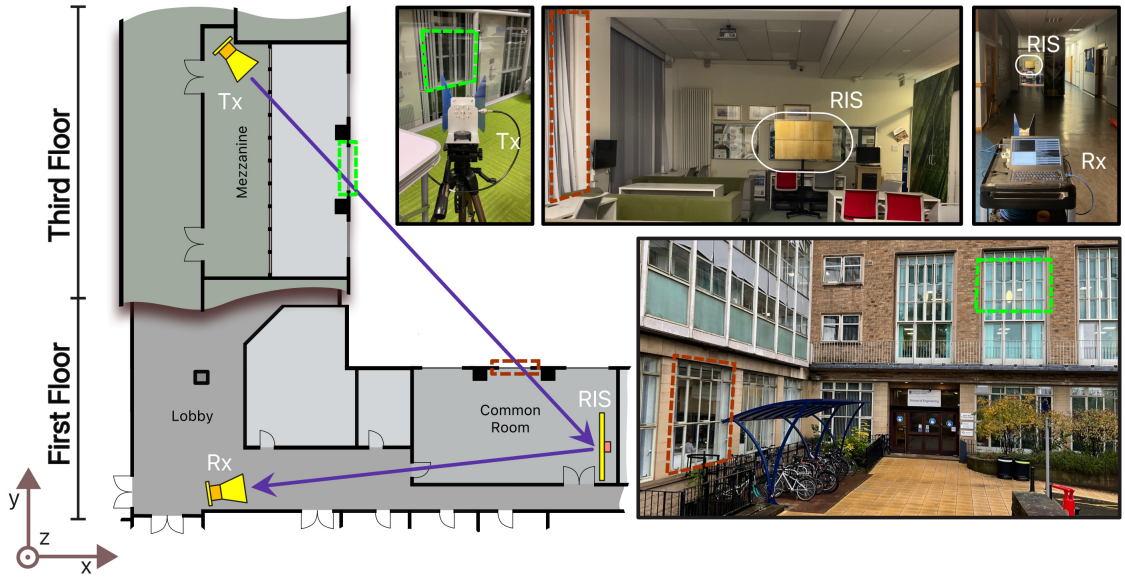

Figure 4.6: Experiment setup for scenario III. The RIS is placed in the common room of scenario I, serving a Rx placed in the lobby. A transmitter is located two floors above, on a mezzanine with a direct path to the RIS via the two windows highlighted bottom-right. The receiver (Rx) is considered point (0, 0, 0), with the transmitter (Tx) and RIS located at (20, 20, 10) and (20, 2, 0), respectively.

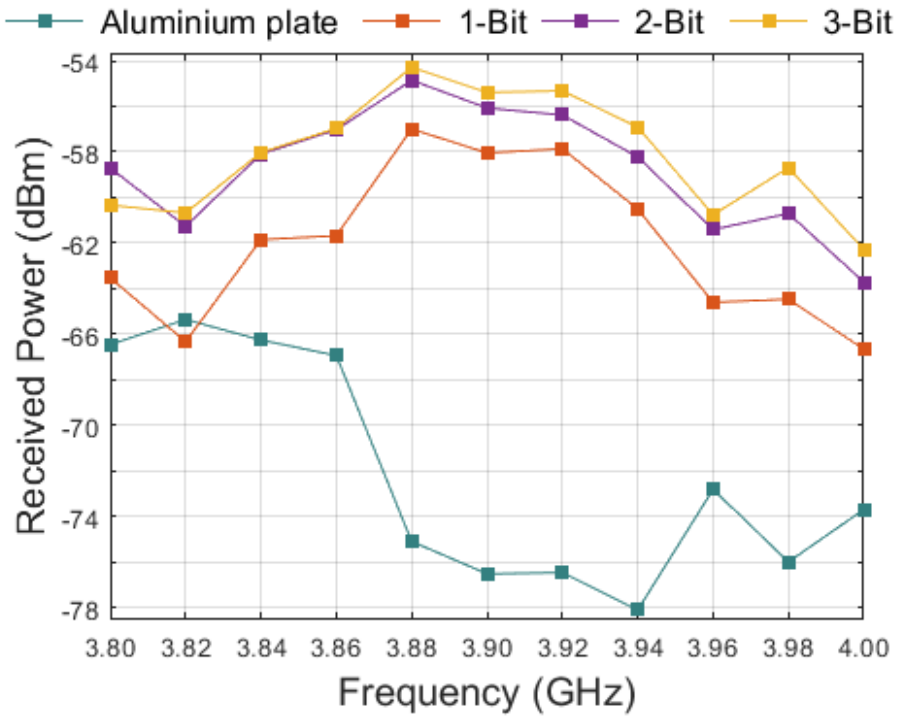

Figure 4.7: Received power versus frequency in scenario III after optimisation at 3.9 GHz. Received power for phase resolution settings of 1-bit, 2-bit, and 3-bit are plotted along with the reference aluminium plate for comparison.

Due to the column-connected architecture of the RIS design introduced here, wave transformation capability in elevation is limited when compared to designs where unit cells are individually addressable. This does not pose a significant problem in scenarios where both the electrical distance of antennas from the RIS is such that plane wave incidence can be approximated and when the antennas are located in the same horizontal plane as the RIS. For indoor communication scenarios, the latter case is quite likely to occur when user equipment is located on the same floor. In order to ascertain whether this RIS architecture can offer coverage improvement when the latter criteria is not met, a multi-floor experiment was devised and is depicted in Fig. 4.6.

The receiver was placed in the first floor lobby from scenario 1, whilst the RIS was placed in the common room with a LoS link to the Rx horn antenna. The transmitter antenna was placed on a mezzanine two floors above, where a wireless link was formed via two windows, highlighted by dashed rectangles. In order to avoid interference with a nearby small cell operating at 3.75 GHz, the carrier frequency was set to 3.9 GHz and a frequency sweep was performed over a 200 MHz bandwidth.

So as to demonstrate the benefit of the high phase resolution of this RIS design, measurements were performed for 1-bit, 2-bit, and 3-bit cases. The digital states available to the optimisation algorithm in each case are listed in table 4.3. The resulting received power has been plotted in Fig. 4.7, where it can be seen that a 21.13 dB improvement over the aluminium plate case was possible in this scenario with the 3-bit phase resolution. When limiting the phase resolution to 2-bit and 1-bit, the optimised received power reduces by 0.68 dB and 2.65 dB, respectively. According to [83], the average directivity reduction for a large reflectarray subject to plane wave excitation compared to a 3-bit design is approximately 0.67 dB and 3.66 dB for 2-bit and 1-bit designs, respectively. However, this approximation does not take into account phase-dependent magnitude and instead assumes an ideal unity reflection magnitude. The combination of phase-dependent magnitude and limited phase range of this design compared to an ideal 3-bit case may explain the 1 dB difference between the measured directivity reduction in the 1-bit case to its theoretical value.

4.5 Discussion

In order to contrast the findings of this work with previous observations, the information in Table 4.4 has been compiled. It is difficult to draw direct comparisons with similar realistic RIS field trial works due to the large variations in operating environments, RIS dimensions, and control degrees of freedom. As can be seen on the right-hand column of Table 4.4, a common trend is the promising signal strength enhancement in each case. These signal strength metrics are usually given with a reference case, as has been employed in this work, and the resulting difference between the reference and optimised RIS measurements can vary profusely. This is particularly the case when the receiver is in close proximity to the RIS as in the indoor scenario

Table 4.4: Comparison of RIS Field Trial Works at Sub-6 GHz

Ref.	**Phase resolution**	**Tuning mechanism**	**Dimensions No. elements (Cols x Rows)**	**Frequency**	**Investigated bandwidth**	**Scenarios**	**Effects on channel response**
[64]	1-bit	Varactor diodes	0.80 m $\times$ 0.31 m ($15.5\lambda \times 6\lambda$) 1100 elements ($55 \times 20$)	5.8 GHz	500 MHz	Indoor NLoS, Outdoor rooftops at 50 and 500 m.	27 dB and 14 dB received power improvement for 50 m and 500 m outdoor links, respectively. 26 dB channel gain enhancement indoors via a thick concrete wall.
[105]	1-bit	PIN diodes	0.41 m $\times$ 0.26 m ($7.9\lambda \times 5\lambda$) 160 elements (16 x 10)	5.8 GHz	150 MHz	Outdoor NLoS via large occlusion.	6 dB average SNR improvement throughout coverage blind spot.
[104]	1-bit	RF switches	2.45 m $\times$ 2.45 m ($19.6\lambda \times 19.6\lambda$) 3200 elements (64 x 50)	2.4 GHz	38 MHz	Indoor office environment with mixed LoS/NLoS	Median 9.8 dB signal level improvement and doubling of channel capacity.
[159]	1-bit	PIN diodes	- 512 elements (16 x 32)	2.64 GHz	160 MHz	Indoor NLoS at a corridor junction.	10 dB signal level improvement compared to reference of RIS with random configuration. Demonstrated 10 Mbps throughput increase.
[106]	Continuous	Varactor diodes	1.14 m $\times$ 1.16 m ($13.3\lambda \times 13.5\lambda$) 2430 elements (30 x 81)	3.5 GHz	-	Indoor NLoS. Room to room wireless link.	15 dB received signal strength enhancement versus RIS unconfigured.
This work	3-bit	PIN diodes	1.02 m $\times$ 0.72 m ($12.8\lambda \times 9\lambda$) 2304 elements (48 x 48)	3.75 GHz	1.5 GHz	Indoor mixed LoS/NLoS. Corridor junctions and multiple floors.	Average 16 dB received signal strength enhancement over entire 1.5 GHz bandwidth in corridor junction. Up to 40 dB signal level improvement in deep fading. Multi-floor signal strength enhancement above 20 dB.

in [64].

Performance of RISs beyond a narrow bandwidth is not widely documented. In comparison to the 1-bit cases in previous works, it was possible in this work to achieve notable channel improvement well beyond the proximity of the design frequency due to the dispersive nature of the many RIS states. For example, on observing the measured global reflection response depicted in Fig. 3.2, if only two states were available, it can be seen that no two states can be selected that would provide a 1-bit response across the 1.5 GHz bandwidth. For example, if one were limited to the 001 and 011 states shown in Fig. 3.2, one could achieve a 1-bit response at 3.75 GHz. However, the global reflection behaviour would degenerate into less than 50 degrees relative phase difference at 3.25 GHz and 4.25 GHz, resulting in the RIS having a much more limited effect on the channel. However, the introduction of additional states in this multi-bit RIS enables at the very least a 1-bit response for the entire band and is capable of a 2-bit response between 3.2 and 4.1 GHz. It would be possible to extend this favorable reflection behaviour across a wider bandwidth by optimising the metasurface geometry for a flat equivalent bit number as opposed to the maximum value opted for at 3.75 GHz. Such modifications may not have notably affected scenario 3, where it can be seen that only a 0.68 dB improvement is offered for the 3-bit case over the 2-bit.

In each scenario here, the RIS is positioned where it might reasonably be installed. In reality, one could see the deployment of these devices with little noticeable change to the observable environment, such as on the facades of buildings and embedded within walls and ceilings. This is in contrast to the corridor scenario in [159] where the RIS presents a clear obstruction to personnel and the indoor through-wall scenario in [64] where the RIS was placed in the middle of a room. To ensure a realistic look at RIS capabilities, in this investigation the RIS was positioned to always be parallel to the interior walls of the building. Amongst the deep fading measured at location 1 in the corridor junction scenario, as much as 40 dB received signal strength improvement was observed. This is in league with the 26 dB channel gain enhancement observed by Pei et al. [64] in their indoor measurements with the RIS and transmitter completely isolated by a 30cm-thick concrete wall, and a receiver horn antenna at a similar number of wavelengths from location 1. In comparison to the work by Araghi et al. [106] employing their continuously-tunable RIS of a marginally larger dimension relative to the wavelength, a similar received signal power improvement was witnessed in an indoor corridor scenario with a RIS of smaller size. However, continuously tunable metasurfaces are much more complex, especially for local control, requiring a digital to analog converter channel for each element or grouping of elements. Our investigation has shown that similar channel enhancement could be achieved whilst utilising digital circuitry in combination with a monoplanar (i.e., VIAless) metasurface. This reduces the implementation and fabrication complexity whilst maintaining a desirably high phase resolution.

In the multi-floor experiment, the phase resolution versus channel improvement via the

multi-bit RIS has been explored. There is notable improvement as the resolution is increased beyond 1-bit, but this is a comparison of the same device with varying degrees of freedom. Therefore, these results should be carefully interpreted. A 1-bit RIS only requires a phase range of 180°, as opposed to 2- and 3-bit RISs requiring phase ranges of 270° and 315°, respectively. To achieve a higher resolution, a deeper resonance is required in order to provide a greater phase difference between the upper and lower phase limits of the local reflection responses. This inevitably results in higher losses due to the increased local electric field strength associated with a strong resonant response [84]. For example, the 1-bit monoplanar unit cell design recently introduced by Trichopoulos et al. [105] exhibited a 1 dB average reflection loss at the centre frequency as opposed to the 1.8 dB average reflection loss in the two states utilised for scenario 3 in our work. A slightly higher achievable power level could be expected with a RIS specifically designed to operate with a 1-bit phase resolution for a similar RIS size and degree of local control.

As has been demonstrated in the diverse indoor settings explored here, RISs have the capability to mitigate the coverage holes plaguing existing mobile networks without introducing more radiation into the congested sub-6 GHz wireless spectrum. All power gains observed in this work arose purely from the optimal biasing of a number of PIN diodes with a DC voltage. Of particular interest to mobile operators may be the multi-floor experiment, which exhibits similarities with an outdoor-to-indoor coverage enhancement scenario common to urban environments. Combining scenarios 1 and 3, with multiple RISs, an operator could reach users in the lobby area, deeper inside the building, and maintain higher quality of service due to the 100-fold received signal strength improvement observed in scenario 3. Alternatively, transmit power at the base station could be reduced proportionally, resulting in operating cost reductions and reduced inter-cell interference. Any power consumption reduction prediction, however, must take into account the additional overhead incurred throughout the optimisation process, such as during computation and maintaining a control link, as well as any power consumed by the RIS.

The minimum observed instantaneous bandwidth in the corridor junction and multi-floor scenarios was above 100 MHz, encompassing all channel bandwidth settings of widely deployed 5G systems at mid-band [160]. From this investigation it can be seen that a single RIS architecture engineered to exhibit a wide operational bandwidth could potentially serve the entire 5G N77 3.3 - 4.2 GHz band.

4.6 Summary

This chapter presented indoor field trials using a 3-bit azimuthal-steering RIS. The wealth of literature on RIS channel models and optimisation algorithms should be complimented by rigorous field trials in realistic communication scenarios. The high phase resolution reconfigurable metasurface introduced and employed in this chapter shows significant NLoS channel improve-

ment over and beyond the 3.4 to 3.8 GHz 5G commercial services band. Indoor received power improvement of up to 40 dB with an instantaneous bandwidth of at least 100 MHz has been realised, easily meeting the demands of network providers for time-division duplexing operation at sub-6 GHz. The benefits of increased phase resolution have been demonstrated in a multiple-floor channel improvement experiment, where nearly double the power is received for the same RIS surface area by inclusion of additional reflection phase states. The RIS design explored here demonstrates that one does not necessarily require individually addressable unit cells to greatly benefit from this technology. Future works might explore more complex groupings of unit cells than a column-connected approach in order to further reduce the control network complexity, potentially rendering large RISs feasible in practice.

Chapter 5

RIS-enhanced MIMO channels in urban environments

5.1 Introduction

The work presented here contains a set of measurements conducted within a real-world MIMO communication setup enhanced by a RIS. A RIS beam search algorithm is introduced and its efficacy demonstrated over a 4×4 MIMO channel in an outdoor urban environment. Ascertaining the impact of RISs on currently deployed wireless communication systems may shed a light on the potential implications of their inclusion in contemporary networks that may not necessarily surface in theoretical analysis [161]. Thus far, outdoor RIS-aided multi-antenna communication systems have not been explored in measurement campaigns. The measurements detailed here aim to extract important information about the RIS-aided MIMO channel that can be used to contrast system performance. The key performance indicators of interest are the network capacity as a function of the extract channel matrices. This is subject to the parameters of the RIS position, orientation, and programmed configurations. Similarly to the field trials of Chapter 4, the control case is the channel with the RIS replaced with an electrically-conducting plate of similar dimensions.

5.2 Reconfigurable intelligent surface testbed

5.2.1 Hardware

The RIS employed for these measurements is the varactor-based dual-polarised 1-bit low power RIS introduced in section 3.3, shown in Fig. 5.1. The RIS consists of 1024 elements in a 32 by 32 arrangement and is designed to operate within the 3.2 to 3.8 GHz 5G band. The elements are individually addressable in both polarisations, with a total of 2048 digitally-tuned varactors. The lateral dimensions are 0.96 m by 0.96 m ($11\lambda_0 \times 11\lambda_0$). The tunable elements and bias

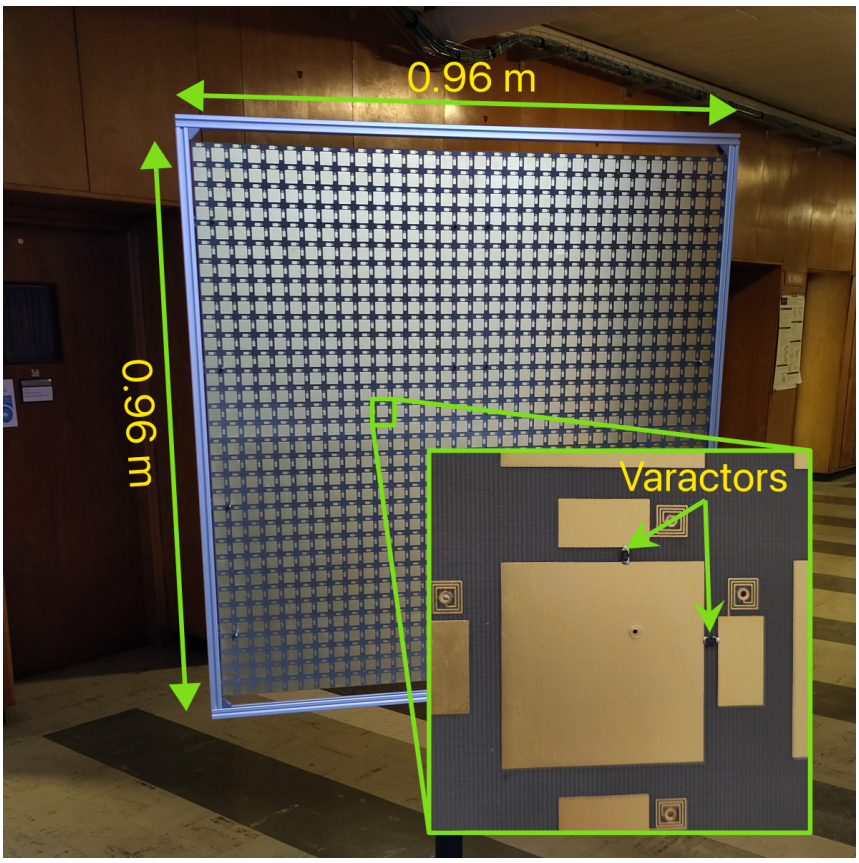

Figure 5.1: The RIS testbed employed in the measurements. Consists of 4 tiles with an arrangement of 16 $\times$ 16 unit cells each. Two varactor diodes are addressable on each unit cell, with two programmable bias voltage levels available to each diode.

circuitry consume approximately 10 mW in their configured state, and the testbed is powered by a portable battery bank. The RIS is controlled wirelessly through a WiFi link to a Raspberry Pi single-board computer.

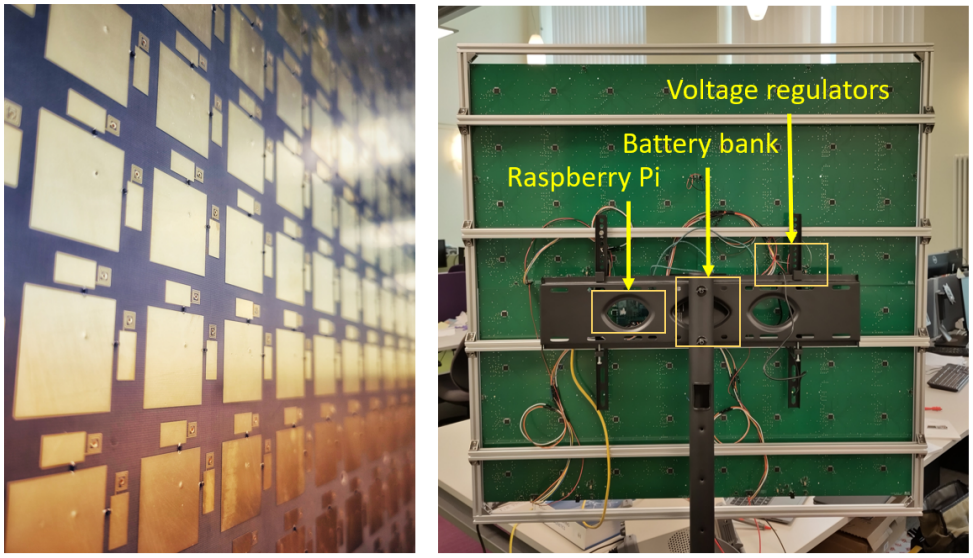

Figure 5.2: Photographs of the front (left) and back (right) of the constructed 32×32 element RIS prototype.

5.2.2 Beamsteering performance

The far-field to far-field beamsteering performance for a single 0.48 m $\times$ 0.48 m RIS tile was ascertained for several configurations and incidence angles. The configurations were selected based on the general macroscopic model for RIS behaviour introduced by Degli-Esposti et al. [23]. Beam pattern measurements for 120° incidence in azimuth (with 90° being broadside to the RIS) are plotted in Fig. 5.3(a) and (b) for vertical and horizontal antenna polarisation, respectively. It can be seen that the forward model provides a relatively reliable approximation for the performance of the main lobe in each configuration, although up to a 2 dB magnitude reduction can be noted for some of the non-specular configurations. In this work, we utilise this forward model within a PSO-based beam search algorithm to determine any performance benefits within a MIMO communication system.

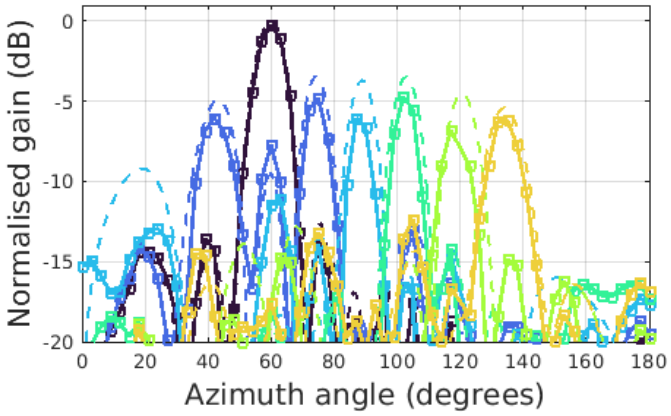

(a) Vertical polarisation

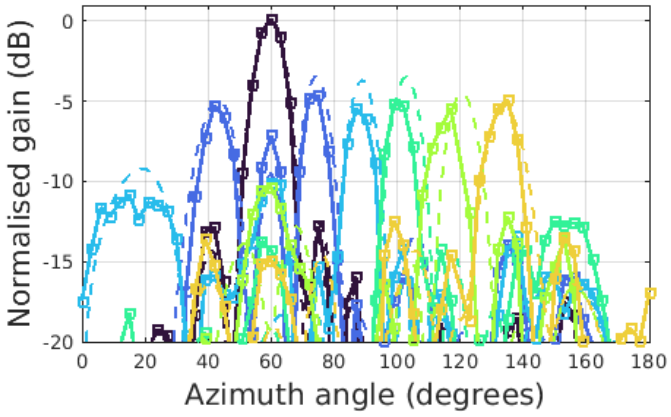

(b) Horizontal polarisation

Figure 5.3: Measured (square curve) normalised gain patterns for 120° far-field incidence on a single 16 $\times$ 16 RIS tile for vertical (a) and horizontal (b) antenna polarisations at 3.5 GHz. Showing beam patterns for maximum power between 45° and 135° in 15° steps. Dashed curves are the approximate gain patterns using equation (3.14).

5.3 Beam search algorithm

During initial access by UE in 5G NR networks, beam searching is typically performed. The 5G base station, or gNodeB (gNB) [162], performs a beam sweep and the user reports its preferred beam which is then set by the gNB. Protocols are in place for continued beam reporting and switching according to the varying channel conditions. Inspired by this simple approach to beam selection, we aim here to determine the utility of a beam search algorithm facilitated by the RIS. When there's an obstruction between the transmitter and receiver, a properly positioned RIS can create a VLoS channel. In cases of significant blockage, this VLoS channel becomes the dominant propagation mechanism, potentially allowing us to use the same model for generating beam patterns such as those in Fig. 5.3 for link enhancement. Assuming we know the position of the transmitter, we limit the unknown parameters to the spherical coordinates of the receiver position, r_{rx}, θ_{rx}, ϕ_{rx}. Additionally, a fourth parameter is introduced which relates to a 180° phase shift in the main lobe between two similar configurations, facilitated by the radiation pattern invariance property [163]. This effectively amounts to flipping all of the bits of a given configuration with the aim of facilitating constructive interference of a single in the VLoS path with additional significant NLoS components. Compared to the iterative approach to RIS configuration that was successfully employed in chapter 4, the global optimisation approach used in these long range field trials is more resilient to harsher propagation conditions. It is relatively straight-forward to detect the perturbations in the channel response with a small change in RIS configuration (such as flipping the bits on a column) at short distances with a highly-directional antenna. At longer distances, however, these changes could easily be shrouded by noise and interference. By varying the RIS configurations across the entire surface, we can expect a larger, more easily detectable perturbation on the channel that is less affected by contamination compared to the iterative, column-wise approach of the indoor field trials of chapter 4.

Here the iterative approach successfully employed in chapter 4 is compared to a PSO-based beamforming algorithm for its performance in the presence of noise. We consider the iterative approach in the context of the 1-bit RIS for a single-polarisation case. The algorithm is summarised in Alg. 2.

Algorithm 2 Maximise Rx signal power

Input: Average received signal power, P_r, in

Output: RIS configuration, Γ, out

for n = 1 to N **do**
  for m = 1 to M **do**
    for k = [1, 2] **do**
      $\Gamma_{n,m} \leftarrow \rho_k e^{j\phi_k}$;
      $s_k = P_r$;
    end for
    $q \leftarrow$ index of maximum of s;
    $\Gamma_{n,m} \leftarrow \rho_q e^{j\phi_q}$;
  end for
end for
return configuration matrix Γ

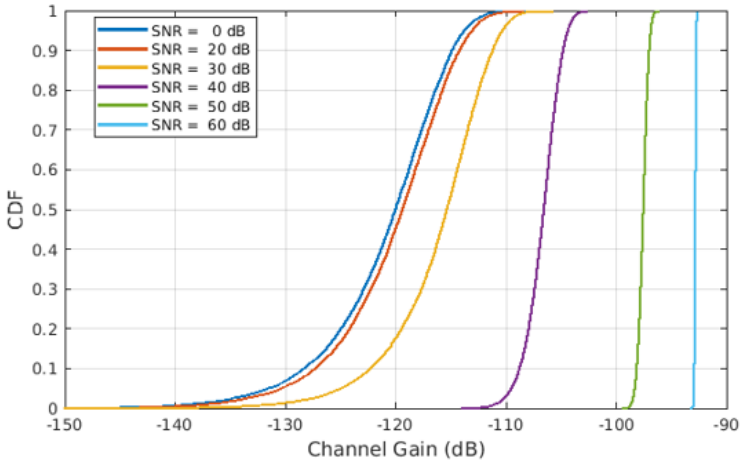

Figure 5.4: CDF of channel gain using the iterative approach for various SNR values.

For high SNR, the small changes in the channel between two quite similar configurations can readily be detected. The curves in Fig. 5.4 show the CDF versus channel gain for a transmitter-RIS-receiver link with the transmitter at (20, 20, 175) and receiver at (-20, -1, 20) relative to the RIS exisiting in the xy-plane for the iterative approach. The RIS is defined as being an arrangement of 1024 1-bit unit cells equally spaced over a 0.96 m $\times$ 0.96 m area. Alg. 2 was run 10^4 times at several values of SNR. It can be seen that the achievable channel gain is highly dependent on the SNR during optimisation. An SNR as high as 60 dB is required for consistent channel gain improvement, where a mean channel gain of -92.9 dB is witnessed. A channel gain value of more than -93.1 dB is achieved 99% of the time. However, a reduction in SNR to a typically-favorable 40 dB deteriorates the mean channel gain by 13.8 dB.

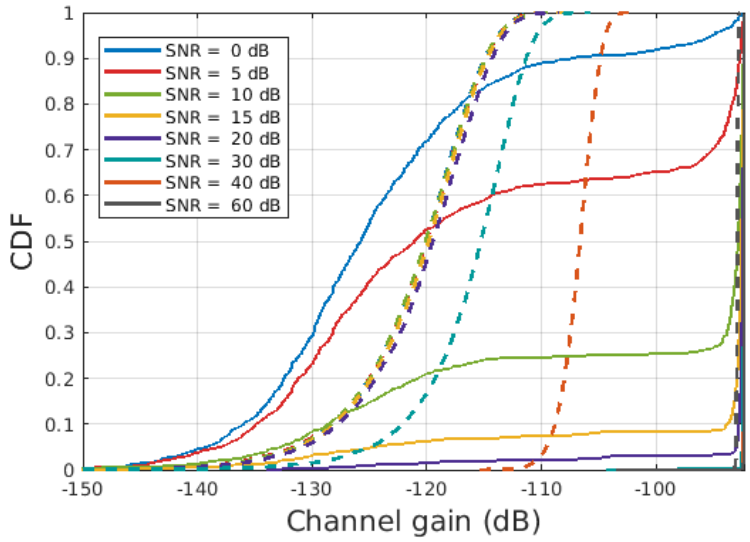

(a)

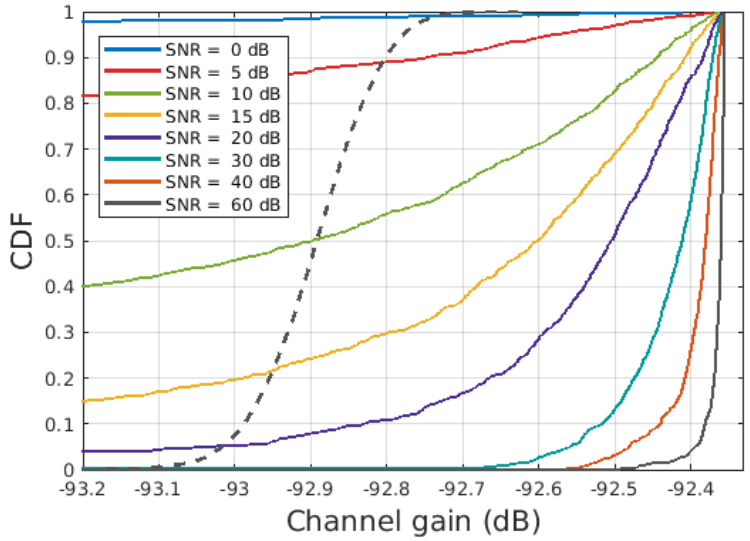

(b)

Figure 5.5: CDF of channel gain using the iterative approach (dashed curves) and PSO-based beam search approach (solid curves) for various SNR values. Zoomed-in plot in (b) highlights the high-SNR behaviour of the PSO-based approach.

For the aforementioned PSO-based beam search algorithm, the CDFs have been plotted as the solid curves in Fig. 5.5. It can be seen that the PSO-based approach is much more resilient to the presence of noise during optimisation. For example, an SNR of 30 dB results in an average channel gain of -92.4 dB, which is within 0.1 dB of that achieved with an SNR of 60 dB, and is within 0.2 dB of the mean value 99% of the time. At SNRs below 20 dB, there is a reasonably high chance ($> 5\%$) that the PSO-based approach will perform worse than the iterative approach. Nevertheless, the PSO-based beam search was deemed as a promising candidate for employment within the long-distance scenario considered in this chapter.

5.4 Experiment setup

5.4.1 Measurement scenario

The scenario under investigation here is within one of British Telecom's research campuses, Adastral Park, situated in the east of England. The base station (transmitter) antenna array position, the RIS, and the receiver array positions are depicted in Fig. 5.6. Two measurement zones, labeled A and B, were selected as they contain occlusions from surrounding buildings between the transmitter and receiver antennas. Additionally, these locations contain areas with a strong line of sight to the transmitter, making them suitable for the placement of a RIS. The distances between the RIS and the transmitter antenna at zones A and B are 175 m and 130 m, respectively. Diagrams of zones A and B are plotted in Fig. 5.7(a) and (b), respectively.

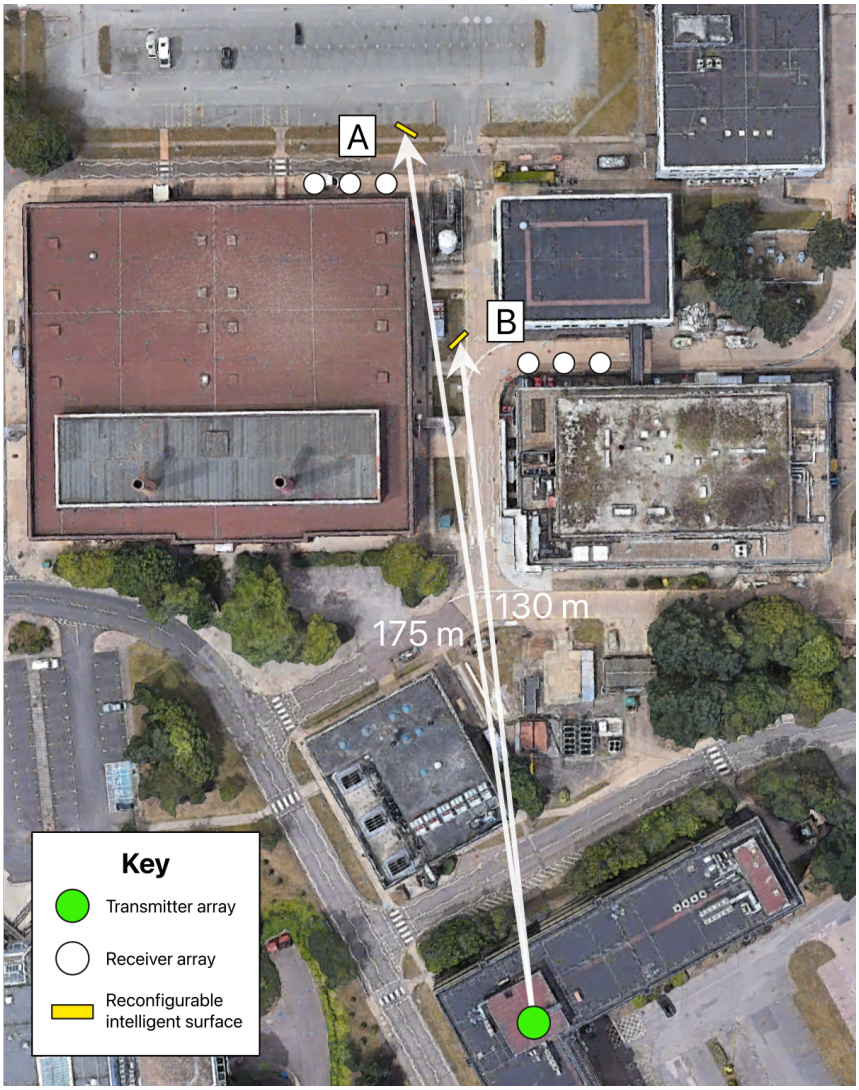

Figure 5.6: Experiment setup at Adastral Park, Ipswich, UK. A rooftop base station antenna is directed northwards towards a RIS and receivers placed at street level. The two measurement locations are denoted A and B.

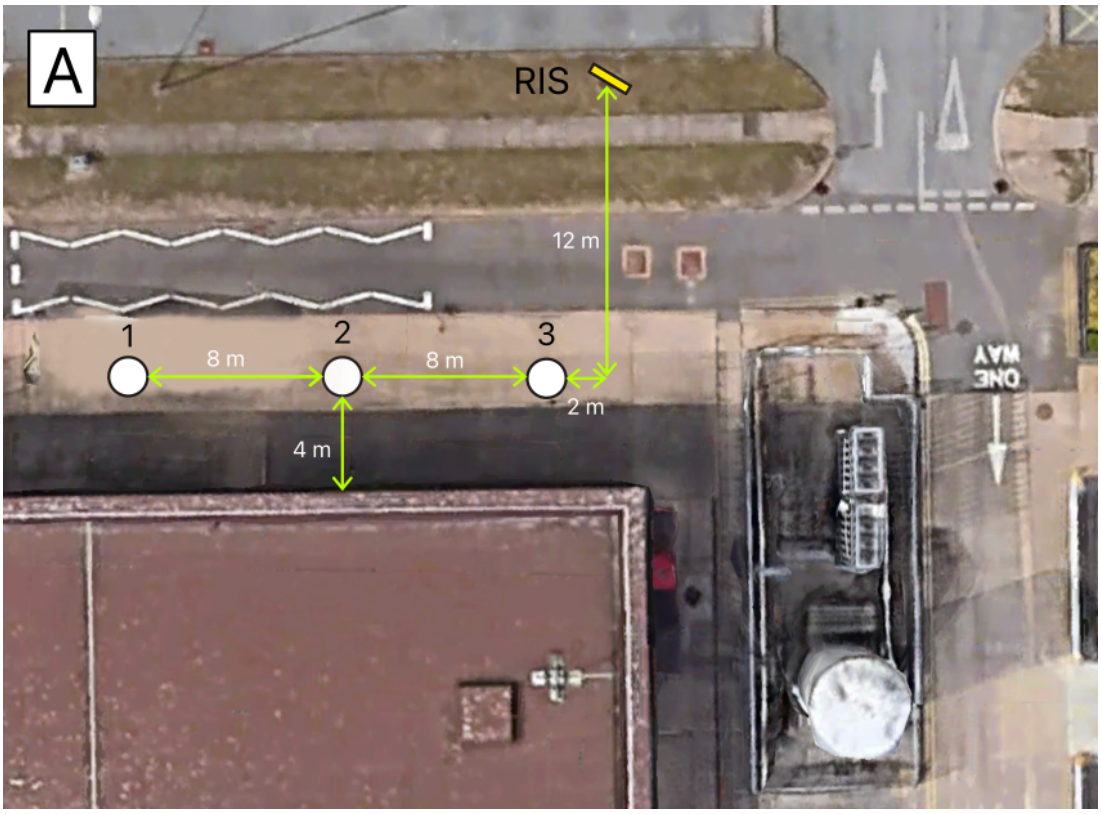

(a) Zone A

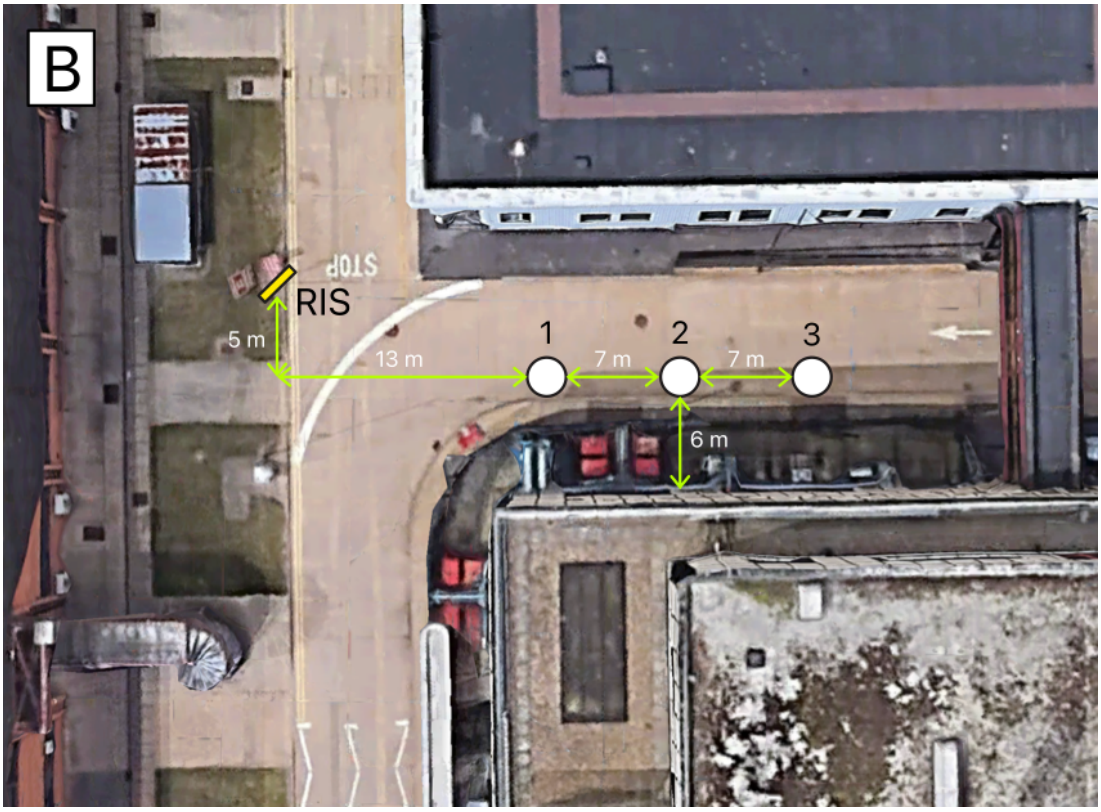

(b) Zone B

Figure 5.7: Measurement zones A and B each showing the RIS position and 3 receiver locations.

Transmitter array

The transmitter antenna is a Commscope RRZZHHTTS4-65B-R7 multiband sector antenna situated on a rooftop, at a height of approximately 25 m from ground level. This antenna ordinarily serves as part of a macrocell for the site. The 8T8R 3300-3800 MHz section of the antenna consists of 4 columns of $\pm 45^\circ$ polarised antenna elements. Each vertical array is driven by two ports, with each corresponding to the respective polarisations, for a total of 8 input ports. In this work, we have utilised the center 4 ports of the array, corresponding to two sets of $\pm 45^\circ$ polarised array columns. Each array column provides a 16 dBi gain with beamwidths of 89° and 6.5° in azimuth and elevation, respectively. The antenna is mechanically and electrically tilted such that the main lobe points toward 0° in elevation.

Figure 5.8: Sector antenna used in the measurements. The antenna points north, with 90° and 6.5° beamwidths in azimuth and elevation, respectively.

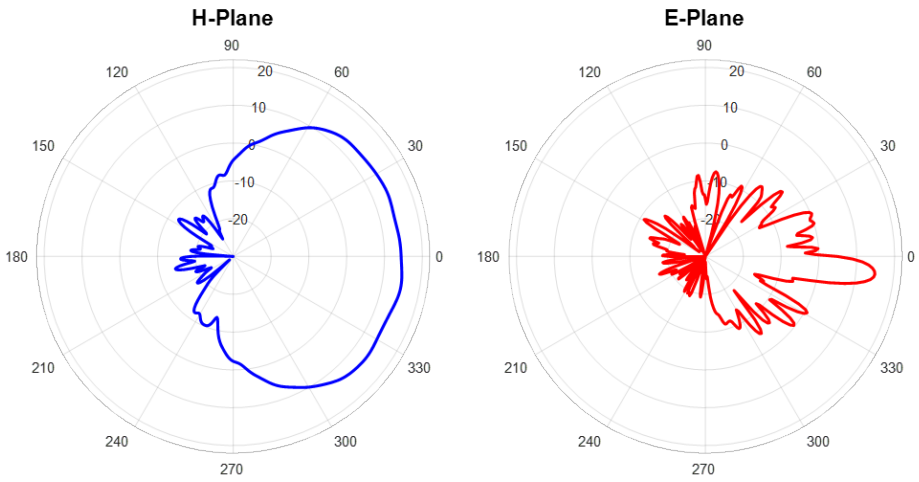

Figure 5.9: Polar far-field radiation pattern cuts for port 20 of the Commscope RRZZHHTTS4-65B-R7 sector antenna with 2° tilt at 3.5 GHz.

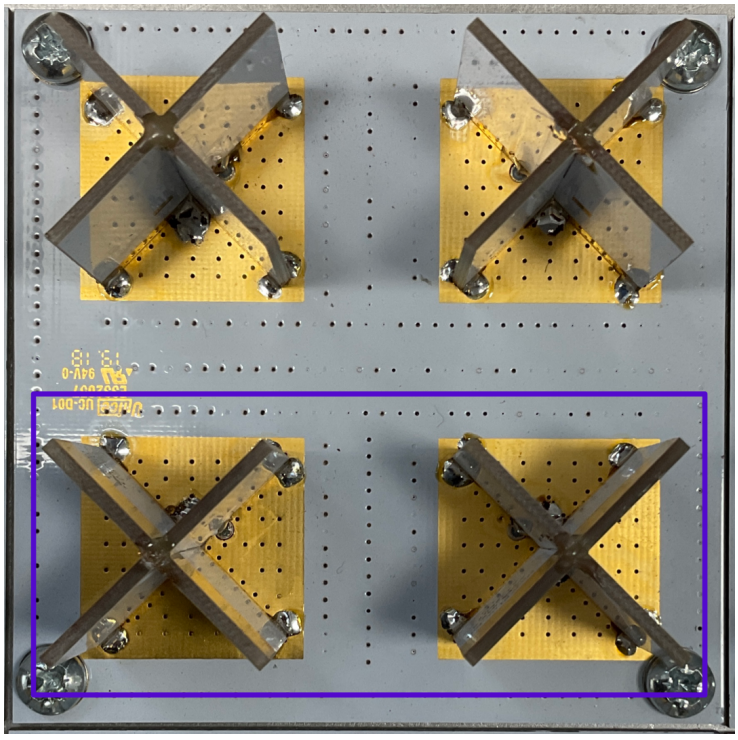

Figure 5.10: Broadband dipole elements used for the receiver. Highlighted elements are addressed while remaining elements are terminated in matched loads.

Receiver array

A notable trend in currently published field trials in the filtering out of potentially beneficial multipath components through use of highly directional antennas at the end nodes. This does not provide a fair reflection of the performance of mobile networks at sub-6 GHz, where handsets typically employ electrically small antennas that are omnidirectional in nature. Instead, it

sets the baseline performance unrealistically low, making the introduction of the RIS appear to significantly benefit the network more than it would in a real-world implementation. For a more realistic analysis, the receiver antenna employed here is a 4-element ground-backed crossed-dipole array. This was selected as a balance between ascertaining realistic channel measurements and minimising perturbations by measurement equipment and personnel in proximity to the antenna.

5.4.2 Performance prediction

Electrically large EM environments can be adequately modeled by the method of ray tracing. By employing a geometrical optics (GO)-based analysis to propagation scenarios in which multiple interacting objects are present, we can greatly reduce the computational complexity compared to full-wave EM solvers. In this chapter, we employ a ray tracing software package called Wireless Insite to predict the performance of RIS-aided communication systems in a large urban environment.

5.4.3 Environment modeling

The building geometries from the site in Fig. 5.6 have been extracted from OpenStreetMap (OSM) data [164]. These geometrical features are shown in Fig. 5.11.

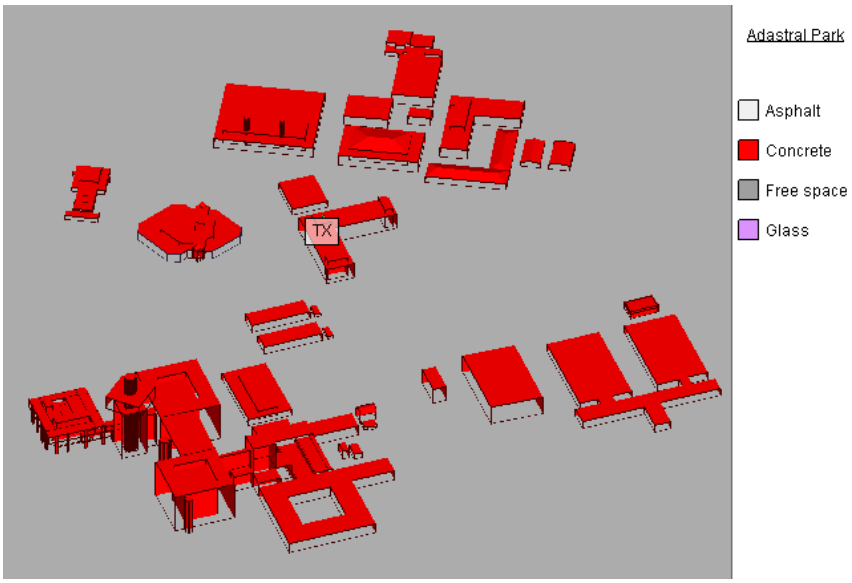

Figure 5.11: Building geometry and terrain imported into Wireless Insite. TX indicates the base station position. Buildings are predominantly modeled as concrete, with some glass features where large windows are present.

In this simplified model, the ground is considered to be entirely asphalt, and the buildings are predominantly concrete, with the addition of glass for more modern buildings composed

of large glass facades. We have access to the north-facing antenna array, and therefore we are interested in the northern-most structures, as these are the dominant interacting objects (IOs).

5.4.4 Antenna modeling

Base station antenna modeling

The transmitter antenna unit available for these field trials is the Commscope RRZZHHTTS4-65B-R7 sector antenna depicted in Fig. 5.12. The unit consists of 9 antenna arrays serving several bands covered by currently deployed mobile networks. We are interested in the antenna performance within the specified 3.3 - 3.8 GHz region. The array associated with this band consists of 4 columns of cross-polarised antennas, with each column providing a fan beam spanning 89° in azimuth and 6.5° in elevation, with a typical gain of 14.5 dBi. The far-field radiation pattern cuts at 3.5 GHz for the antenna driven from port 20 for a tilt setting of 6° are plotted in Fig. 5.9.

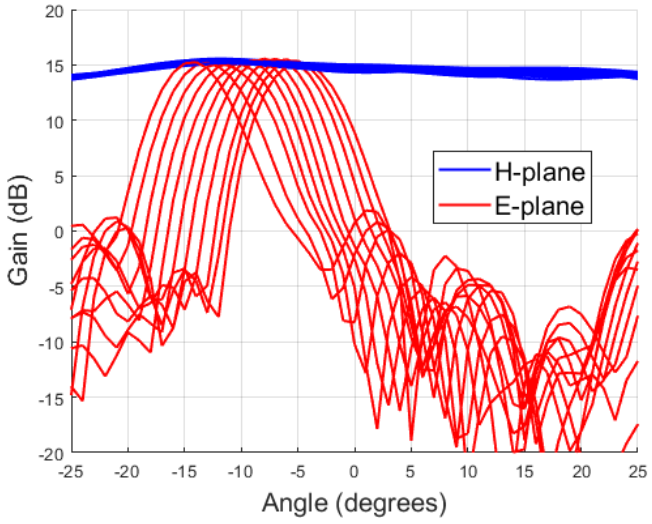

Figure 5.13: Far-field radiation pattern cuts for port 20 subject to beam tilt settings 2° to 12° with 1° steps.

(a)

(b)

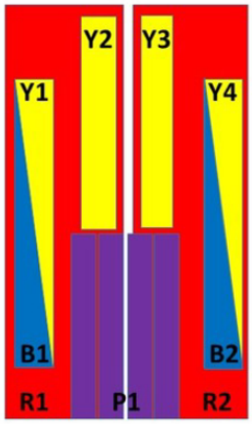

Array	Freq (MHz)	Conns	RET (SRET)	AISG RET UID
R1	694-960	1-2	1	CPxxxxxxxxxxxxxxxR1
R2	694-960	3-4	2	CPxxxxxxxxxxxxxxxR2
B1	1695-2180	5-6	3	CPxxxxxxxxxxxxxxxB1
B2	1695-2180	7-8		
Y1	2490-2690	9-10	4	CPxxxxxxxxxxxxxxxY1
Y4	2490-2690	15-16		
Y2	1427-2690	11-12	5	CPxxxxxxxxxxxxxxxY2
Y3	1427-2690	13-14	6	CPxxxxxxxxxxxxxxxY3
P1	3300-3800	17-24	7	CPxxxxxxxxxxxxxxxP1

(Sizes of colored boxes are not true depictions of array sizes)

(c)

Figure 5.12: Commscope RRZZHHTTS4-65B-R7 sector antenna. Front view (a) with reference axis. Port view (b) with the eight 3.3 - 3.8 GHz ports to the top-right. The port allocations from the datasheet are shown in (c), where array P1 is of interest in this work.

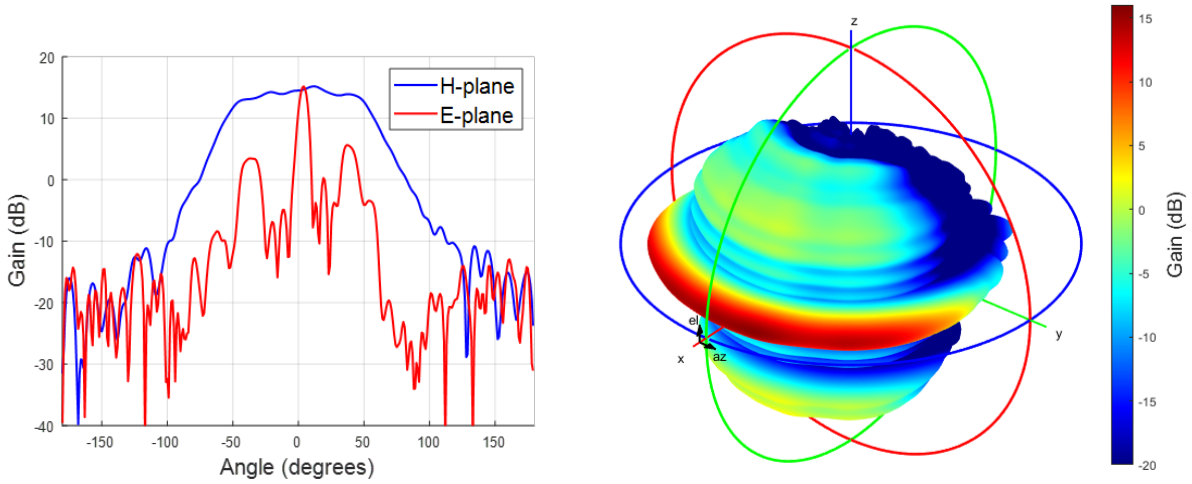

(a) (b)

Figure 5.14: Measured far-field cuts of the base station antenna, fed from port 20, used for reconstruction (a). Reconstructed 3D radiation patterns for the base station antenna (b).

A remote electrical tilt (RET) system controls the beam tilt associated with each array column. This enables variation in the beam tilt in elevation to be adjusted between 2° and 12°. The beam pattern cuts associated with the range of tilt settings are plotted in Fig. 5.13. It can be seen that the beam tilt at the frequency of interest appears to be 3° larger than specified, with the 2° beam setting resulting in a peak at −5° as opposed to −2°, etc.

Wireless Insite is compatible with an antenna pattern file format known as *user-defined antenna* (.uan). A 3D radiation pattern can be described by specifying the antenna gain in spherical coordinates. However, only 2D far-field cuts were available from the antenna manufacturer, and an approximation of the 3D pattern is relied upon for this work. Given an azimuthal radiation pattern cut coinciding with the main lobe in elevation, and the elevation cut between 0° and 180°, the predicted 3D radiation pattern has been ascertained by employing the MATLAB function *patternFromSlices()* employing the summing method. This function has its limitations in that the back-plane information from the elevation (E-plane) cut is discarded.

Handset antenna modeling

The user handsets are currently modeled as vertically-polarised dipole antennas and native functions in Wireless Insite are sufficient for our purposes. The receiver antennas used in the measurement campaign will differ, and these will be modelled using the manufacturer-provided radiation patterns in a similar fashion to the transmitter antenna array.

5.4.5 Baseline performance prediction

The scenario in Fig. 5.6 has been simulated to ascertain a reference for the wireless communication system performance. The resulting received power versus position is shown in Fig. 5.15. Region *A* has been highlighted, and the system performance within this region will be investigated here as a test case prior to further RIS placement within the model.

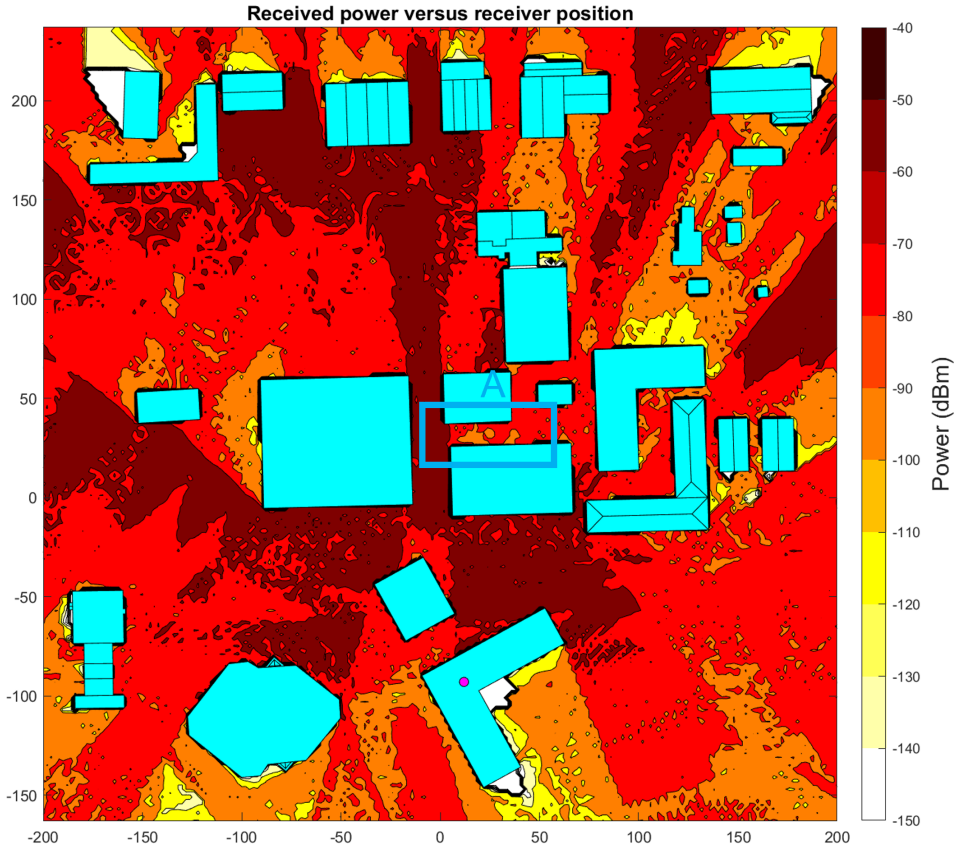

Figure 5.15: Received power versus position for the transmitter antenna positioned on Callisto house. System performance in highlighted area 'A' is explored as a test case for RIS deployment.

5.4.6 RIS modeling

The RIS behaviour within a ray tracing model has been recently explored by de Jong [117] and his model has been employed by Wireless Insite to simulate engineered electromagnetic surfaces (EESs). EESs within the software package are currently subject to the following constraints:

- The metasurface must be electrically large, rendering a high-frequency approximation valid.
- The metasurface must be adequately described by a modal surface impedance profile.

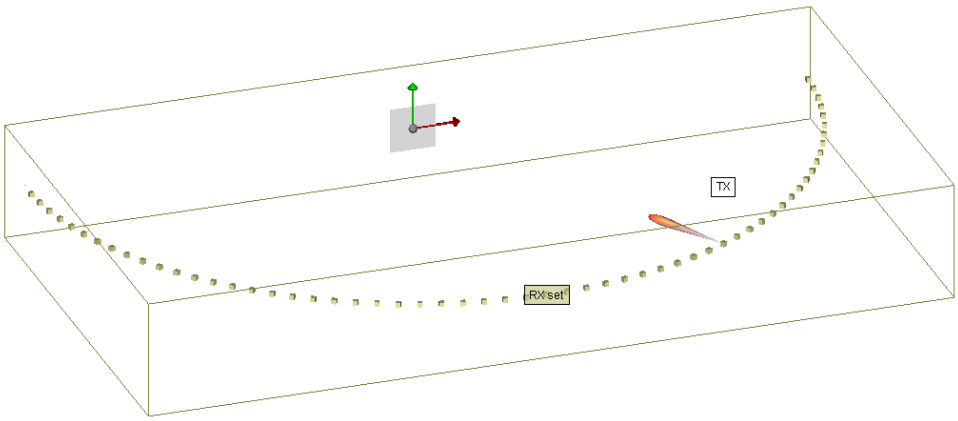

(a)

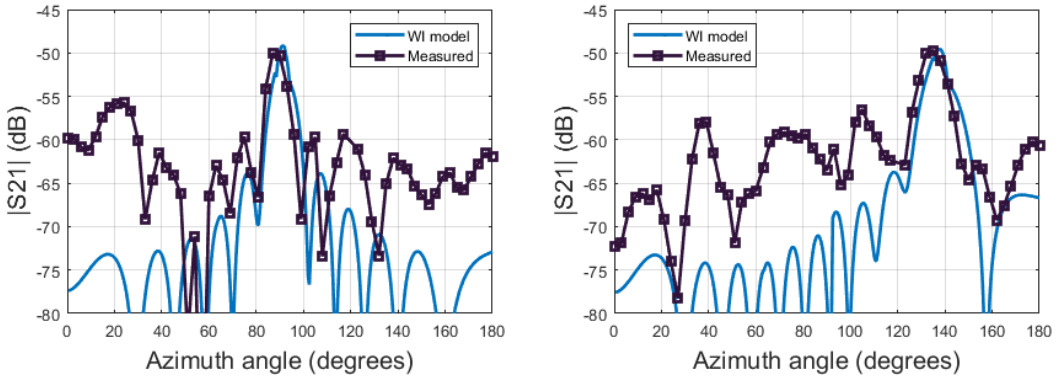

(b) (c)

Figure 5.16: Wireless insite simulation setup to ascertain the metasurface beam deflection patterns (a). Simulated received power (solid curves) for beam deflection towards 90° (b) and 135° (c), compared to the measured patterns from the 1-bit metasurface tile. The poorer sidelobe performance of the 1-bit metasurface compared to the continuous phase profile of the ideal simulated metasurface is clear. Importantly, however, the main beam behaviour is in close alignment.

- This surface impedance profile is a function of a smoothly varying phase parameter (i.e., a slowly varying periodicity).

The type of EES of interest here is the reflective diffuser described by modulating the phase gradient, for the azimuthal diffuser case, to [117]:

$$g_\psi = \left[\frac{\sin\phi_1 + \sin\phi_2}{2} + \frac{x}{X}(\sin\phi_1 - \sin\phi_2)\right]\hat{x} \tag{5.1}$$

where ϕ_1 and ϕ_2 define the range of deflection angles, x the horizontal coordinate, and X the metasurface width. The surface impedance profile employed here is determined by the reflection coefficient, which is a function of (5.1):

$$\Gamma(\psi) = \Gamma^{(1)} e^{jk\psi} \tag{5.2}$$

with $0 \leq \psi < \lambda$. The reflection coefficient corresponding to the first Floquet mode, $\Gamma^{(1)}$, determines the global reflection loss.

Work is still underway to find a means of simulating digital metasurfaces, such as the 1-bit design in chapter 3, within WI. The problem lies in the non-smooth nature of the 1-bit phase profile not being consistent with the smooth-varying requirement for the model to be valid.

As an illustrative example, the ray-tracing simulation setup with a 0.48 m $\times$ 0.48 m reflecting metasurface is shown in Fig. 5.16(a). The metasurface is modulated with the phase gradient given in equation (5.1), compensating for an incidence angle of 120°. Reflection magnitudes were determined that matched the received signal strength with the main lobes of the measured patterns from chapter 3. These have been plotted in Fig. 5.16(b) and (c) for the cases of deflection to 90° (i.e., normal to the surface) and 135°, respectively. While the side-lobe performance is clearly not accurate for this model, due to the continuous phase profile, the main lobe behaviour closely resembles that of the measured 1-bit patterns. Therefore, the EES feature in WI may provide some useful information about the RIS prototype's performance within the scenario of interest.

5.4.7 Performance prediction with RIS introduction

By introducing an EES into the scenario in Fig. 5.15, we can determine the behaviour of the wireless channel with a given RIS configuration. Here we employ a simple, likely sub-optimal approach to RIS configuration selection. This is based on constraining the RIS to perform as an anomalous reflector (i.e., $\phi_1 = \phi_2$ in 5.1). We consider just one region of the model in this subsection, with further work currently being undertaken to model other regions of interest. Area *A* is adjacent to an area of favorable signal strength of approximately -50 dBm, but is subjected to up to 40 dB of attenuation in the NLoS region. Knowing the transmitter position relative to the RIS, it is straightforward to program the continuously-tunable RIS to compensate for the incident phase front, prior to coupling the incident power into the first Floquet harmonic.

For the simulation setup, a 0.96 $m \times 0.96$ m RIS is positioned at coordinates (-9.8, -2, 2) m. 2525 vertically-polarised dipole receivers are arranged in a 101×25 grid, spaced 0.5 m apart, centered at coordinate (8.3, -11.7, 2). Received power versus receiver position has been plotted for several deflection angles, a subset of which have been plotted in Fig. 5.17(c) - (f). Fig. 5.17(c) shows the reference case, without the introduction of a RIS. It can be seen that the signal strength varies significantly between 5 m and 45 m in x, with the region between 10 m and 20 m subjected to significant attenuation. This is typical of a NLoS channel. The CDF of the receiver power for 10 m to 20 m region is plotted as the reference curve, *Ref*, in Fig. 5.17(b). When the RIS is programmed to deflect incident power between the adjacent buildings, it can be seen that an average power improvement of approximately 8 dB is possible within this zone. The 38° and 44° configurations offer the best average improvement in this example, each providing an average of 8.7 dB power level improvement.

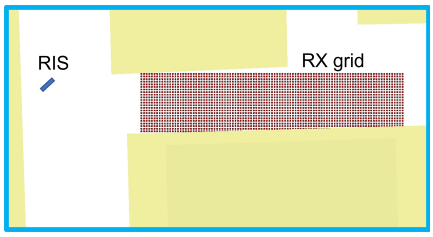

(a)

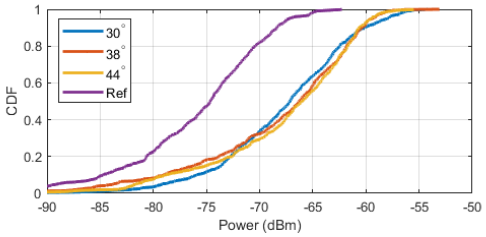

(b)

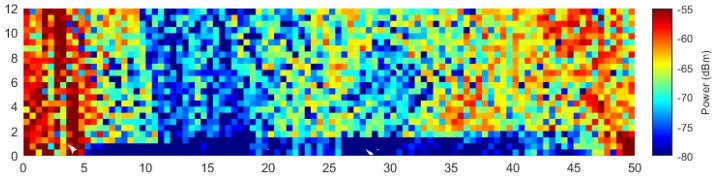

(c) Without RIS

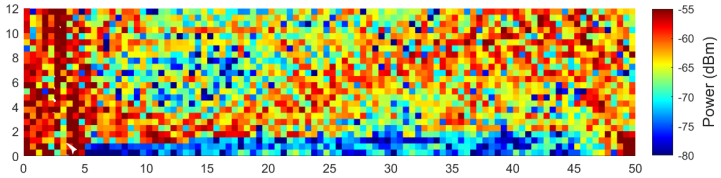

(d) 30°

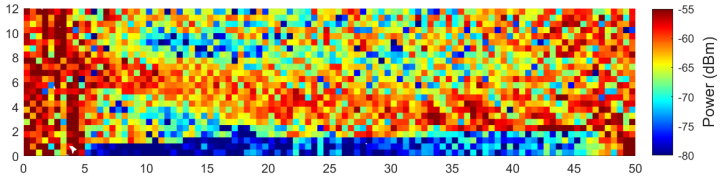

(e) 38°

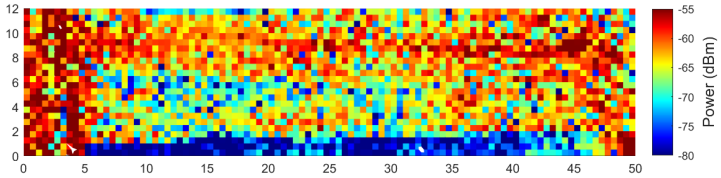

(f) 44°

Figure 5.17: Receivers at area A shown in Fig. 5.15 (a). CDF of the received power for the reference case and beam deflection angles of 30°, 38°, and 44° (b) between the region of 10 and 20 m in x. Received power versus position for the reference case without the RIS (c). Received power versus receiver position for beam deflection angles of 30°, 38°, and 44° (d) - (f). Receivers are arranged in a 100 × 24 grid with 0.5 m spacing.

5.4.8 Measurement system

The measurement system is centered around a Rohde and Schwarz ZNBT 12-port vector network analyser (VNA) located on a rig at the receiver location. A system diagram of the rig is shown in Fig. 5.18(a). To form a closed-loop measurement system over such a long distance, thus retaining accurate phase information, we extended the range of the VNA through an RFOptic radio over fiber (RoF) transmitter and receiver pair, shown in Fig. 5.20(a). This was made feasible due to existing optical fiber infrastructure at the measurement location.

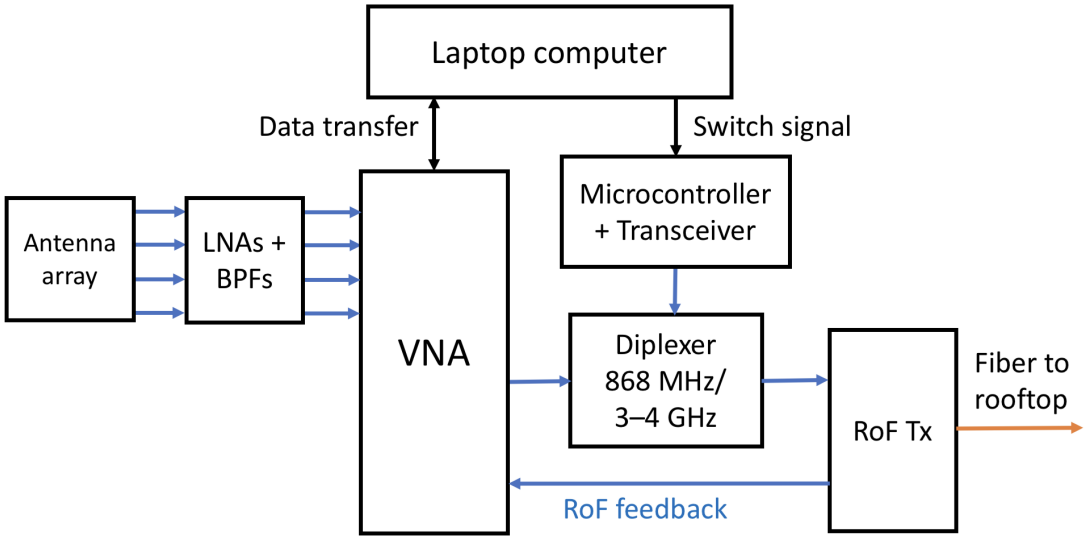

(a) Rig module

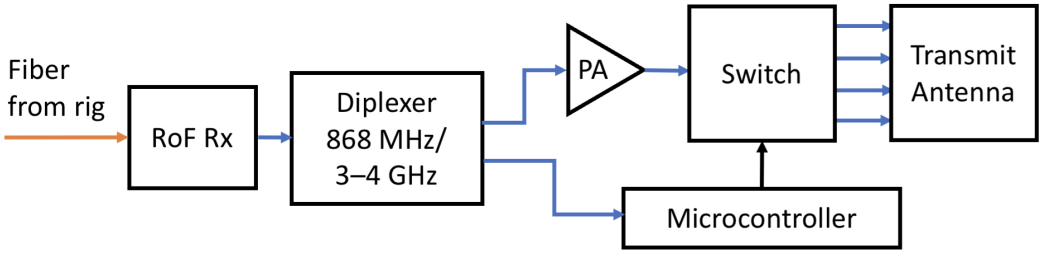

(b) Rooftop module

Figure 5.18: System diagrams for the rig (a) and rooftop (b) modules.

A sounding signal is sent from one of the VNA ports to a RoF transmitter module which modulates a laser. Additionally, a switch control signal line is added through a diplexer. These signals are optically transmitted across the site over single-mode fiber to a room directly beneath the base station antenna, where they are detected and transformed back into electrical signals by a RoF receiver equipped with a photodetector, as shown in Fig. 5.18(b). In a similar fashion to [165], part of the received optical signal is sent back down the fiber and detected at the rig in order to be used as a reference to calibrate out the delay introduced by the fiber. Following the RoF receiver is a diplexer used to separate the switch control signal path from the sounding signal path. The sounding signal is fed into a 16 W Minicircuits ZHL-16W-43-S+ power am-

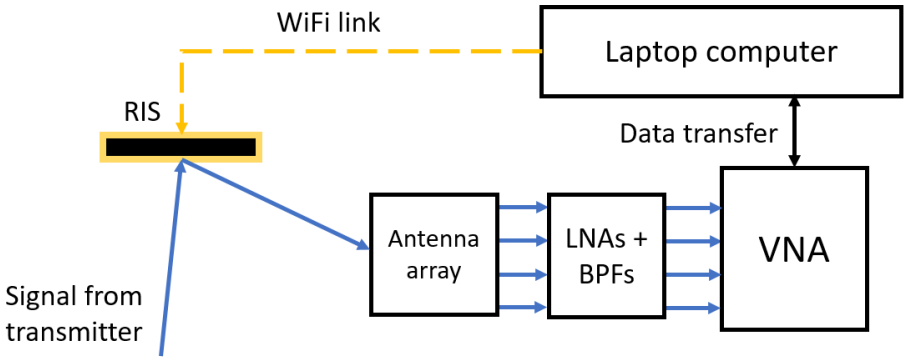

Figure 5.19: RIS feedback loop used during optimisation. Following configuration over a WiFi link, perturbations in the channel response are detected by a vector network analyser. Channel gain data is then used as an input to the algorithm deciding on the next configuations to test.

plifier (PA), followed by a SP4T mechanical switch. The switch output ports are connected to 4 ports of the antenna array via 15 m low-loss cables (8.17 dB/100 m @ 3.5 GHz). The switch control signal is received by a transceiver connected to a microcontroller, which in turn sets the mechanical switch states, addressing the respective transmitter antenna ports. To close the loop, the 4 ports of the receiver array are each connected to low noise amplifiers (LNAs) followed by bandpass filters (BPFs). The receiver antennas are connected to four ports on the VNA, allowing concurrent measurements of the received signals from the receiver array elements.

5.4.9 Radio over fiber

The RoF units utilised in the measurement system were the RFOptic RFoF6T3FR-PA-11 6 GHz modules operating with an optical wavelength of 1310 nm. A transmitter and receiver pair are shown in Fig. 5.20(a). The gain of the system is shown in Fig. 5.20(b) for two different module pairs. The units were programmed in their default setting, which provides a gain when connected to 100 m optical fiber between 7 and 10 dB in the 3 - 4 GHz band.

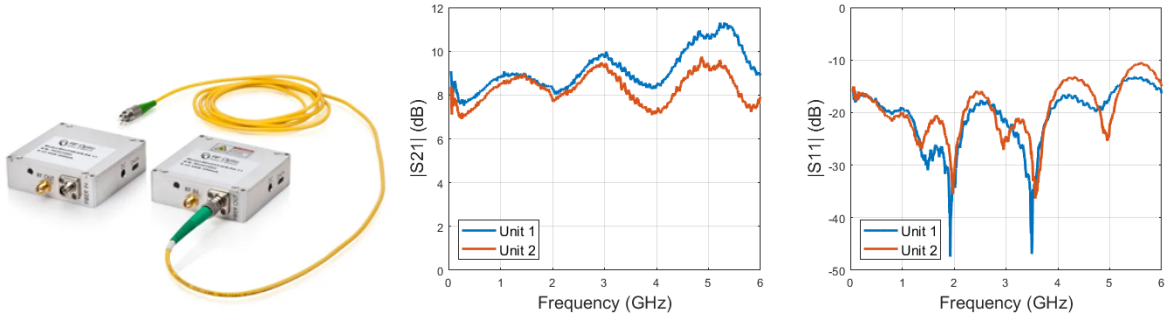

(a) (b) (c)

Figure 5.20: Radio over fiber unit with transmitter, receiver, and fiber optic cable (a). Gain for two units (b) and return loss (c).

When exposed to mechanical or thermal variations, optical fiber suffers from changes to its magnitude and phase response. In RoF systems, these effects become more pronounced with frequency [166]. With an optical feedback system, these changes can be removed from the measurements in post-processing [167]. The feedback system utilised in this work is depicted in Fig. 5.21 and consists of a single RoF transmitter, two RoF receivers, a 3 dB optical splitter, and two optical circulators. These were connected with patch cables and additional connectors where necessary.

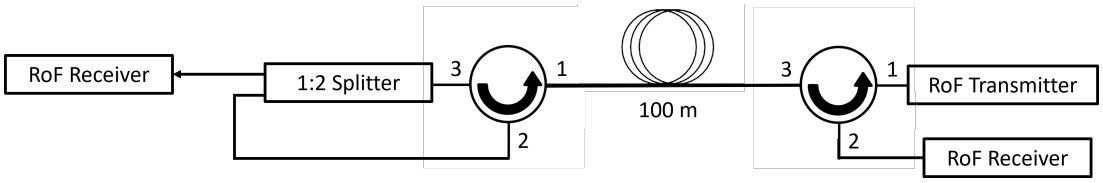

Figure 5.21: Diagram of the radio over fiber feedback system for phase compensation.

The receiver unit, placed in a room beneath the transmitter antenna, is shown in Fig. 5.22. This photo was taken prior to mounting the components in the case for mechanical stability. The transmitter unit is shown in Fig. 5.23.

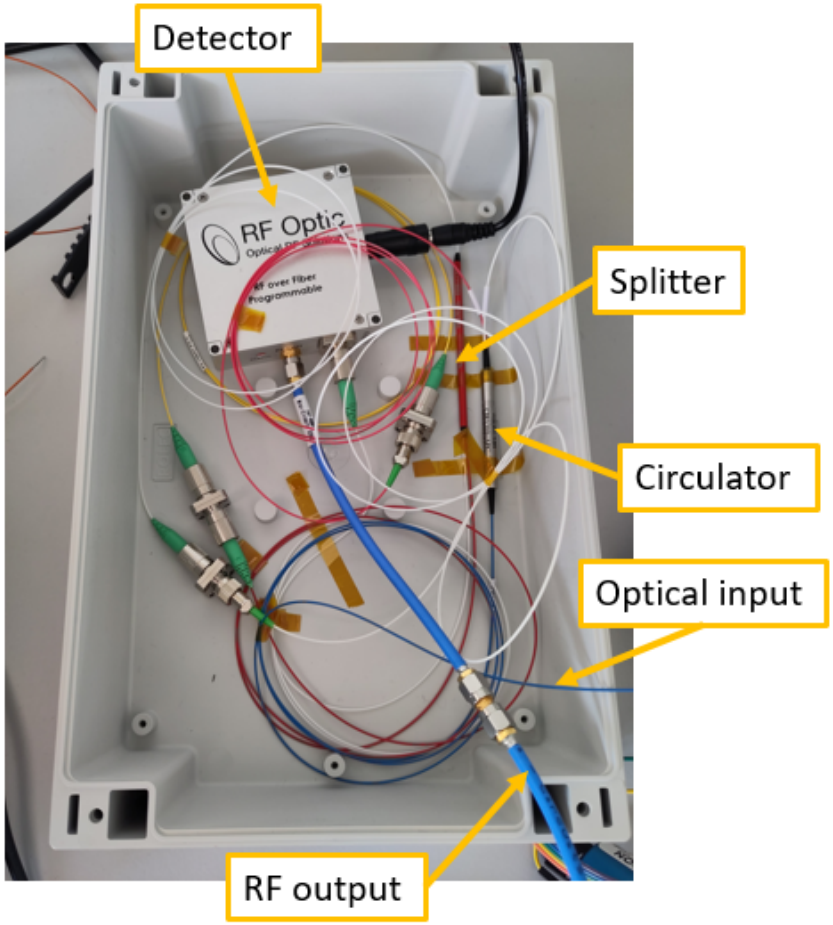

Figure 5.22: Radio over fiber-based receiver with associated feedback optical components prior to mounting.

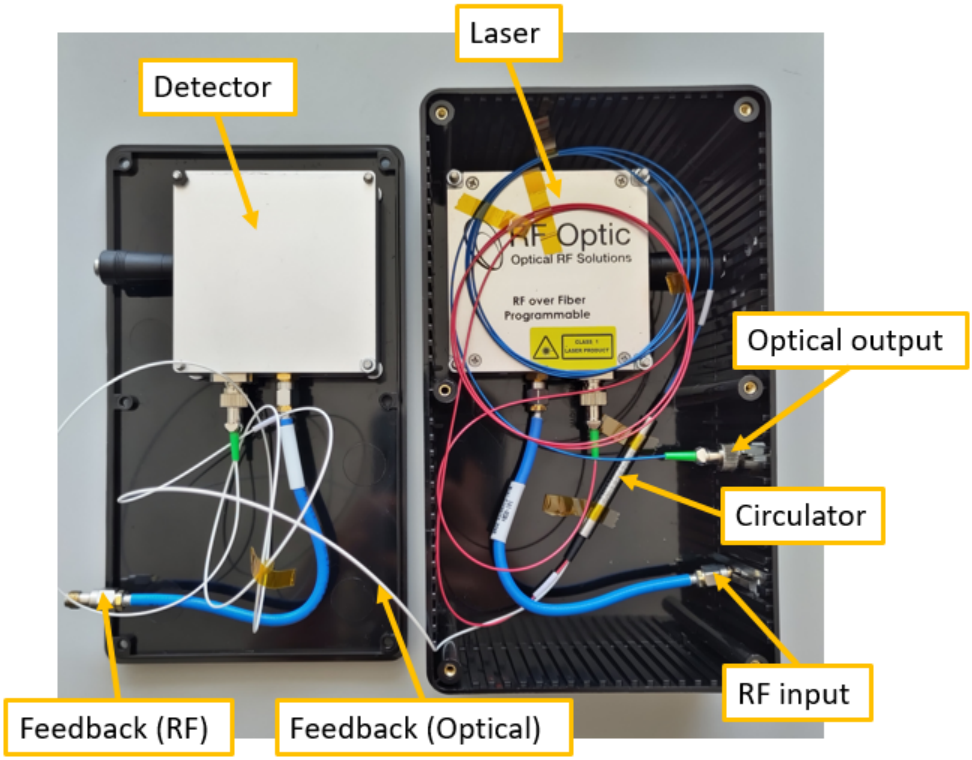

Figure 5.23: Radio over fiber-based transmitter with associated feedback optical components.

The RoF system and associated feedback circuitry was tested over a 100 m length of optical fiber. The resulting PDP of the initial system is plotted in Fig. 5.24(a). The resulting forward signal appears to suffer from significant noise. On adding an additional length of 1 m patch cable between the optical splitter and port 2 of the nearest circulator, this apparently unstable forward response smoothed out, resembling something closer to expected. This is shown in Fig. 5.24(b). Peaks in the PDP can be seen at approximately 530 and 1060 ns for the forward and feedback paths, respectively. The delay for the feedback path corresponding to a complete traversal of the 100 m fiber, twice. The delay introduced by the fiber can be removed from subsequent measurements by subtracting approximately half the phase shift measured at the feedback port at the VNA side.

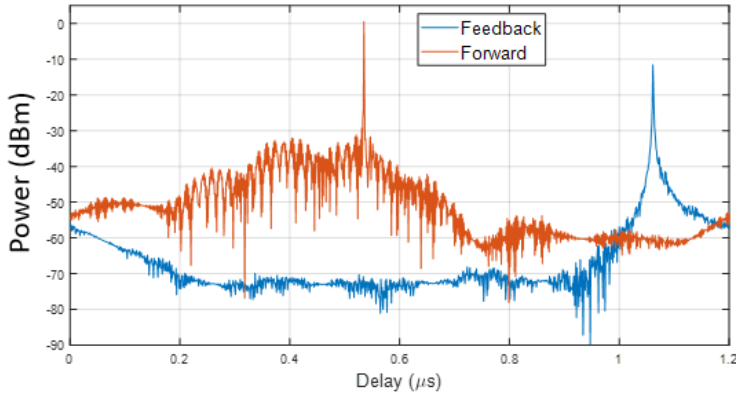

(a)

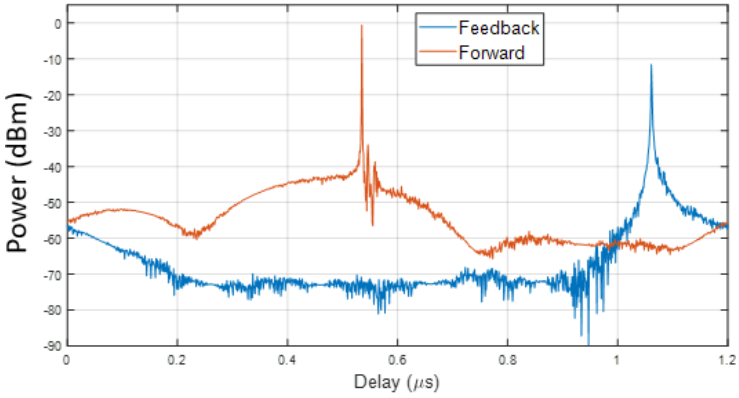

(b)

Figure 5.24: Power delay profile for the forward and feedback links of the radio over fiber system over 100m fiber before (a) and after (b) feedback line length correction.

The system was investigated for magnitude and phase drift over time. The setup in Fig. 5.21 was left undisturbed on a lab bench over a 24 hour period, with a VNA programmed to take snapshots of the S21 at time 30 minute intervals. The magnitude drift compared to the baseline at the start time is plotted in Fig. 5.25.

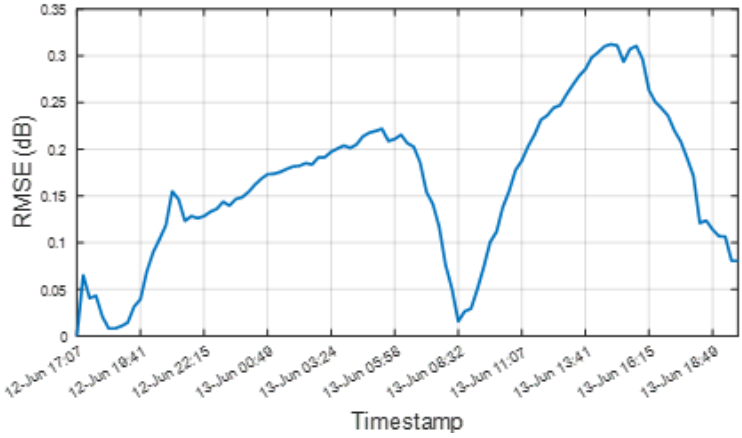

Figure 5.25: Drift in the magnitude response of the radio over fiber system with respect to time.

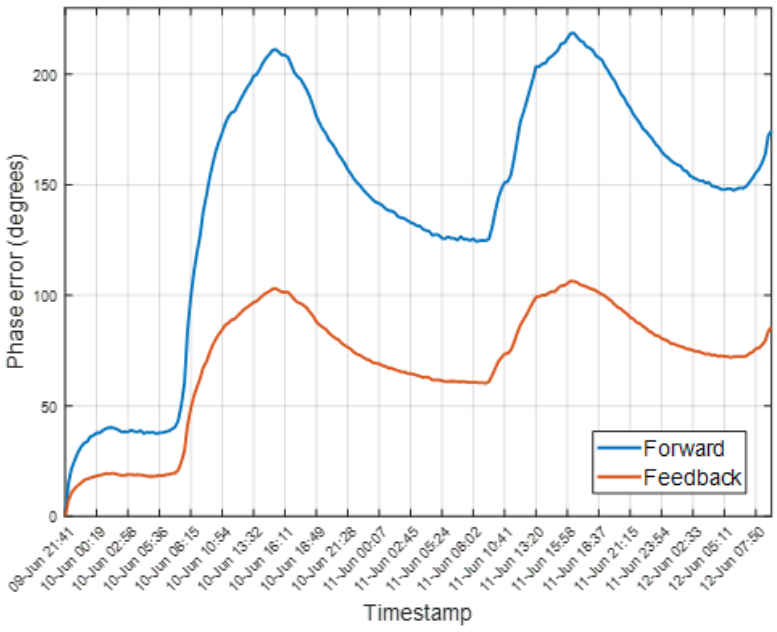

(a)

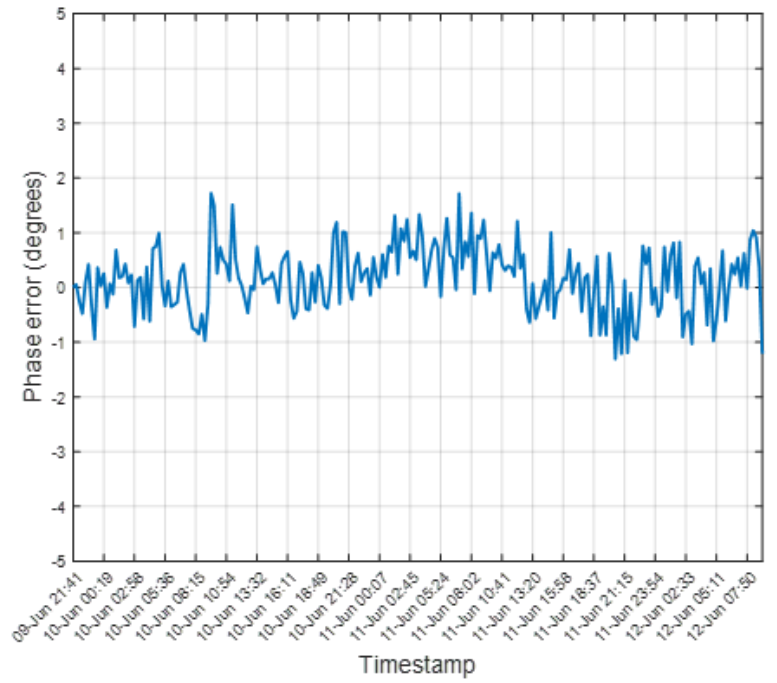

(b)

Figure 5.26: Drift in the phase response versus time for the forward and feedback paths of the radio over fiber system (a). Phase error after phase correction from feedback (b).

The phase response measured at 30 minute intervals over the course of a weekend is plotted in Fig. 5.26(a). The forward and feedback phases appear to follow the same trend that is somewhat periodic in nature. This is likely due to temperature fluctuations in the laboratory throughout the day. Fig. 5.26(b) is the resulting curve when subtracting the feedback phase from the forward phase after multiplication by a faction of 1/2.05. This factor was found to result in an RMS phase error of 0.686°. The divergence from the expected value of 1/2 is likely due to the additional lengths of optical fiber at the splitter and circulator sections.

5.4.10 Mechanical switch and switch control

A diplexer was designed to isolate the switch control signal derived from a transceiver operating at 868 MHz from the VNA sounding signal operating from 3 to 4 GHz. This enabled both signals to be propagated over the optical fiber, thereby eliminating any need for a separate switch control link and any synchronisation issues that might occur as a result. A custom design was necessary due to the unconventional combination of frequencies. The layout for the diplexer is depicted in Fig. 5.27(a). The circuit consists of a microstrip low pass filter (LPF) in parallel with a coupled line BPF. The circuit was designed on a 1.5 mm thick Rogers 4350B substrate. The LPF was optimised for a cutoff frequency of 1 GHz and to present an open circuit between 3 and 4 GHz. The BPF was optimised for a passband between 2.9 and 4.1 GHz, with the 100 MHz margin to compensate for any fabrication tolerances. The resulting S-parameters for the diplexer are plotted in Fig. 5.27(b). It can be seen that the circuit is well-matched at the respective bands, with minimal (< 40 dB) transmission to ports 2 and 3 at the upper and lower bands, respectively.

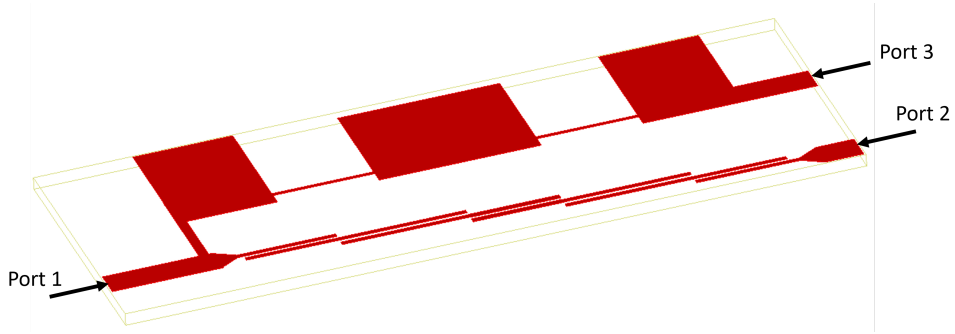

(a)

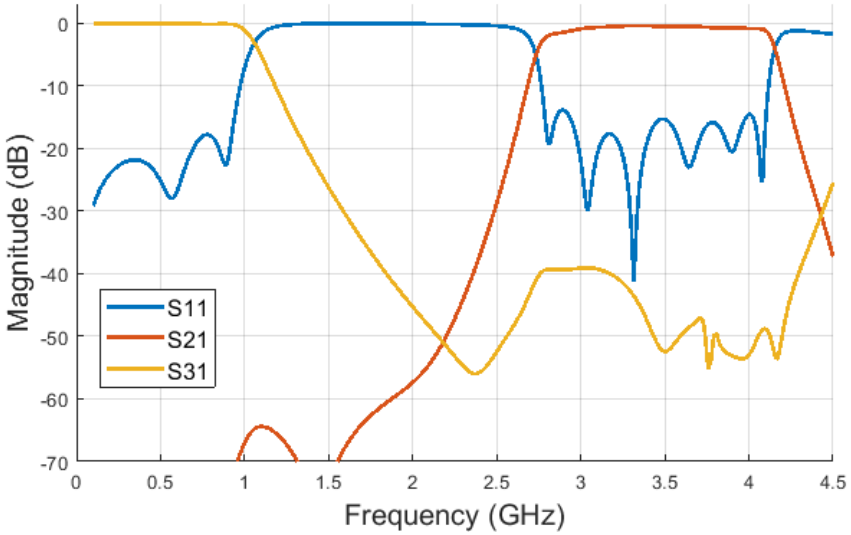

(b)

Figure 5.27: Microstrip diplexer implementation in Keysight ADS (a). Resulting S-parameters (b).

5.4.11 Measurement system gain

The transmission S-parameters of the measurement system section between the RoF transmit port and the output of the PA, with the diplexer omitted, is plotted in Fig. 5.28. This measurement was ascertained over 2km of optical fiber, with a 40 dB attenuator placed at the PA output. The attenuator was subsequently de-embedded from the measurement. A gain of approximately 32 dB is maintained in the 3 - 4 GHz band. Performance begins to quickly degrade beyond 6 GHz due to the frequency limitations of the RoF system.

5.4.12 Calibration and de-embedding

An overview of the measurement system highlighting the calibration planes is shown in Fig. 5.29. For this work, the ideal calibration planes are situated at the antenna ports. This is due to practical reasons, as it was not possible to characterise the in-situ antenna response in a

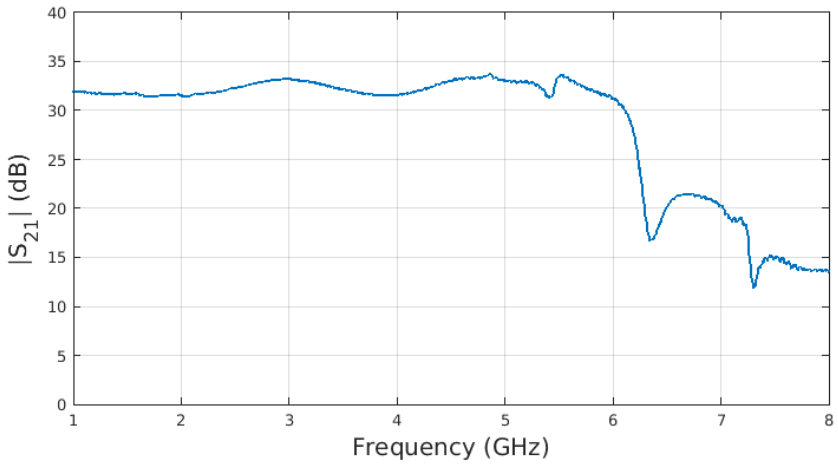

Figure 5.28: Measured gain of the long-range measurement system between the radio over fiber transmitter and the output of the power amplifier via 2 km of optical fiber.

reasonable amount of time. The contribution of the antennas is thus considered part of the channel response in this work, maintaining realism due to operation over existing infrastructure. To de-embed the channel, we have characterised the parts of the measurement system between the VNA calibration planes and the ideal calibration planes through a combination of back-to-back measurements and RoF feedback.

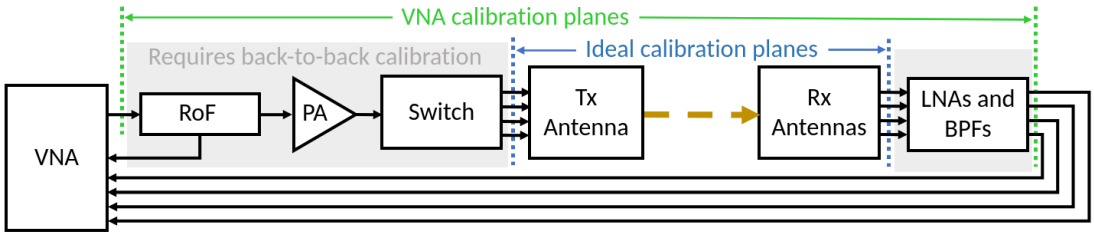

Figure 5.29: Diagram of the long-range measurement system highlighting the calibration planes.

The VNA calibration planes are set through short-open-load-through (SOLT) calibration at the ends of the connecting cables to the respective transmit and receive section ports. These ports are the input ports to the RoF transmitter and the output ports from the receiver BPFs and RoF feedback. An S-parameter measurement, S_{n1}, contains the frequency response between VNA port 1 and a receive port, n. The contribution of the diplexers, PA, switch, and associated cables on the transmit side, $G_{t1}(f)$, as well as the LNA, BPF, and associated cables on the receive side, $G_{rn}(f)$, are removed through division of the respective frequency responses:

$$\widetilde{H}_{n1}(f) = \frac{S_{n1}(f)}{G_{t1}(f)G_{rn}(f)} \tag{5.3}$$

Removing the contribution of the RoF sections becomes more complex due to the distance between the end nodes. For these experiments, we have approximated the magnitude response of the RoF system, $|G_{RoF}|$, by measuring its frequency response when connected to 2 km of

optical fiber. The delay over the fiber during measurements is determined via the phase response of the RoF feedback port, ϕ_{fb}. The de-embedded channel response, H_{n1}, being the frequency response between the input to transmitter port 1 and the output of antenna port n is determined via:

$$|H_{n1}| = \frac{|\widetilde{H}_{n1}(f)|}{|G_{RoF}|} \tag{5.4}$$

$$H_{n1} = \angle\widetilde{H}_{n1}(f) - \frac{1}{2}\phi_{fb} \tag{5.5}$$

The above procedure is applied to the remaining transmitter and receiver ports in a similar fashion, thereby generating the complete de-embedded channel response, **H**.

An artificial channel was constructed to test the de-embedding procedure. This consisted of a two-way power splitter with one of its outputs connected to a coaxial T-junction to form a 3-tap channel. The artificial channel is depicted in Fig. 5.30(a). The splitter to T-junction and splitter to combiner lengths of cable were 0.5 and 1.5 m, respectively. The lengths between the T-junction and the combiner were also 0.5 and 1.5 m, respectively. The resulting path lengths were therefore 1, 1.5, and 2 m, respectively. The PDP of the artificial channel response without the RoF system is plotted as the blue curve in Fig. 5.30(b). When connecting the RoF system with a 100 m length of optical fiber cable prior to the artificial channel, a delay is introduced accordingly, as seen in the red curve. When applying equations 5.3 to 5.5 to de-embed the artificial channel response, the corrected PDP is ascertained as shown in Fig. 5.30(c). Zooming in on the most significant signal components as in Fig. 5.30(d), it can be seen that the de-embedding procedure results in a reasonable approximation of the baseline case.

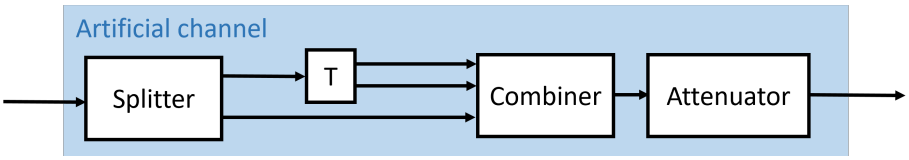

(a)

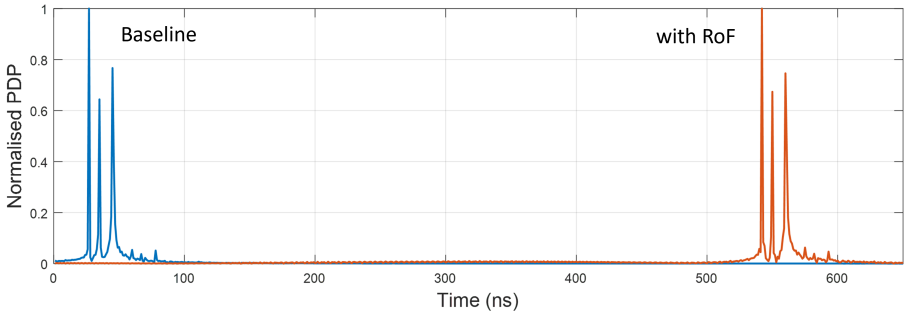

(b)

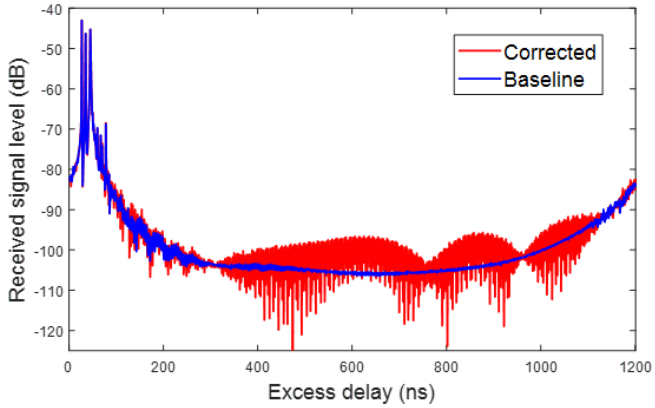

(c)

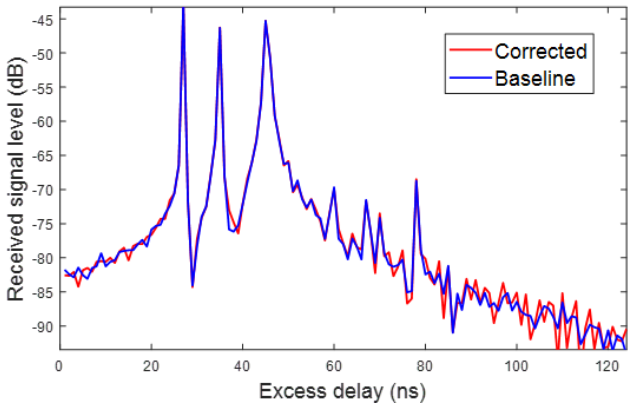

(d)

Figure 5.30

5.5 System performance

5.5.1 Measurement procedure

For each receiver location, the PSO-based beam search algorithm introduced in section 5.3 was employed to find the configuration which maximised the channel gain for a 50 MHz band. Although the RIS was tuned to operate at 3.5 GHz, there was an active 5G cell on the site operating between 5.53 and 5.58 GHz. Therefore, two 50 MHz bands operating above and below this range were selected in order to avoid unnecessary interference. Namely, 3.47 to 3.52 GHz and 3.59 to 3.64 GHz. Channel measurements were taken before and after the introduction of the RIS. These consist of 16 frequency domain sweeps corresponding to the complex transmission parameters between each transmitter and receiver. Additionally, a feedback measurement from the RoF section is taken to compensate for the fiber delay in post-processing. A subset of the channel parameters after de-embedding are plotted in **??**(a) to (c) for locations 1 to 3, respectively. Additionally, the total power gain for the complete 4×4 MIMO channel matrix is plotted according to equation (5.6):

$$G = \mathrm{Tr}\left(\mathbf{H}\mathbf{H}^{H}\right) \tag{5.6}$$

This is the gain of the MIMO channel assuming energy is spread equally between all four transmit antennas [50].

5.5.2 Zone A

The measurement zone A is shown in Fig. 5.7(a). The RIS in Zone A was oriented so that its broadside direction was set at a 30° clockwise angle relative to the line of receiver locations. This angle was chosen to ensure a sufficiently large capture area for incident radiation while also reducing the obliqueness of the angle presented to Location 1. The end nodes and the view from behind the RIS at Zone A are shown in Figs. 5.31, 5.32, and 5.33, respectively.

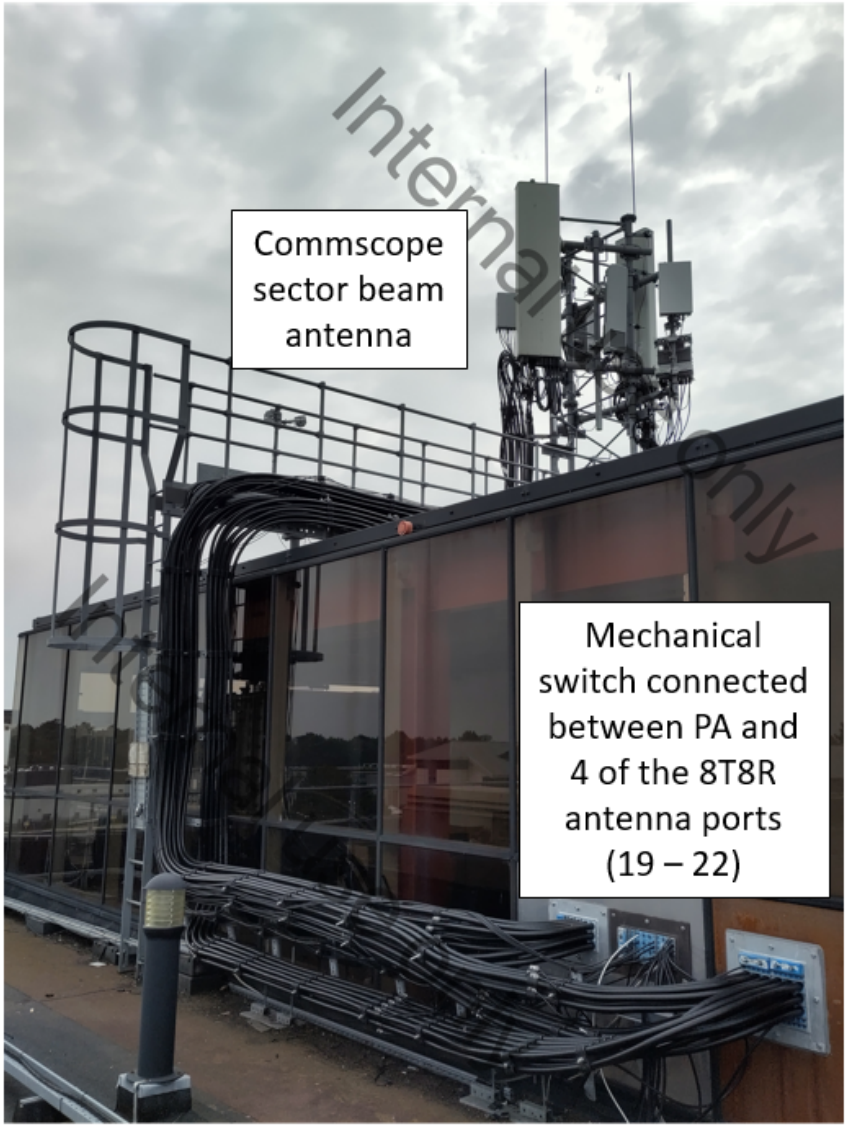

Figure 5.31: Photo showing rooftop antenna and connecting cables.

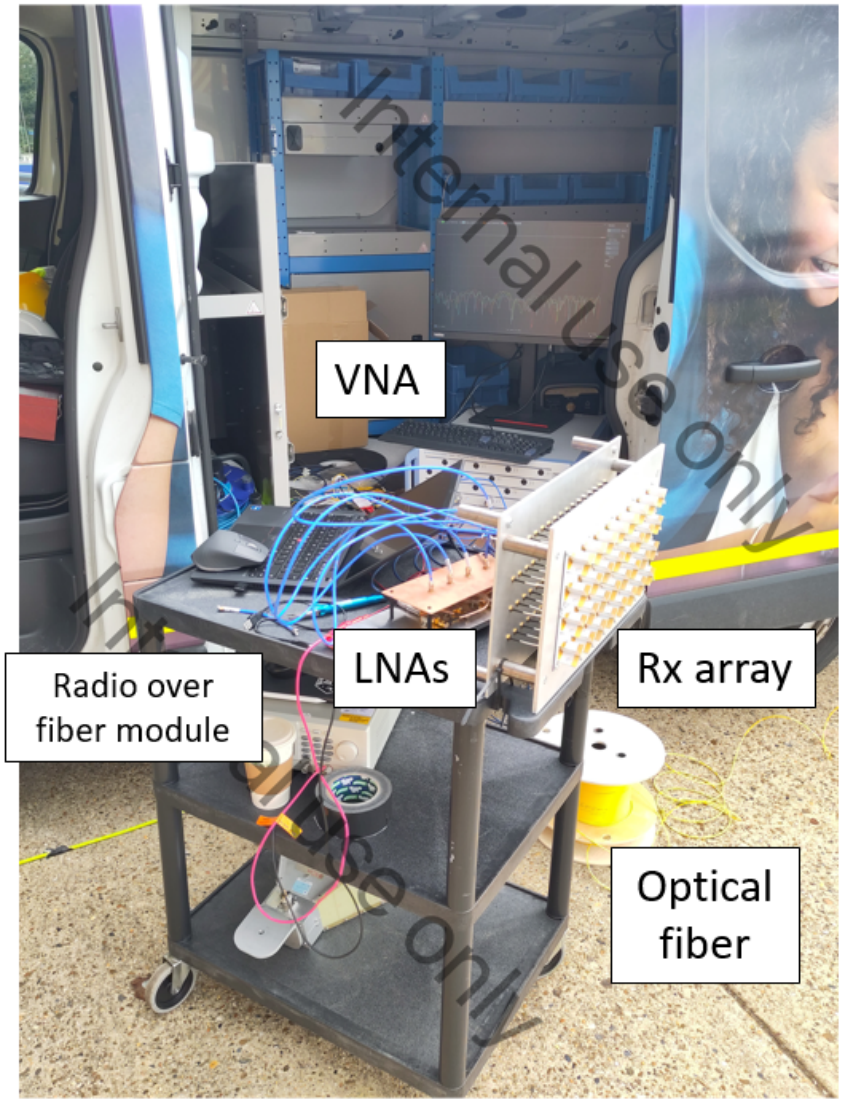

Figure 5.32: Photo of the receiver rig in Zone A, in proximity to position 1 prior to measurements.

Figure 5.33: Photo of the rear side of the RIS at Zone A, with rooftop antenna and rig in proximity to position 3 visible.

The RIS in Zone A was oriented so that its broadside direction was set at a 30° clockwise angle relative to the line of receiver locations. This angle was chosen to ensure a sufficiently large capture area for incident radiation while also reducing the obliqueness of the angle presented to Location 1. The squared magnitude of the diagonal channel coefficients versus frequency for the 3.47 to 3.52 GHz band have been plotted in Figs. 5.34 to 5.36 for positions 1 to 3, respectively.

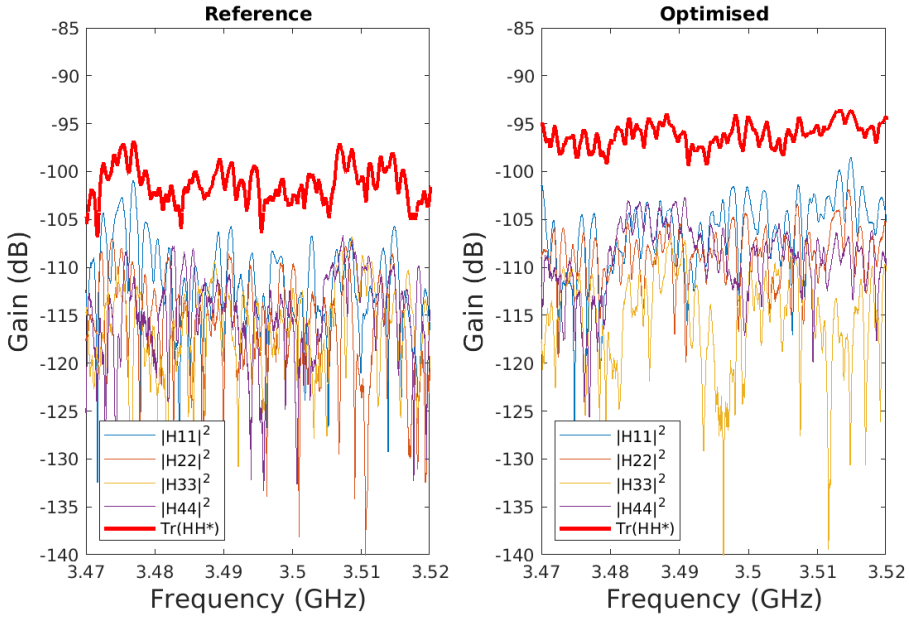

Figure 5.34: Selected channel magnitudes, H_{11} to H_{44}, and MIMO channel gain for the 3.47 to 3.52 GHz band in zone A, position 1.

The resulting MIMO channel power gain derived from equation (5.6) has also been plotted for the respective reference and optimised cases. It can be seen that the introduction of the RIS has a positive impact on the overall channel gain. This effect becomes more pronounced the closer the receiver is to the RIS. Referring to Fig. 5.36, it can be seen that the channel response begins to resemble a frequency-flat channel not unlike that expected from a LoS setup. A similar trend can be observed at the higher band. Figs. 5.37 to 5.39 show the magnitudes of the channel coefficients for the 3.59 to 3.64 GHz band.

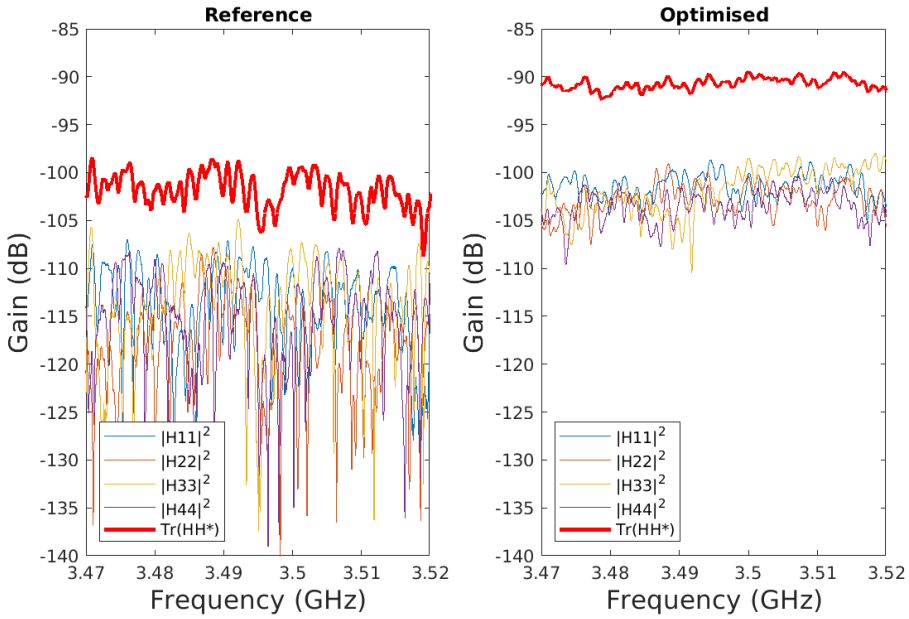

Figure 5.35: Selected channel magnitudes, H_{11} to H_{44}, and MIMO channel gain for the 3.47 to 3.52 GHz band in zone A, position 2.

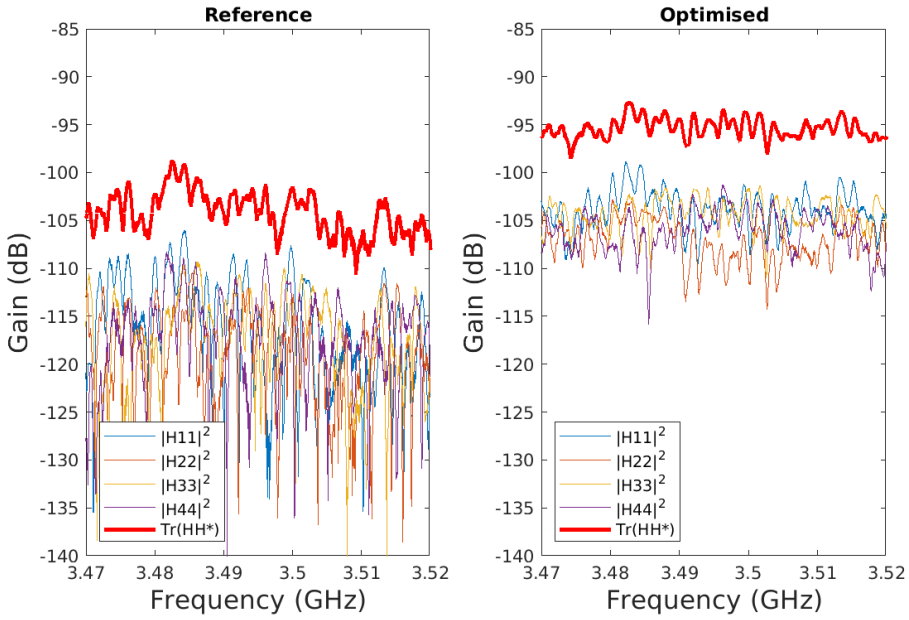

Figure 5.36: Selected channel magnitudes, H_{11} to H_{44}, and MIMO channel gain for the 3.47 to 3.52 GHz band in zone A, position 3.

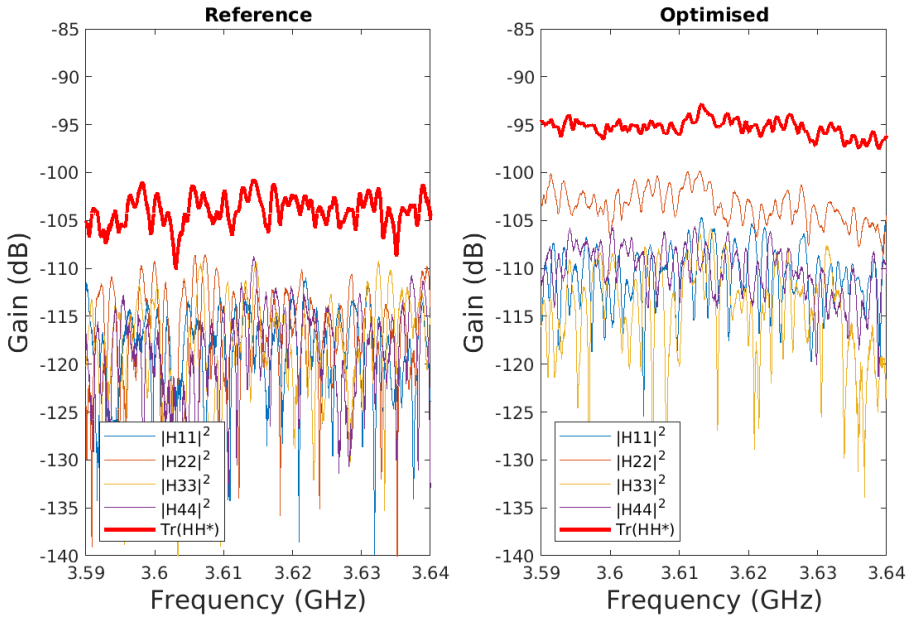

Figure 5.37: Selected channel magnitudes, H_{11} to H_{44}, and MIMO channel gain for the 3.59 to 3.64 GHz band in zone A, position 1.

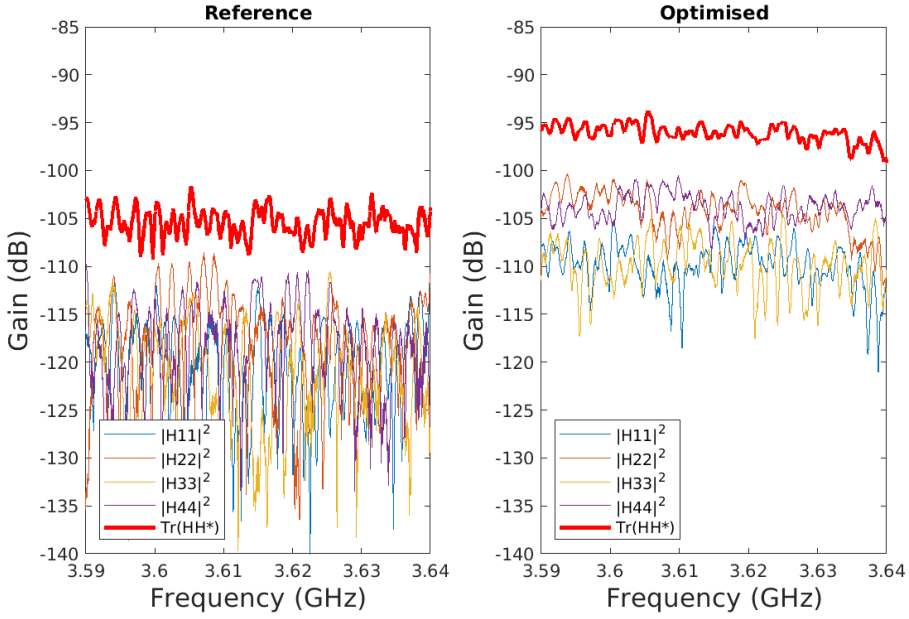

Figure 5.38: Selected channel magnitudes, H_{11} to H_{44}, and MIMO channel gain for the 3.59 to 3.64 GHz band in zone A, position 2.

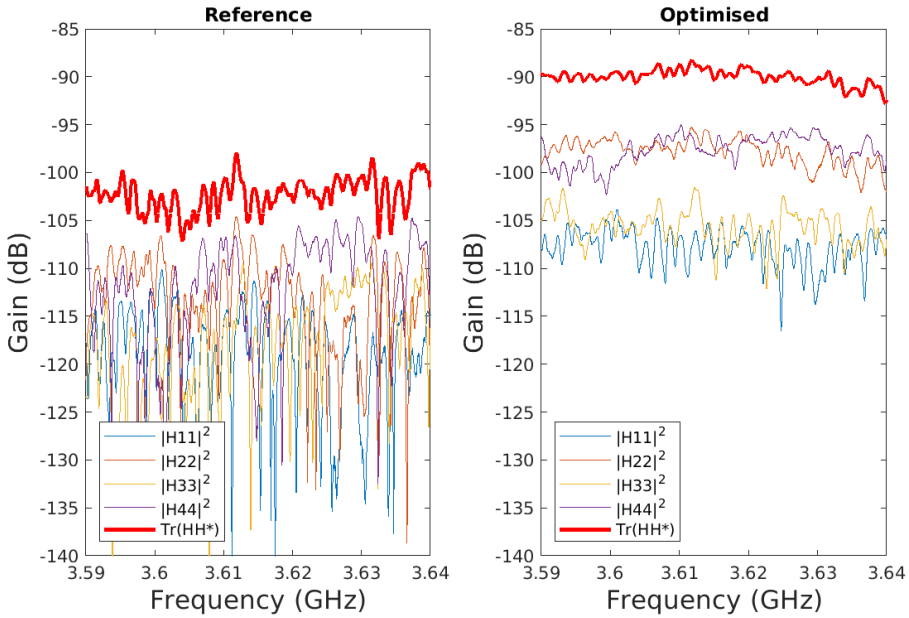

Figure 5.39: Selected channel magnitudes, H_{11} to H_{44}, and MIMO channel gain for the 3.59 to 3.64 GHz band in zone A, position 3.

The maximum channel capacity is found by applying the water-filling principle on the transmit covariance matrix [18]. Predicted maximum channel capacity versus transmit power for the 3 measurement positions for the reference and optimised cases are plotted for the 3.59 to 3.64 GHz band. As a tangible example, in the UK, a typical EIRP limit in active antenna systems in the sub-6 GHz bands is 44 dBm/5 MHz per sector. For a 50 MHz channel bandwidth, this results in a maximum EIRP of 54 dBm. Given the base station antenna gain of 20.4 dBi, this results in a maximum transmission power of 33.6 dBm. Referring to Fig. 5.44, for positions 1 to 3, the reference case (i.e., before the RIS introduction) can theoretically facilitate transmission rates of up to 0.635, 0.590, and 0.687 Gbps, respectively. With the introduction of the RIS, these values are increased to 0.908, 0.933, 1.07 Gbps, respectively, thereby approaching and even exceeding the maximum downlink data rates of 1 Gbps at 5G mid-band.

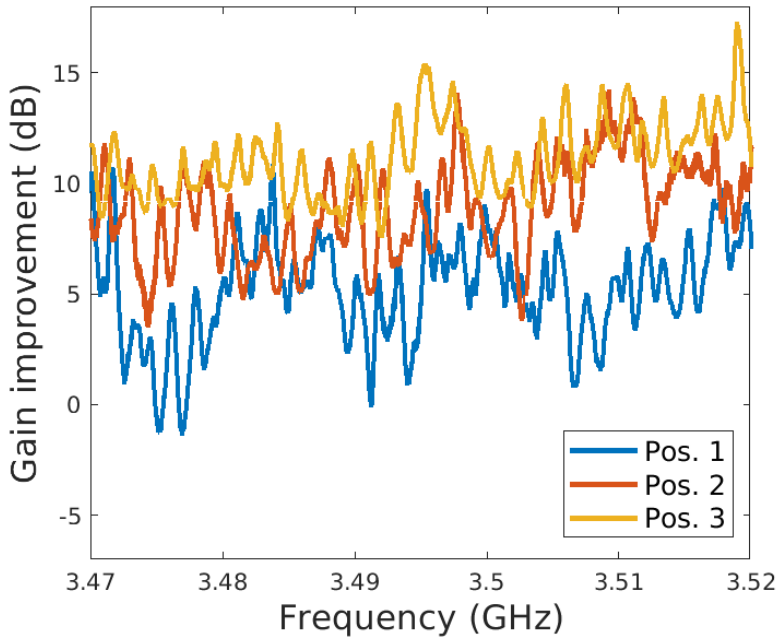

(a)

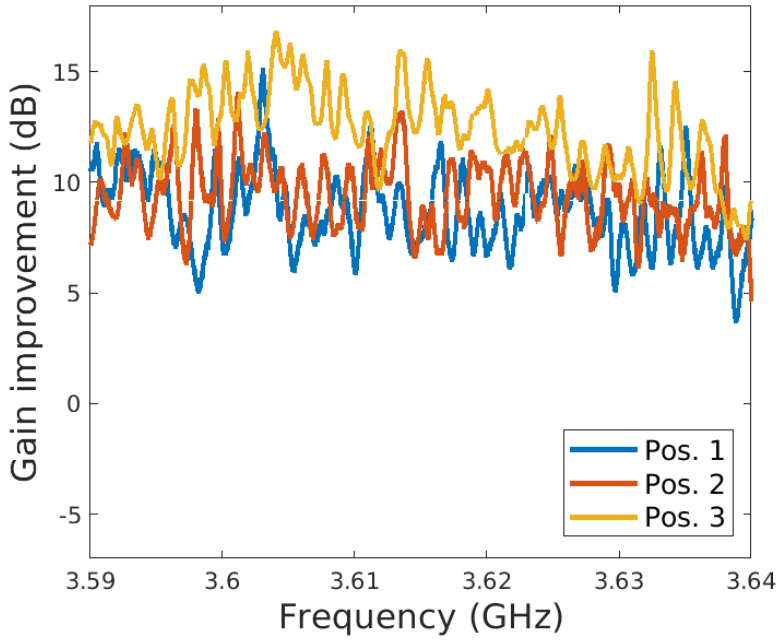

(b)

Figure 5.40: MIMO channel gain improvement for zone A within the 3.47 to 3.52 GHz band (a) and the 3.59 to 3.64 GHz band (b).

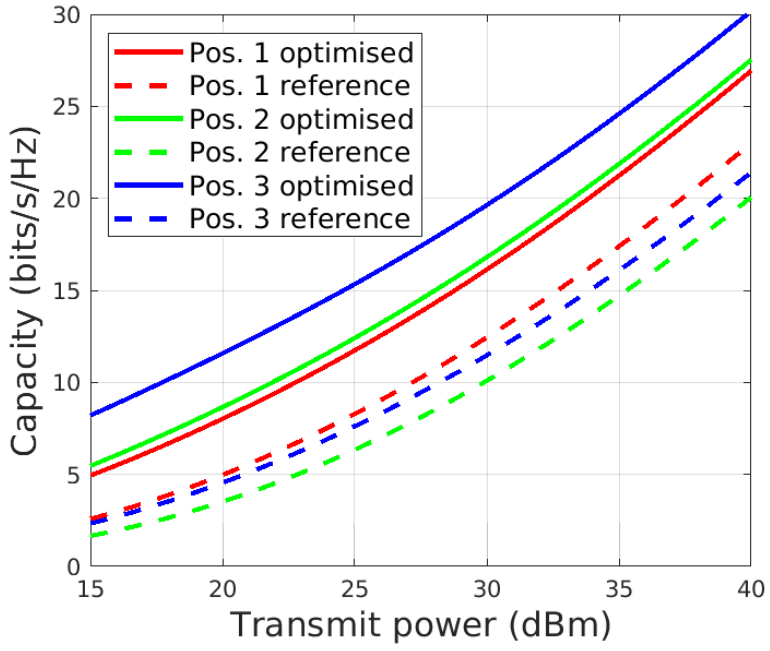

(a)

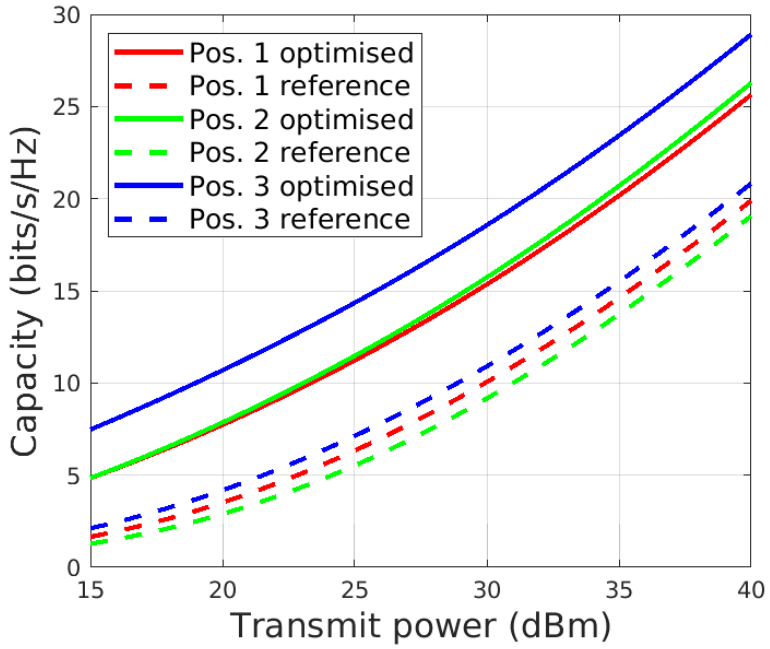

(b)

Figure 5.41: Predicted channel capacity for zone A within the 3.47 to 3.52 GHz band (a) and the 3.59 to 3.64 GHz band (b).

5.5.3 Zone B

Referring to Fig. 5.7(b), the RIS in Zone B was oriented at 45° clockwise with respect to the north-south axis. Due to time constraints, optimisation was only performed at locations 2 and 3. Fig. 5.42 shows a subset of the channel gains versus frequency for the reference and optimised cases. In contrast to the performance enhancement witnessed in Zone A, the differences between the reference and optimised cases are not as significant. Position 2 appears to benefit most from the RIS introduction, with average channel gain improvements of 2.4 and 1.8 dB in the lower and upper bands, respectively.

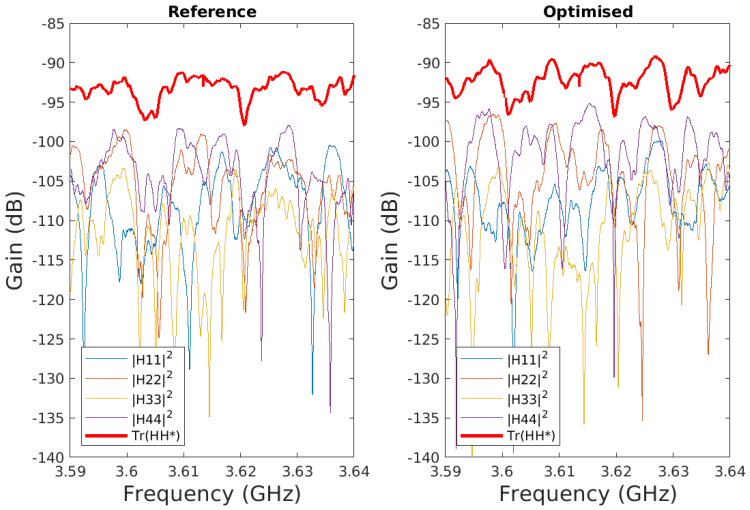

(a) Position 2

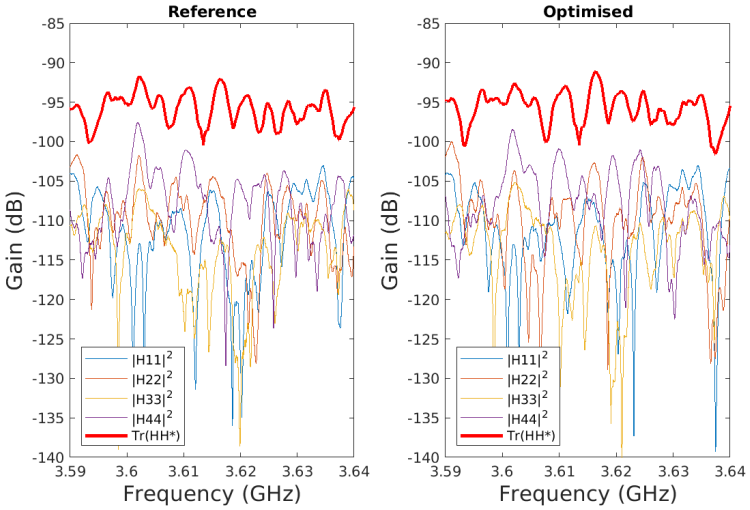

(b) Position 3

Figure 5.42: Selected channel magnitudes, H_{11} to H_{44}, and MIMO channel gain for the 3.59 to 3.64 GHz band in zone B. Reference and optimised cases at positions 2 and 3, (a) and (b), respectively.

The lack of significant performance benefit in Zone B can be understood in part by observ-

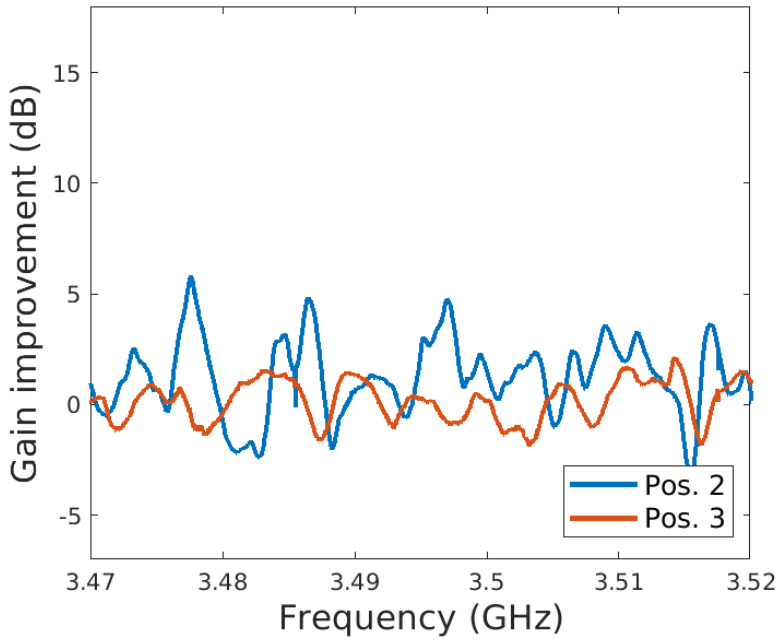

(a)

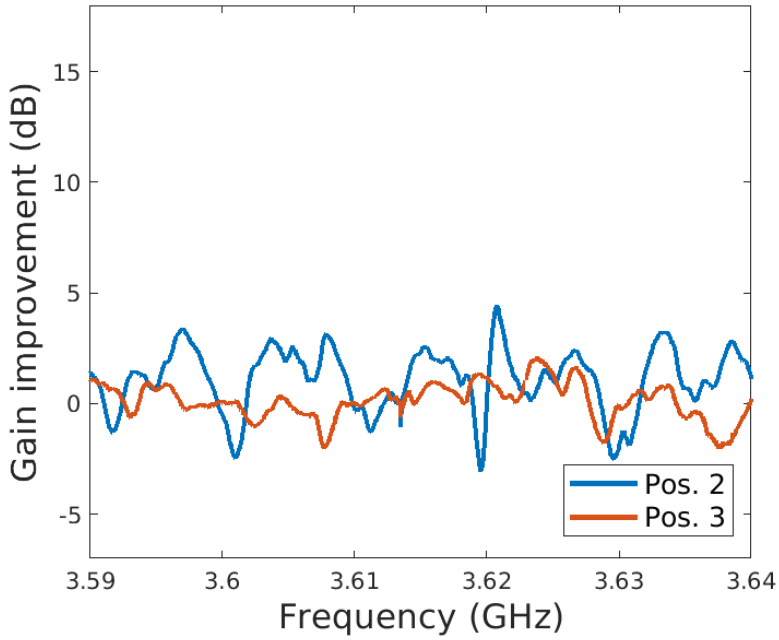

(b)

Figure 5.43: MIMO channel gain improvement over the reference case for zone A within the 3.47 to 3.52 GHz band (a) and the 3.59 to 3.64 GHz band (b).

ing the surrounding environments of the two respective measurement zones. The receivers in Zone A do not benefit from being in close proximity to as large a source of multipath, such as the buildings to the west and north of the receivers in Zone B, and therefore the reference channel performance is worse. Since we have utilised low-directivity antennas on the receiver, we benefit from the richer wave interactions from the buildings in Zone B, circumventing the occlusions between the transmitter and receiver, resulting in more favorable channel conditions in the reference case. Additionally, the tilt of the transmitter antenna beam should be taken into account. The beamwidth of the antenna in elevation is 6.5° and, as previously mentioned, the beam tilt in elevation was fixed at 0°. The elevation angles of the RISs in Zone A and Zone B relative to the transmitter antenna are 8.1° and 10.9°, respectively. Observing the E-plane cut of the beam pattern in Fig. 5.9, it can be seen that the RIS in Zone B sits close to a pattern null. The combination of this circumstance and the richer multipath is the likely explanation for the limited impact that the RIS in Zone B has on the channel.

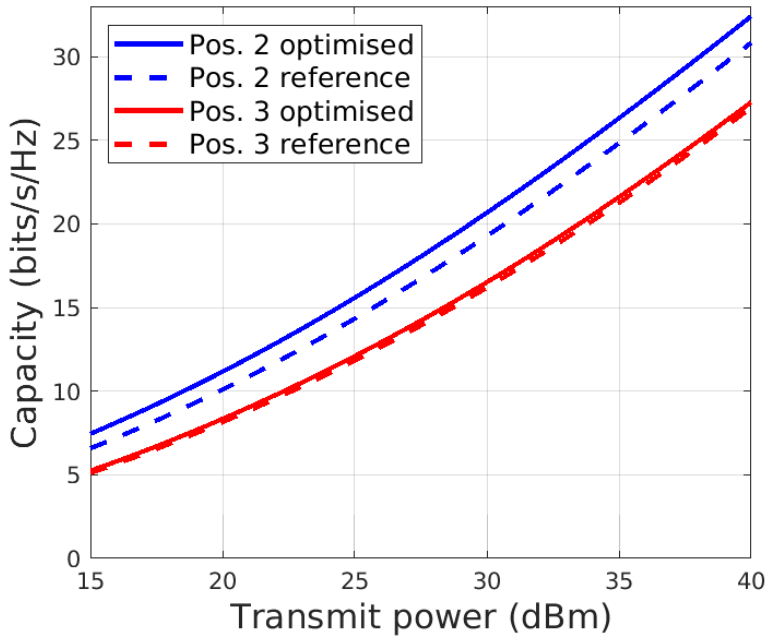

(a)

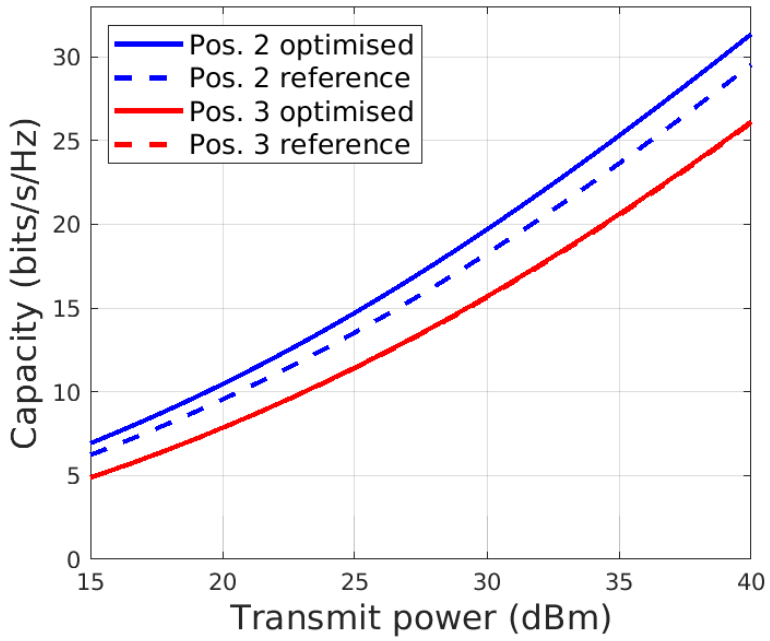

(b)

Figure 5.44: Predicted channel capacity for zone B within the 3.47 to 3.52 GHz band (a) and the 3.59 to 3.64 GHz band (b).

5.6 Azimuthal beam sweep performance

While we may be improving channel conditions for individual users at fixed locations for optimised configurations, what effect does a given configuration have on nearby users? Due to constraints placed on the measurement logistics, it was not possible to optimise for each location, followed by measuring the effects of the respective optimal configurations on the remaining positions. Instead, we performed beam sweeping in the azimuthal plane. These measurement were performed in zone A, and involved iterating over the same set of configurations at each position. The data gathered from these measurements then allow us to determine any introduced interference effects associated with the RIS deployment.

With the center point of the RIS as the origin, the transmitter antenna array was calculated as being located in the spherical coordinates $r_{tx} = 175$ m, $\theta_{tx} = 5.1^\circ$, and $\phi_{tx} = 55.1^\circ$. The channel was measured for a set of 161 configurations corresponding to maximum re-radiation at 1° steps in azimuth between 20° and 160°. To determine the effects of RIS orientation on the beam-sweeping performance, measurements were performed with the RIS oriented along the east-west line for the 0° case as well as at a clockwise rotation of 30°. The 30° case offers a larger aperture in the direction of the receivers and will be explored here first.

The resulting channel gains versus configuration for the 30° RIS orientation for the 3 receiver positions are plotted in Fig. 5.45. It is immediately apparent that there is a symmetry about configuration 80, corresponding with a re-radiation angle of 90°. This symmetry is due to the inherent split-beam behaviour of 1-bit reflecting metasurfaces in the far-field to far-field beamsteering regime [168]. This split beam behaviour was measured in the configuration corresponding with maximising power at both 45° and 75° in Fig. 3.27(c), for example. Three of the measured beam patterns for the case of normal incidence on a single $0.48\ m \times 0.48\ m$ tile have been plotted in Fig. 5.47. These correspond to maximisation of the channel gain towards 15°, 45°, and 75°, respectively, using the measurement setup from section 3.3.5. It can be observed that the beamwidth broadens as the dominant re-radiation angle diverges from 90° due to the effective narrowing of the re-radiating aperture. A similar effect can clearly be seen when moving from position 1 to position 3, but with narrower overall beamwidth due to the increased RIS aperture area. The configurations corresponding with the maximum channel gain are 90, 105, and 145, respectively. These configurations result in an improvement over the mean channel gain of 5.1, 11.5, and 11.1 dB, respectively. These results could be utilised to populate a codebook of RIS configurations corresponding to the positions of potential users, with a relatively small number of RIS configurations iterated over to serve a given position. The instantaneous bandwidth of the preferred configurations (i.e., the configurations corresponding to a noticeably improved channel gain) can be seen to easily support the 50 MHz-wide channel between 3.47 and 3.52 GHz for each location.

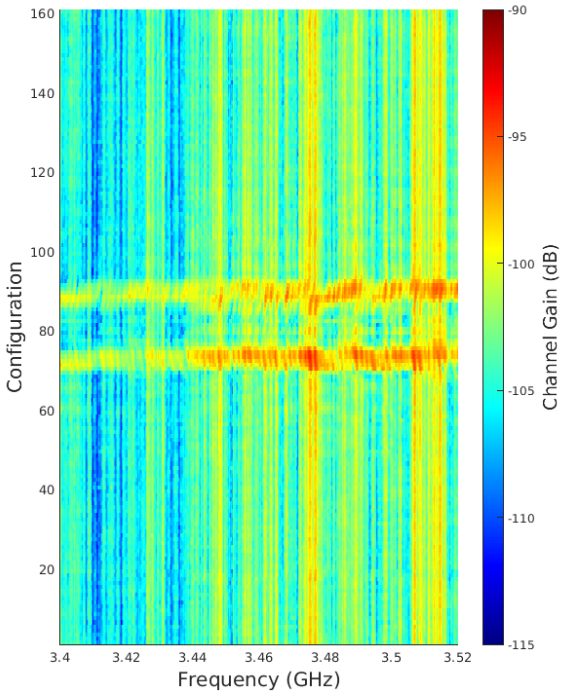

(a) Position 1

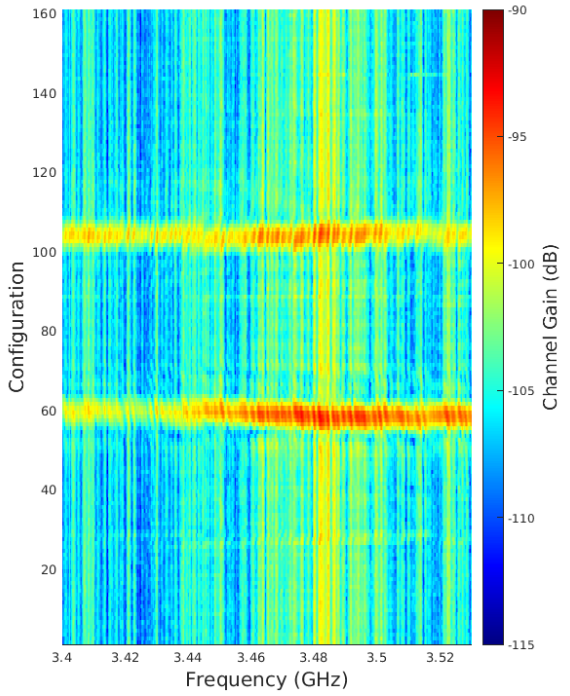

(b) Position 2

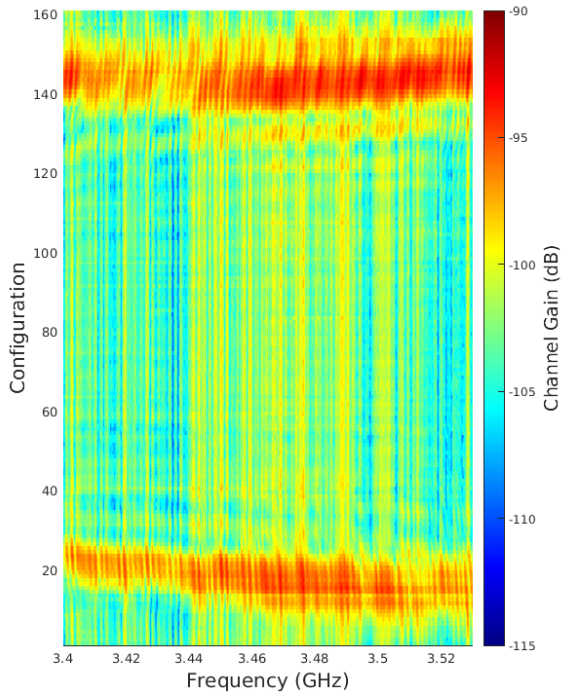

(c) Position 3

Figure 5.45: Beam sweep performance in Zone A for 3.4 to 3.52 GHz for positions 1 to 3, (a) to (c) respectively with a RIS orientation of 30°.

While a given configuration may greatly benefit a user at a particular location, this may be

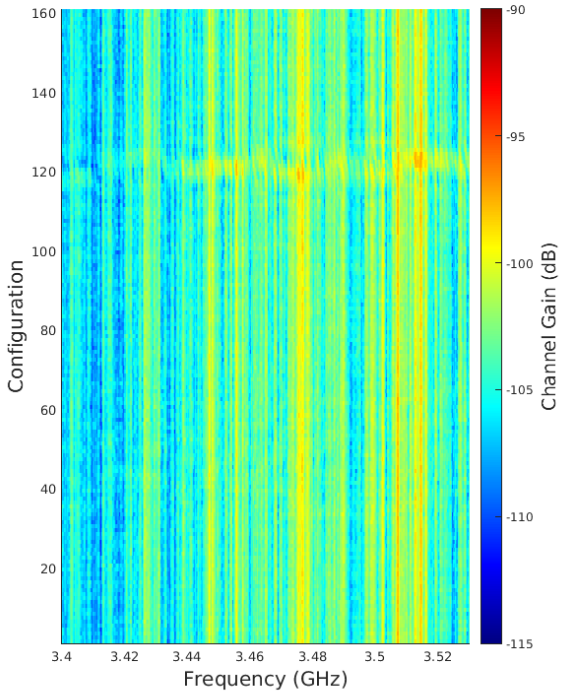

(a) Position 1

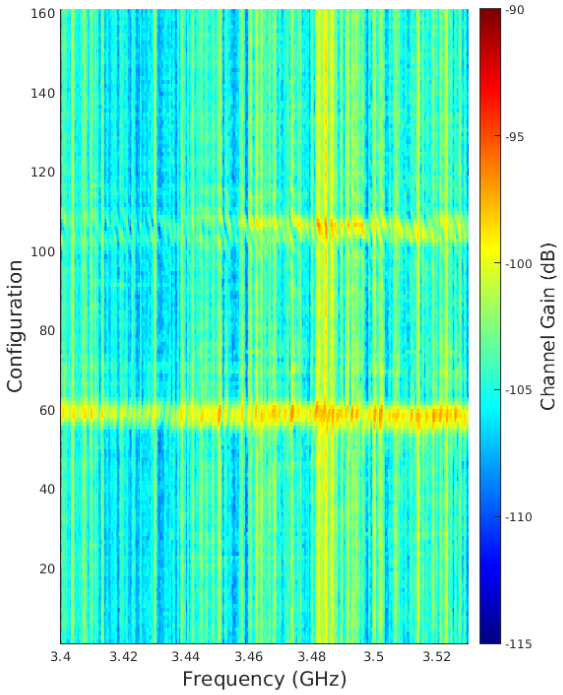

(b) Position 2

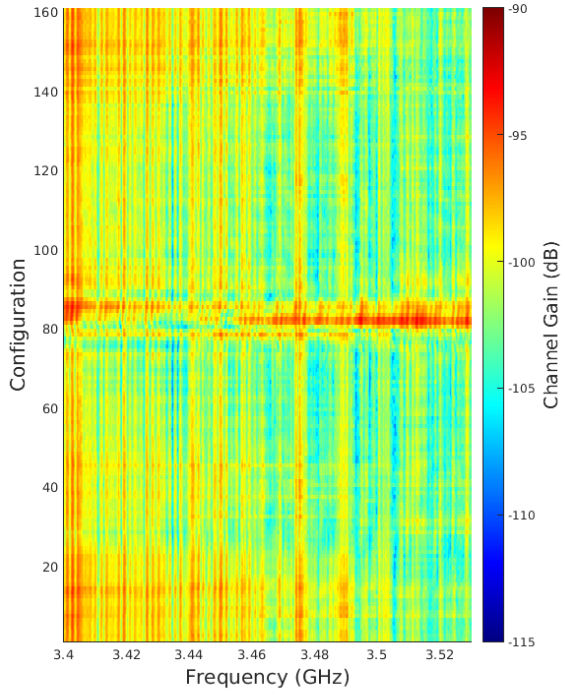

(c) Position 3

Figure 5.46: Beam sweep performance in Zone A for 3.4 to 3.52 GHz for positions 1 to 3, (a) to (c) respectively with a RIS orientation of 0°.

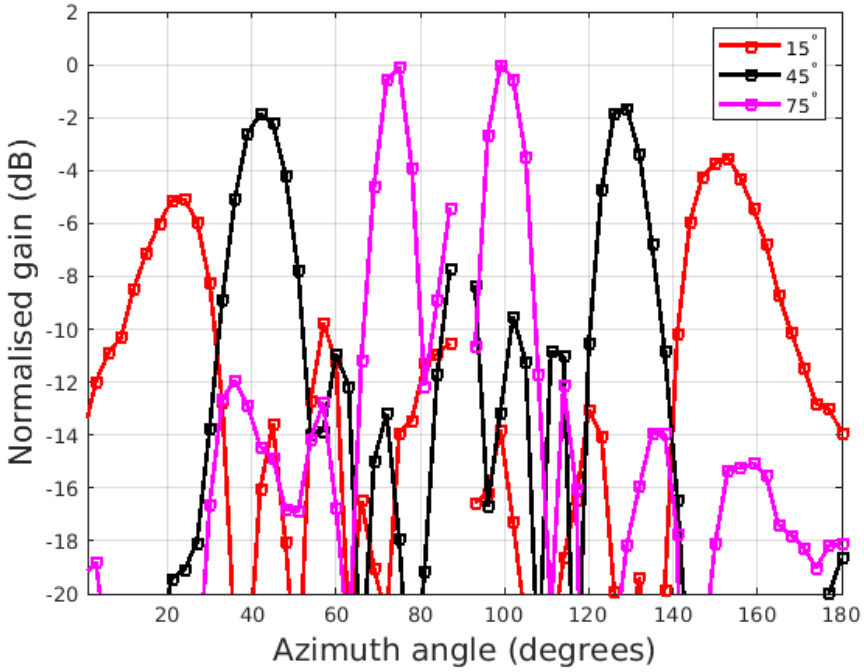

Figure 5.47: Measured beam patterns for maximum re-radiation towards 15°, 45°, and 75°, for incidence at broadside.

to the detriment of another user who may wish to be served by a neighboring cell, only to be subject to increased interference via the RIS. For example, the channel gain versus configuration for the 3 Zone A positions at 3.5 GHz is plotted in Fig. 5.49. The main lobes do not appear to overlap due to the finite beamwidth of the RIS amongst the sparse receiver locations. However, observing the channel gain response at configuration 144, it can be seen that a spike in channel gain at position 1 appears and is associated with one of the configurations resulting in a favorable channel gain at position 2. This means that, without some form of mitigation, a signal sent via the RIS programmed to configuration 144 will unwittingly result in an interfering signal at position 2 that is 5.3 dB stronger in magnitude than the reference case. Mitigation of this might include null steering at the side of the receiver in the form of equalisation.

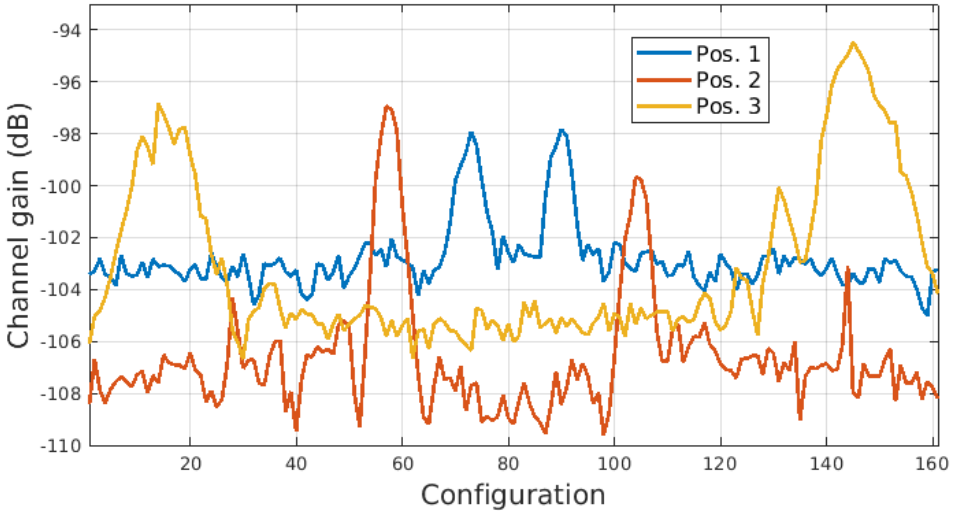

Figure 5.48: Channel gain versus configuration at 3.5 GHz in Zone A for the 3 receiver positions with a RIS orientation of 30°.

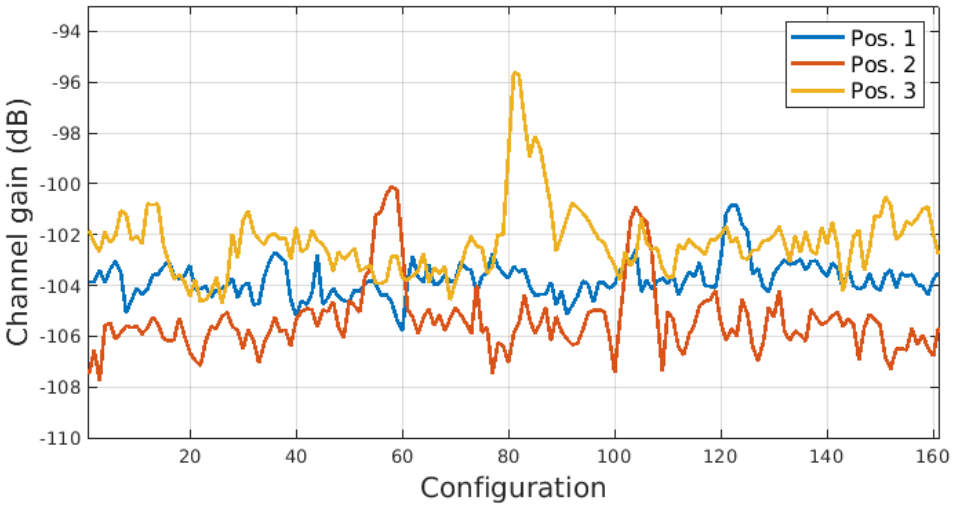

Figure 5.49: Channel gain versus configuration at 3.5 GHz in Zone A for the 3 receiver positions with a RIS orientation of 0°.

The beam sweeping measurement in zone A was also performed for a RIS orientation of 0°. The resulting channel gain versus configuration is plotted in Fig. 5.46 for the 3 receiver locations. A similar trend can be witnessed in terms of the variation in the preferred configuration versus user position, as could be expected. However, the user at position 1 would not benefit from as much improvement as the 30° case. This is likely due to the obliqueness of the re-radiation angle compared to the previous case.

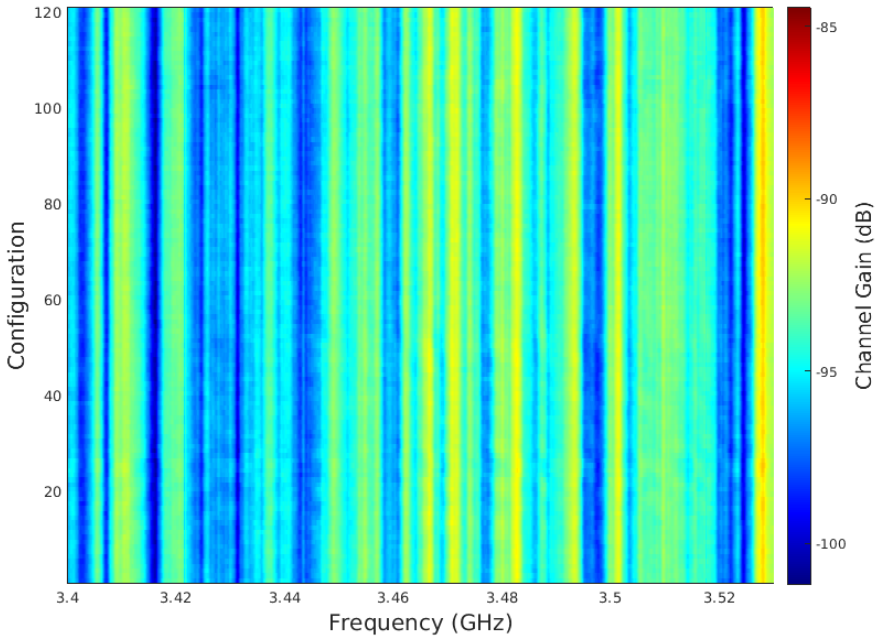

Figure 5.50: Beam sweep performance in Zone B for 3.4 to 3.52 GHz for position 3.

The approach given above was repeated for Zone B, position 3. The resulting beam sweep for zone B, position 3 is plotted in Fig. 5.50. It can be seen that, similarly to the results discussed in 5.5.3, the impact of the RIS on the MIMO channel gain in this location appears to be negligible for this set of configurations. This is likely owing to the fact that the the main from the transmit antenna is not aligned in such a way as to be intercepted by the RIS. Instead, strong multipath components from the surrounding building benefit the wireless link in the fashion intended for sub-6 GHz MIMO links.

5.7 Temporal channel characteristics

The temporal channel characteristics of Zone A are considered here. The power delay profile (PDP) of the H_{11} channel in Position 3, Zone A, is plotted in 5.51(a) for the reference and optimised cases. Referring to the scaled PDP plot of Fig. 5.51(b), it can be seen that there is a notable peak at approximately 0.71 μs. This corresponds with the optimised RIS. The root mean square (RMS) delay spread is derived by taking the square root of the second moment of the normalized power density spectrum:

$$\tau_{rms} = \sqrt{\frac{\int_0^\infty (\tau - \bar{\tau})^2 A_c(\tau) d\tau}{\int_0^\infty A_c(\tau) d\tau}} \tag{5.7}$$

where A_c is the power delay profile and $\bar{\tau}$ is the mean channel delay given by:

$$\bar{\tau} = \sqrt{\frac{\int_0^\infty \tau A_c(\tau) d\tau}{\int_0^\infty A_c(\tau) d\tau}} \tag{5.8}$$

The delay spread for the reference and optimised cases are 4.83 and 4.70 μs, respectively. The respective mean delays are 1.61 and 1.76 μs. These discrepancies are due to the bulk of the power being delivered earlier by the RIS in the optimised case, which is an interacting object in close proximity to the receiver. These results suggest that the deployment of a RIS may help to reduce inter-symbol interference (ISI) by cleaning up the delay spectrum of the channel.

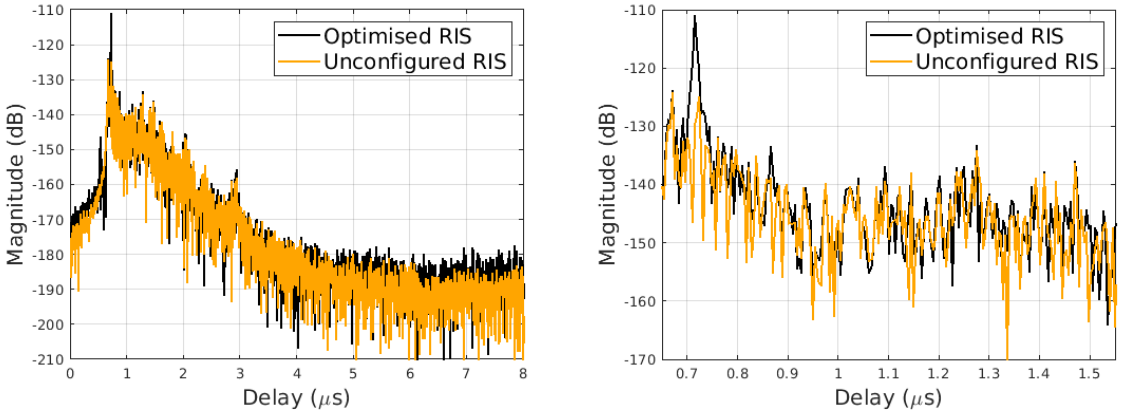

(a) (b)

Figure 5.51: Power delay profile of H_{11} for the unconfigured and optimised RIS settings.

5.8 Spatial channel characteristics

In this section, the spatial characteristics of the most interesting measurement area, Zone A, are explored. The significant spectral efficiency enhancement associated with MIMO systems depends on maintaining multiple orthogonal spatial streams. One measure of the orthogonality of the channel, $\mathbf{H}$, that supports these streams is the condition (in dB) of the channel matrix, κ, defined as [51]:

$$\kappa(H) = 10\log\left(\frac{\lambda_{\max}(\mathbf{H})}{\lambda_{\min}(\mathbf{H})}\right) \tag{5.9}$$

Where $\lambda_{\max}(\mathbf{H})$ and $\lambda_{\min}(\mathbf{H})$ are the largest and smallest singular values of the channel matrix $\mathbf{H}$. The condition number of a matrix is a measure of its numerical stability and, in the context of MIMO systems, reflects how well the system can separate and transmit independent data streams through its spatial channels. A higher condition number indicates that the spatial channels are more correlated, and this means there is less spatial diversity available for data transmission. In other words, when the condition number is high, it becomes more challenging to distinguish between different spatial channels, reducing the system's capacity and performance. A perfectly orthogonal channel has a condition number of 0 dB. In terms of capacity, a 0 dB condition number implies that the channel can support the equivalent of $\min(N_{tx}, N_{rx})$ parallel SISO channels. Condition numbers of up to 10 dB are generally considered acceptable for MIMO communications [51]. The condition numbers for the reference and optimised cases are plotted in Fig. 5.52. The mean condition numbers for the respective positions and bands are shown in Table 5.1.

Position	Band 1		Band 2	
	Reference	Optimised	Reference	Optimised
Pos. 1	10.3	13.2	10.0	11.6
Pos. 2	10.7	14.3	8.5	12.9
Pos. 3	10.8	15.8	9.5	14.0

Table 5.1: Mean condition numbers (dB) for Zone A

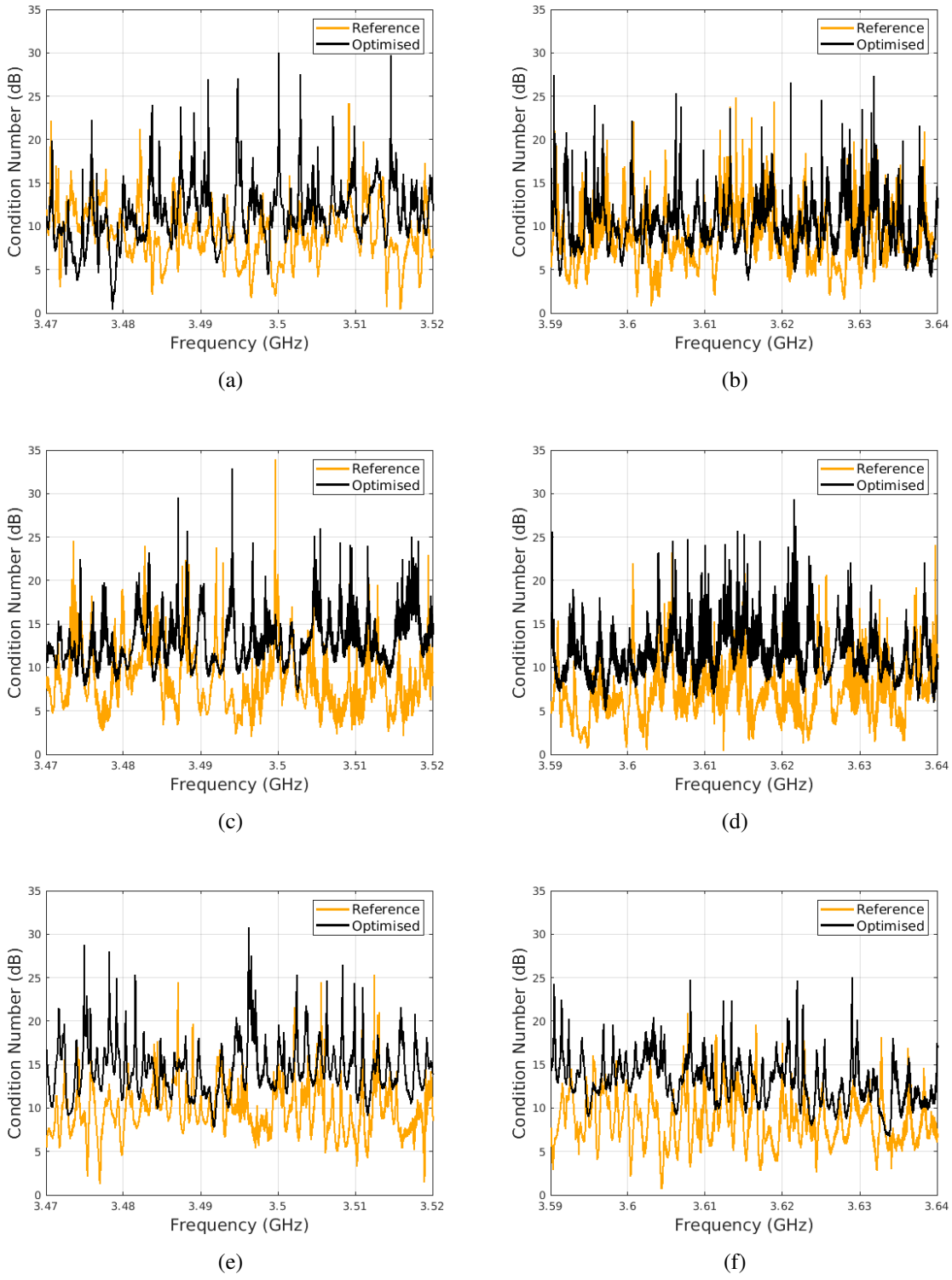

Figure 5.52: Condition numbers of the channel for Position 3, Zone A.

In the reference case, it can be seen that the mean condition numbers for the 3 positions are close to the acceptable 10 dB margin for MIMO operation. It would appear that when the RIS becomes the dominant propagation path, after optimisation, then the condition number deteriorates at all positions. It can be seen that as the receiver moves closer to the RIS, the

condition number difference increases. This behaviour is apparent in both the lower and higher bands of interest. These results can be expected, as a lower condition number is associated with richer multipath propagation. As the VLoS link via the RIS becomes the dominant propagation mechanism, effectively lowering the spatial diversity.

Another measure of the channel dimensionality is the *effective rank* introduced by Roy and Vetterli [169]. The effective rank quantifies the number of independent spatial dimensions effectively utilised by the channel, determined by the effective number of non-negligible singular values. For the 4×4 MIMO system employed here, a maximum effective rank of 4 is possible. In practice, the effective rank can vary profusely and is largely dependent on the richness of the multipath and mutual coupling between the antennas. This has been plotted for position 3, Zone A, in Fig. 5.53. The introduction of the RIS has detrimental implications for the spatial structure of the channel in this instance, with an effective rank reduction across the band. The mean effective ranks for positions 1 to 3, Zone A, for the reference case were calculated as 2.74, 2.87, and 2.61, respectively. With the introduction of the RIS, these are reduced to 2.24, 2.43, and 2.02, respectively. In this implementation, the increase in channel gain clearly comes at the cost of reduced diversity. This effective rank reduction could, for example, result in the communication system being more sensitive to interference [50].

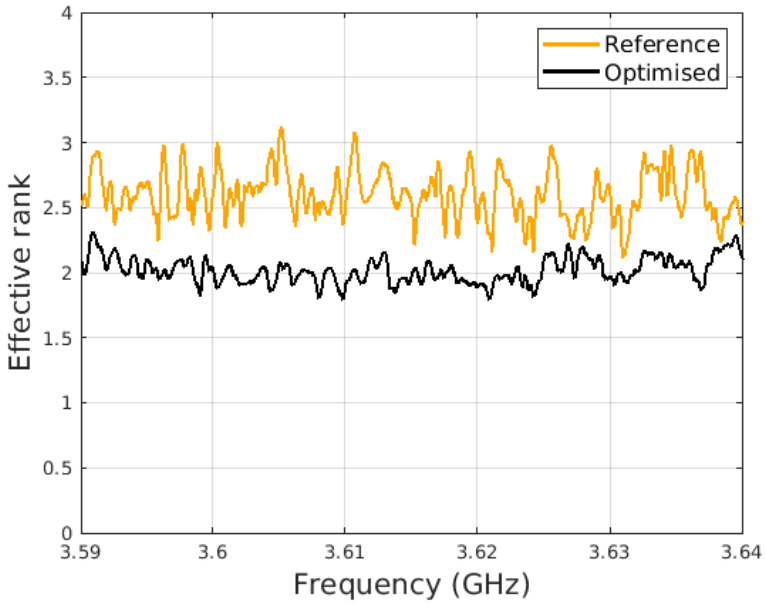

Figure 5.53: Effective rank for position 3, zone A within the 3.59 to 3.64 GHz band.

5.9 Summary

In this chapter, the results obtained from a comprehensive measurement campaign on RIS-aided MIMO communications within existing 5G network infrastructure have been presented. Analysis of these results has revealed a channel gain enhancement of 10 to 15 dB under specific conditions, achieved through the deployment of a RIS with a low-complexity beam search algorithm. These gain increases are realised with a RIS power consumption in the region of 10 mW. The introduction of RISs into currently deployed 5G networks holds the promise of significantly improving network performance by addressing underperforming regions within cells. However, this may come at the cost of deterioration of the spatial diversity of the MIMO channel. Future directions for this research may include measuring the potential impacts of real-world RIS deployment on inter-user and neighboring cell interference as well as potential performance benefits to multi-user MIMO communication systems.

Chapter 6 was focused on performance of RIS-aided communication systems at sub-6 GHz frequencies. This is relevant for mobile networks such as the iteration of 5G currently deployed in the UK. The rollout of 5G mmWave is currently underway and efforts have begun for cost-effective deployment. Operating bands from 24 to 40 GHz have been opened up and this would create a much wider operating bandwidth, with associated higher data rates, and lower latency communications. A major caveat is that there are significant propagation challenges associated with these bands. RISs have been poised as a potential technology to overcome some of the limitations of mmWave communication systems [170]. These challenges include high path loss, limited range and penetration, and increased infrastructure cost .

At sub-6 GHz, large-scale fading is prominent due to the strong presence of multipath [171]. This was reflected in the measurements carried out in this chapter, where the NLoS channels gave rise to significant fluctuations in channel gain experienced at each antenna pair. However, enough degrees of freedom existed in the spatial channel characteristics to perform effective equalisation even prior to the introduction of the RIS. On extension to mmWave frequencies, the following observations might be expected:

- We could expect a significant gain improvement for the same RIS surface area due to the electrical size of the RIS with increasing with increasing frequency [172]. This would mitigate the significant larger path loss at mmWave [173].

- For similar receiver positions, the channel gain characteristics for the reference case (i.e., without the RIS) would be signficantly less favorable. This is mainly due to reduced multipath propagation, resulting in the blockage caused by adjacent buildings being more severe [174].

- The observed channel rank trend may be the opposite of that measured at sub-6 GHz. That is, an increase in the channel rank might be observed on introduction of the RIS due to

the addition of a prominent propagation path [175]. This is in contrast to the RIS-aided system resulting in greater channel sparsity in our sub-6 GHz trials.

Chapter 6

Conclusion and future work

6.1 Concluding remarks

This work has sought to shed light on the practical implications of RISs as an enabler for the smart radio environment paradigm. The objectives of this research were the development of novel RIS prototypes, a thorough investigation of their performance and limitations, and deployment in RIS-aided communication systems to determine potential performance benefits in real-world scenarios. To meet these objectives, a data-driven approach has been taken from the outset. Chapter 2 laid the foundation by providing an extensive review of RIS operating principles, system descriptions, measurement approaches, and existing field trials. Chapter 3 advanced the field by exploring novel design strategies for digital RISs. Leveraging nature-inspired approaches, two distinct prototypes were developed—a high-resolution 3-bit RIS enabling precise beamsteering in azimuth and a low-power 1-bit dual-linear polarised RIS with 3-dimensional beam control. Building upon these designs, Chapter 4 presented results from indoor field trials employing a 3-bit RIS. An iterative optimisation algorithm enhanced NLoS communication scenarios, demonstrating significant channel improvements in diverse environments. In Chapter 5, the investigation was extended to outdoor urban macrocells with a 1-bit RIS. Overcoming challenges of low SNR, a noise-resistant RIS beam search algorithm was introduced, showcasing improvements in channel gain and revealing variations in spatial and temporal channel characteristics. This cumulative research, detailed across chapters, not only expands our theoretical understanding of RISs but also presents tangible prototypes and field trial results, bridging the gap between theory and real-world application.

Key findings

Some of the key findings of this work are the following:

- High-performance 3-bit RISs can be practically implemented with the minimal 3 active components per unit cell by employing nature-inspired optimisation algorithms.

- Digital control of varactor-based RISs enables a truly near-passive RIS with 3D beamsteering control with commercial off-the-shelf components.
- Introducing additional degrees of freedom in RIS reflection coefficient selection appears to enable a very wide operating band, potentially warranting further investigation into high phase agility reflecting metasurfaces.
- Even when limited to beamsteering control in azimuth, RISs may have a role to play in indoor wireless communication systems, vastly reducing the complexity of implementation.
- 3-bit RISs appear to retain their performance advantage over 1- and 2-bit devices even in complex propagation scenarios, but the performance gains may not warrant the significant increase in complexity compared to lower resolution designs.
- A practical beam-search algorithm relying on a forward model has shown resilience to noise when compared to iterative-based approaches when employed for long-range RIS-aided communications field trials.
- Existing urban macrocells may benefit from the introduction of RISs in specific scenarios. For instance, with a significant blockage alongside proper RIS beam alignment with the transmitter antenna.
- Analysis of the impacts of RISs on the spatial structure of a MIMO channel has revealed that RIS introduction into existing networks may in fact be detrimental to the effective channel rank if not carefully configured.

Limitations

This work has not specifically focused on the optimality of the RIS configuration schemes employed, rather opting for simple approaches that are 'good enough'. With this in mind, the results presented in the various field measurements in this thesis could be considered as sub-optimal and one might expect further performance enhancement and overhead reduction through more intelligent configuration schemes. In addition to the simplicity of the configuration schemes, the works focused mostly on maximising the channel gain at a single user position for single and multiple antennas. While this information is useful, the effects of a given RIS configuration on nearby users was not explored in great detail. A more in-depth investigation would reveal the impact RISs have on co-channel and inter-cell interference, being particularly important for mobile operator coexistence.

The respective field trials studies were limited to a small number of positions in two different locations. Although this work has generated some initial data on RIS-aided communication systems in the real world, a much wider range of channel measurements should be made in more

diverse settings and this will no doubt be the subject of future works. Due to practical limitations in the measurement setups, it was not possible to ascertain mobility-related effects in the RIS-aided communication system field trials. While this does not represent a significant limitation in indoor communications, where users may be mostly static or slowly-moving, outdoor channel characterisation may require such measurements. The frequency-domain channel sounder setup employed for the outdoor field trials required tethering to an AC power outlet and a fiber optic cabinet. Additionally, it was not possible to secure permission to move the VNA in the manner required for such measurements. For mobility measurements, a time-domain highly-mobile channel sounder such as that introduced by Choi et al. [176] could be used to overcome these limitations.

Potential implications

Carriers and network infrastructure providers are the most likely industrial stakeholders to benefit from this technology [177] [120], contending with the scarcity of spectrum, high deployment and maintainance costs, and high power consumption of current mobile networks. The findings and contributions of this research have significant implications for the industrial deployment of RISs in wireless communication systems. In this realm, efforts towards standardisation have already begun, with approval in June 2021 for the European Telecommunications Standards Institute (ETSI) Industry Specification Group on RISs [120]. The practical outcomes and insights gained from this thesis can potentially shape the evolution of communication technologies and influence industry practices. Several key industrial implications can be drawn from the research:

- **Green communications**: The significant channel gain enhancements demonstrated with the 1-bit RIS prototype in section 5.5.2 were realised with a RIS prototype consuming approximately 10 mW. To meet the 1 Gbps channel capacity desired for a 5G network, the transmit power could be reduced by a factor of 8 compared to the scenario before the RIS introduction. A low-cost, low-maintenance RIS introduced into a network could offer significant reductions in power consumption. Furthermore, RISs may serve as an alternative to active nodes in wireless networks, such as access points and relays, thereby reducing the carbon footprint of network operation further.

- **Network deployment costs**: The planar, column-driven design of the 3-bit RIS introduced in Chapter 3 represents a low cost solution to RISs when a more limited beam-steering agility is acceptable. If RISs were to play a role in widening the operational area of cells, inexpensive RIS designs employing well-established manufacturing techniques could lead to network deployment costs that are orders of magnitude lower than for contemporary infrastructure.

- **Band-tunability**: Both of the RIS prototypes employed in field trials in this work have been determined to exhibit a wide enough instantaneous bandwidth to serve the current

iteration of 5G sub-6 GHz networks. The band-tunability demonstrated with the 3-bit RIS in section 4.4.3 offers a potential deployment technique so as to serve individual carriers from the same RIS aperture in different time intervals. This flexibility could also ensure compatibility with legacy infrastructure.

- **Integration into the built environment**: The positioning of RISs in the measurements performed in this thesis was carefully considered in all cases. This was to ensure that one of the main selling points of RISs remained in-tact throughout - their ease of integration into our built environment. Indoor deployments are more inflexible owing to large planar objects causing more of an obstruction. Nonetheless, the three scenarios considered in Chapter 4 exhibited substantial performance enhancements on introducing RISs parallel and in close proximity to walls, indicating that embedding RISs subject to environmental constraints is viable.

- **Channel configuration considerations:** The analysis of the impacts of RISs on the spatial structure of a MIMO channel emphasises the importance of careful configuration. Industries integrating RISs into existing networks must consider the potential effects on channel rank to ensure optimal network performance.

In conclusion, the industrial implications of this research extend beyond theoretical insights, providing actionable guidance for the development and deployment of RISs in real-world wireless communication scenarios.

6.2 Future work

Integration and manufacturing processes: Future research efforts could focus on the development of RISs that can more seamlessly be integrated into our built environments. Although the prototypes introduced in this thesis employed well-established fabrication techniques in combination with commercial off-the-shelf components, these processes are still relatively expensive owing to the low-loss substrates and large numbers of semiconductor components. The recent rise in printable electronics research and development could offer a means of scalable fabrication of RISs. Alongside flexible substrates and/or optically-transparent conductors, the impact of a mass rollout of smart surfaces would only be noticeable in the additional signal bars we witness on our cell phones. This would be a significant divergence from the conspicuous mobile base station infrastructure arising with the latest generation of cellular networks.

Further MIMO channel characterisation: Experimental verification of the smart radio environment paradigm is very much still in its infancy. A starting point for future research efforts would be to address a number of the points raised in the *limitations* section above. The impact of mobility on the outdoor RIS-aided MIMO channel would offer valuable insights into the real-

world performance benefits of RIS. This could be assessed in combination with a mobility-aware optimisation algorithm.

In-band full-duplex communication systems: The capability of RISs to dynamically alter the wireless channel could have significant implications for full-duplex (FD) communication systems. FD communication systems are limited by self-interference and rely on sophisticated analog and digital cancellation techniques to mitigate this. Self-interference occurs through coupling between the transmit and receive ports both locally and from environmental reflections. Since we can control environmental reflections with RISs, we can also improve self-interference cancellation by exploiting the spatial domain, as shown experimentally in [178]. However, there is much scope for further extension of this work to combine self-interference cancellation with RIS-aided beamforming as well as multi-antenna self-interference cancellation.

Joint communications and sensing: Integrated sensing and communications (ISAC) may hold the key to alleviating electromagnetic congestion and system complexity through operation of radar and/or localisation and wireless communications functionalities within the same infrastructure. Experimental demonstrations in RIS-enabled ISAC literature are currently relatively few but provide enormous scope for future contributions.

Bibliography

[1] H. F. Alvarez, M. E. de Cos Gomez, and F. Las-Heras, "Paving the way for suitable metasurfaces' measurements under oblique incidence: Mono-/bistatic and near-/far-field concerns," *IEEE Transactions on Instrumentation and Measurement*, vol. 69, pp. 1737–1744, apr 2020.

[2] D. Wang, L.-Z. Yin, T.-J. Huang, F.-Y. Han, Z.-W. Zhang, Y.-H. Tan, and P.-K. Liu, "Design of a 1 bit broadband space-time-coding digital metasurface element," *IEEE Antennas and Wireless Propagation Letters*, vol. 19, pp. 611–615, apr 2020.

[3] V. Popov, M. Odit, J.-B. Gros, V. Lenets, A. Kumagai, M. Fink, K. Enomoto, and G. Lerosey, "Experimental demonstration of a mmwave passive access point extender based on a binary reconfigurable intelligent surface," *Front. Comms. Net 2:733891*.

[4] A. Wolff, L. Franke, S. Klingel, J. Krieger, L. Mueller, R. Stemler, and M. Rahm, "Continuous beam steering with a varactor-based reconfigurable intelligent surface in the ka-band at 31 GHz," *Journal of Applied Physics*, vol. 134, sep 2023.

[5] S. Spatola, J. S. Gomez-Diaz, and E. Carrasco, "Time modulated reflectarray unit-cells with nonreciprocal polarization control," in *2020 14th European Conference on Antennas and Propagation (EuCAP)*, IEEE, mar 2020.

[6] H. Yang, X. Cao, F. Yang, J. Gao, S. Xu, M. Li, X. Chen, Y. Zhao, Y. Zheng, and S. Li, "A programmable metasurface with dynamic polarization, scattering and focusing control," *Scientific Reports*, vol. 6, oct 2016.

[7] L. Dai, B. Wang, M. Wang, X. Yang, J. Tan, S. Bi, S. Xu, F. Yang, Z. Chen, M. D. Renzo, C.-B. Chae, and L. Hanzo, "Reconfigurable intelligent surface-based wireless communications: Antenna design, prototyping, and experimental results," *IEEE Access*, vol. 8, pp. 45913–45923, 2020.

[8] Z. Chen, *Handbook of antenna technologies*. Singapore: Springer Reference, 2016.

[9] Ericsson, "Ericsson mobility report: Global 5g growth amid macroeconomic challenges," Nov. 2023.

[10] J. Lee, E. Tejedor, K. Ranta-aho, H. Wang, K.-T. Lee, E. Semaan, E. Mohyeldin, J. Song, C. Bergljung, and S. Jung, "Spectrum for 5g: Global status, challenges, and enabling technologies," *IEEE Communications Magazine*, vol. 56, pp. 12–18, mar 2018.

[11] I. F. Akyildiz, S. Nie, S.-C. Lin, and M. Chandrasekaran, "5g roadmap: 10 key enabling technologies," *Computer Networks*, vol. 106, pp. 17–48, sep 2016.

[12] Özlem Tugfe Demir, E. Björnson, and L. Sanguinetti, "Foundations of user-centric cell-free massive MIMO," *Foundations and Trends® in Signal Processing*, vol. 14, no. 3-4, pp. 162–472, 2021.

[13] N. Wang, E. Hossain, and V. K. Bhargava, "Backhauling 5g small cells: A radio resource management perspective," *IEEE Wireless Communications*, vol. 22, pp. 41–49, oct 2015.

[14] A. BenMimoune and M. Kadoch, "Relay technology for 5g networks and IoT applications," in *Studies in Big Data*, pp. 3–26, Springer International Publishing, 2017.

[15] E. Bjornson, O. Ozdogan, and E. G. Larsson, "Intelligent reflecting surface versus decode-and-forward: How large surfaces are needed to beat relaying?," *IEEE Wireless Communications Letters*, vol. 9, pp. 244–248, feb 2020.

[16] M. D. Renzo, K. Ntontin, J. Song, F. H. Danufane, X. Qian, F. Lazarakis, J. D. Rosny, D.-T. Phan-Huy, O. Simeone, R. Zhang, M. Debbah, G. Lerosey, M. Fink, S. Tretyakov, and S. Shamai, "Reconfigurable intelligent surfaces vs. relaying: Differences, similarities, and performance comparison," *IEEE Open Journal of the Communications Society*, vol. 1, pp. 798–807, 2020.

[17] M. D. Renzo, A. Zappone, M. Debbah, M.-S. Alouini, C. Yuen, J. de Rosny, and S. Tretyakov, "Smart radio environments empowered by reconfigurable intelligent surfaces: How it works, state of research, and the road ahead," *IEEE Journal on Selected Areas in Communications*, vol. 38, pp. 2450–2525, nov 2020.

[18] A. L. Robert W. Heath Jr, *Foundations of Mimo Communication*. CAMBRIDGE, 2018.

[19] F. Yang and Y. Rahmat-Samii, eds., *Surface Electromagnetics*. Cambridge University Press, jun 2019.

[20] C. Caloz and Z.-L. Deck-Leger, "Spacetime metamaterials—part i: General concepts," mar 2020.

[21] K. Achouri, M. A. Salem, and C. Caloz, "General metasurface synthesis based on susceptibility tensors," *IEEE Transactions on Antennas and Propagation*, vol. 63, pp. 2977–2991, jul 2015.

[22] K. Achouri and C. Caloz, "Design, concepts, and applications of electromagnetic metasurfaces," *Nanophotonics*, vol. 7, pp. 1095–1116, jun 2018.

[23] V. Degli-Esposti, E. M. Vitucci, M. D. Renzo, and S. A. Tretyakov, "Reradiation and scattering from a reconfigurable intelligent surface: A general macroscopic model," *IEEE Transactions on Antennas and Propagation*, vol. 70, pp. 8691–8706, Oct. 2022.

[24] N. M. Estakhri and A. Alù, "Wave-front transformation with gradient metasurfaces," *Physical Review X*, vol. 6, oct 2016.

[25] C. A. Balanis, *Advanced Engineering Electromagnetics*. John Wiley Sons Inc, 2012.

[26] W. Tang, M. Z. Chen, X. Chen, J. Y. Dai, Y. Han, M. D. Renzo, Y. Zeng, S. Jin, Q. Cheng, and T. J. Cui, "Wireless communications with reconfigurable intelligent surface: Path loss modeling and experimental measurement,"

[27] Munk, *Frequency Selective Surfaces*. John Wiley and Sons, 2000.

[28] J. Xia, A. K. Jordan, and J. A. Kong, "Electromagnetic inverse-scattering theory for inhomogeneous dielectrics: the local reflection model," *J. Opt. Soc. Am. A*, vol. 11, pp. 1081–1086, Mar 1994.

[29] M. J. Mencagli, E. Martini, S. Maci, and M. Albani, "A physical optics approach to the analysis of metascreens," *IEEE Access*, vol. 8, pp. 162634–162641, 2020.

[30] S. Abeywickrama, R. Zhang, Q. Wu, and C. Yuen, "Intelligent reflecting surface: Practical phase shift model and beamforming optimization," *IEEE Transactions on Communications*, vol. 68, pp. 5849–5863, sep 2020.

[31] D. M. Pozar, *Microwave Engineering*. John Wiley Sons Inc, 2011.

[32] V. E. C. Model, "Varactor spice models for rf vco applications," 2010.

[33] H. Taghvaee, S. Abadal, A. Pitilakis, O. Tsilipakos, A. C. Tasolamprou, C. Liaskos, M. Kafesaki, N. V. Kantartzis, A. Cabellos-Aparicio, and E. Alarcon, "Scalability analysis of programmable metasurfaces for beam steering," *IEEE Access*, vol. 8, pp. 105320–105334, 2020.

[34] A. Diaz-Rubio, V. S. Asadchy, A. Elsakka, and S. A. Tretyakov, "From the generalized reflection law to the realization of perfect anomalous reflectors," *Science Advances*, vol. 3, p. e1602714, aug 2017.

[35] Q. Wu, S. Zhang, B. Zheng, C. You, and R. Zhang, "Intelligent reflecting surface aided wireless communications: A tutorial,"

[36] H. Taghvaee, A. Cabellos-Aparicio, J. Georgiou, and S. Abadal, "Error analysis of programmable metasurfaces for beam steering," *IEEE Journal on Emerging and Selected Topics in Circuits and Systems*, vol. 10, pp. 62–74, mar 2020.

[37] J. Budhu and A. Grbic, "Perfectly reflecting metasurface reflectarrays: Mutual coupling modeling between unique elements through homogenization," *IEEE Transactions on Antennas and Propagation*, vol. 69, pp. 122–134, jan 2021.

[38] Y. Abdallah, C. Menudier, M. Thevenot, and T. Monediere, "Investigations of the effects of mutual coupling in reflectarray antennas," *IEEE Antennas and Propagation Magazine*, vol. 55, pp. 49–61, apr 2013.

[39] W. Chen, L. Bai, W. Tang, S. Jin, W. X. Jiang, and T. J. Cui, "Angle-dependent phase shifter model for reconfigurable intelligent surfaces: Does the angle-reciprocity hold?," *IEEE Communications Letters*, vol. 24, pp. 2060–2064, sep 2020.

[40] W. Tang, X. Chen, M. Z. Chen, J. Y. Dai, Y. Han, S. Jin, Q. Cheng, G. Y. Li, and T. J. Cui, "On channel reciprocity in reconfigurable intelligent surface assisted wireless networks," *IEEE Wireless Communications*, vol. 28, pp. 94–101, dec 2021.

[41] A. Enqvist, T. Demir, C. Cavdar, and E. Björnson, "Optimizing reconfigurable intelligent surfaces for short transmissions: How detailed configurations can be afforded?," *IEEE Transactions on Wireless Communications*, vol. 23, pp. 3377–3391, Apr. 2024.

[42] M. D. Renzo, A. Ahmed, A. Zappone, V. Galdi, G. Gradoni, M. Moccia, and G. Castaldi, "Digital reconfigurable intelligent surfaces: On the impact of realistic reradiation models,"

[43] H. Zhang, B. Di, L. Song, and Z. Han, "Reconfigurable intelligent surfaces assisted communications with limited phase shifts: How many phase shifts are enough?," *IEEE Transactions on Vehicular Technology*, vol. 69, pp. 4498–4502, apr 2020.

[44] J. Wang, W. Tang, J. C. Liang, L. Zhang, J. Y. Dai, X. Li, S. Jin, Q. Cheng, and T. J. Cui, "Reconfigurable intelligent surface: Power consumption modeling and practical measurement validation," *IEEE Transactions on Communications*, pp. 1–1, 2024.

[45] E. Bjornson and L. Sanguinetti, "Power scaling laws and near-field behaviors of massive MIMO and intelligent reflecting surfaces," *IEEE Open Journal of the Communications Society*, vol. 1, pp. 1306–1324, 2020.

[46] E. Bjornson and L. Sanguinetti, "Demystifying the power scaling law of intelligent reflecting surfaces and metasurfaces," in *2019 IEEE 8th International Workshop on Computational Advances in Multi-Sensor Adaptive Processing (CAMSAP)*, IEEE, dec 2019.

[47] F. H. Danufane, M. D. Renzo, J. de Rosny, and S. Tretyakov, "On the path-loss of reconfigurable intelligent surfaces: An approach based on green's theorem applied to vector fields,"

[48] R. Faqiri, C. Saigre-Tardif, G. C. Alexandropoulos, N. Shlezinger, M. F. Imani, and P. del Hougne, "PhysFad: Physics-based end-to-end channel modeling of RIS-parametrized environments with adjustable fading," *IEEE Transactions on Wireless Communications*, vol. 22, pp. 580–595, jan 2023.

[49] E. Bjornson and L. Sanguinetti, "Rayleigh fading modeling and channel hardening for reconfigurable intelligent surfaces," *IEEE Wireless Communications Letters*, vol. 10, pp. 830–834, apr 2021.

[50] D. Tse and P. Viswanath, *Fundamentals of Wireless Communication*. Cambridge University Press, May 2005.

[51] L. Liu, W. Hong, H. Wang, G. Yang, N. Zhang, H. Zhao, J. Chang, C. Yu, X. Yu, H. Tang, H. Zhu, and L. Tian, "Characterization of line-of-sight MIMO channel for fixed wireless communications," *IEEE Antennas and Wireless Propagation Letters*, vol. 6, pp. 36–39, 2007.

[52] W.-J. Tsay and D. Pozar, "Application of the FDTD technique to periodic problems in scattering and radiation," *IEEE Microwave and Guided Wave Letters*, vol. 3, pp. 250–252, aug 1993.

[53] O. Yesilyurt and G. Turhan-Sayan, "Metasurface lens for ultra-wideband planar antenna," *IEEE Transactions on Antennas and Propagation*, vol. 68, pp. 719–726, feb 2020.

[54] H. F. Alvarez, M. E. de Cos Gomez, and F. Las-Heras, "Angular stability of metasurfaces: Challenges regarding reflectivity measurements [measurements corner]," *IEEE Antennas and Propagation Magazine*, vol. 58, pp. 74–81, oct 2016.

[55] J. Perruisseau-Carrier, F. Bongard, R. Golubovic-Niciforovic, R. Torres-Sánchez, and J. R. Mosig, "Contributions to the modeling and design of reconfigurable reflecting cells embedding discrete control elements," *IEEE Transactions on Microwave Theory and Techniques*, vol. 58, pp. 1621–1628, jun 2010.

[56] P. Hannan and M. Balfour, "Simulation of a phased-array antenna in waveguide," *IEEE Transactions on Antennas and Propagation*, vol. 13, pp. 342–353, may 1965.

[57] D. Rodrigo, L. Jofre, and J. Perruisseau-Carrier, "Unit cell for frequency-tunable beam-scanning reflectarrays," *IEEE Transactions on Antennas and Propagation*, vol. 61, pp. 5992–5999, dec 2013.

[58] J.-B. Gros, V. Popov, M. A. Odit, V. Lenets, and G. Lerosey, "A reconfigurable intelligent surface at mmWave based on a binary phase tunable metasurface," *IEEE Open Journal of the Communications Society*, vol. 2, pp. 1055–1064, 2021.

[59] S. V. Hum, M. Okoniewski, and R. J. Davies, "Modeling and design of electronically tunable reflectarrays," *IEEE Transactions on Antennas and Propagation*, vol. 55, pp. 2200–2210, aug 2007.

[60] C. Diakite, J. Lanteri, and C. Migliaccio, "An outdoor measurement technique for large structures antennas," in *2017 IEEE Conference on Antenna Measurements &amp Applications (CAMA)*, IEEE, dec 2017.

[61] J. Han, L. Li, X. Ma, X. Gao, Y. Mu, G. Liao, Z. J. Luo, and T. J. Cui, "Adaptively smart wireless power transfer using 2-bit programmable metasurface," *IEEE Transactions on Industrial Electronics*, vol. 69, pp. 8524–8534, aug 2022.

[62] P. Leather and D. Parsons, "Equalization for antenna-pattern measurements: Established technique - new application," *IEEE Antennas and Propagation Magazine*, vol. 45, pp. 154–161, apr 2003.

[63] L. Zhang and T. J. Cui, "Angle-insensitive 2-bit programmable coding metasurface with wide incident angles," in *2019 IEEE Asia-Pacific Microwave Conference (APMC)*, IEEE, dec 2019.

[64] X. Pei, H. Yin, L. Tan, L. Cao, Z. Li, K. Wang, K. Zhang, and E. Björnson, "Ris-aided wireless communications: Prototyping, adaptive beamforming, and indoor/outdoor field trials," *arXiv preprint arXiv:2103.00534*.

[65] B. O. Zhu, J. Zhao, and Y. Feng, "Active impedance metasurface with full 360° reflection phase tuning," *Scientific Reports*, vol. 3, oct 2013.

[66] J. Wang, W. Tang, J. C. Liang, L. Zhang, J. Y. Dai, X. Li, S. Jin, Q. Cheng, and T. J. Cui, "Reconfigurable intelligent surface: Power consumption modeling and practical measurement validation," Nov. 2022.

[67] S. V. Hum and J. Perruisseau-Carrier, "Reconfigurable reflectarrays and array lenses for dynamic antenna beam control: A review," *IEEE Transactions on Antennas and Propagation*, vol. 62, pp. 183–198, jan 2014.

[68] J. P. Turpin, J. A. Bossard, K. L. Morgan, D. H. Werner, and P. L. Werner, "Reconfigurable and tunable metamaterials: A review of the theory and applications," *International Journal of Antennas and Propagation*, vol. 2014, pp. 1–18, 2014.

[69] O. Tsilipakos, F. Liu, A. Pitilakis, A. Tasolamprou, D.-H. Kwon, M. Mirmoosa, N. Kantartzis, E. Economou, M. Kafesaki, C. Soukoulis, and S. Tretyakov, "Tunable perfect anomalous reflection in metasurfaces with capacitive lumped elements," in *2018 12th International Congress on Artificial Materials for Novel Wave Phenomena (Metamaterials)*, IEEE, aug 2018.

[70] J. Zang, D. Correas-Serrano, J. Do, X. Liu, A. Alvarez-Melcon, and J. Gomez-Diaz, "Nonreciprocal wavefront engineering with time-modulated gradient metasurfaces," *Physical Review Applied*, vol. 11, may 2019.

[71] A. Z. Ashoor and S. Gupta, "Metasurface reflector with real-time independent magnitude and phase control,"

[72] J. ur Rehman Kazim, M. Ur-Rehman, M. Al-Hasan, I. B. Mabrouk, M. A. Imran, and Q. H. Abbasi, "Design of 1-bit digital subwavelength metasurface element for sub-6 GHz applications," in *2020 International Conference on UK-China Emerging Technologies (UCET)*, IEEE, aug 2020.

[73] F. Yang, S. Xu, X. Pan, X. Yang, J. Luo, M. Wang, Y. Wang, and M. Li, "Reconfigurable reflectarrays and transmitarrays: From antenna designs to system applications," in *12th European Conference on Antennas and Propagation (EuCAP 2018)*, Institution of Engineering and Technology, 2018.

[74] S. Montori, E. Chiuppesi, L. Marcaccioli, R. V. Gatti, and R. Sorrentino, "1-bit RF-MEMS-reconfigurable elementary cell for very large reflectarray," in *2010 10th Mediterranean Microwave Symposium*, IEEE, aug 2010.

[75] C. Huang, C. Zhang, J. Yang, B. Sun, B. Zhao, and X. Luo, "Reconfigurable metasurface for multifunctional control of electromagnetic waves," *Advanced Optical Materials*, vol. 5, p. 1700485, sep 2017.

[76] T. J. Cui, M. Q. Qi, X. Wan, J. Zhao, and Q. Cheng, "Coding metamaterials, digital metamaterials and programming metamaterials,"

[77] B. G. Kashyap, P. C. Theofanopoulos, Y. Cui, and G. C. Trichopoulos, "Mitigating quantization lobes in mmWave low-bit reconfigurable reflective surfaces," *IEEE Open Journal of Antennas and Propagation*, pp. 1–1, 2020.

[78] X. Zhang, H. Zhang, J. Su, and Z. Li, "2-bit programmable digital metasurface for controlling electromagnetic wave," in *2017 Sixth Asia-Pacific Conference on Antennas and Propagation (APCAP)*, IEEE, oct 2017.

[79] Y. Shuang, H. Zhao, W. Ji, T. J. Cui, and L. Li, "Programmable high-order OAM-carrying beams for direct-modulation wireless communications," *IEEE Journal on Emerging and Selected Topics in Circuits and Systems*, vol. 10, pp. 29–37, mar 2020.

[80] F. Zhang, Y. Saifullah, G.-M. Yang, and Y.-Q. Jin, "1-bit, 2-bit polarization insensitive reflection programable metasurface," in *2018 IEEE International Symposium on Antennas and Propagation & USNC/URSI National Radio Science Meeting*, IEEE, jul 2018.

[81] X. Yang, S. Xu, F. Yang, and M. Li, "A novel 2-bit reconfigurable reflectarray element for both linear and circular polarizations," in *2017 IEEE International Symposium on Antennas and Propagation & USNC/URSI National Radio Science Meeting*, IEEE, jul 2017.

[82] C.-C. Cheng and A. Abbaspour-Tamijani, "Design and experimental verification of steerable reflect-arrays based on two-bit antenna-filter-antenna elements," in *2009 IEEE MTT-S International Microwave Symposium Digest*, IEEE, jun 2009.

[83] B. Wu, A. Sutinjo, M. Potter, and M. Okoniewski, "On the selection of the number of bits to control a dynamic digital MEMS reflectarray," *IEEE Antennas and Wireless Propagation Letters*, vol. 7, pp. 183–186, 2008.

[84] C. Qu, S. Ma, J. Hao, M. Qiu, X. Li, S. Xiao, Z. Miao, N. Dai, Q. He, S. Sun, and L. Zhou, "Tailor the functionalities of metasurfaces based on a complete phase diagram," *Physical Review Letters*, vol. 115, dec 2015.

[85] Y. Saifullah, F. Zhang, G.-M. Yang, and F. Xu, "3-bit programmable reflective metasurface," in *2018 12th International Symposium on Antennas, Propagation and EM Theory (ISAPE)*, IEEE, dec 2018.

[86] L. Zhang, Z. X. Wang, R. W. Shao, J. L. Shen, X. Q. Chen, X. Wan, Q. Cheng, and T. J. Cui, "Dynamically realizing arbitrary multi-bit programmable phases using a 2-bit time-domain coding metasurface," *IEEE Transactions on Antennas and Propagation*, vol. 68, pp. 2984–2992, apr 2020.

[87] X. G. Zhang, W. X. Jiang, H. L. Jiang, Q. Wang, H. W. Tian, L. Bai, Z. J. Luo, S. Sun, Y. Luo, C.-W. Qiu, and T. J. Cui, "An optically driven digital metasurface for programming electromagnetic functions," *Nature Electronics*, vol. 3, pp. 165–171, mar 2020.

[88] X. Artiga, "Row–column beam steering control of reflectarray antennas: Benefits and drawbacks," *IEEE Antennas and Wireless Propagation Letters*, vol. 17, pp. 271–274, feb 2018.

[89] K. M. Kossifos, L. Petrou, G. Varnava, A. Pitilakis, O. Tsilipakos, F. Liu, P. Karousios, A. C. Tasolamprou, M. Seckel, D. Manessis, N. V. Kantartzis, D.-H. Kwon, M. A. Antoniades, and J. Georgiou, "Toward the realization of a programmable metasurface absorber enabled by custom integrated circuit technology," *IEEE Access*, vol. 8, pp. 92986–92998, 2020.

[90] L. Petrou, P. Karousios, and J. Georgiou, "Asynchronous circuits as an enabler of scalable and programmable metasurfaces," in *2018 IEEE International Symposium on Circuits and Systems (ISCAS)*, IEEE, 2018.

[91] A. C. Tasolamprou, M. S. Mirmoosa, O. Tsilipakos, A. Pitilakis, F. Liu, S. Abadal, A. Cabellos-Aparicio, E. Alarcon, C. Liaskos, N. V. Kantartzis, S. Tretyakov, M. Kafesaki, E. N. Economou, and C. M. Soukoulis, "Intercell wireless communication in software-defined metasurfaces," *2018 IEEE International Symposium on Circuits and Systems (ISCAS)*.

[92] A. C. Tasolamprou, A. Pitilakis, S. Abadal, O. Tsilipakos, X. Timoneda, H. Taghvaee, M. S. Mirmoosa, F. Liu, C. Liaskos, A. Tsioliaridou, S. Ioannidis, N. V. Kantartzis, D. Manessis, J. Georgiou, A. Cabellos-Aparicio, E. Alarcon, A. Pitsillides, I. F. Akyildiz, S. A. Tretyakov, E. N. Economou, M. Kafesaki, and C. M. Soukoulis, "Exploration of intercell wireless millimeter-wave communication in the landscape of intelligent metasurfaces," *IEEE Access*, vol. 7, pp. 122931–122948, 2019.

[93] S. Abadal, C. Liaskos, A. Tsioliaridou, S. Ioannidis, A. Pitsillides, J. Sole-Pareta, E. Alarcon, and A. Cabellos-Aparicio, "Computing and communications for the software-defined metamaterial paradigm: A context analysis," *IEEE Access*, vol. 5, pp. 6225–6235, 2017.

[94] Z. Yin, H. Tian, G. Chen, and L. O. Chua, "What are memristor, memcapacitor, and meminductor?," *IEEE Transactions on Circuits and Systems II: Express Briefs*, vol. 62, pp. 402–406, apr 2015.

[95] T. Driscoll, H.-T. Kim, B.-G. Chae, B.-J. Kim, Y.-W. Lee, N. M. Jokerst, S. Palit, D. R. Smith, M. D. Ventra, and D. N. Basov, "Memory metamaterials," *Science*, vol. 325, pp. 1518–1521, aug 2009.

[96] J. Georgiou, K. M. Kossifos, M. A. Antoniades, A. Jaafar, and N. T. Kemp, "Chua memcomponents for adaptive RF metamaterials," in *2018 IEEE International Symposium on Circuits and Systems (ISCAS)*, IEEE, may 2018.

[97] K. M. Kossifos, M. A. Antoniades, J. Georgiou, A. H. Jaafar, and N. T. Kemp, "An optically-programmable absorbing metasurface," in *2018 IEEE International Symposium on Circuits and Systems (ISCAS)*, IEEE, may 2018.

[98] C. Pollock, L. K. Barrett, P. G. del Corro, A. Stange, T. G. Bifano, and D. J. Bishop, "PWM as a low cost method for the analog control of MEMS devices," *Journal of Microelectromechanical Systems*, vol. 28, pp. 245–253, apr 2019.

[99] Q. Hu, K. Chen, N. Zhang, J. Zhao, T. Jiang, J. Zhao, and Y. Feng, "Arbitrary and dynamic poincaré sphere polarization converter with a time-varying metasurface," *Advanced Optical Materials*, vol. 10, p. 2101915, dec 2021.

[100] L. Bao, Q. Ma, R. Y. Wu, X. Fu, J. Wu, and T. J. Cui, "Programmable reflection–transmission shared-aperture metasurface for real-time control of electromagnetic waves in full space," *Advanced Science*, vol. 8, p. 2100149, may 2021.

[101] L. Zhang, X. Q. Chen, R. W. Shao, J. Y. Dai, Q. Cheng, G. Castaldi, V. Galdi, and T. J. Cui, "Breaking reciprocity with space-time-coding digital metasurfaces," *Advanced Materials*, vol. 31, p. 1904069, aug 2019.

[102] Y. Liu, X. Mu, J. Xu, R. Schober, Y. Hao, H. V. Poor, and L. Hanzo, "STAR: Simultaneous transmission and reflection for 360° coverage by intelligent surfaces," *IEEE Wireless Communications*, vol. 28, pp. 102–109, dec 2021.

[103] Y. Hadad, D. L. Sounas, and A. Alu, "Space-time gradient metasurfaces," *Physical Review B*, vol. 92, p. 100304, sep 2015.

[104] V. Arun and H. Balakrishnan, "Rfocus: Beamforming using thousands of passive antennas," in *17th USENIX Symposium on Networked Systems Design and Implementation (NSDI 20)*, (Santa Clara, CA), pp. 1047–1061, USENIX Association, Feb. 2020.

[105] G. C. Trichopoulos, P. Theofanopoulos, B. Kashyap, A. Shekhawat, A. Modi, T. Osman, S. Kumar, A. Sengar, A. Chang, and A. Alkhateeb, "Design and evaluation of reconfigurable intelligent surfaces in real-world environment," *arXiv preprint arXiv:2109.07763*.

[106] A. Araghi, M. Khalily, M. Safaei, A. Bagheri, V. Singh, F. Wang, and R. Tafazolli, "Reconfigurable intelligent surface (RIS) in the sub-6 GHz band: Design, implementation, and real-world demonstration," *IEEE Access*, vol. 10, pp. 2646–2655, 2022.

[107] X. Pei, H. Yin, L. Tan, L. Cao, and T. Yang, "Prototyping and real-world field trials of ris-aided wireless communications," 2023.

[108] J. Sang, M. Zhou, J. Lan, B. Gao, W. Tang, X. Li, S. Jin, E. Basar, C. Li, Q. Cheng, and T. J. Cui, "Multi-scenario broadband channel measurement and modeling for sub-6 ghz ris-assisted wireless communication systems," May 2023.

[109] F. Capra, F. Albi, A. Benoni, D. Erricolo, G. Oliveri, P. Rocca, M. Salucci, S. Yang, and A. Massa, "Smart electromagnetic environments empowering future communication

systems: A real-world indoor experimental validation," in *2023 12th International Conference on Modern Circuits and Systems Technologies (MOCAST)*, IEEE, jun 2023.

[110] M. A. ElMossallamy, H. Zhang, L. Song, K. G. Seddik, Z. Han, and G. Y. Li, "Reconfigurable intelligent surfaces for wireless communications: Principles, challenges, and opportunities," *IEEE Transactions on Cognitive Communications and Networking*, vol. 6, pp. 990–1002, sep 2020.

[111] Q. Wu, S. Zhang, B. Zheng, C. You, and R. Zhang, "Intelligent reflecting surface-aided wireless communications: A tutorial," *IEEE Transactions on Communications*, vol. 69, pp. 3313–3351, may 2021.

[112] Y. Liu, X. Liu, X. Mu, T. Hou, J. Xu, M. D. Renzo, and N. Al-Dhahir, "Reconfigurable intelligent surfaces: Principles and opportunities," *IEEE Communications Surveys &amp Tutorials*, vol. 23, no. 3, pp. 1546–1577, 2021.

[113] R. C. Hansen, *Small antenna handbook*. Hoboken, N.J.: J. Wiley Sons, 2011. Includes bibliographical references and index. - Description based on print version record.

[114] J. Sang, Y. Yuan, W. Tang, Y. Li, X. Li, S. Jin, Q. Cheng, and T. J. Cui, "Coverage enhancement by deploying RIS in 5g commercial mobile networks: Field trials," *IEEE Wireless Communications*, pp. 1–21, 2022.

[115] G. Oliveri, M. Salucci, and A. Massa, "Generalized analysis and unified design of EM skins," *IEEE Transactions on Antennas and Propagation*, vol. 71, pp. 6579–6592, aug 2023.

[116] D. Pozar and T. Metzler, "Analysis of a reflectarray antenna using microstrip patches of variable size," *Electronics Letters*, vol. 29, no. 8, p. 657, 1993.

[117] Y. L. C. de Jong, "Uniform ray description of physical optics scattering by finite locally periodic metasurfaces," *IEEE Transactions on Antennas and Propagation*, vol. 70, pp. 2949–2959, apr 2022.

[118] E. Björnson, Özgecan Özdogan, and E. G. Larsson, "Reconfigurable intelligent surfaces: Three myths and two critical questions,"

[119] Y. Yuan, *LTE-Advanced relay technology and standardization*. Springer Science & Business Media, 2012.

[120] R. Liu, Q. Wu, M. D. Renzo, and Y. Yuan, "A path to smart radio environments: An industrial viewpoint on reconfigurable intelligent surfaces," *IEEE Wireless Communications*, vol. 29, pp. 202–208, feb 2022.

[121] Y. Yuan, D. Wu, Y. Huang, and C.-L. I, "Reconfigurable intelligent surface relay: Lessons of the past and strategies for its success," *IEEE Communications Magazine*, vol. 60, pp. 117–123, Dec. 2022.

[122] M. Jung, W. Saad, M. Debbah, and C. S. Hong, "On the optimality of reconfigurable intelligent surfaces (riss): Passive beamforming, modulation, and resource allocation,"

[123] Y. Sun, B. Duan, X. Su, H. Wang, Q. Gu, J. Jin, and Y. Yuan, "3gpp release-18," *Frontiers of Information Technology & Electronic Engineering*, vol. 24, pp. 1815–1828, Dec. 2023.

[124] C. Huang, A. Zappone, G. C. Alexandropoulos, M. Debbah, and C. Yuen, "Reconfigurable intelligent surfaces for energy efficiency in wireless communication," *IEEE Transactions on Wireless Communications*, vol. 18, pp. 4157–4170, aug 2019.

[125] J. Ye, A. Kammoun, and M.-S. Alouini, "Spatially-distributed riss vs relay-assisted systems: A fair comparison," *IEEE Open Journal of the Communications Society*, vol. 2, pp. 799–817, 2021.

[126] M. Dunna, C. Zhang, D. Sievenpiper, and D. Bharadia, "ScatterMIMO," in *Proceedings of the 26th Annual International Conference on Mobile Computing and Networking*, ACM, apr 2020.

[127] E. Bjornson, H. Wymeersch, B. Matthiesen, P. Popovski, L. Sanguinetti, and E. de Carvalho, "Reconfigurable intelligent surfaces: A signal processing perspective with wireless applications," *IEEE Signal Processing Magazine*, vol. 39, pp. 135–158, Mar. 2022.

[128] A. Zappone, M. Di Renzo, F. Shams, X. Qian, and M. Debbah, "Overhead-aware design of reconfigurable intelligent surfaces in smart radio environments," *IEEE Transactions on Wireless Communications*, vol. 20, pp. 126–141, Jan. 2021.

[129] T. Ohyama, Y. Kawamoto, and N. Kato, "Standalone intelligent reflecting surface with automatic update of phase-shift switching schedule for improved communication and localization," *IEEE Transactions on Vehicular Technology*, pp. 1–11, 2024.

[130] E. Arslan, F. Kilinc, E. Basar, and H. Arslan, "Network-independent and user-controlled ris: An experimental perspective," in *2023 26th International Symposium on Wireless Personal Multimedia Communications (WPMC)*, IEEE, Nov. 2023.

[131] "3gpp release 18," 2023.

[132] Y. Huo, X. Dong, and W. Xu, "5g cellular user equipment: From theory to practical hardware design," *IEEE Access*, vol. 5, pp. 13992–14010, 2017.

[133] F. W. Vook, A. Ghosh, E. Diarte, and M. Murphy, "5g new radio: Overview and performance," in *2018 52nd Asilomar Conference on Signals, Systems, and Computers*, IEEE, Oct. 2018.

[134] K. Zhi, C. Pan, H. Ren, and K. Wang, "Power scaling law analysis and phase shift optimization of ris-aided massive mimo systems with statistical csi," *IEEE Transactions on Communications*, vol. 70, pp. 3558–3574, May 2022.

[135] X. Pei, H. Yin, L. Tan, L. Cao, Z. Li, K. Wang, K. Zhang, and E. Bjornson, "RIS-aided wireless communications: Prototyping, adaptive beamforming, and indoor/outdoor field trials," *IEEE Transactions on Communications*, vol. 69, pp. 8627–8640, dec 2021.

[136] G. Sun, R. He, B. Ai, Z. Ma, P. Li, Y. Niu, J. Ding, D. Fei, and Z. Zhong, "A 3d wideband channel model for ris-assisted mimo communications," *IEEE Transactions on Vehicular Technology*, vol. 71, pp. 8016–8029, Aug. 2022.

[137] A. Benoni, F. Capra, M. Salucci, and A. Massa, "Towards real-world indoor smart electromagnetic environments – a large-scale experimental demonstration," Apr. 2023.

[138] V. Ntranos, M. A. Maddah-Ali, and G. Caire, "Cellular interference alignment: Omnidirectional antennas and asymmetric configurations," *IEEE Transactions on Information Theory*, vol. 61, pp. 6663–6679, Dec. 2015.

[139] T. Sharma, A. Chehri, and P. Fortier, "Reconfigurable intelligent surfaces for 5g and beyond wireless communications: A comprehensive survey," *Energies*, vol. 14, p. 8219, Dec. 2021.

[140] W. Li, S. Xia, B. He, J. Chen, H. Shi, A. Zhang, Z. Li, and Z. Xu, "A reconfigurable polarization converter using active metasurface and its application in horn antenna," *IEEE Transactions on Antennas and Propagation*, vol. 64, pp. 5281–5290, Dec. 2016.

[141] J.-B. Gros, V. Popov, M. A. Odit, V. Lenets, and G. Lerosey, "A reconfigurable intelligent surface at mmwave based on a binary phase tunable metasurface," *IEEE Open Journal of the Communications Society*, vol. 2, pp. 1055–1064, 2021.

[142] Y. Han, X. Li, W. Tang, S. Jin, Q. Cheng, and T. J. Cui, "Dual-polarized ris-assisted mobile communications," *IEEE Transactions on Wireless Communications*, vol. 21, no. 1, pp. 591–606, 2022.

[143] M. D. Renzo, F. H. Danufane, and S. Tretyakov, "Communication models for reconfigurable intelligent surfaces: From surface electromagnetics to wireless networks optimization," *arXiv preprint, arXiv:2110.00833*.

[144] D. Wang, D. Tan, and L. Liu, "Particle swarm optimization algorithm: an overview," *Soft Computing*, vol. 22, pp. 387–408, jan 2017.

[145] H. Luyen, J. H. Booske, and N. Behdad, "2-bit phase quantization using mixed polarization-rotation/non-polarization-rotation reflection modes for beam-steerable reflectarrays," *IEEE Transactions on Antennas and Propagation*, pp. 1–1, 2020.

[146] S. Tretyakov, *Analytical Modeling in Applied Electromagnetics*. ARTECH HOUSE INC, 2003.

[147] K. Ntokos, P. Mavrikakis, A. C. Iossifides, and T. V. Yioultsis, "A systematic approach for reconfigurable reflecting metasurface synthesis: From periodic analysis to far-field scattering," *AEU - International Journal of Electronics and Communications*, vol. 170, p. 154780, Oct. 2023.

[148] X. Wan, M. Q. Qi, T. Y. Chen, and T. J. Cui, "Field-programmable beam reconfiguring based on digitally-controlled coding metasurface," *Scientific Reports*, vol. 6, feb 2016.

[149] X. G. Zhang, Q. Yu, W. X. Jiang, Y. L. Sun, L. Bai, Q. Wang, C.-W. Qiu, and T. J. Cui, "Polarization-controlled dual-programmable metasurfaces," *Advanced Science*, vol. 7, p. 1903382, apr 2020.

[150] K. Chen, N. Zhang, G. Ding, J. Zhao, T. Jiang, and Y. Feng, "Active anisotropic coding metasurface with independent real-time reconfigurability for dual polarized waves," *Advanced Materials Technologies*, vol. 5, p. 1900930, dec 2019.

[151] M. Jung, W. Saad, M. Debbah, and C. S. Hong, "On the optimality of reconfigurable intelligent surfaces (riss): Passive beamforming, modulation, and resource allocation," *IEEE Transactions on Wireless Communications*, vol. 20, pp. 4347–4363, July 2021.

[152] H. Xie and D. Li, "How much time is required for phase shift delivery in ris-aided wireless systems?," *IEEE Wireless Communications Letters*, vol. 13, pp. 819–823, Mar. 2024.

[153] G. C. Alexandropoulos, K. D. Katsanos, M. Wen, and D. B. Da Costa, "Counteracting eavesdropper attacks through reconfigurable intelligent surfaces: A new threat model and secrecy rate optimization," *IEEE Open Journal of the Communications Society*, vol. 4, pp. 1285–1302, 2023.

[154] J. Rodriguez Sanchez, F. Rusek, O. Edfors, and L. Liu, "Distributed and scalable uplink processing for lis: Algorithm, architecture, and design trade-offs," *IEEE Transactions on Signal Processing*, vol. 70, pp. 2639–2653, 2022.

[155] J. Tosi, F. Taffoni, M. Santacatterina, R. Sannino, and D. Formica, "Performance evaluation of bluetooth low energy: A systematic review," *Sensors*, vol. 17, p. 2898, Dec. 2017.

[156] M. Hoppari, M. Uitto, J. Mäkelä, I. Harjula, and S. Rantala, "Performance of the 5th generation indoor wireless technologies-empirical study," *Future Internet*, vol. 13, p. 180, jul 2021.

[157] P. Kafle, A. Intarapanich, A. Sesay, J. Mcrory, and R. Davies, "Spatial correlation and capacity measurements for wideband MIMO channels in indoor office environment," *IEEE Transactions on Wireless Communications*, vol. 7, pp. 1560–1571, may 2008.

[158] J. W. Wallace, W. Ahmad, Y. Yang, R. Mehmood, and M. A. Jensen, "A comparison of indoor MIMO measurements and ray-tracing at 24 and 2.55 GHz," *IEEE Transactions on Antennas and Propagation*, vol. 65, pp. 6656–6668, dec 2017.

[159] F. Dan, C. Chen, Z. Peng, Y. Mingbo, D. Jianwen, W. Wei, Z. Jiayi, A. Bo, J. Shi, and C. T. Jun, "Research and experimental verification of reconfigurable intelligent surface in indoor coverage enhancement," *Journal of Electronics & Information Technology*, vol. 44, no. 220068, 2022.

[160] B. Bertenyi, S. Nagata, H. Kooropaty, X. Zhou, W. Chen, Y. Kim, X. Dai, and X. Xu, "5g nr radio interface," *Journal of ICT Standardization*, vol. 6, no. 1, pp. 31–58, 2018.

[161] J. Wang, S. Gong, Q. Wu, and S. Ma, "Ris-aided mimo systems with hardware impairments: Robust beamforming design and analysis," *IEEE Transactions on Wireless Communications*, vol. 22, pp. 6914–6929, Oct. 2023.

[162] L. Miller and J. Cavazos, *5G and Beyond for Dummies*. John Wiley and Sons, 2022.

[163] A. Hassanien, M. G. Amin, Y. D. Zhang, and F. Ahmad, "Signaling strategies for dual-function radar communications: an overview," *IEEE Aerospace and Electronic Systems Magazine*, vol. 31, pp. 36–45, oct 2016.

[164] OpenStreetMap contributors, "Planet dump retrieved from https://planet.osm.org." https://www.openstreetmap.org , 2017.

[165] A. W. Mbugua, W. Fan, K. Olesen, X. Cai, and G. F. Pedersen, "Phase-compensated optical fiber-based ultrawideband channel sounder," *IEEE Transactions on Microwave Theory and Techniques*, vol. 68, pp. 636–647, feb 2020.

[166] W. Young, K. Remley, J. Ladbury, C. Holloway, C. Grosvenor, G. Koepke, S. Floris, W. Numan, and A. Garuti, "Measurements to support public safety communications: At-

tenuation and variability of 750 mhz radio wave signals in four large building structures: Nist technical note 1552," 2009-08-07 00:08:00 2009.

[167] Y. Lyu, A. W. Mbugua, Z. Yuan, K. Olesen, and W. Fan, "Design and validation of a multilink phase- compensated long-range ultrawideband vna-based channel sounder," *IEEE Transactions on Microwave Theory and Techniques*, vol. 70, pp. 4528–4543, Oct. 2022.

[168] R. Y. Wu, C. B. Shi, S. Liu, W. Wu, and T. J. Cui, "Addition theorem for digital coding metamaterials," *Advanced Optical Materials*, vol. 6, p. 1701236, jan 2018.

[169] O. Roy and M. Vetterli, "The effective rank: A measure of effective dimensionality," in *2007 15th European Signal Processing Conference*, pp. 606–610, 2007.

[170] H. Du, J. Zhang, J. Cheng, and B. Ai, "Millimeter wave communications with reconfigurable intelligent surfaces: Performance analysis and optimization," *IEEE Transactions on Communications*, vol. 69, pp. 2752–2768, Apr. 2021.

[171] F. Pasic, D. Schutzenhofer, E. Jirousek, R. Langwieser, H. Groll, S. Pratschner, S. Caban, S. Schwarz, and M. Rupp, "Comparison of sub 6 ghz and mmwave wireless channel measurements at high speeds," in *2022 16th European Conference on Antennas and Propagation (EuCAP)*, IEEE, Mar. 2022.

[172] S. Lin, B. Zheng, G. C. Alexandropoulos, M. Wen, M. D. Renzo, and F. Chen, "Reconfigurable intelligent surfaces with reflection pattern modulation: Beamforming design and performance analysis," *IEEE Transactions on Wireless Communications*, vol. 20, pp. 741–754, Feb. 2021.

[173] A. I. Sulyman, A. T. Nassar, M. K. Samimi, G. R. Maccartney, T. S. Rappaport, and A. Alsanie, "Radio propagation path loss models for 5g cellular networks in the 28 ghz and 38 ghz millimeter-wave bands," *IEEE Communications Magazine*, vol. 52, pp. 78–86, Sept. 2014.

[174] M. R. Akdeniz, Y. Liu, M. K. Samimi, S. Sun, S. Rangan, T. S. Rappaport, and E. Erkip, "Millimeter wave channel modeling and cellular capacity evaluation," *IEEE Journal on Selected Areas in Communications*, vol. 32, pp. 1164–1179, June 2014.

[175] J. Yang, Y. Chen, M. Jian, J. Dou, and M. Fang, "Capacity improvement in reconfigurable intelligent surface assisted mimo communications," *IEEE Access*, vol. 9, pp. 137460–137469, 2021.

[176] T. Choi, F. Rottenberg, J. Gomez-Ponce, A. Ramesh, P. Luo, C. J. Zhang, and A. F. Molisch, "Experimental investigation of frequency domain channel extrapolation in massive MIMO systems for zero-feedback FDD," *IEEE Transactions on Wireless Communications*, vol. 20, pp. 710–725, jan 2021.

[177] R. Flamini, D. D. Donno, J. Gambini, F. Giuppi, C. Mazzucco, A. Milani, and L. Resteghini, "Toward a heterogeneous smart electromagnetic environment for millimeter-wave communications: An industrial viewpoint," *IEEE Transactions on Antennas and Propagation*, vol. 70, pp. 8898–8910, oct 2022.

[178] G. Pan, J. Ye, J. An, and M.-S. Alouini, "When full-duplex transmission meets intelligent reflecting surface: Opportunities and challenges,"

Appendix A

Documentation for the 1-bit RIS prototype

A.1 Schematics

The schematic diagrams for the 1-bit dual-polarised RIS have been made available here. These schematics are for a single RIS tile consisting of an arrangement of 16×16 RIS elements. Fig. A.1 shows a top-level view of the circuit. The peripherals consist of connectors for the input signals and voltage distribution to provide power to adjacent tiles. These are in the form of standard pin headers.

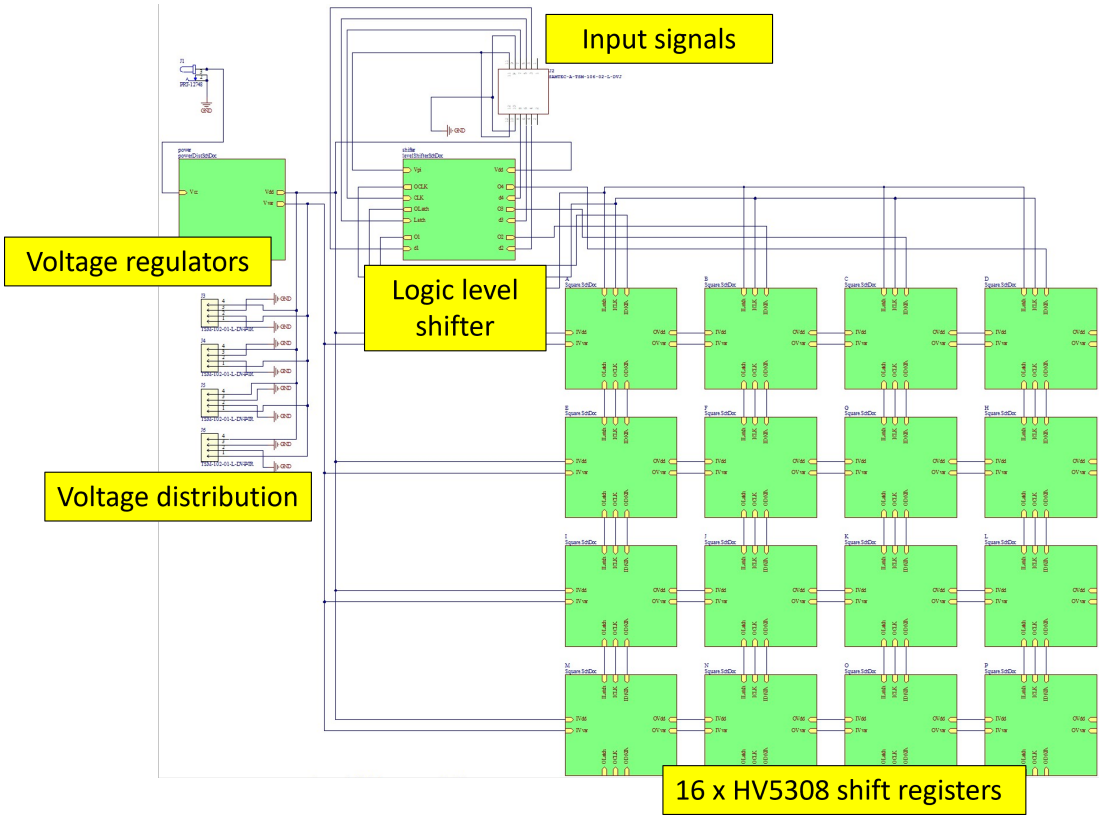

Figure A.1: Top-level schematic for the 1-bit RIS tile

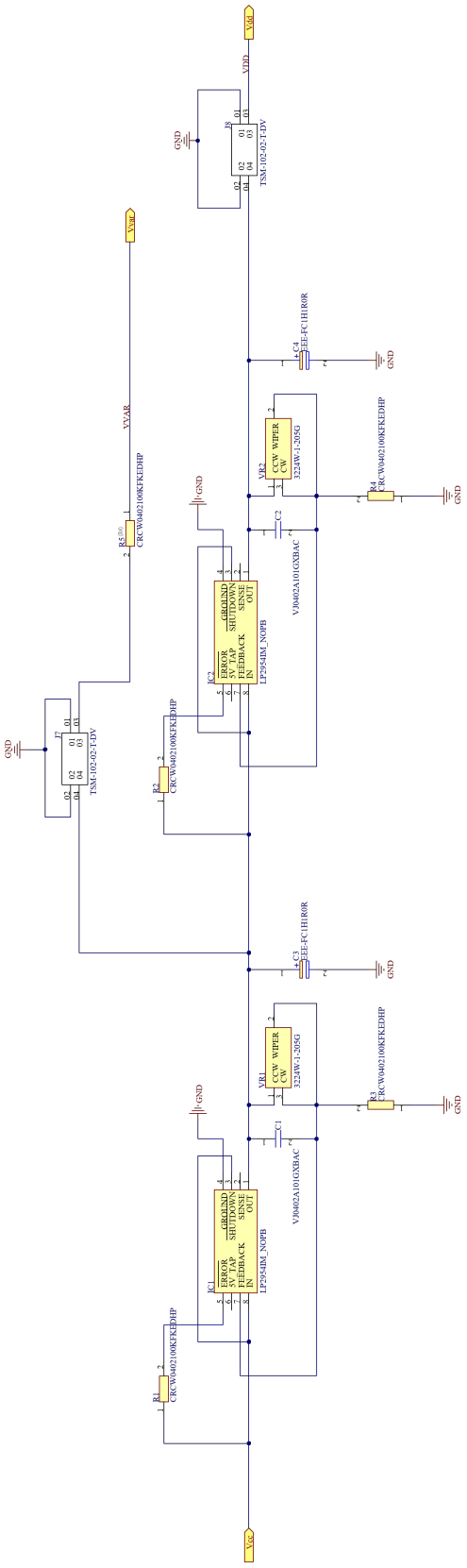

Figure A.2: Voltage regulator schematic for the 1-bit RIS tile

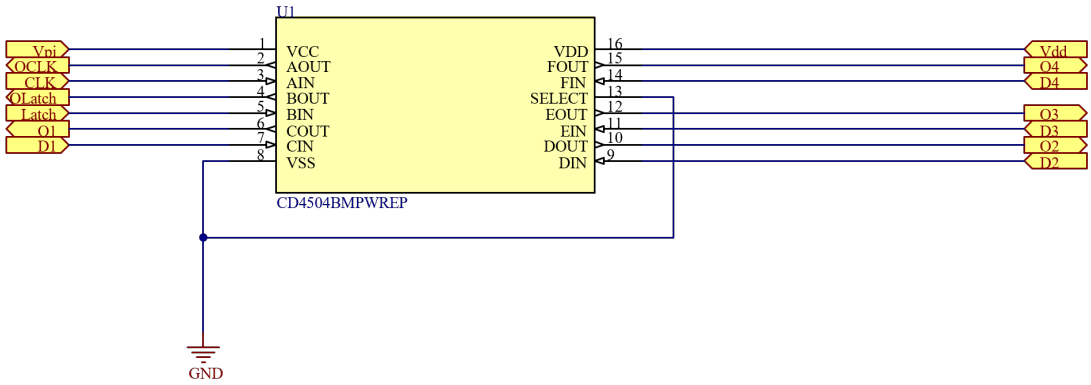

Figure A.3: Level shifter schematic for the 1-bit RIS tile

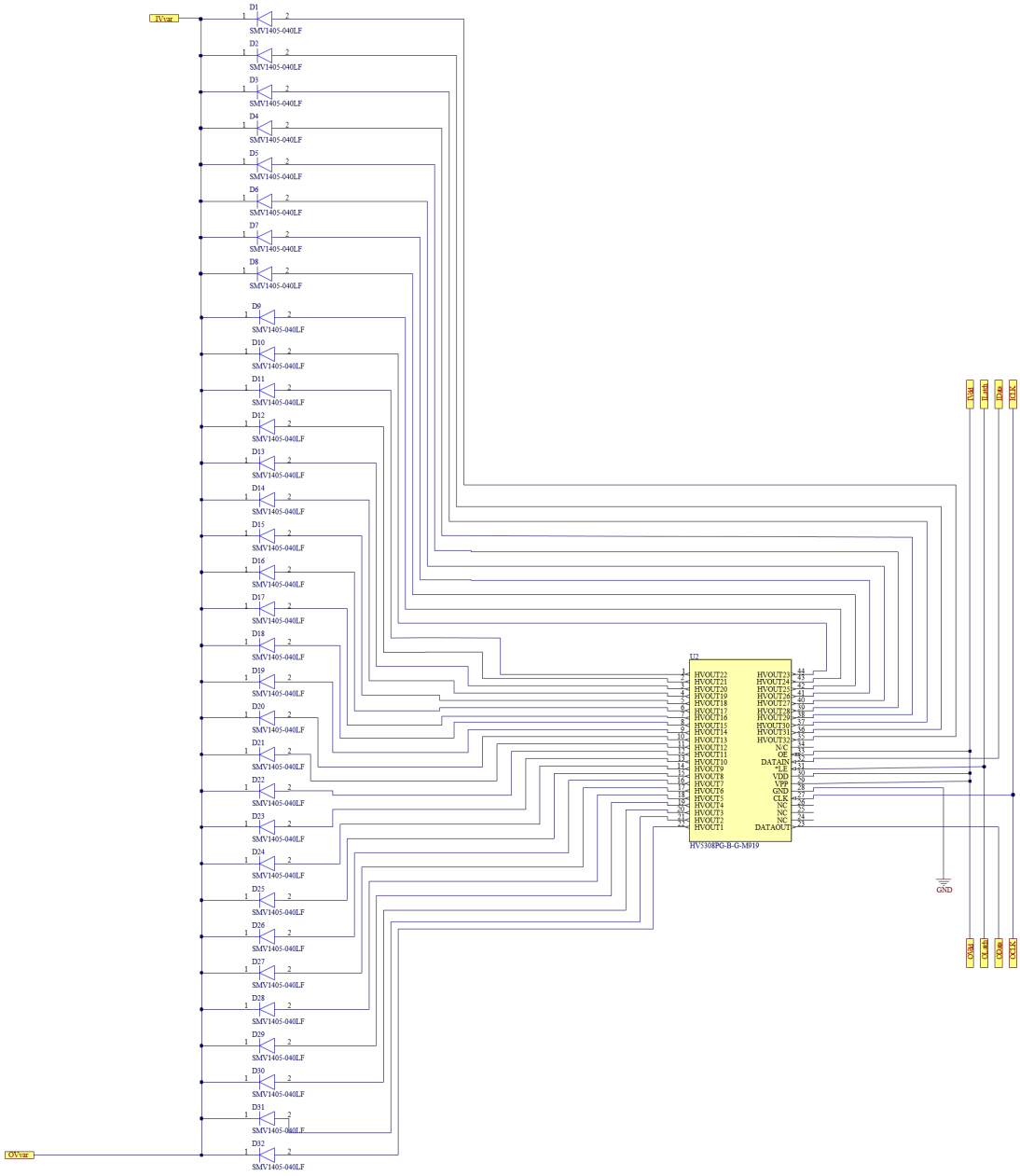

Figure A.4: Shift register schematic for the 1-bit RIS tile

A.2 PCB layout

The top layer of the PCB is populated by the components in the above schematics with the exception of the varactor diodes, which are confined to the bottom layer. The bottom layer hosts the F4BM-2 220 microwave substrate with a thickness of 1.5 mm. The remaining layers employ FR4 material for its rigidity and cost-effectiveness.

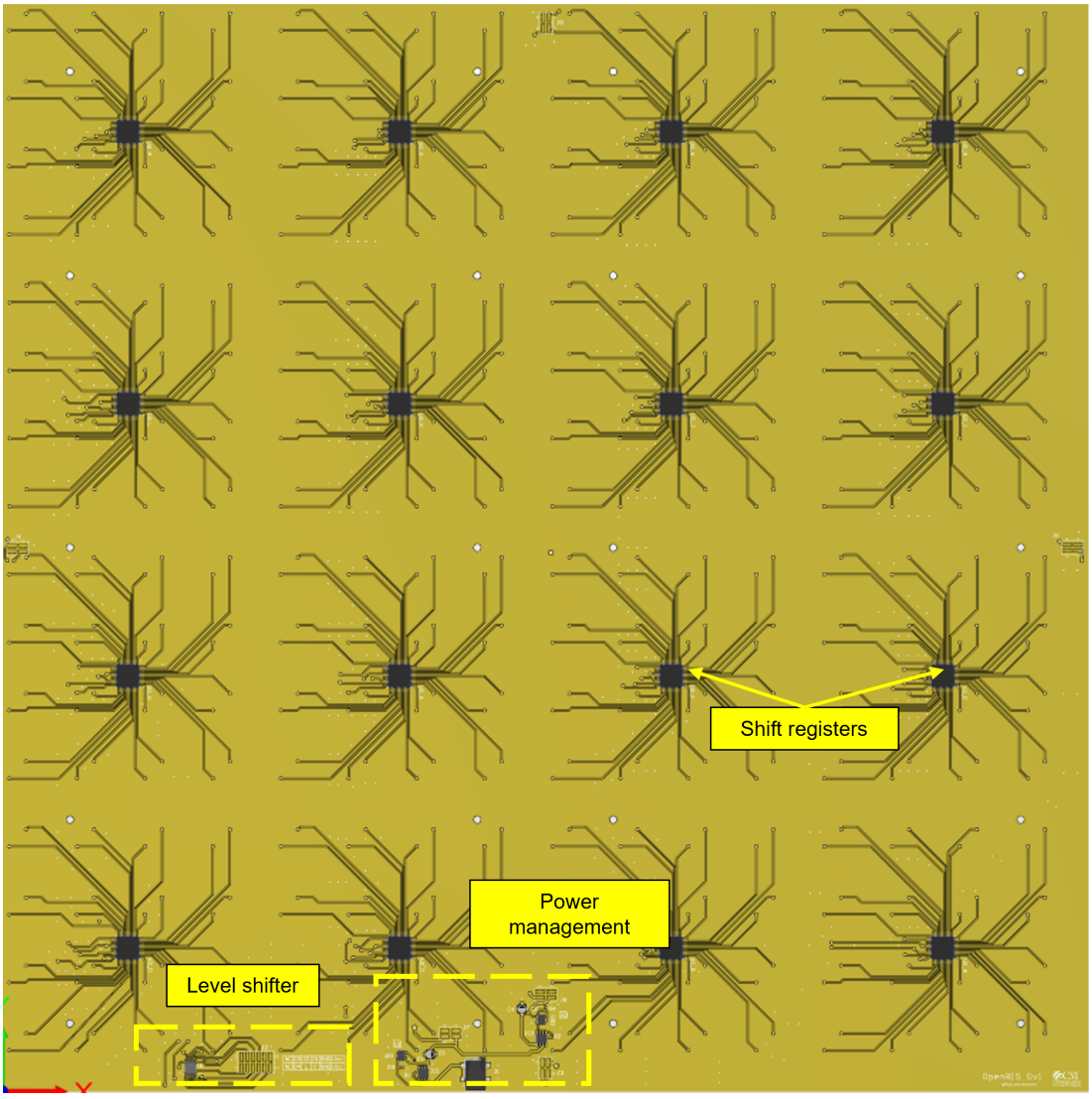

Figure A.5: Top-level schematic for the 1-bit RIS tile

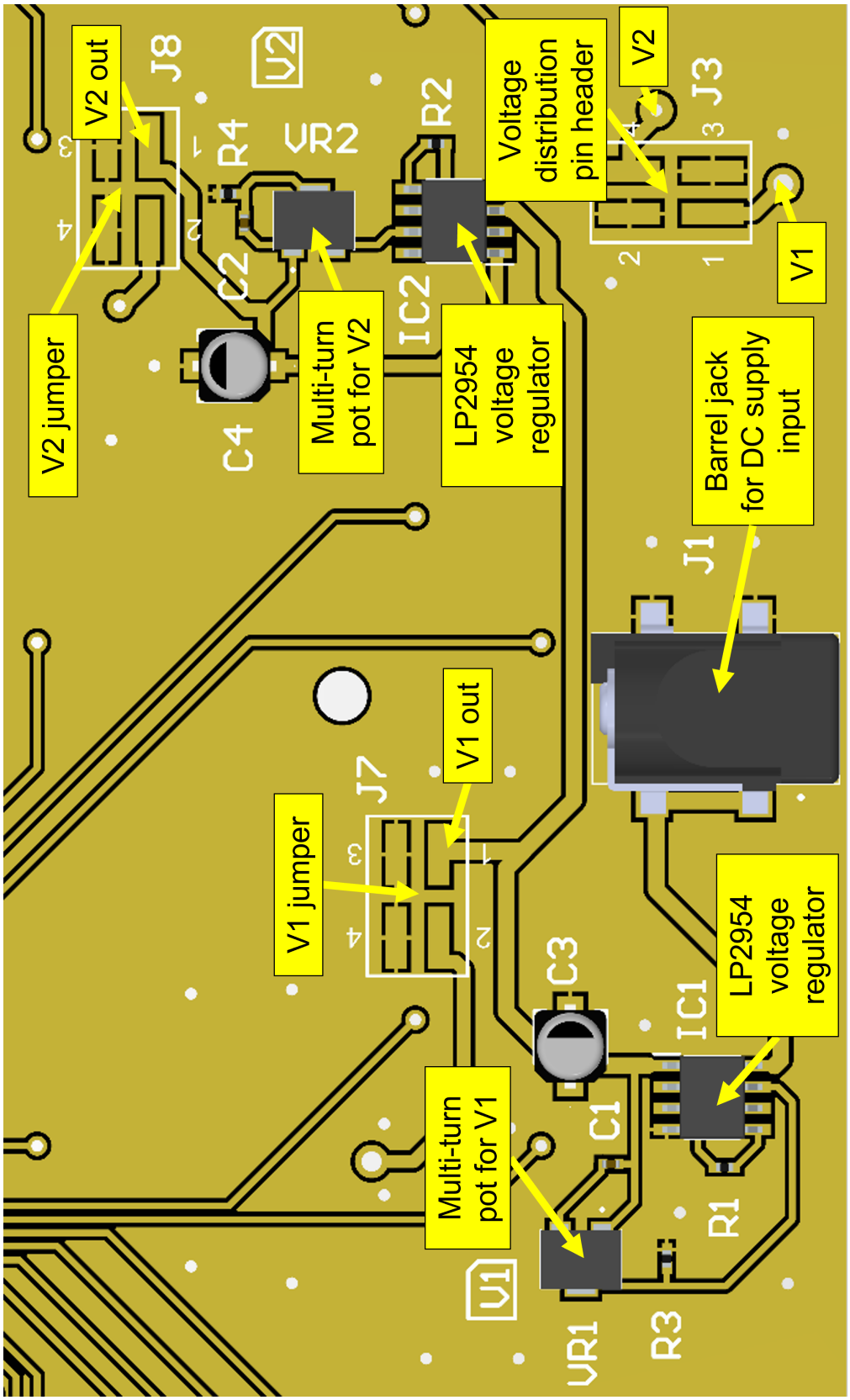

Figure A.6: Voltage regulator PCB layout for the 1-bit RIS tile

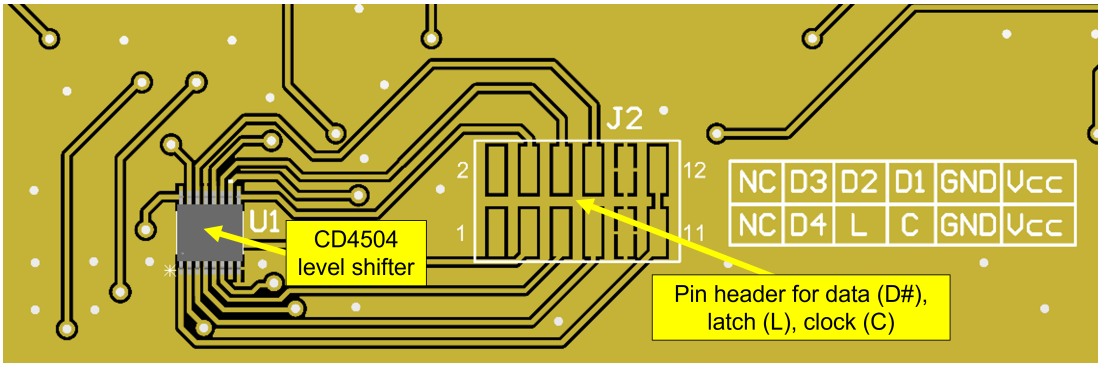

Figure A.7: Level shifter and signal pin PCB layout for the 1-bit RIS tile

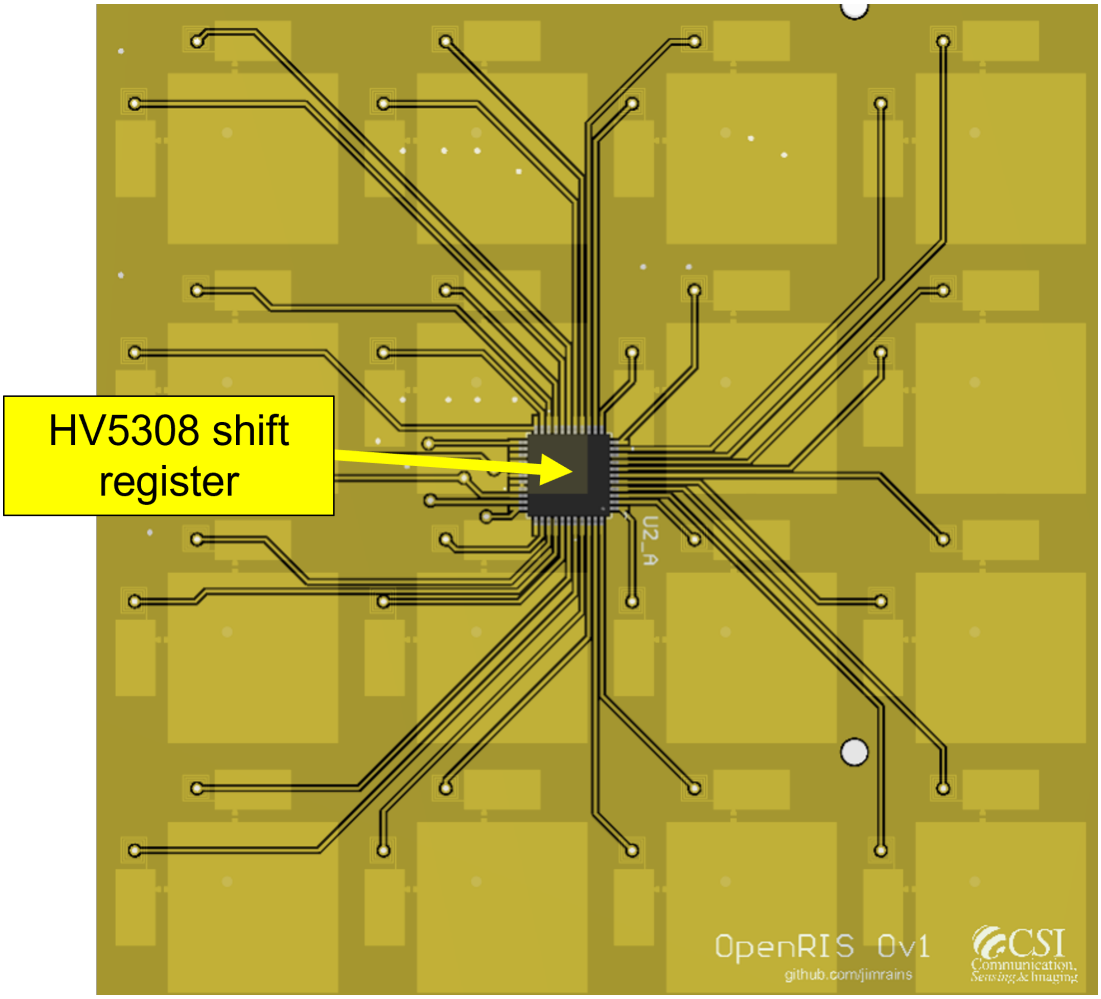

Figure A.8: Shift register PCB layout for the 1-bit RIS tile, with unit cells visible through transparency introduced into the model.